Towards brain-scale modelling of the human cerebral blood flow : hybrid approach and high performance computing

Myriam Peyrounette

THÈSE

En vue de l'obtention du

DOCTORAT DE L'UNIVERSITÉ DE TOULOUSE

Délivré par :

Institut National Polytechnique de Toulouse (INP Toulouse)

Discipline ou spécialité :

Dynamique des fluides

Présentée et soutenue par :

Mme MYRIAM PEYROUNETTE

le mercredi 25 octobre 2017

Titre :

Towards brain-scale modelling of the human cerebral blood flow: hybrid approach and high performance computing

---

Ecole doctorale :

Mécanique, Energétique, Génie civil, Procédés (MEGeP)

Unité de recherche :

Institut de Mécanique des Fluides de Toulouse (I.M.F.T.)

Directeur(s) de Thèse :

MME SYLVIE LORTHOIS

M. YOHAN DAVIT

Rapporteurs :

M. BENOÎT NOETINGER, IFPEN

M. PIERRE-YVES LAGREE, UNIVERSITE PIERRE ET MARIE CURIE

Membre(s) du jury :

Mme STEPHANIE PITRE-CHAMPAGNAT, UNIVERSITE PARIS 11, Président

M. MICHEL QUINTARD, INP TOULOUSE, Membre

M. PATRICK JENNY, ECOLE POLYTECHNIQUE FEDERALE DE ZURICH, Membre

Contents

Abstract

Towards brain-scale modelling of the human cerebral blood flow: hybrid approach and high performance computing

The brain microcirculation plays a key role in cerebral physiology and neuronal activation. In the case of degenerative diseases such as Alzheimer's, severe deterioration of the microvascular networks (e.g. vascular occlusions) limit blood flow, thus oxygen and nutrients supply, to the cortex, eventually resulting in neurons death. In addition to functional neuroimaging, modelling is a valuable tool to investigate the impact of structural variations of the microvasculature on blood flow and mass transfers.

In the brain microcirculation, the capillary bed contains the smallest vessels (1-10 μm in diameter) and presents a mesh-like structure embedded in the cerebral tissue. This is the main place of molecular exchange between blood and neurons. The capillary bed is fed and drained by larger arteriolar and venular tree-like vessels (10-100 μm in diameter).

For the last decades, standard network approaches have significantly advanced our understanding of blood flow, mass transport and regulation mechanisms in the human brain microcirculation. By averaging flow equations over the vascular cross-sections, such approaches yield a one-dimensional model that involves much fewer variables compared to a full three-dimensional resolution of the flow. However, because of the high density of capillaries, such approaches are still computationally limited to relatively small volumes ($<$100 mm^3). This constraint prevents applications at clinically relevant scales, since standard imaging techniques only yield much larger volumes ($\sim$100 cm^3), with a resolution of 1-10 mm^3.

To get around this computational cost, we present a hybrid approach for blood flow modelling where the capillaries are replaced by a continuous medium. This substitution makes sense since the capillary bed is dense and space-filling over a cut-off length of $\sim$50 μm. In this continuum, blood flow is characterized by effective properties (e.g. permeability) at the scale of a much larger representative volume. Furthermore, the domain is discretized on a coarse grid using the finite volume method, inducing an important computational gain. The arteriolar and venular trees cannot be homogenized because of their quasi-fractal structure, thus the network approach is used to model blood flow in the larger vessels.

The main difficulty of the hybrid approach is to develop a proper coupling model at the points where arteriolar or venular vessels are connected to the continuum. Indeed, high pressure gradients build up at capillary-scale in the vicinity of the coupling points, and must be properly described at the continuum-scale. Such multiscale coupling has never been discussed in the context of brain microcirculation. Taking inspiration from the Peaceman "well model" developed for petroleum engineering, our coupling model relies on to use analytical solutions of the pressure field in the neighbourhood

of the coupling points. The resulting equations yield a single linear system to solve for both the network part and the continuum (strong coupling).

The accuracy of the hybrid model is evaluated by comparison with a classical network approach, for both very simple synthetic architectures involving no more than two couplings, and more complex ones, with anatomical arteriolar and venular trees displaying a large number of couplings. We show that the present approach is very accurate, since relative pressure errors are lower than 6 %. This lays the goundwork for introducing additional levels of complexity in the future (e.g. non uniform hematocrit).

In the perspective of large-scale simulations and extension to mass transport, the hybrid approach has been implemented in a C++ code designed for High Performance Computing. It has been fully parallelized using Message Passing Interface standards and specialized libraries (e.g. PETSc). Since the present work is part of a larger project involving several collaborators, special care has been taken in developing efficient coding strategies.

Résumé

Vers une modélisation de l'écoulement sanguin cérébral humain à l'échelle du cerveau : approche hybride et calcul haute performance

La microcirculation cérébrale joue un rôle clé dans la physiologie cérébrale. Lors de maladies dégénératives comme celle d'Alzheimer, la détérioration des réseaux microvasculaires (e.g. occlusions et baisse de densité vasculaires) limite l'afflux sanguin vers le cortex. La réduction associée de l'apport en oxygène et nutriments risque de provoquer la mort de neurones. En complément des techniques d'imagerie médicale, la modélisation est un outil précieux pour comprendre l'impact de telles variations structurelles sur l'écoulement sanguin et les transferts de masse. Dans la microcirculation cérébrale, le lit capillaire contient les plus petits vaisseaux (diamètre de 1-10 μm) et présente une structure maillée, au sein du tissu cérébral. C'est le lieu principal des échanges moléculaires entre le sang et les neurones. Le lit capillaire est alimenté et drainé par les arbres artériolaires et veinulaires (diamètre de 10-100 μm). Depuis quelques décennies, les approches "réseau" ont significativement amélioré notre compréhension de l'écoulement sanguin, du transport de masse et des mécanismes de régulation dans la microcirculation cérébrale humaine. Cependant, d'un point de vue numérique, la densité des capillaires limite ces approches à des volumes relativement petits ($<$100 mm^3). Cette contrainte empêche leur application à des échelles cliniques, puisque les techniques d'imagerie médicale permettent d'acquérir des volumes bien plus importants ($\sim$100 cm^3), avec une résolution de 1-10 mm. Pour réduire ce coût numérique, nous présentons une approche hybride pour la modélisation de l'écoulement dans laquelle les capillaires sont remplacés par un milieu continu. Cette substitution a du sens puisque le lit capillaire est dense et homogène à partir d'une longueur de coupure de $\sim$50 μm. Dans ce continuum, l'écoulement est caractérisé par des propriétés effectives (e.g. perméabilité) à l'échelle d'un volume représentatif plus grand. De plus, le continuum est discrétisé par la méthode des volumes finis sur un maillage grossier, ce qui induit un gain numérique important. Les arbres artério- et veinulaires ne peuvent être homogénéisés à cause de leur structure quasi-fractale. Nous appliquons donc une approche "réseau" standard dans les vaisseaux les plus larges. La principale difficulté de l'approche hybride est de développer un modèle de couplage aux points où les vaisseaux artério- et veinulaires sont connectés au continuum. En effet, de forts gradients de pression apparaissent à proximité de ces points, et doivent être homogénéisés proprement à l'échelle du continuum. Ce genre de couplage multi-échelle n'a jamais été introduit dans le contexte de la microcirculation cérébrale. Nous nous inspirons ici du "modèle de puits" développé par Peaceman pour l'ingénierie pétrolière, en utilisant des solutions analytiques du champ des pressions dans le voisinage des points de couplage. Les équations obtenues forment un unique système linéaire à résoudre pour l'ensemble du domaine d'étude. Nous validons l'approche hybride par comparaison avec une approche "réseau" classique, pour des architectures synthétiques simples qui n'impliquent qu'un ou deux couplages, et pour des structures plus complexes qui impliquent des arbres artério- et

veinulaires anatomiques avec un grand nombre de couplages. Nous montrons que cette approche est fiable, puisque les erreurs relatives en pression sont faibles (<6 %). Cela ouvre la voie à une complexification du modèle (e.g. hématocrite non uniforme). Dans une perspective de simulations à grande échelle et d'extension au transport de masse, l'approche hybride a été implémentée dans un code C++ conçu pour le calcul haute performance. Ce code a été entièrement parallélisé en utilisant les standards MPI et des librairies spécialisées (e.g. PETSc). Ce travail faisant partie d'un projet plus large impliquant plusieurs collaborateurs, une attention particulière a été portée à l'établissement de stratégies d'implémentation efficaces.

Remerciements

Les travaux de thèse présentés dans ce manuscrit ont été réalisés au sein du Groupe d'Étude des Milieux Poreux (GEMP) de l'Institut de Mécanique des Fluides de Toulouse (IMFT). Ils ont été financés par une allocation de recherche de l'Institut National Polytechnique de Toulouse (INPT) et par l'ERC Consolidator BrainMicroFlow (GA615102). C'est donc tout naturellement que je tiens à remercier ces différentes institutions, sans lesquelles ce projet de recherche n'aurait pu être mené.

Mercis élémentaires représentatifs

J'amorce la déferlante de remerciements en exprimant ma plus profonde gratitude envers ma directrice de thèse, Sylvie Lorthois. Merci de m'avoir ouvert les portes du monde de la recherche et de m'y avoir tout appris. Merci de l'avoir fait avec tant d'humanité et de justesse. Merci de m'avoir fait confiance et d'avoir supporter mes peyrounetteries en tout genre. J'admire la manière que tu as de te dévouer à ce qui te tient à coeur et je suis fière d'avoir pu participer à l'aventure BrainMicroFlow, ce beau projet, à la belle ambition, que tu portes avec brio.

Aux côtés de Sylvie, adjoint précieux, je tiens à remercier Yohan Davit. Ta curiosité et ton enthousiasme communicatifs m'ont toujours (re)motivée. J'ai beaucoup apprécié toutes les discussions scientifiques (ou non) que l'on a pu avoir. Tu as de plus su porter sans anicroche la double casquette de directeur de thèse et de camarade, aux côtés des autres doctorants et post-doctorants du groupe GEMP. Je te souhaite de belles années de recherche !

J'aimerais ensuite remercier les deux rapporteurs de ma thèse, Pierre-Yves Lagrée et Benoît Noetinger, qui ont pris le temps de lire avec soin ce manuscrit. Vos retours ont été précieux. Merci également aux autres membres de mon jury, Stéphanie Pitre-Champagnat, Patrick Jenny et Michel Quintard. Merci pour l'intérêt que vous avez porté à ces travaux et pour vos questionnements constructifs.

Un merci particulier à Michel, qui a suivi mes travaux de thèse depuis le début. Merci de m'avoir guidée à la fois dans mes intégrations volumes finis, et dans des dédales spéléologiques inconnus.

Remerciements multi-échelle

À l'échelle internationale, j'aimerais remercier Chris Schaffer et Nozomi Nishimura, qui m'ont accueillie pendant un mois dans leur laboratoire, à la Cornell University. J'y ai beaucoup appris sur la recherche "à l'américaine" et ai pris beaucoup de plaisir à visiter les environs.

À l'échelle de la région, je tiens à remercier le mésocentre CALMIP, pour avoir mis à disposition leur puissance de calcul, mais également un support technique et pédagogique efficace. Je pense notamment aux nombreux messages échangés avec Pierrette Barbaresco lors de ma découverte du supercalculateur EOS.

À l'échelle de l'IMFT, je tiens à remercier le service COSINUS, pour m'avoir conseillée et aidée dans le développement de mon code de simulation. Je pense en particulier à Annaig Pedrono, Kevin Larnier et Pierre Elyakime. Merci d'avoir recompilé PETSc moultes fois sans broncher et de m'avoir guidée dans mes choix de programmation.

Je souhaite également saluer les différents permanents avec qui j'ai eu le plaisir d'enseigner, animer ou seulement discuter. Gérald Debenest, Rachid Ababou, Ludovic Cassan, Rémi Zamansky, Thomas Bonometti, Dominique Anne-Archard, Pauline Assémat, Pascal Swider. Merci d'avoir fait de mon passage à l'IMFT une expérience riche et variée.

Hors cadre scientifique, j'ai une pensée particulière pour Sandrine Chupin. J'ai beaucoup apprécié nos discussions et nos moments de partage. Je souhaite également ne pas remercier Ruddy Soeparno, pour toutes nos conversations inutiles et le temps perdu qu'implique systématiquement le fait de te croiser dans les couloirs. Et j'aimerais saluer affectueusement André Rouch, que j'avais toujours plaisir à croiser en arrivant ou partant du labo. Un sourire ou quelques mots échangés avec chacun d'entre vous étaient un petit rayon de soleil dans la journée.

À l'échelle du groupe GEMP, je tiens à remercier Suzy Bernard, notre gestionnaire de groupe, pour son professionalisme et son agréabilité à toute épreuve. Grâce à toi, l'aventure administrative devient beaucoup plus facile.

Et évidemment, je tiens à remercier les copains : Sylvain, Frédéric, Martin, Ange, Jacques, Hamza, re-Yohan, re-Pauline, Pierre, Tawfik, Baptiste, Yara, Romain, Amy, Adlan, Maxime, Edith, Vincent, Mauricio, Benjamin, Laetitia, Lingguo, Jianwei, Maha, Antoine,... Je garderai de très bons souvenirs de nos parties endiablées de tarot, des quelques soirées et repas partagés, ainsi que du mariage de Fred et Camille ! Merci à tous pour avoir instauré une ambiance de travail fort sympathique.

MerC++

Je profite encore un peu de ces pages pour souligner le plaisir que j'ai eu à travailler avec toute la clique BrainMicroFlow : Adlan *("y a Faustine à la fenêtre !")*, Maxime *(*check*)*, Amy *("that come into play!")* et Vincent *("là je mets plutôt un pointeur ou une référence ? Hum... bon, je vais voir Vincent.")*. Vous avez été un réél appui, scientifique et amical. Je pense simplement à votre gentillesse et votre générosité, auxquelles j'ai été très sensible. Vous allez me BrainMicroFlower[1]. Prenez BrainMicroFlow[2] des petits BrainMicroFlows[3], Florian et Arthur.

Et dans un coin du bureau, il y avait aussi Edith, qui est devenue bien plus qu'une co-bureau avec le temps. Merci Edith pour ton soutien, tes conseils, toutes nos discussions, les courbatures à cause du bloc,... et surtout nos séances musicales ! J'ai énormément apprécié toutes ces occasions de partager avec toi.

[1] manquer
[2] soin
[3] derniers

Puis s'il y a une autre personne qui mérite bien son paragraphe personnel de remerciements, c'est... Laetitia !! Merci d'avoir été présente à des moments délicats de ma thèse-vie, merci pour les bières, les clopes, les coinches, les balades, les heures de blablas,... Merci pour ta franchise et ta générosité, merci pour tes encouragements, merci d'être venue à ma soutenance,... Merci pour pas mal de choses en fait ! Je vais m'en tenir là. À très bientôt, pour de nouvelles aventures !

Effets de bord

Je souhaite en fin prendre le temps de remercier ma famille. Tout spécialement mes parents, qui ont rendu possibles toutes ces années d'étude et qui m'ont laissée être curieuse, essayer, changer d'avis, choisir. Je vous dois beaucoup. Merci aussi aux sœurs, Sandra et Rachel, pour leur soutien indéfectible, et au petit frère, Thomas. Merci d'avoir été présent ces derniers temps, pour t'occuper de moi et me changer les idées.

Aussi, je glisse un merci à Benjamin. Pour le support technico-logistico-psycholigico-affectif, pour le canard à l'orange, et surtout pour ta présence qui a le don de m'apaiser. Tout est important, mais rien n'est grave !

Nomenclature

Abbreviations

FV	:	Finite Volume
REV	:	Representative Elementary Volume
CN	:	Complete Network
SH	:	Simple Hybrid
HbFi	:	Hemodynamically-based Functioning imaging
Pi	:	Perfusion imaging
VR	:	Virshow-Robin
HNFV-Code	:	HybridNetworkFiniteVolume-Code
CPU	:	Central Processing Unit
GPU	:	Graphics Processing Unit
MPI	:	Message Passing Interface
DMDA	:	Distributed Arrays

Notations

Network

l_{cap}	:	the typical length of a capillary (m)
d_{cap}	:	the typical diameter of a capillary (m)
α, β, etc	:	a network vertex
$[\alpha\beta]$	:	the vessel defined by the vertices α and β
$\mathcal{N}_\alpha$	:	the set of neighbouring vertices of the vertex α
$\mathcal{N}_{\alpha,\text{in}}$	:	the set of inner neighbouring vertices of the vertex α
$d_{\alpha\beta}$	:	the diameter of the vessel $[\alpha\beta]$ (m)
$l_{\alpha\beta}$	:	the length of the vessel $[\alpha\beta]$ (m)
$G_{\alpha\beta}$	:	the conductance of the vessel $[\alpha\beta]$ $(kg^{-1} \cdot m^4 \cdot s)$
$\mu_{\alpha\beta}^{\text{app}}$	:	the apparent viscosity of blood in the vessel $[\alpha\beta]$ $(kg \cdot m^{-1} \cdot s^{-1})$
$H_{\alpha\beta}$	:	the hematocrit of the vessel $[\alpha\beta]$
π_α	:	the pressure defined at the vertex α $(kg \cdot m^{-1} \cdot s^{-2})$
$q_{\alpha\beta}$	:	the flow rate defined in the vessel $[\alpha\beta]$ $(m^3 \cdot s^{-1})$
π_Γ	:	the weighted average pressure in the capillaries connected to a coupling point $(kg \cdot m^{-1} \cdot s^{-2})$
l_Γ	:	the weighted average length of the capillaries connected to a coupling point (m)
R_Γ	:	the harmonic average resistance of the capillaries connected to a coupling point $(kg \cdot m^{-4} \cdot s^{-1})$

π_{CN} ..... : a network pressure obtained by complete network simulations ($kg \cdot m^{-1} \cdot s^{-2}$)
π_{H} ..... : a network pressure obtained by hybrid simulations ($kg \cdot m^{-1} \cdot s^{-2}$)
q_{CN} ..... : a network flow rate obtained by complete network simulations ($m^3 \cdot s^{-1}$)
q_{H} ..... : a network flow rate obtained by hybrid simulations ($m^3 \cdot s^{-1}$)

Continuum

h ..... : the side of a discretization cell (m)

i, j, etc ... : a discretization cell
$[ij]$ ..... : the surface between two discretization cells i and j
N_i ..... : the set of neighbouring cells of the cell i
$\overline{N}_i$ ..... : the set of neighbouring cells of the cell i + the cells sharing a corner with i

K^{eff} ..... : the effective permeability (m^2)
K^{ref} ..... : a reference effective permeability (m^2)
μ^{eff} ..... : the effective viscosity of blood ($kg \cdot m^{-1} \cdot s^{-1}$)
μ^{ref} ..... : a reference effective viscosity of blood ($kg \cdot m^{-1} \cdot s^{-1}$)

$\boldsymbol{U}$ ..... : the Darcy velocity ($m \cdot s^{-1}$)
P ..... : the pressure of the continuum ($kg \cdot m^{-1} \cdot s^{-2}$)
Q ..... : the flow rate of the continuum ($m^3 \cdot s^{-1}$)
P_i ..... : the pressure of the cell i ($kg \cdot m^{-1} \cdot s^{-2}$)
Q_{ij} ..... : the flow rate at the interface between the two cells i and j ($m^3 \cdot s^{-1}$)

Coupling

s ..... : a coupling point
S ..... : the set of coupling points

d_{off} ..... : the distance between the coupling point and the center of the coupled FV cell (m)
d_{AV} ..... : the distance between two arteriolar and venular coupling points (m)
d_{boundary} .. : the distance between a coupling point and the domain boundary (m)
$d_{k,s}$ ..... : the distance between the coupling point s and the center of the FV cell k (m)

π_s ..... : the pressure defined at the coupling point s ($kg \cdot m^{-1} \cdot s^{-2}$)
q_s ..... : the flow rate source term defined at the coupling point s ($m^3 \cdot s^{-1}$)
$q_{s,i}$ ..... : a fraction of the source term q_s assigned to the FV cell i ($m^3 \cdot s^{-1}$)
τ_i ..... : a partition coefficient to assign a partial source term $q_{s,i}$ to the FV cell i

f ..... : the linear coupling expression
$C_{s,\Gamma}$ ..... : the coupling coefficient, equivalent to a resistance ($kg \cdot m^{-4} \cdot s^{-1}$)

Domains

Ω_{AV} ..... : the set of network vessels in the arteriolar and venular trees
Ω_{cap} ..... : the set of capillary vessels connected to a coupling point
$\Omega_{lin,s}$ ..... : a spherical subdomain of $\mathbb{R}^3$ of radius l_Γ, centered in the coupling point s

Ω_{FV} ..... : the set of cells used to discretize the continuum
$\Omega^s_{FV,neigh}$ .. : the cell coupled to the point s and its neighbours, including the diagonal ones
$\overline{\Omega}^s_{FV,neigh}$ .. : a reduction of $\Omega^s_{FV,neigh}$, which excludes the coupled cell
Ω^ε_{FV} ..... : a reduction of Ω_{FV}, which excludes the sets $\Omega^s_{FV,neigh}$

$\overline{\Omega}^s_{sph}$ ..... : the set of cells that share a face with $\Omega^s_{FV,neigh}$
$\Omega^{s,\varepsilon}_{sph}$ ..... : an extension of $\overline{\Omega}^s_{sph}$, which includes the cells sharing a corner with $\Omega^s_{FV,neigh}$
Ω^s_{sph} ..... : a subdomain of $\mathbb{R}^3$ that corresponds to $\Omega^s_{FV,neigh} \cup \overline{\Omega}^s_{sph}$

Errors

ε^p_ω..... : the pressure error related to the component ω (vertex or cell)
ε^q_ω..... : the flow rate error related to the component ω (edge or surface between two cells)
ε^p_Ω ..... : the mean pressure error computed in the domain Ω
ε^q_Ω ..... : the mean flow rate error computed in the domain Ω

Partitioning

M ..... : the number of discretization cells of the continuum
M_x..... : the number of discretization in the x-direction
M_y..... : the number of discretization in the y-direction
M_z..... : the number of discretization in the z-direction

p..... : the number of available processing units
p_x..... : the number of processing units assigned to the domain partitioning in the x-direction
p_y..... : the number of processing units assigned to the domain partitioning in the y-direction
p_z..... : the number of processing units assigned to the domain partitioning in the z-direction

1 Introduction

The aim of this Introduction section is to outline the motivations of the present thesis, while a detailed state-of-the-art and literature survey will be presented in the next section. Here, our goal is to provide a global perspective on the problem we want to address, highlighting the importance of better understanding cerebral hemodynamics, molecular exchanges between blood and the neuronal network, and neurovascular coupling, i.e. the relationship between blood flow regulation and neuronal activity. By presenting the main limitations of the existing investigation tools, we want to point out the challenges of this thesis. Further, we detail both the overall strategy and the specific goals of the present work with a view toward whole-brain investigation, focusing on the multiscale nature of the human brain architecture.

1.1 Why is the brain microcirculation important?

The brain microcirculation plays a key role in cerebral physiology, since blood flowing through the cerebral microvasculature is the primary driver of oxygen delivery and metabolic waste removal in the cortex. In particular, cerebral blood flow is the main energy supplier of neurons [Boas et al., 2008, Hirsch et al., 2012, Sakadžić et al., 2014, Lücker et al., 2015, Schmid et al., 2017]. As a consequence, it is closely related to neuronal activation, i.e. the solicitation of specific neurons in response to internal or external stimuli (e.g. visual). Thus, better understanding the physiological mechanisms involved in the human brain microcirculation would provide a new angle of investigation on the relationship between blood flow regulation and neuronal activity, which is crucial for the study of the neurovascular coupling [Buxton et al., 2004, Girouard and Iadecola, 2006, Metea and Newman, 2006, Hamilton et al., 2010].

Further, the brain microcirculation is also linked to neurodegenerative diseases, such as Alzheimer's Disease (AD), or sudden stroke events. In both cases, severe deterioration of the microvascular networks may occur (e.g. vascular occlusions or capillary rarefaction [Hunter et al., 2012]). Such structural modifications limit blood flow, thus oxygen, nutrients and waste transfers with the cortex, possibly resulting in supply shortage and neuronal death [Shih et al., 2015]. Understanding how such disease-induced modifications of the microvascular structure affect blood flow and transport mechanisms in the brain is a fundamental challenge with regard to diagnosis and prevention issues [Iadecola, 2013]. For instance, it has been recently demonstrated in humans that blood flow de-

creases early in AD, before any measurable change in other biomarkers or onset of cognitive decline [Iturria-Medina et al., 2016]. Thus the development of new clinical procedures based on the relationship between brain hemodynamics (e.g. regional blood flow), mass transfers (e.g. diffusion of markers) and pathologies could lead to clinical breakthroughs with regard to diagnosis and treatment strategies.

Yet cerebral microcirculation received much less interest than "more fascinating" components of the brain, such as the central nervous system and the associated neuronal networks [Itti and Koch, 2001, Guenther et al., 2006, Friston, 2009, Rottschy et al., 2012]. Comparatively, we still understand little about the structure and functions of the microvascular networks, let alone their regulation mechanisms, robustness to perturbations and involvement into pathologies. In particular, we still need to improve the accuracy of the available investigation tools at the scale of the whole brain, for the purpose of understanding the systemic impact of localized effects, such as a vascular occlusion, in both physiology and physiopathology.

1.2 The cerebral vasculature: a multiscale architecture

The cerebral circulation involves a broad range of spatial scales [Perdikaris et al., 2016]. This multiscale architecture makes it difficult not only to understand the mechanisms occurring at the different levels, but also to understand and assess their interdependency. It also makes it difficult to combine investigation tools that are confined to separate scales (e.g. neurofunctional imaging and numerical models, as discussed below). To support our speech, we take the time here to detail the structural organization of the entire cerebral vasculature, the scales of interest and the vocabulary that will be used in the remainder of this manuscript.

The role of the cerebral circulation is to supply cells of the neuronal network (e.g. neurons, astrocytes or glial cells), which are embedded in the cerebral tissue, with nutrients, and to drain the metabolic waste out of this tissue. To perform this function, the circulation is divided into two distinct parts, the *macro* and *micro*circulation, that each have different roles.

1.2.1 The brain *macro*circulation

The *macro*circulation contains the largest vessels and is aimed at rapid, stable and resilient transport. As displayed in Fig. 1.1**(a)**), the *carotids* are the largest arteries of this macrocirculation. They

carry blood from the heart to the brain. They are connected to the *Circle of Willis*, which is a circulatory anastomosis, i.e. a loop of interconnected arteries, as displayed in Fig. 1.1**(b)i**. By creating redundancy, this very specific arrangement provides resilience and prevents supply shortage in the event that parts of the upstream arteries are blocked or narrowed, for instance in case of stenoses or aneurysms rupture [Cassot et al., 1995]. This roundabout structure is also perfectly adapted to distribute blood toward all the regions of the cortex, through the cerebral arteries, as schematized in Fig. 1.1**(b)ii**. Further away, these cerebral arteries are extended by *pial arteries*, which also have a redundant structure. As shown in Fig. 1.1**(b)ii**, these pial vessels deploy on the entire surface of the cortex. When they enter into the cortex, the vessels are below hundred microns in diameter and the pulse wave induced by the heart pumpage has been damped in the upstream vessels [Santisakultarm et al., 2012]. While this arteriolar pial system is in charge of supplying oxygen and nutrient, a similar venular pial network is in charge of carrying the blood back to the heart and draining the metabolic waste out of the cortex.

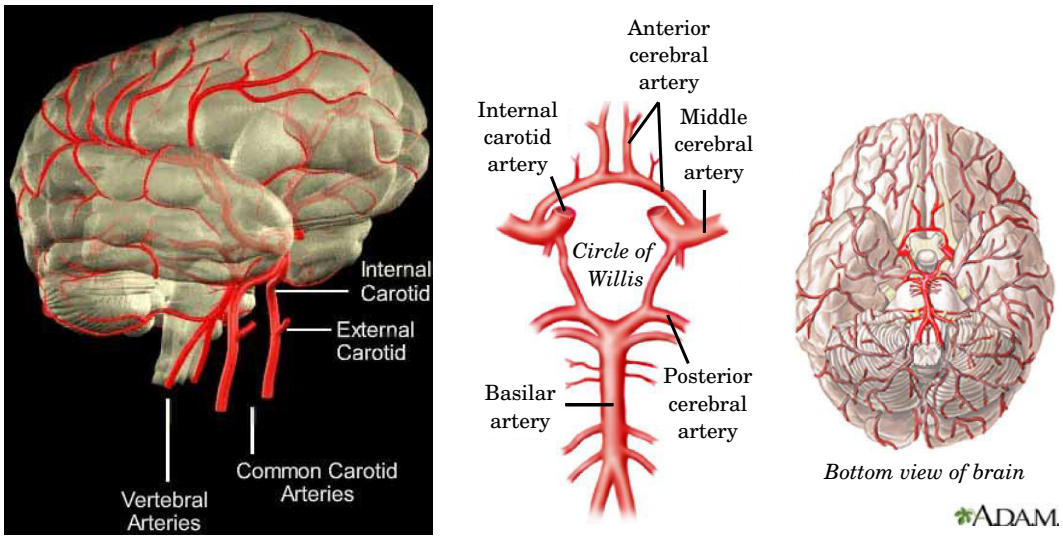

Figure 1.1: **Schematics of the larger vessels of the human cerebral circulation.** **(a)** The carotids bring the blood pumped by the heart to the brain. Source: http://www.strokecenter.org/professionals/brain-anatomy/blood-vessels-of-the-brain/. **(b)** At the bottom of the brain, the circle of Willis distribute blood to all the regions of the brain through the cerebral arteries. Adapted from: http://pennstatehershey.adam.com/content.aspx?productId=116&pid=2&gid=18009.

1.2.2 The brain *micro*circulation

The intracortical vasculature is commonly called the brain *micro*circulation, which is the region of interest in the present work. Fig. 1.2 displays its multiscale architecture. As detailed below, the microvasculature is composed of two main classes of vessels: the *capillaries* and the *arteriolar and venular trees*.

Embedded in the cortex, the *capillaries* are the smallest vessels of the cerebral vasculature (1-10 μm in diameter), as displayed in red in Fig. 1.2**(c)** and **(d)**. They form a dense structure that is termed "capillary bed". This is the main place of molecular exchanges between the blood and the brain cells, which are located within the surrounding tissue. In capillaries, the red blood cells and the molecules transported by the plasma carry oxygen and nutrients, respectively. To supply brain cells, they pass through the endothelial cells that compose the vascular wall and diffuse in the cerebral tissue. The space-filling mesh-like structure of the capillary bed ensures supply to all regions of the cerebral tissue by minimizing the distance between any point of the brain tissue and the capillary vasculature [Lorthois and Cassot, 2010]. As a result, it involves a huge number of vessels, which is estimated at tens of billions in a whole human brain.

The *penetrating arterioles* and *ascending venules* connect this capillary bed to the upstream pial arteries and downstream pial veins at the surface of the cortex. Contrary to the capillary network, they present a tree-like structure [Cassot et al., 2009, Lorthois and Cassot, 2010] composed of a main trunk perpendicular to the cortical surface and connected to branches, with diameters in the range ∼10-100 μm. They are displayed in black in Fig. 1.2**(c)**. While the penetrating arterioles supply the capillary bed with blood carrying oxygen and nutrients, the ascending venules drain the blood transporting the metabolic waste, which is produced by the functioning of the neurons. Their tree-like structure is adapted to their function of efficiently delivering blood down to the bottom of the cortex.

1.2.3 Scales terminology

For consistency, the scales terminology used in the remainder of this manuscript is as follows (see also Fig. 1.2):

- the *microscopic* or *capillary scale* refers to a the scale of a capillary vessel, which length is typically $\sim 50\,\mu$m (Fig. 1.2**(d)**);

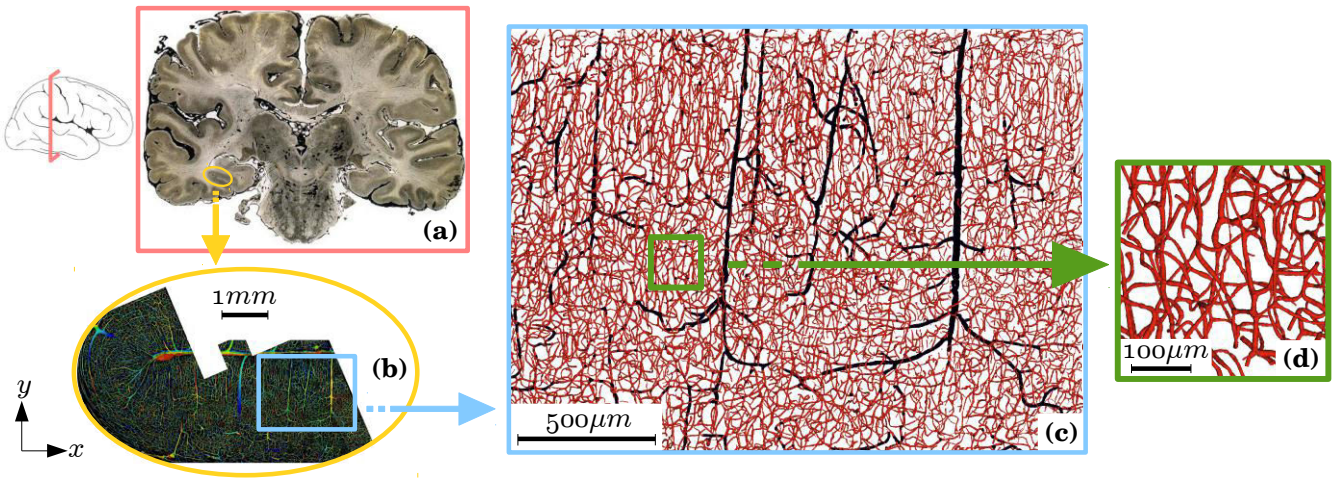

Figure 1.2: **Multiscale architecture of microvascular networks in human brain.** **(a)** *Brain scale (∼60 cm^2×300 μm)*: 300 μm-thick cortical section, where blood vessels have been injected with India ink for contrast enhancement [Duvernoy et al., 1981]. **(b)** *Macroscopic scale or cortical scale (∼20 mm^2×300 μm)*: reconstruction of parts of the collateral sulcus by confocal laser microscopy [Cassot et al., 2006]. **(c)** *Mesoscopic scale (∼5 mm^2×300 μm)*: region of interest in which vessels of more than 10 μm in diameter are colored in black and vessels of less than 10 μm in diameter are colored in red (diameters have been multiplied by 2 for visualization). In contrast with the capillary bed, the arteriolar and venular trees have a quasi-fractal structure [Lorthois and Cassot, 2010]. **(d)** *Representative Elementary Volume the capillary bed (∼0.05 mm^2×300 μm)*: detailed view of the capillary bed. The capillary bed is dense and space-filling over a cut-off length of ∼ 50 μm [Lorthois and Cassot, 2010].

- the *mesoscopic scale* refers to a representative volume of the microvasculature, as displayed in Fig. 1.2**(c)**. Such volume includes both tree-like structures (in black) and the space-filling mesh-like capillary bed (in red). The duality of this architecture will be at the heart of the present work, as discussed in more detail in the remainder of the manuscript;
- the *macroscopic* or *cortical scale* refers to a representative volume of the cortex, e.g. a circonvolution, as displayed in Fig. 1.2**(b)**;
- the *brain scale* refers to the whole cortex (Fig. 1.2**(a)**).

1.3 Limitations of the existing investigation tools

As already mentioned, the brain microvasculature is the place of crucial hemodynamics and transport mechanisms with regard to neuronal functioning. This has motivated the development of a large number of investigation tools for the last decades. In this section, we focus on approaches that became standard in either communities of *cerebral physiology and neuroimaging*, which both rely on invasive or non-invasive imaging techniques in the framework of animal experiments or cognitive clinical studies, or *numerical simulation*. However, all these approaches still present limitations that

prevent investigation of the microcirculation at the scale of a whole human brain. More detail about the progress allowed by such technologies and their limitations will be brought in Section 2. The goal of this section is to lay the groundwork for introducing the objectives of the present thesis.

1.3.1 Investigation tools in "relatively small" volumes

i. Brain imaging techniques. In the last decade, advances in imaging techniques led to rapid progress in the experimental investigation of brain microcirculation. In particular, multiphoton laser scanning microscopy [Shih et al., 2012, Hirsch et al., 2012], a cutting-edge fluorescence microscopy with unprecedented microscopic scale resolution and cortical penetration depth, has enabled the spatio-temporal investigation of hemodynamics and mass transfers at macroscopic scale in the living brain of healthy or diseased rodents [Nishimura et al., 2006, Boas et al., 2008, Tsai et al., 2009]. This corresponds to a cerebral volume up to 10 mm^3 containing tens of thousands of vessels.

Furthermore, recent whole-brain post-mortem imaging techniques make it already realistic to obtain three-dimensional datasets of the whole microvascular network in mice, with a spatial resolution enabling the reconstruction of the network representation down to the scale of capillaries [Mayerich et al., 2011]. This corresponds to volumes of $\sim$500 mm^3 containing millions of vessels.

However, such volumes are still relatively small compared to the volume of a whole human brain ($\sim$700 cm^3 containing tens of billions of vessels), and such performance is not possible in humans yet. Nowadays, the best way of obtaining three-dimensional post-mortem human anatomical datasets is to combine confocal microscopy that generates images of thick cortical sections ($\sim$300 μm, as displayed in Fig. 1.2), and computer-assisted methods of reconstruction to connect them to each other. *Such methods allow the description of three-dimensional microvascular structures down to the scale of capillaries, in volumes up to $\sim$1 mm^3* [Cassot et al., 2006], as displayed in Fig. 1.3**(a)**.

ii. Numerical simulation. Numerical approaches have also proven themselves for understanding regulation mechanisms induced by structural variation of the microvasculature, and their impact on blood flow and mass transfers. In particular, a lot of emphasis has been put on *network approaches*. In these approaches, the vasculature is treated as a network of interconnected tubes and transport mechanisms are averaged at the scale of individual vessels, down to the microscopic scale. While this is an advantage to investigate the details of blood flow dynamics, microscopic knowledge of the geometry and topology of the vascular network is required to perform such computations, *therefore*

limiting the computational volume to that of available anatomical databases in humans (∼1 mm^3) [Reichold et al., 2009, Lorthois and Cassot, 2010], as displayed in Fig. 1.3**(b)**.

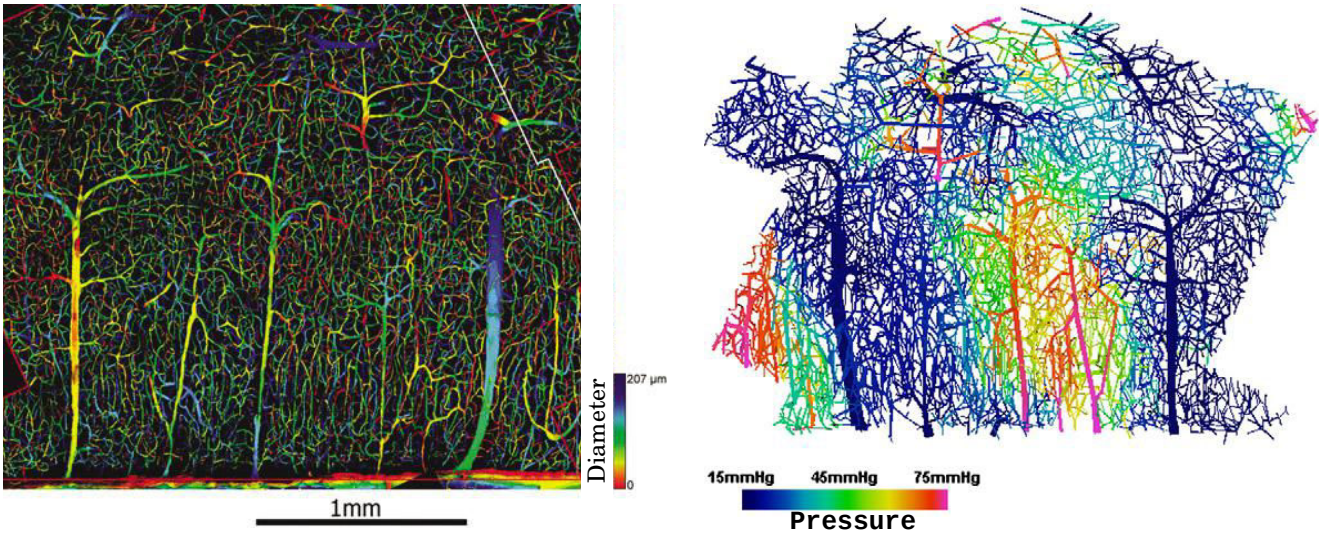

(a) **(b)**

Figure 1.3: **Blood flow dynamics in "relatively small" volumes compared to human whole-brain dimensions. (a)** This figure has been extracted from [Cassot et al., 2006]. This displays a two-dimensional projection of a three-dimensional reconstruction of the collateral sulcus in the temporal lobe of a human brain. Such reconstruction stems from the combination of confocal microscopy and computer-assisted methods of three-dimensional reconstruction. **(b)** This figure has been extracted from [Lorthois et al., 2011a]. This displays the pressure distribution obtained by simulation of blood flow in the human anatomical dataset displayed in **(a)**. Note that the two representations are mirror images.

1.3.2 With a view to brain-scale investigation

i. Brain imaging techniques. Perfusion imaging (Pi) techniques and hemodynamically-based functional imaging (HbFi) techniques both enable brain imaging at the scale of a whole human cortex. Both Pi and HbFi techniques are based on the use of a contrast agent, or tracer, which produces contrast while carried by the blood stream and flowing through the observed organ. The signal changes induced by the tracer are measured dynamically and converted into concentration-time curves by application of a modality-specific signal model. This allows the generation of a series of maps, representing the spatio-temporal evolution of the tracer concentration at a scale defined by the spatial resolution of the imager [Sourbron, 2014].

Various tracer classes are associated to these techniques (see Table 1): intravascular tracers, which do not cross the blood-brain-barrier and remain in blood, or diffusible tracers, which can be transported across vessel walls and diffuse into the brain tissue; exogenous tracers, that must be injected to the subject making the imaging technique invasive, or endogenous tracers, that are

naturally present in blood (or can be remotely excited, e.g. using a radiofrequency field in MRI).

Tracer	**Imaging modality**	**Tracer properties**	
Gadolinium	MRI	Exogenous	Intravascular
Deoxygenated Haemoglobin	BOLD-fMRI	Endogenous	Intravascular
Excited protons	ASL-MRI	Endogenous	Diffusible
Radiolabeled water	PET	Exogenous	Diffusible

Table 1: **Example of tracers and tracer properties associated to various imaging modalities.**

In Pi techniques (e.g. Positron Emission Tomography, PET, or Arterial Spin Labeling, ASL-MRI), the resulting concentration-time tracer profiles are analyzed using very simple compartmental models to deduce cerebral blood flow (CBF, see Fig. 1.4**(a)**). Such models are well known to be highly oversimplified, leading to large errors in flow estimates [Sourbron, 2014, Lorthois et al., 2014]. Nevertheless, they are largely used in the clinics [Wintermark et al., 2005], mainly because of their simplicity and the lack of alternate modelling approaches.

HbFi techniques (e.g. PET or Blood-Oxygen Level Dependent functional Magnetic Resonance Imaging, BOLD-fMRI) rely on the same basic principles, but are used to study the variations of tracer concentrations or CBF induced by a change of cerebral activity. Two acquisition sessions are performed sequentially, the first one associated with a reference task (often rest), and the second one while the task of interest (e.g. visual, motor, memory test) is performed by the subject (healthy human or patient). The underlying idea is that, because of the strong regulation of blood flow as a function of local neural activity (neuro-vascular coupling [Harrison et al., 2002]), the associated hemodynamic variations can be interpreted as changes in neuronal activity. Such techniques are widely used for research in fundamental cognitive neurosciences [Fan et al., 2003, Werring et al., 2004]. They are also widely used in clinics to support diagnosis and help design prevention strategies [D'Esposito et al., 2003]. However, many authors have noted that better understanding the relationship between neuronal activity and signal changes is still needed. In particular, how the underlying vascular architecture (e.g. capillary density) modulates this relationship is still poorly understood [D'Esposito et al., 2003, Weber et al., 2008, Lorthois et al., 2011b, Schmid et al., 2017].

Such imaging methods may differ by quantitative accuracy, but they typically characterize hemodynamics and neuronal activation in large brain-scale volumes (100 cm^3) at the scale of voxels (1-10 mm^3). Importantly, the volume of these voxel corresponds to the mesoscopic scale introduced

in this manuscript (Fig. 1.2**(c)**). Thus, no distinction can be made in the image maps between the tree-like arterioles and venules, and the capillary bed: the details of the underlying vasculature is not discernible. Therefore, *while HbFi and Pi techniques are able to image a whole human brain, they are limited by their resolution, which is quite poor to study blood flow dynamics.*

ii. Numerical simulation. Contrary to HbFi techniques, numerical network approaches are able to describe hemodynamics and mass transfers at the scale of individual vessels. For the purpose of applying network approaches to larger volumes despite the lack of human anatomical data at this scale, synthetic networks may be used to replace the capillaries and/or the arteriolar and venular trees, as in Fig. 1.4**(b)**. For that purpose, complex algorithms have been developed to generate synthetic networks with anatomically accurate statistical properties (e.g. mean vascular length and diameter, trifurcations, presence or not of vascular loops) [Lorthois and Cassot, 2010, Linninger et al., 2013, Smith, 2016, Merrem et al., 2017]. However, even if such networks were generated at the scale of the whole brain, the huge number of vessels involved (tens of billions) still represents a significant numerical obstacle. Thus *these approaches are computationally limited to relatively small cortical volumes, with no volume larger than 30 mm^3 (Fig. 1.4**(b)**) exploited yet in the context of brain microcirculation.*

To summarize, today brain imaging techniques allow the visualization of the whole human brain, but only at the scale of voxels, i.e. at mesoscopic scale. In parallel, numerical network approaches have proven themselves to accurately describe blood flow and mass transfers at the scale of individual vessels, i.e. at microscopic scale. However, the computational limitations of today supercomputers prevent any simulation resolved at this scale to be performed in a whole human brain using such detailed models. Finally, in a perspective of whole-brain studies, imaging techniques and numerical simulations are confined to separate scales of the cerebral microvasculature. As a consequence, the combination of these two investigation tools, which would considerably accelerate our understanding of crucial physiological mechanisms in human brain microcirculation, is not possible yet.

1.4 Objective of the present work

This thesis is part of the BrainMicroFlow project (http://brainmicroflow.inp-toulouse.fr/en/home.html), which has been awarded to Sylvie Lorthois in 2014 by the European Research Council (ERC). In

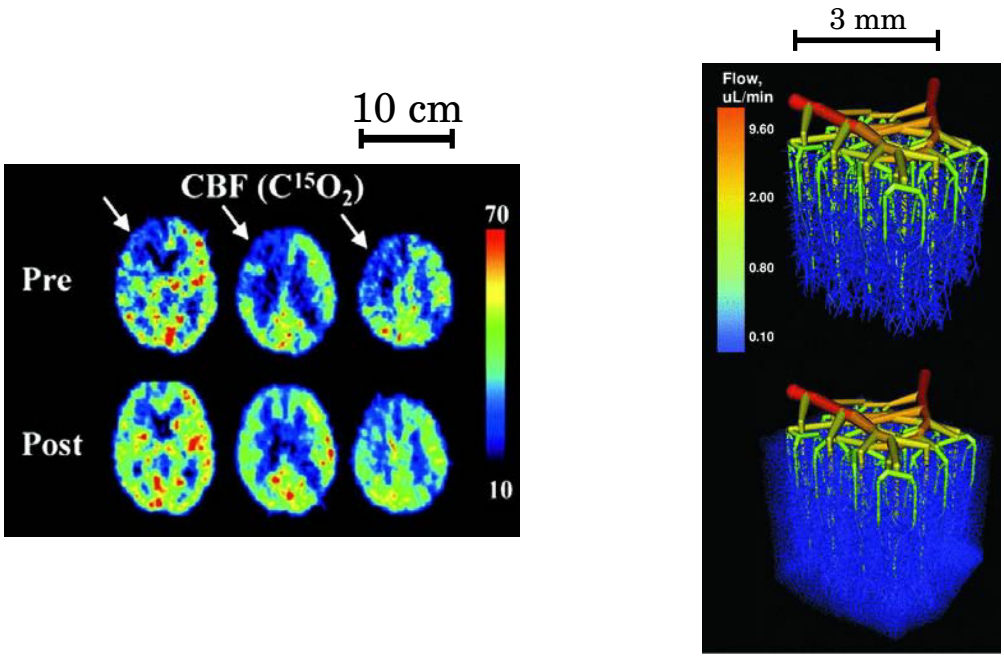

(a) **(b)**

Figure 1.4: **Scale difference between images obtained by a standard brain imaging technique and the flow rate distributions computed by a standard network approach. (a)** This figure has been extracted from the review of Wintermark *et al.* [Wintermark et al., 2005]. This represents the PET CBF images of a patient with moyamoya disease, before (Pre) and after (Post) a right-hand side bypass surgery. **(b)** This figure has been extracted from the paper of Linninger *et al.* [Linninger et al., 2013]. A vasculature of volume $3\,mm \times 3\,mm \times 3\,mm$ is presented. Both the larger vessels (on the top) and the capillaries (added on the bottom image) have been generated from algorithmic methods. Blood flow has been simulated in this structure using a standard network approach, which expresses the average flow rate in each vessel as a linear function of the local pressure drop.

a long-term view, the perspective of this project is to allow the combination of brain imaging techniques and numerical models at clinically relevant scale. This would be a valuable tool to understand the structure/function relationships of brain microcirculation in humans, in healthy or diseased condition, with a focus on the role of vascular factors in Alzheimer's Disease.

For that purpose, we must bridge the gap between the accuracy of the network approaches in describing blood flow and transport mechanisms at microscopic scale, and the ability of the HbFi techniques to investigate the whole human brain with a mesoscopic resolution. For that purpose, as computational modellers, we focus on building new numerical tools, which will allow the simulation of blood flow and mass transfers: *(1) at mesoscopic scale,* and *(2) in the whole human brain.*

To our knowledge, no such numerical tools have been developed yet in the context of brain microcirculation. Thus, the specific goal of the present manuscript is to build solid theoretical foundations for introducing a completely new simulation paradigm. Because we are at the beginning

of a step by step validation process, we focus here on blood flow distributions only, under some simplifying assumptions (e.g. isotropy of the capillary bed or uniform hematocrit) that will be further detailed in Section 3. The aim here is to establish and validate a relevant strategy, which will open the way to account for additional levels of complexity in the future, in particular to mass transfers.

1.5 Strategy adopted

In this section, we detail our strategy to achieve the simulation of blood flow distributions: (1) at mesoscopic scale, and (2) in the whole human brain. This also gives the opportunity to introduce the structure of the present thesis, which is in line with this strategy.

1.5.1 For the simulation of blood flow *at mesoscopic scale*

i. The idea. The idea is to upscale the flow equations used in network approaches from the scale of individual vessels to larger volumes that are representative at mesoscopic scale. This upscaling process is termed *homogenization*, and requires the existence of a unique characteristic length-scale of the medium. This is the case of the mesh-like capillary bed that has been proven to become dense and homogeneous over a cut-off length of $\sim 50\,\mu m$ [Lorthois and Cassot, 2010, Cassot et al., 2010]. However, this is not the case of the arteriolar and venular tree-like vessels that present a quasi-fractal structure [Lorthois and Cassot, 2010]. As a consequence, we will only apply the homogenization process to the capillary bed, and use a standard network approach in the larger vessels of the brain microvasculature. The resulting approach is called *hybrid*, since it will involve two separate frameworks, according to the dual architecture of the cerebral microcirculation.

Homogenizing the flow equations in the capillary bed consists in replacing it by a continuum, where the flow is characterized by partial differential equations and effective properties (e.g. permeability) at the scale of a much larger representative volume [Bear, 1972, Erbertseder et al., 2012]. As will be justified later, such volume is typically in the order of magnitude of $(100\,\mu\mathrm{m})^3$, which corresponds to the mesoscopic scale. The first advantage of this approach is that the use of effective properties prevents the need for microscopic knowledge of the capillary geometry and topology in the whole cortex. Second, the flow equations in the continuum will be discretized on a coarse grid, using the finite volume method [Eymard et al., 2000, Versteeg and Malalasekera, 2007]. This will tremendously decrease the computational cost compared to the classical network approaches, since a

cell of the coarse finite volume grid may contain hundreds of capillaries, thereby reducing the number of unknowns of the problem. Finally, the resulting pressures and flow rates will be representative at the scale of the finite volume cells, i.e. at mesoscopic scale, in the same spirit as the information obtained by HbFi and Pi imaging techniques at the scale of voxels.

ii. What already exists. Homogenization is commonly used in the community of porous media [Bear, 1972, Whitaker, 1986, Quintard and Whitaker, 2000, Davit et al., 2013a]. As detailed in **Section 2**, such upscaling process has already been used for the modelling of blood flow and molecular exchanges in the context of lung tumor or brain microcirculation, which both involve arteriolar and venular trees connected to capillary networks [El-Bouri and Payne, 2015]. However, the tree-like constraint of the largest vessels, which prevent such structure to be homogenized, is sometimes overlooked [Hyde et al., 2014]. In this work, as in previous work [Erbertseder et al., 2012], we account for the dual architecture of microvascular networks by developing a hybrid approach. The network and continuum models involved will be presented in **Section 3**. As presented below, our contribution further aims at improving the existing hybrid methods by developing a proper multiscale coupling strategy at the interface between the arteriolar and venular trees modelled by network approaches, and the homogenized capillary bed.

iii. What is new. One of the main difficulty of the hybrid method, which has been overlooked in previous work and will be at the heart of this manuscript, is the development of a proper coupling model at the interface between the arteriolar and venular trees, and the capillary bed, i.e. at the interface between the network and continuum approaches. Indeed, high pressure gradients build up at the scale of the capillaries in the vicinity of the coupling points, i.e. where the arteriolar or venular end-tips are connected to a capillary, and must be properly described at the scale of the continuum. This is difficult primarily because variables that are seemingly identical do not have the same physical meaning. In particular, the blood pressure in the continuum approach represents a field that is spatially averaged over a representative volume of the capillary bed, while the pressure of the network approach represents a cross-sectional average within each tube. Simply imposing a condition of pressure continuity at the interface between the two frameworks may imply important errors that could propagate through the whole system. To our knowledge, this kind of multiscale coupling has never been discussed in the context of brain microcirculation. By contrast, numerous multiscale coupling models exist in hydrology or petroleum engineering to describe flow fields in

fractured aquifers, or interactions between a wellbore and the surrounding porous rock.

Taking inspiration of the "well models" developed by Peaceman in this last context [Peaceman, 1978], we will introduce a coupling model based on the use of analytical solutions to describe the pressure field in the vicinity of coupling points. This development will be detailed in **Section 4**. The main advantage of this approach is that the resulting equations yield a strong coupling, i.e. a single linear system to solve for both the network part and the continuum, thus limiting the computational cost compared to iterative methods that are often used to couple separate frameworks.

iv. How we will validate our approach Our hybrid approach will be validated in **Section 5** by comparing our results with "complete network" (CN) simulations, where all the vessels are modelled using a classical network approach, including the capillaries. Since network approaches have been proven to accurately describe blood flow in microvascular networks [Pries et al., 1990], they are considered as a reference in the context of brain microcirculation. To further highlight the need for a proper multiscale coupling model, our results will be compared to "simple hybrid" (SH) computations, where a simple condition of pressure continuity will be imposed at the interface between the network part and the continuum. Such coupling condition overlooks the coupling issues described above.

In **Section 5.2**, we will first validate the multiscale coupling model, which is at the heart of our hybrid approach. For that purpose, we will compare the results of CN and SH simulations in idealized configurations involving periodic synthetic capillary networks. Furthermore, these idealized test cases will involve only a few couplings induced by the connection of the continuum with *isolated* arteriolar and/or venular vessels, i.e. arteriolar and/or venular vessels that are not interconnected. In this way, the flow fields in the vicinity of couplings will interact only via the continuum, not via the network part. As will be detailed, the use of both simplified capillary networks and isolated arteriolar/venular vessels enables us to avoid two kinds of uncertainties in the computation of errors: those induced by the estimation of effective properties of the continuum, and those induced by the rheology of blood flow dynamics in complex arteriolar and venular trees.

In **Section 5.3**, the comparison of our results with CN and SH simulations will be progressively extended to more realistic, i.e. anatomically accurate, configurations. First, the synthetic representation of capillary networks will be complexified by adding morphometrical and topological constraints that typically occur in the brain microcirculation (e.g. trifurcations or distribution of vessels diameters). In this case, the network part will still involve isolated arteriolar and/or venular vessels. The point will be to assess the robustness of the continuum approach in accounting for microscopic

variations of the underlying capillary structure. Second, we will extend the validation of our model to configurations involving anatomic, thus complex, arteriolar and/or venular trees. In this case, the capillary networks will still be represented by idealized synthetic lattices. The point will be to evaluate the interaction between couplings that are *interconnected*, i.e. connected via the network part. Finally, an application to a fully realistic configuration will be presented in **Section 5.4**. This application will involve both anatomical arteriolar and venular trees, which display a large number of interconnected couplings, and a realistic capillary network.

1.5.2 For the simulation of blood flow *in the whole human brain*

As mentioned above, replacing the capillary bed by a continuum implies an important computational gain. However, it is far from being sufficient to consider the extension to mass transfers and simulations at the scale of a whole human brain. That is why the hybrid approach is implemented in a C++ code designed for High Performance Computing (HPC), as detailed in **Section 6.3**. First, it is fully parallelized using Message Passing Interface (MPI) standards. The parallel architecture of the linear system to solve is handled using the PETSc library, and the distribution of the structure among the processing units is operated by specialized partitioning tools, including the ParMETIS library. The performance of our code will be presented in **Section 6.3.4**.

Further, since the present work is part of a larger project, which involves several collaborators, the numerical platform has been thought as a long-term wide-variety computational tool. In particular, special care has been taken in developing efficient coding strategies (e.g. testing, pair-programming) to ensure the performance, the reliability and the portability of the code. Details about these strategies will be provided in **Section 6.1**.

The aim of the present manuscript is to validate the potential of combining a hybrid approach and high performance computing to simulate blood flow at mesoscopic scale *in a whole human brain*. To assess this statement, we will finally present, in **Section 7**, the computational performance of our code (e.g. execution time) when running a simulation of blood flow in a volume of $\sim$16.2 cm^3 of the brain microvasculature. No such volume has been investigated in the context of the human brain microcirculation yet. This execution will assess the computational potential of our approach with regard to whole-brain simulations of blood flow in humans.

While no anatomical datasets containing the arteriolar and venular structure of a whole human

brain exists yet, such imaging performance will be soon possible. Indeed, recent brain imaging techniques are already able to image all vessels above 7 μm, i.e. all tree-like arterioles and venules, in rat brains of volume $\sim$2 000 mm^3 [Zhang et al., 2015]. With the evergrowing improvement in technologies, we can imagine that this capacity will extend to larger mammals, including humans (brains of volume$\sim$ 700 cm^3), in the next decades. This perspective support our own project, which is to build in parallel a numerical tool capable of exploiting such datasets.

2 Current approaches for modelling blood flow and mass transfers in human brain microcirculation

In this section, we present an overview of the main works of previous decades that support the current models of blood flow and mass transfers in the human cerebral microcirculation. We focus on applications to human brain, but references to similar applications (e.g. human lung microcirculation or animal cortex) are also made as comparison or sources of inspiration. This overview covers several topics, from the morphological study of the human cerebral microvasculature to the existing hybrid approaches for modelling blood flow and mass transfers in microvascular networks. The first goal of this presentation is to provide an insight of the current landscape, in which our work is included, to then introduce the equations of our model in Section 3. The second goal is to understand the limitations of the current approaches, especially with regard to computational performance and multiscale coupling in the hybrid approaches.

2.1 Microvascular architecture and blood rheology

2.1.1 Anatomical material and investigation of the microvascular architecture

As mentioned in the Introduction, the oxygenation of the cerebral tissue is strongly dependent on the spatial arrangement of the microvessels. Thus the investigation of blood flow and mass transfers in the brain microvascular networks first requires a good knowledge of their morphology and topology.

In the human cortex, most of the anatomical material comes from the work of Duvernoy *et al.* [Duvernoy et al., 1981], who injected the intravascular network of twenty-five different brains with Indian ink and gelatin. As displayed in Fig. 2.1, this technique is able to outline the inner space of the vessels down to the scale of the capillaries, using stereoscopic or scanning electron microscopy. Such level of details supported major advances from the 1980s concerning the classification and the morphological study of the cortical vessels in healthy or pathological conditions [Duvernoy et al., 1983, Raybaud et al., 1989, Hirsch et al., 2012].

The classification work of Duvernoy mainly relied on the observation of the variations of vascular

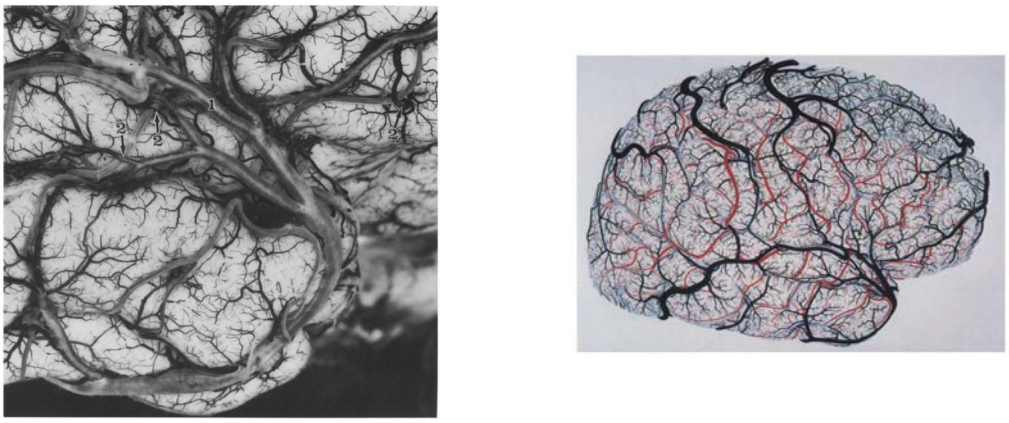

(a) Superficial cortical vessels

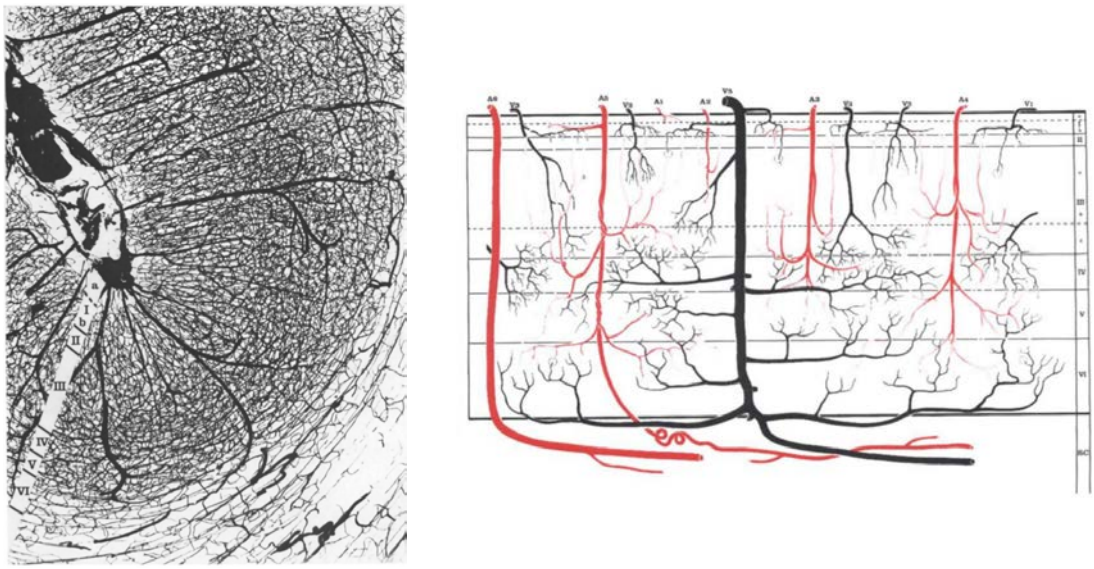

(b) Intracortical vessels

Figure 2.1: **Duvernoy *et al.*'s study [Duvernoy et al., 1981] of the morphology of the cortical vessels in the human brain. (a)** *Left*: photograph of the medial orbital gyrus of 49 years old male. *Right*: drawing of the cortical pial vessels of a 50 years old female. **(b)** *Left*: photograph of a cortical section of the temporal lobe of a 54 years old male. *Right*: drawing of the morphological features of the penetrating arteries (red) and ascending veins (black).

density in intracortical regions of the brain. In particular, he highlighted the stratified structure of the intracortical vasculature and differentiated about ten different layers according to their vascular density and the depth of penetration of the arteriolar and venular trees (see Fig. 2.1**(b)**). Furthermore, he observed capillary-free zones in the vicinity of the penetrating arterioles and ascending venules, as displayed in Fig. 2.2. This capillary-free zone has received several names (e.g. Pfeiffer space). In this work, it will be termed *Virshow-Robin space*, according to the clinical vocabulary [Heier et al., 1989]. As confirmed later by [Kasischke et al., 2011], Duvernoy suggested that the

supply of this zone with oxygen and nutrients is not provided by the capillaries, but rather by the largest arteriolar and venular vessels, whose wall characteristics allow molecular exchange with the surrounding cerebral tissue. Further, [Al-Kilani et al., 2008] proved later that this typical spatial organization mainly stems from the remodelling of the capillaries into arterioles or venules during the morphogenesis of the brain microcirculation. Consistent with this idea, the radial distance between the capillaries and the largest vessels has recently been estimated to $\sim 50\,\mu$m [Kasischke et al., 2011], which corresponds to the typical length of a capillary vessel.

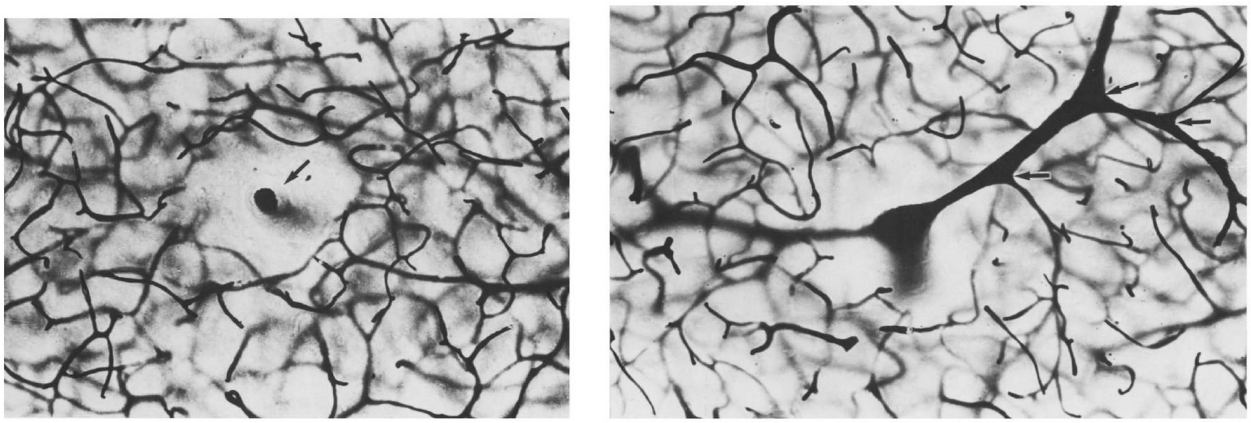

(a) **(b)**

Figure 2.2: **Observation of capillary-free regions in the vicinity of the largest intracortical vessels by Durvernoy.** The study of the vascular density in the intracortical vasculature highlighted capillary-free areas in the vicinity of both the penetrating aterioles **(a)** and the ascending venules **(b)**.

While the work of Duvernoy enabled significant advances in the understanding of the morphological characteristics of the human brain microcirculation, the lack of three-dimensional quantitative data was still an obstacle with regard to topological analysis of microvascular networks.

In 2006, Cassot *et al.* developed a computer-assisted method to derive three-dimensional images from confocal laser microscopy [Cassot et al., 2006]. By applying this method to 300 μm-thick sections of an Indian ink-injected brain of the Duvernoy collection, they reconstructed volumes of several cubic millimeters of the intracortical vasculature, opening the way to the spatial characterization of human microvascular networks [Cassot et al., 2010, Lauwers et al., 2008, Lorthois and Cassot, 2010]. Such studies highlighted a large heterogeneity in microvessels (e.g. vessels length, diameter or tortuosity), depending on their hierarchical position in the brain microcirculation. Moreover, they pointed out the multiscale architecture of the microvasculature by differentiating homogeneous and fractal patterns. This study identified the dual architecture of the microcirculation composed

of quasi-fractal tree-like arteriolar and venular trees, plunging in a space-filling mesh-like capillary bed, as displayed in Fig. 1.2. In particular, it has been shown that capillary bed becomes dense and homogeneous beyond a cut-off length of $\sim$50 μm, which corresponds to the typical length of a capillary [Lorthois and Cassot, 2010].

Such multiscale classifications have also been discussed in animals [Heinzer et al., 2006]. Further than establishing a hierarchy in microvessels, these studies led to important hypotheses on microvascular angiogenesis (i.e. growth of new vessels from pre-existing ones during the embryonic development [Le Noble et al., 2005]), and to the characterization of the microvascular networks in healthy and pathological conditions (e.g. fractal properties of tumourous microvascular structures in primate and rat [Risser et al., 2007]). Moreover, the topological analysis of the space-filling mesh-like structure of the capillary bed opened the way to the generation of synthetic network representations that accurately mimic the capillary architecture (e.g. based on Voronoi diagrams [Lorthois and Cassot, 2010]). Such synthetic capillary networks are essential for investigating the brain microcirculation in large cortical volumes, i.e. larger than $\sim 1\,\mathrm{mm}^3$. Indeed, as mentioned in the Introduction, today imaging techniques do not allow the observation of the cerebral microvasculature down to the scale of capillaries in such volumes yet.

Besides the fundamental interest in understanding the architectural organization of brain microvascular networks, their morphometrical and topological characteristics impact the blood flow dynamics through the complex rheology of blood in presence of confined vessels and bifurcations. That is why, in the next paragraph, we detail the three main non-linear rheological properties of blood in microvessels and their impact on blood flow dynamics.

2.1.2 Blood rheology in microvascular networks

The complex rheology of blood is mainly induced by the circulation of red blood cells. Indeed, while 50 % of the blood volume is composed of plasma, which is a Newtonian fluid similar to water in density, the remaining 50 % are mainly composed of red blood cells (99 % of the molecular components), which are in charge of carrying and releasing oxygen. The percentage of the blood volume occupied by the red blood cells (RBCs) is called *hematocrit*, and is about 45 % in humans. More specifically, the *tube hematocrit* H_T, i.e. the volume fraction of RBCs within a vessel at a given time, must be differentiated from the *discharge hematocrit* H_D, i.e. the volume fraction of RBCs

in the blood entering or leaving the vessel. Both tube and discharge hematocrits do not coincide, mainly due to the presence of a cell-free layer near the vascular wall [Zhang et al., 2009].

With regard to the blood rheology, the hematocrit is involved in three important effects:

- the *Fåhræus effect* [Barbee and Cokelet, 1971, Pries et al., 1986], which corresponds to the relative decrease of tube hematocrit by comparison with discharge hematocrit, as displayed in Fig. 2.3**(a)** (up);
- the *Fåhræus-Lindqvist* effect [Zilow and Linderkamp, 1989, Pries et al., 1992], which corresponds to the dependence of the blood viscosity upon both the vessel diameter and the discharge hematocrit, as displayed in Fig. 2.3**(a)** (down);
- the *phase separation* [Pries, 1996, Roman et al., 2016], which corresponds to the non-proportional distribution of hematocrit at diverging bifurcations. In other words, the fraction of RBCs flow (FQ_E) in a given daughter branch is not necessarily equal to the fraction of blood flow (FQ_B) in this branch (see Fig. 2.3**(b)**).

Both the Fåhræus and Fåhræus-Lindqvist effects have an important impact on the blood flow distributions in brain microcirculation. By contrast, the phase separation has a small influence on flow fields [Guibert et al., 2009]. However, with regard to mass transport, this last effect is essential for the description of oxygen fields in microvascular networks.

2.2 Standard modelling of blood flow and mass transfers in the microcirculation

In this section, we present existing models for the simulation of blood flow and/or mass transfers in microvascular networks. A few representative equations will be given for the purpose of illustrating the dynamics of interest. For more detail, references to relevant papers are also proposed. Further, with a view to brain-scale simulations, we will focus here on the computational performance of each model.

2.2.1 Blood flow modelling to understand regulation mechanisms

The accuracy of the approaches developed for modelling blood flow in brain microcirculation is closely related to the ability of describing the complex rheology of blood. In this section, we present

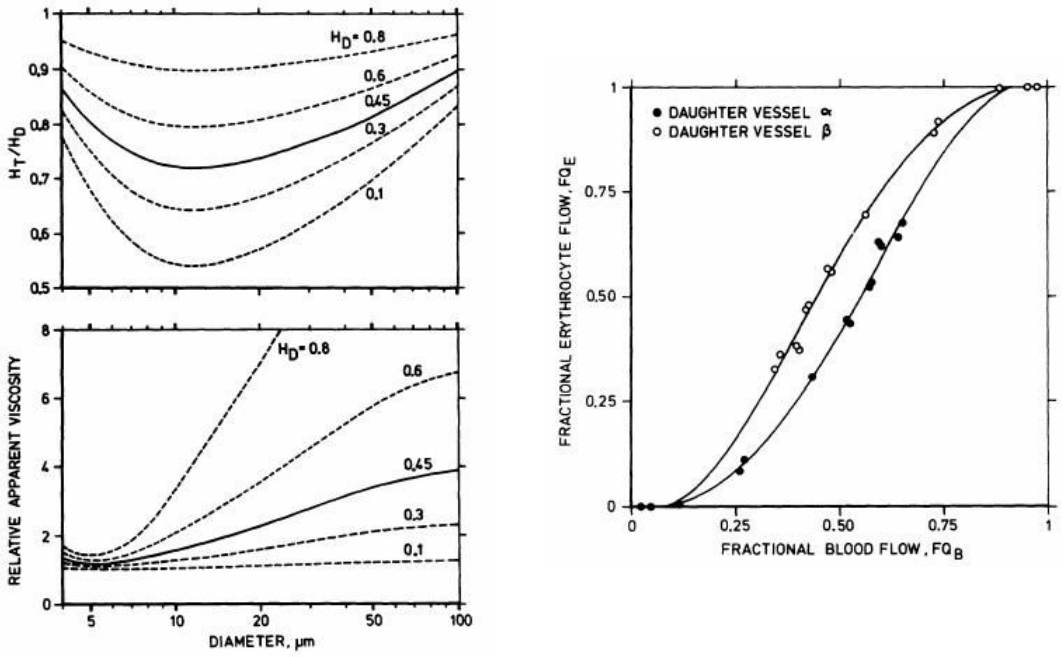

(a) **(b)**

Figure 2.3: **Illustration of the three main rheological properties of blood in microvascular networks. Figures and captions are extracted from [Pries et al., 1990].** **(a)** "Upper panel: Graph showing the Fåhræus effect. The ratio between the tube hematocrit (H_T) and discharge hematocrit (H_D) versus tube diameter is described [...]; Lower panel: Graph showing the Fåhræus-Lindqvist effect. Apparent viscosity of blood divided by plasma viscosity (relative apparent viscosity) versus tube diameter is given [...]." **(b)** "Graph showing phase separation at a microvascular bifurcation. The relation between fractional erythrocyte flow (FQ_E) and fractional blood flow (FQ_B) into the two daughter branches is seen. Data points do not fall on a line of identity, indicating that the hematocrit in the daughter branches differs from that in the feeding vessel."

several models that have been proposed to simulate blood flow in microvasculature, while taking into account these rheological phenomena.

At the scale of microvessels, several molecular modelling methods have been developed, which aim at describing the impact of the circulation of RBCs on blood flow dynamics. Such methods are commonly based on Lagrangian particle methods. For instance, the Molecular Dynamics (MD) models are classical stochastic approaches to characterize the fluid motion by integrating Newton's equations at the scale of the particle [Hansson et al., 2002, Karniadakis et al., 2005]. Such techniques

have become established tool in the studies of biomolecules, complementary to the experimental study. However, the description of the dynamics at the scale of a molecule restricts the simulations to a system size of a few millions of particles [Dzwinel et al., 2003] (or a cortical volume of $\sim 1\,000\ \mu\text{m}^3$). The Dissipative Particle Dynamics (DPD) method received much attention in the last decade. In such models, the blood is treated as a group of molecular clusters interacting through conservative (F_C), dissipative (F_D), and random (F_R) forces [Filipovic et al., 2008, Li et al., 2013, Witthoft et al., 2016]. By considering clusters instead of single molecules, this approach opens the way to simulations involving hundreds of millions of particles [Tang and Karniadakis, 2014] (or a cortical volume estimated at $\sim 10\,000\ \mu\text{m}^3$), but is still untractable for simulations in larger volumes.

To reduce the computational cost in the perspective of simulations in macroscopic cortical volumes, *reduced-order models* have also been introduced. Such methods aim at reducing the complexity of the problem while keeping variables physically and biologically relevant. In 1990, Pries *et al.* developed a reduced-model, which we term *network approach*, for the purpose of simulating blood flow in relatively large microvascular networks [Pries et al., 1990] (up to 913 vessels). The objective was to study the interactions, within a complex network, between rheological and hemodynamic factors that had been observed and quantified at the scale of individual microvessels, down to the capillary level. In this approach, the vasculature is treated as a one-dimensional network of interconnected tubes, as schematized in Fig. 2.4. Then the flow equations are averaged over the cross-sections and lengths of vessels, in which the relationship between the blood flow q and the pressure drop $\Delta\pi$ is described by a local resistance R as

$$q = \frac{1}{R}\Delta\pi. \tag{2.1}$$

This resistance R depends on both morphometric factors, such as the vessel length L, diameter D, and apparent viscosity μ^{app}, according to the expression

$$R = \frac{128\mu^{\text{app}}L}{\pi D^4}. \tag{2.2}$$

Further, empirical laws account for the three rheological properties described in Section 2.1.2. First, the empirical law corresponding to the Fåhræus-Lindqvist effect enables to express the above resistance as a function of the discharge hematocrit H_D and the vessel diameter D, by defining the

apparent viscosity μ^{app} as

$$\mu^{\text{app}} = \mu_{\text{p}} \left[1 + \left(\mu^{0.45} - 1\right) \frac{\left(1 - H_D\right)^C - 1}{\left(1 - 0.45\right)^C - 1} \times \left(\frac{D}{D - 1.1} \right)^2 \right] \left(\frac{D}{D - 1.1} \right)^2, \tag{2.3}$$

where μ_{p} represents the viscosity of the plasma, $\mu^{0.45}$ is the apparent viscosity of blood for a discharge hematocrit of 0.45

$$\mu^{0.45} = 6e^{-0.085D} + 3.2 - 2.44e^{-0.06D^{0.645}} \tag{2.4}$$

and C is a coefficient describing the dependence upon discharge hematocrit

$$C = \left(0.8 + e^{-0.075D}\right) \left(-1 + \frac{1}{1 + 10^{-11} D^{12}} \right) + \frac{1}{1 + 10^{-11} D^{12}}. \tag{2.5}$$

The Fåhræus effect is expressed as

$$\frac{H_D}{H_T} = H_D + (1 - H_D) \cdot \left(1 + 1.7e^{-0.415D} - 0.6e^{-0.011D}\right), \tag{2.6}$$

and the phase separation effect is described by

$$logit\left(FQ_E\right) = A + B\, logit\left(\frac{FQ_B - X_0}{1 - 2X_0} \right), \tag{2.7}$$

where $logit\left(x\right) = ln\left(x/1-x\right)$, X_0 is the minimal fractional blood flow required to induce the circulation of RBCs from the mother to the daughter branches, A characterizes the asymmetry between the two daughter branches, and B represents the non-linear relationship between FQ_E and FQ_B (see [Pries et al., 1990] for more details). All the parameters used in Eqs. 2.6-2.7 have been fitted using extensive *in vitro* and *in vivo* experimental datasets obtained in the mesenteric network of rodents [Pries et al., 1990].

For a uniform hematocrit, the network approach finally yields a simple linear system with relatively few variables compared to a complete three-dimensional resolution of the flow. Additional non-linearities, such as the hematocrit distributions induced by the phase separation (Eq. 2.7), are commonly treated using iterative methods, as in [Lorthois et al., 2011a].

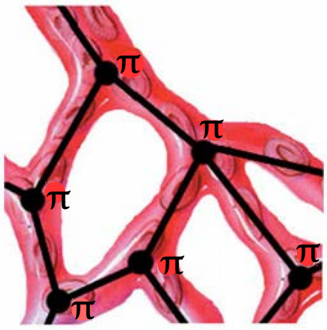

Figure 2.4: **One-dimensional representation of a vascular network.** This figure has been adapted from [Erbertseder et al., 2012]. It represents the one-dimensional representation (in black) of a microvascular network (in red).

The network model has been validated in a statistical point of view, since the distribution of hemodynamic variables (e.g. pressure or hematocrit distributions) resulting from the simulations showed very good agreement with *in vivo* experimental distributions [Pries et al., 1990]. The network approaches have been widely exploited, in particular to study the link between dynamic heterogeneities and architectural variations of the microvascular networks. Further, the reduction in computational cost obtained by such an approach enabled researchers to investigate relatively large volumes of the human cortex ($\sim$1 mm^3). Simulations in such volumes facilitated the understanding of quantitative differences between the average properties of a network (e.g. perfusion rate) and the projections of quantities derived from a smaller representative network [Pries et al., 1995]. Noteworthy, this kind of approach can be used to better interpreting measured signals using perfusion imaging (Pi) techniques or hemodynamically based functional imaging (HbFi), which describe hemodynamics at the larger scale of voxels. In particular, network models have been used to estimate regional blood flow at the scale of the typical spatial resolution of fMRI (voxel size of 500μm) [Lorthois et al., 2011a, Lorthois et al., 2011b]. Such an estimation can further be used to identify the local blood flow variations induced by the metabolic demand of activated neurons through neurovascular coupling. For instance, such a coupling has been simulated in [Reichold et al., 2009, Lorthois et al., 2011a, Lorthois et al., 2011b] by locally vasodilating arteriolar vessels, the diameter of which can be adjusted to the neuronal demand by specialized contractile smooth muscle cells. By defining the functional arteriolar territory, i.e. the set of microvessels where blood flow has been impacted by the vasodilation, such a study is a valuable tool to understand the hemodynamical origin of information measured at the scale of voxels by brain imaging techniques. In addition, such an understanding could help develop better quantitative models for the determination of blood flow from Pi techniques based on the use

of simple intravascular tracers. Extension to diffusible tracers or oxygen, the neuronal consumption of which controls the concentration of deoxygenated haemoglobin in BOLD-fMRI, requires modelling approaches enabling the description of mass transfers between blood and tissue.

The network approaches presented in this section made progress possible in the investigation of blood flow mechanisms. In particular, crucial rheological properties of blood are accurately taken into account. Furthermore, the reduction in computational cost they represent, compared to simulations at the scale of the RBCs, enable researchers to investigate relatively large volumes ($\sim$1 mm^3). However, to go further, models must also describe mass transfers between the microvascular and neuronal networks [Reichold et al., 2009].

2.2.2 Adding mass transfers to investigate oxygen and nutrients delivery

As described above, the modelling of oxygen and nutrients delivery is needed in the framework of brain imaging. Moreover, understanding oxygen transfers is crucial to understand how vascular alterations in pathology, e.g. capillary rarefaction of occlusions of larger vessels, translates to insufficient oxygen supply and neuron death. Developing such modelling approach is beyond the scope of this manuscript.

Along with the models developed for blood flow modelling, several approaches have been presented for the simulation of oxygen transfers in the brain microcirculation. In particular, models exist for the description of time-varying advection-diffusion equation of oxygen in the microvessels and the surrounding tissue [Fang et al., 2008]. The set of physical processes involved are schematized in Fig. 2.5. In the same spirit as reduced models developed for blood flow modelling, such models commonly consider the vascular network as a one-dimensional network of interconnected tubes. In [Fang et al., 2008], the modelling of blood flow in vessels is coupled to an advection equation for oxygen transport. This reads

$$\frac{\partial C_v}{\partial t} + \boldsymbol{u} \cdot \boldsymbol{\nabla} C_v = \nabla \cdot (D_v \boldsymbol{\nabla} C_v)\,, \tag{2.8}$$

with C_v the concentration of oxygen in the vessel, and D_v the diffusion coefficient in the vessel. In

the tissue, the diffusion equation reads

$$\frac{\partial C_t}{\partial t} + \boldsymbol{u} \cdot \boldsymbol{\nabla} C_t = \nabla \cdot (D_t \boldsymbol{\nabla} C_t) - \kappa_t C_t, \tag{2.9}$$

with C_t the concentration of oxygen in the tissue, D_t the diffusion coefficient in tissue, and κ_t the metabolic consumption rate. By contrast to the one-dimensional treatment of Eq. 2.8, Eq. 2.9 is discretized on a tetrahedral mesh that covers the tissue volume in a parallelepipedic bounding box. Finally, the oxygen flux F_w across the thin vessel wall is described by a diffusion process based on the conservation of oxygen, and characterized by the permeability K_w of the wall. Such a process reads

$$F_w = -K_w \frac{(C_t - C_v)}{\alpha w}, \tag{2.10}$$

where α is a solubility coefficient, and w is the thickness of the vascular wall. The exchange equations are discretized on a triangular mesh covering the vascular surface. This model has been validated for both static and dynamic configurations by comparison with two-photon microscopy measurements in a volume of $230 \times 230 \times 450\,\mu\text{m}^3$ of a rodent microvasculature network. The results showed good qualitative agreement with *in vivo* experiments.

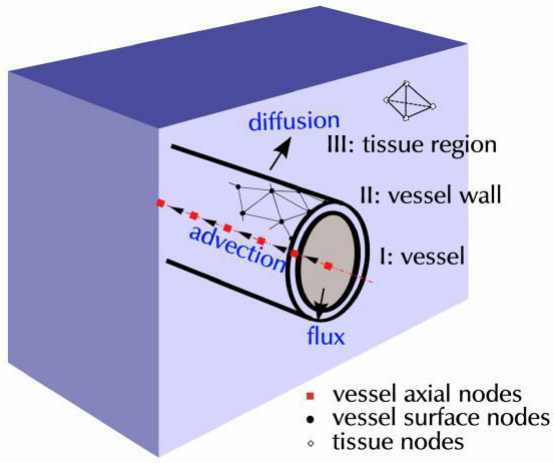

Figure 2.5: **Schematics of the problem of oxygen transport and diffusion in the microvessels and the surrounding cerebral tissue.** This figure has been extracted from [Fang et al., 2008]. It illustrates the three main physical processes involved in the description of oxygen fields: advection in the vessels, diffusion in the tissue, and description of the flux through the vascular wall.

The study of Fang et al. involved anatomical datasets, thus was limited to relatively small volumes ($\sim$1 mm^3). To go further, similar studies has been led in anatomically accurate synthetic networks [Linninger et al., 2013]. This strategy opens the way to much larger simulations. For example, in

[Linninger et al., 2013], the quantification of oxygen transport, diffusion and consumption has been performed in a volume of $3 \times 3 \times 3\,\mathrm{mm}^3$ of a synthetic microvascular network designed to represent the human secondary cortex (about 256 000 vessels, see Fig. 1.4).

To go further, Secomb *et al.* developed a model for the analysis of oxygen delivery to the cortical tissue, which is based on Green's functions [Hsu and Secomb, 1989, Secomb et al., 2004]. The main idea of this method is to consider the microvasculature as a set of discrete oxygen sources and to represent the oxygen field in the tissue as a superposition of fields resulting from these sources. In this way, the extravascular domain does not need to be discretized, implying an important computational gain. Furthermore, it is applicable to complex geometries. For instance, application to a microvascular network of $0.2\,\mathrm{mm}^3$ of the hamster cremaster muscle is presented in [Secomb et al., 2004]. Another advantage of this approach is that it provides a new angle of investigation of the impact of the boundary conditions. Indeed, Green's function can be either defined in an infinite domain, minimizing the effect of finite configurations on the oxygen distribution, or modified to satisfy specific boundary conditions. While this approach is promising, it has not been coupled yet with a realistic blood flow model for applications in the human brain microcirculation.

Number of numerical models exist for modelling oxygen transport and diffusion in brain microcirculation. While such approaches enabled significant advances in the understanding of the neurovascular coupling, they are still limited to relatively small volumes, with no volumes large than $\sim 10\,\mathrm{mm}^3$ reported in this context.

2.3 Upscaling approaches

To reduce the computational cost of blood flow and mass transfers simulations in microvascular networks, one idea is to upscale the governing equations from the scale of individual vessels to larger volumes that are representative at mesoscopic scale. This generally induces an important improvement of the computational performance since the problem is described at larger scale, with fewer variables.

In this section, we focus on three papers that are representative of three different upscaling methods proposed in the literature for the simulation of blood flow and/or mass transfers in microvascular networks. The philosophy of each of these approaches will be presented. As will be detailed, they all imply the treatment of several models defined at separate scales. Thus, a discussion about the

coupling methods developed at the interface between these models will also be provided.

2.3.1 The use of a coarser network representation

One solution to reduce the computational cost of the network approaches is to build a coarser network representation of the capillary bed. This can be done by merging several capillary vertices into one *upscaled vertex*. In [Reichold et al., 2009], this strategy is applied for the simulation of blood flow and mass transport in the cerebral microvasculature of rats. The idea is to divide the capillary volume into "sufficiently big" *subdomains*, so that the computational cost is theoretically divided by the number of capillaries contained in one subdomain. In this paper, the side of one subdomain is chosen as at least twice the length of a capillary, as represented in Fig. 2.6.

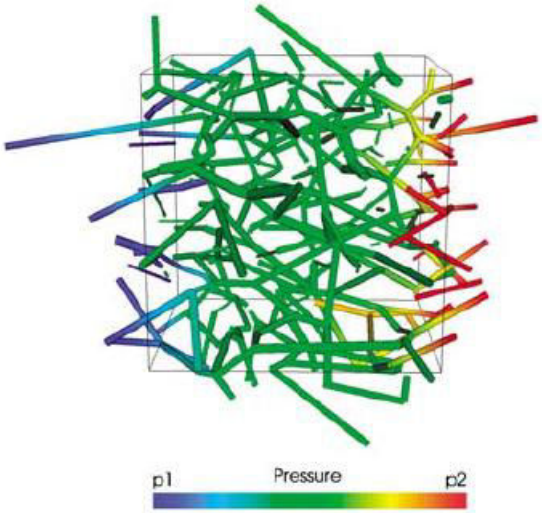

Figure 2.6: **Illustration of a typical subdomain of the capillary network.** This figure has been extracted from [Reichold et al., 2009]. Flow is simulated in a cubic volume of the capillary bed by imposing a pressure drop $(p_2 - p_1)$ in one direction of the space. No-flux conditions are imposed on the four other faces of the cube.

To further describe the morphometrical properties of the coarser network representation, integral quantities (e.g. vascular volume) are determined in each subdomain and assigned to the corresponding upscaled vertex. Finally, the averaged conductance of one subdomain is estimated by simulating blood flow at microscopic scale in each subdomain separately, using the network approach (Eq. 2.1). For that purpose, a global pressure drop $\Delta\pi$ is imposed between two opposite faces of a subdomain, no-flux at the four others (see Fig. 2.6), and the flow equations are solved at microscopic scale. The resulting global flow rate q is then deduced, and the averaged conductance G of the subdomain is

defined by

$$G = \frac{q}{\Delta\pi}. \tag{2.11}$$

The conductance at the interface between two subdomains is finally defined as the harmonic average of the conductances of the two subdomains of interest.

In [Reichold et al., 2009], simulations involving a few arteriolar and venular trees connected to an upscaled representation of the capillary bed are presented. Compared to the corresponding configuration defined at the scale of the capillaries, the upscaled version involved three times less vertices, leading to improved computational performance. However, no detail was provided in this paper concerning the size of the subdomains, suggesting that they can be arbitrarily defined, as long as they are at least twice larger than the length of a capillary. Furthermore, the use of a coarser network representation downstream of the arteriolar and venular coupling points results in a larger capillary length. Thus the pressure relaxation around the couplings is likely shifted to larger length scales. In other words, the strong pressure gradients around the couplings at microscopic scale might not be properly upscaled.

2.3.2 Homogenization: the microvascular networks as a porous medium

Another upscaling approach, which is widely used in the community of porous medium, is *homogenization*. Homogenizing the flow equations in a microvascular network consists in replacing it by a continuum, where the flow is characterized by partial differential equations and effective properties (e.g. permeability) at the scale of a much larger representative volume, termed Representative Elementary Volume (REV) [Bear, 1972, Erbertseder et al., 2012]. At this scale, flow equations are governed by Darcy's law, which can be obtained from homogenization via *volume averaging* (see e.g. [Whitaker, 1986, Quintard and Whitaker, 2000, Davit et al., 2013a]) of creeping flow at microscopic scale. Assuming that the continuum is homogeneous and isotropic, one form of the Darcy's law reads

$$\boldsymbol{U} = -\frac{K}{\mu}\boldsymbol{\nabla} P, \tag{2.12}$$

where $\boldsymbol{U}$ represents the flow velocity, P the pressure, K the effective permeability of the domain, and μ the effective viscosity of blood. For Newtonian fluids, i.e. uniform viscosity, the effective parameters K and μ are commonly used to define a single resistivity K/μ of the network. As presented in [El-Bouri and Payne, 2015], this resistivity is commonly computed by simulating blood flow at microscopic

scale in a REV of the network, in the same spirit as [Reichold et al., 2009] (see also Fig. 2.6).

Replacing the microvascular network by a continuum presents two main advantages:

- the Darcy's law can be discretized on a coarse grid using finite volume or finite element methods. This implies an important computational gain since a single discretization cell may replace a large number of vertices;
- the knowledge of the whole microvascular structure is no more required since only a REV of the vasculature is needed to compute the effective parameters that will characterize the flow at much larger scale.

This upscaling process has been widely used in both cardiac and tumoral applications [Hyde et al., 2014, Waters et al., 2011, Shipley and Chapman, 2010]. For instance, Hyde *et al.* [Hyde et al., 2013] uses the homogenization to simulate blood flow in a synthetic microvascular network of 8 mm^3 representative of the cardiac vasculature. The goal of this study is to use continuum flow models to characterize perfusion at mesoscopic scale. For that purpose, the whole set of microvessels, from the largest arterio-venular trees to the smallest capillaries, is divided into several continuous compartments, termed *Darcy compartments* (see Fig. 2.7). This partitioning is imposed according to the hierarchical position of vessels, which is mainly based on diameter cut-offs, with the condition that each partition presents low topological variations. The homogenization approach is then applied separately on each compartment.

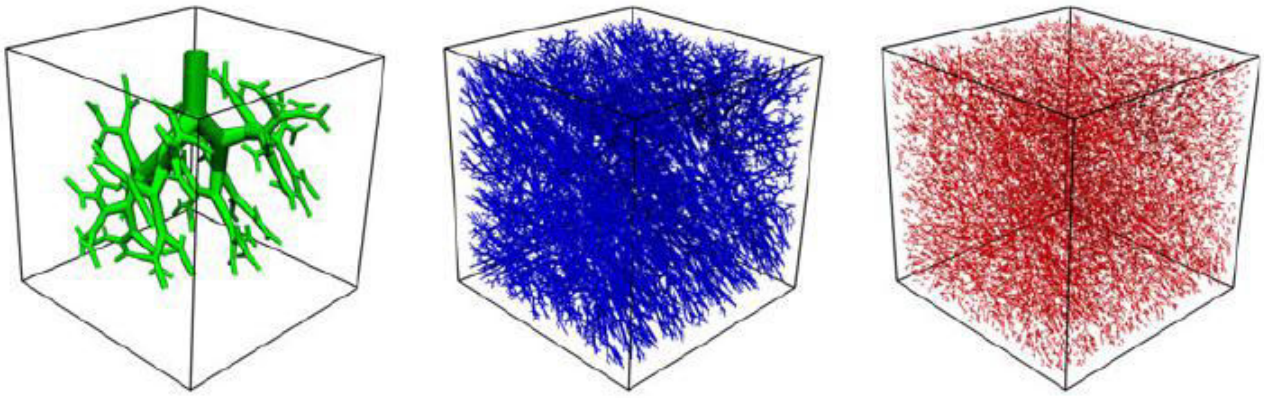

Figure 2.7: **Representation of three Darcy compartments involved a synthetic microvascular network of 8 mm^3.** This figure has been extracted from [Hyde et al., 2013]. A synthetic networks is divided in three Darcy compartments.

Further, the transition between the Darcy compartments is defined by a local permeability computed from the averaged flux transfer that occur at the interface between the partitions, at mi-

croscopic scale. The robustness of such a coupling is closely related to the partitioning metric. In particular, the scale difference at the interface between two Darcy compartments must be very smooth to ensure the accuracy of the model. Finally, the estimation of the flow fields at the interfaces between the compartments have been proven to be accurate, in a given range of pressure boundary conditions. However, the representation of the larger vessels as a continuum in [Hyde et al., 2013] is questionable. Indeed, while the capillary bed is dense and homogeneous over a cut-off length of $\sim$50 μm, the arteriolar and venular trees present a quasi-fractal structure that prevents the existence of a unique characteristic length, thus the assimilation to a continuum (see Section 2.1.1).

In the approaches presented in the next section, homogenization is applied only to the capillary network and the larger vessels of the microvascular networks are modelled using standard network approaches. Such a method is termed *hybrid* since it involves two separate modelling frameworks.

2.3.3 Hybrid approaches

In [Erbertseder et al., 2012], a hybrid approach is used for the modelling of blood flow and mass transfers in the microvascular networks of a human lung. The use of reduced-order models is crucial in such an application, since the number of capillary vessels in the pulmonary system is estimated at $\sim 5.4 \times 10^{11}$. Before presenting the models, the pulmonary vasculature is presented in Fig. 2.8**(a)**. It is composed of large feeding arteries and draining veins, which are coupled to intermediate capillary networks. These capillary networks deploy at the surface of alveola. This is the place of molecular exchange with the pulmonary tissue. As illustrated in Fig. 2.8**(b)**, the modelling of blood flow and mass transfers in such a structure involve both network and continuum representations. In the arteries and veins, blood flow and mass transport are modelled using a standard network approach (Eq. 2.8). In the continuums that replace the capillary networks and the local pulmonary tissue, dynamics are described by Darcy's law (similar to Eq. 2.12).

To further describe the interaction between the three domains, independent coupling variables are used as source or sink terms in the network and continuum domains. The models associated to these domains are then linked by a sequential iterative process of data transfer, which ensured flow conservation, through these coupling variables. However, such a coupling process is more a correction process than a proper description of the multiscale relationship between the variables involved. Furthermore, the sequential process represents a computational loss with regard to large-scale sim-

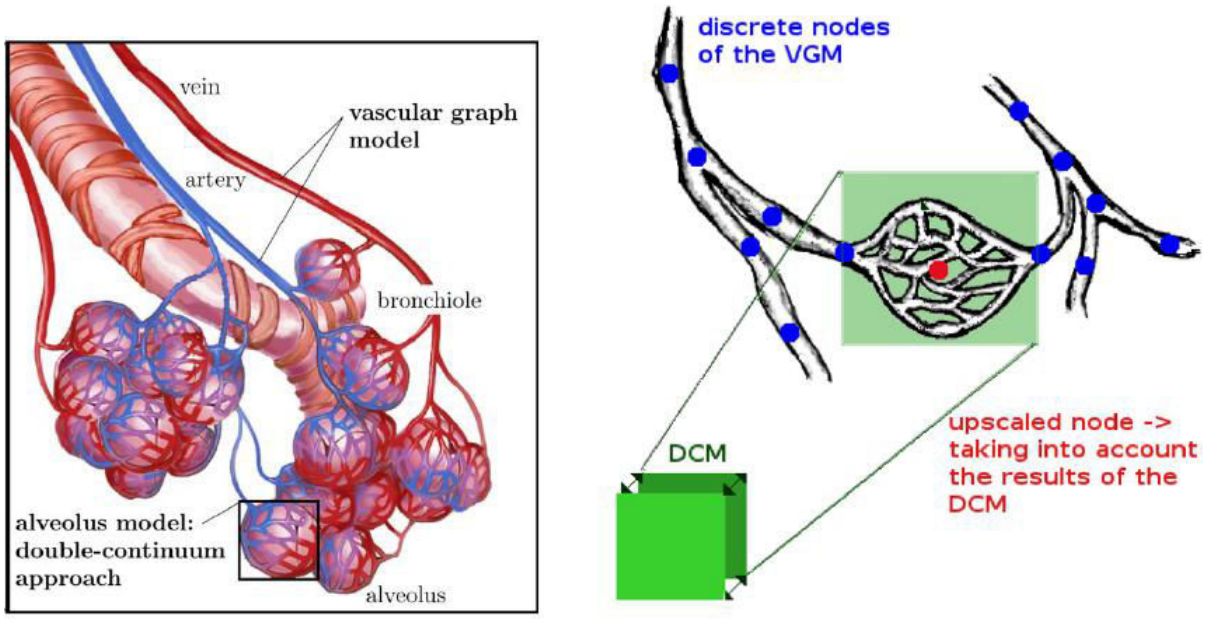

(a) **(b)**

Figure 2.8: **The general model concept used in** [Erbertseder et al., 2012]**.** These figures has been extracted from [Erbertseder et al., 2012]. **(a)** Illustration of the pulmonary microvasculature: the feeding arteries and draining veins are represented in red and blue, respectively. At the endpoints of the arteries and veins, capillary network deploy at the surface of alveola. This is the place of molecular exchange with the pulmonary tissue. **(b)** *Illustration of the hybrid approach*: the artery and the vein (blue dots) are modelled by a standard network approach, or Vascular Graph Model (VGM). They are connected to an upscaled node (red node) representative of the capillary network, which is considered as a continuum. The upscaled node is finally coupled to the surrounding pulmonary tissue (green square) for the description of mass transfers.

ulations that require parallel implementation and execution. Nevertheless, this hybrid approach also led to an essential computational gain, which the reduction of the number of unknowns. Indeed, in the application presented in [Erbertseder et al., 2012], this number has been divided by 1 800.

As presented in this section, the use of upscaling methods to build reduced-order models represents an important computational gain, due to the associated reduction of the number of unknowns. However, the coupling between network and continuum approaches received little attention in the context of brain microcirculation. By comparison, they are widely discussed for the modelling of blood flow and mass transfers in the largest arteries of the cerebral circulation (Circle of Willis) [Formaggia et al., 1999, Figueroa et al., 2006, Passerini et al., 2009, Blanco et al., 2009, Perdikaris et al., 2016]. This idea of a hybrid formulation mixing models at different scales has also spread across fields, for instance to couple atomic and continuum descriptions [Fish et al., 2007] or discrete cellular-level and PDE models [Kim et al., 2007], always with difficulties in coupling both frameworks [Davit et al., 2013b].

In this work, we will consider a hybrid approach to model blood flow in the human cerebral microcirculation, in the same spirit as [Erbertseder et al., 2012]. As will be detailed in Section 3, the largest arteriolar and venular trees will be modelled by a standard network approach (Eq. 2.1), and the capillary network will be replaced by a continuum where blood flow is governed by Darcy's law (Eq. 2.12). This strategy relies on the combination of to modelling frameworks that are associated to separate scales. Thus, we will take special care in developing a proper multiscale coupling model at the interface between these two frameworks (Section 4). Furthermore, in the perspective of simulations at the scale of the whole human brain and further extension to mass transfers, we will avoid to use iterative coupling methods. To our knowledge, no such model exists in the context of cerebral microcirculation.

3 Modelling groundwork for the hybrid approach

In this section, we present the models describing blood flow dynamics (mass and momentum conservation) in the brain microcirculation for the network approach that we apply to the arteriolar and venular trees (black networks in Fig. 3.1), and the continuum representation of the capillary bed (green mesh in Fig. 3.1). As presented in previous sections, both methods are classical in the domains of brain microcirculation and porous media, respectively. The main contribution of this work is to devise a proper multiscale coupling model at the interface between these two frameworks, i.e. where the arteriolar or venular end-tips are connected to a capillary (red dots in Fig. 3.1). The development of this coupling model will be presented in Section 4 below, after having presented the standard flow equations for both network and continuum parts.

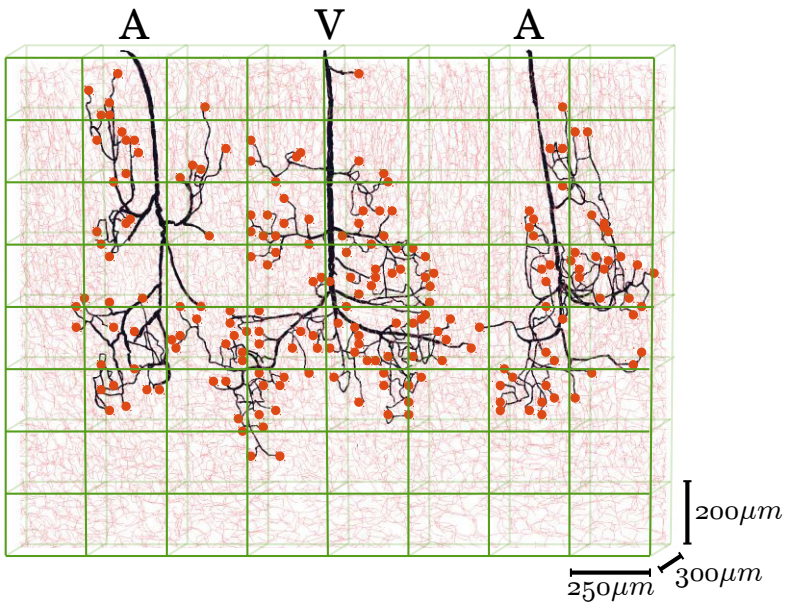

Figure 3.1: **Concept of the hybrid approach.** At mesoscopic scale, the capillary bed (light red vessels) is considered as a continuum, where the flow equations are averaged and discretized over a coarse mesh (green grid) using a finite volume formulation. The arteriolar and venular trees (black vessels) cannot be homogenized because of their quasi-fractal structure. In these vessels, the flow is modelled using a classical network approach. At the interface between these two frameworks, a proper multiscale coupling model must be applied at coupling points (highlighted by red dots).

3.1 Main simplifications and hypotheses

In this manuscript, we focus on blood flow with the following main assumptions: the capillary bed is assumed to be isotropic and homogeneous; further, the non-linearities induced by the non-proportional distribution of the red blood cells at microvascular bifurcations are neglected, following [Boas et al., 2008, Reichold et al., 2009, Linninger et al., 2013, Blinder et al., 2013, Gagnon et al., 2015], so that the hematocrit is assumed to by uniform. These simplifications are needed to introduce the analytical coupling model presented in detail in Section 4.

In addition, we use several other hypotheses that are common to all frameworks. First, blood typically flows at about $10\,\mathrm{mm}\cdot\mathrm{s}^{-1}$ in the arteriolar and venular trees and at about $1\,\mathrm{mm}\cdot\mathrm{s}^{-1}$ in the capillary network, so that the Reynolds number is everywhere significantly lower than 1 [Fung and Zweifach, 1971] and inertial effects can be neglected. Second, the pulsatility is negligible because the Womersley number is lower than 0.1 [Santisakultarm et al., 2012]. We further assume that the mass density of blood ρ and the gravity vector $\boldsymbol{g}$ are constant in the brain microcirculation, so that the pressures used in all equations are defined as the fluid pressures minus the hydrostatic pressures.

3.2 Network model for the arteriolar and venular trees

3.2.1 Geometry, vocabulary and conventions

As schematized in Fig. 3.2, the arteriolar and venular tree-like vasculature are treated as a network of interconnected tubes, also termed *edges* according to the vocabulary used in graph theory [Bollobás, 2013]. Each edge is characterized by its length l and mean diameter d. As displayed in Fig. 3.2, it is defined at its end-tips by two *vertices*, which correspond to bifurcations, i.e. connections to other vessels. A bifurcation is classified as an *inner vertex* if it has more than one neighbour (green dots in Fig. 3.2). Otherwise, the vertex corresponds to either an arteriolar inlet or venular outlet, or a coupling point connected to a capillary. In the first case, the vertex is classified as a *boundary vertex* (blue dots in Fig. 3.2). In the second case, it is termed *coupled vertex* (red dots in Fig. 3.2).

Furthermore, to describe the uniqueness of a given network composed of vertices and edges, its connectivity must be specified. For that purpose, we use a *adjacency matrix*. In such matrix, each line corresponds to one vertex of the network, and all its neighbouring vertices are stored in this line. As an illustration, the adjacency matrix corresponding to the network displayed in Fig. 3.2 is presented in Fig. 3.3.

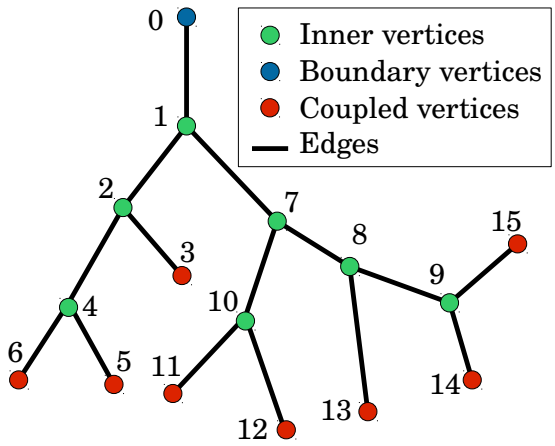

Figure 3.2: **Architectural components of an arteriolar or venular tree.** Vertices (dots) are connected by edges (black lines) to form a network. The inner vertices are highlighted by green dots, the single boundary vertex by a blue dot, and coupled vertices by red dots. Each vertex is numbered for the purpose of describe the connectivity of the network (see Fig. 3.3).

$$
\begin{array}{r}
\text{node } 0 \rightarrow \\
\text{node } 1 \rightarrow \\
\text{node } 2 \rightarrow \\
\text{etc}
\end{array}
\begin{pmatrix}
1 & & \\
0 & 2 & 7 \\
1 & 3 & 4 \\
2 & & \\
2 & 5 & 6 \\
4 & & \\
4 & & \\
1 & 8 & 10 \\
7 & 9 & 13 \\
8 & 14 & 15 \\
7 & 11 & 12 \\
10 & & \\
10 & & \\
8 & & \\
9 & & \\
9 & &
\end{pmatrix}
$$

Figure 3.3: **Adjacency matrix of the network displayed in Fig. 3.2.** Each line of the matrix corresponds to one vertex of the network, and contains its neighbouring vertices.

For consistency, all the variables referring to the network model are subscripted by Greek letters. A vertex is defined by one index (e.g. α), while an edge is defined by the two indexes corresponding to its endpoint vertices (e.g. $[\alpha\beta]$ for the edge delimited by the vertices α and β). The only exception to this convention concerns the coupled vertices, which will be subscripted by s (as *sources*, see Section 4 below).

With regard to flow modelling, the objective is to describe the pressure field by assigning a pressure value π_α at each inner vertex α, provided that boundary and coupling conditions are imposed at the

boundary and coupled vertices, respectively. The flow rate value $q_{\alpha\beta}$ of each edge $[\alpha\beta]$ is then derived from this pressure field.

3.2.2 Flow equations

In arteriolar and venular tree-like networks, blood flow is described by a succession of linear relationships between the vessel flow rate and the pressure drop [Pries et al., 1990, Boas et al., 2008, Reichold et al., 2009, Lorthois et al., 2011a, Lorthois et al., 2011b]. The flow $q_{\alpha\beta}$ in each vessel connecting vertices α and β is written as

$$q_{\alpha\beta} = G_{\alpha\beta}\left(\pi_\alpha - \pi_\beta\right), \tag{3.1}$$

with π_α, π_β the pressures at α and β vertices and $G_{\alpha\beta}$ the vessel conductance defined as

$$G_{\alpha\beta} = \frac{\pi d_{\alpha\beta}^4}{128\mu_{\alpha\beta}^{\text{app}} l_{\alpha\beta}}, \tag{3.2}$$

with $d_{\alpha\beta}$ the vessel mean diameter and $l_{\alpha\beta}$ the vessel length. The apparent viscosity $\mu_{\alpha\beta}^{\text{app}}$ in computed using the *in vivo* viscosity law derived by Pries *et al.* already presented in Section 2, Eq. 2.3.

Assuming pressure continuity at the bifurcations [Pedley et al., 1971], mass balance at each inner vertex α reads

$$\sum_{\beta\in\mathcal{N}_{\alpha,\text{in}}} G_{\alpha\beta}\left(\pi_\alpha - \pi_\beta\right) = 0, \tag{3.3}$$

where $\mathcal{N}_{\alpha,\text{in}}$ represents the set of inner neighbouring vertices that are connected to α. If the vertex α is connected to a boundary vertex $\widetilde{\alpha}$, Eq. 3.3 reads

$$\sum_{\beta\in\mathcal{N}_{\alpha,\text{in}}} G_{\alpha\beta}\left(\pi_\alpha - \pi_\beta\right) = q_{\alpha\widetilde{\alpha}}, \tag{3.4}$$

where $q_{\alpha\widetilde{\alpha}}$ is the flow rate source term that describes boundary conditions for arteriolar inlets ($q_{\alpha\widetilde{\alpha}} > 0$) or venular outlets ($q_{\alpha\widetilde{\alpha}} < 0$). Alternately, when a pressure condition $\pi_{\widetilde{\alpha}}$ is imposed on a boundary vertex $\widetilde{\alpha}$, Eq. 3.4 may be rewritten

$$\sum_{\beta\in\mathcal{N}_{\alpha,\text{in}}} G_{\alpha\beta}\left(\pi_\alpha - \pi_\beta\right) + G_{\alpha\widetilde{\alpha}}\pi_\alpha = G_{\alpha\widetilde{\alpha}}\pi_{\widetilde{\alpha}}. \tag{3.5}$$

If the vertex α is connected to a coupled vertex s, Eqs. 3.4 reads

$$\sum_{\beta \in \mathcal{N}_{\alpha,\text{in}}} G_{\alpha\beta} \left(\pi_\alpha - \pi_\beta\right) = q_s, \tag{3.6}$$

where q_s is the flow rate source term that describe coupling conditions of the network with the homogenized capillary bed (red dots in Fig. 3.1**(a)**). This latter case is detailed in Section 4.

3.2.3 Setting of linear system

Let M_{network} be the matrix corresponding to the linear system built from Eqs 3.3-3.6. This matrix is of size (number of inner vertices)^2. The expression related to an inner vertex α corresponds to the α^{th} row of this matrix, which is filled as follows:

$$M_{\text{network}}\left(\alpha, \alpha\right) = \sum_{\beta \in \mathcal{N}_{\alpha,\text{in}}} G_{\alpha\beta} \tag{3.7}$$

and, for each inner neighbours β of α,

$$M_{\text{network}}\left(\alpha, \beta\right) = -G_{\alpha\beta}. \tag{3.8}$$

If the vertex α is connected to a boundary vertex $\widetilde{\alpha}$, two boundary conditions can be applied: either a flow rate $q_{\alpha\widetilde{\alpha}}$ in the vessel $[\alpha, \widetilde{\alpha}]$ (Eq. 3.4) or a pressure $\pi_{\widetilde{\alpha}}$ at the boundary vertex $\widetilde{\alpha}$ (Eq. 3.5). In the first case, the α^{th} row of the right-hand side R_{network} reads

$$R_{\text{network}}\left(\alpha\right) = q_{\alpha\widetilde{\alpha}}. \tag{3.9}$$

In the second case, the diagonal component of the matrix is incremented

$$M_{\text{network}}\left(\alpha, \alpha\right) += G_{\alpha\widetilde{\alpha}} \tag{3.10}$$

and the α^{th} row of the right-hand side reads

$$R_{\text{network}}\left(\alpha\right) = G_{\alpha\widetilde{\alpha}} \pi_{\widetilde{\alpha}}. \tag{3.11}$$

If the vertex α is connected to a coupled vertex s, Eqs. 3.9-3.11 are valid, replacing the subscript $\widetilde{\alpha}$ by s.

The linear system associated to the network modelling yields a sparse symmetric matrix. As displayed in Fig. 3.4, the intrinsic non-structured organization of a network (i.e. need for a adjacency matrix) further yields a non-structured arrangement of the non-zero components. The right-hand side, which contains the inlets and outlets of the network, also has a sparse structure.

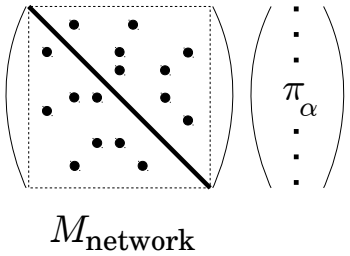

Figure 3.4: **Visualization of the matrix corresponding to the linear system built using the network approach.** The network approach yields a sparse symmetric matrix. The black line represents the diagonal filled with non-zero components and the black dots represents off-diagonal non-zero components. The non-structured arrangement of the non-zero components stems from the intrinsic non-structured organization of a microvascular network.

3.3 Continuum approach for the capillary bed

3.3.1 Geometry, vocabulary and conventions

In the hybrid approach, the capillary bed is considered as a continuum where knowing the details of the microscopic architecture is not required. As presented below, the flow equations averaged at mesoscopic scale are discretized using the finite volume method. In this method, the domain is discretized over a structured mesh composed of parallelepipedic *cells* of side h (green grid in Fig. 3.1). Such cells must be *coarse enough* to correspond to a representative volume of the capillary bed ($h \gg l_{cap}$), and *fine enough* to enable the spatial characterization of the flow fields in the whole FV domain. This last criterion is mainly constrained by the thickness of the cortex, which is ∼3 mm deep in humans. To give an idea, the typical volume of a discretization cell is displayed in Fig. 1.2**(d)** and corresponds to $h \sim 250\,\mu$m, or $^1/_{10}$ of the cortical thickness.

By contrast to the notation adopted for the network approach, all the variables referring to the continuum approach are subscripted by Latin letters. A cell is defined by one letter (e.g. cell i) while the exchange surface between two cells (e.g. i and j) is defined by the combination of the two corresponding indexes (e.g. surface ij).

With regard to flow modelling, the objective is to describe the pressure field by assigning a mean pressure P_i to each cell i. The mean flow rate value Q_{ij} of each exchange surface ij is then derived from the pressure field.

3.3.2 Flow equations

At mesoscopic scale, we describe momentum transport using Darcy's law, which can be obtained from homogenization via volume averaging (see e.g. [Whitaker, 1986, Quintard and Whitaker, 2000, Davit et al., 2013a]) of creeping flow at microscopic scale. We have

$$\mathbf{U} = -\frac{1}{\mu^{\text{eff}}}\mathbf{K}^{\text{eff}} \cdot \boldsymbol{\nabla} P, \tag{3.12}$$

where $\mathbf{U}$ is the Darcy velocity, i.e. a spatially averaged velocity representative at mesoscopic scale, P is the mesoscopic pressure, μ^{eff} is the effective viscosity of blood and $\mathbf{K}^{\text{eff}}$ is the permeability tensor. We assume that the capillary network is isotropic and homogeneous, so we have $\mathbf{K}^{\text{eff}} = K^{\text{eff}}\mathbf{I}$. The effective parameters K^{eff} and μ^{eff} are calculated by solving microscopic-scale flow (Eqs. 3.3 and 3.6) at mesoscopic scale [Bear, 1972]. Both coefficients are usually lumped together into a single effective resistivity ${}^{K^{\text{eff}}}\!/_{\mu^{\text{eff}}}$ of the network [Reichold et al., 2009, Smith et al., 2014]. In this manuscript, as detailed in Section 3.4, the effective permeability K^{eff} rather represents the permeability of the network with uniform viscosity, while the effective viscosity μ^{eff} represents the impact of the Fåhræus-Lindqvist effect (Eq. 2.3).

Mass balance in the porous medium is written as

$$\nabla \cdot \mathbf{U} = -\sum_{s \in S} \delta\left(\mathbf{x} - \mathbf{x}_s\right) q_s, \tag{3.13}$$

with q_s the flow rate source term, which results from the coupling condition applied at the coupling point s located at the position $\mathbf{x}_s$, at any endpoint of feeding arteriolar or draining venular trees (more detail in Section 4). S represents the set of all sources and $\delta\left(\mathbf{x} - \mathbf{x}_s\right)$ the Dirac delta corresponding to the point source s.

3.3.3 Numerical approach: finite volume method

The solution of the partial differential equation combining Eqs. 3.12 and 3.13 is computed using a standard cell-centered finite volume (FV) approach [Eymard et al., 2000, Versteeg and Malalasekera,

2007] on a Cartesian grid. The idea of such a method is: **(1)** to integrate the mass balance equation (Eq. 3.13) over the volume of each discretization cell in order to work with variables averaged at the mesoscopic scale; **(2)** to substitute Eq. 3.12 into Eq. 3.13 in order to obtain a system of equations involving only pressures; and **(3)** to close the problem using pressure and flux continuity at the interface between two discretization cells.

For convenience, we consider cubic cells of volume h^3. The extension to non-cubic cells, which is straightforward, will be detailed in Section 3.3.5.

(1) *Integration of the mass balance equation.* Let i be a cell of interest, and l, r, d, u, f and b their neighbours, *l*eft, *r*ight, *d*own, *u*p, *f*ront and *b*ack, respectively. By integrating Eq. 3.13 over the volume V_i of the cell i, we have

$$\int_{V_i} \nabla \cdot \mathbf{U} \; dV = - \int_{V_i} \sum_{s \in S} \delta \left(\mathbf{x} - \mathbf{x}_s \right) q_s \; dV. \tag{3.14}$$

By definition of the Dirac delta, this can be rewritten

$$\int_{V_i} \nabla \cdot \mathbf{U} \; dV = - \sum_{s \in S_i} q_s, \tag{3.15}$$

with S_i the set of sources located in cell i. The divergence theorem then yields

$$\int_{\partial V_i} \mathbf{U} \cdot n \; dS = - \sum_{s \in S_i} q_s, \tag{3.16}$$

with ∂V_i the boundary of the cell i and n the outward pointing unit normal field of the boundary ∂V_i. The outward flux can also be expressed

$$\int_{\partial V_i} \mathbf{U} \cdot n \; dS = \sum_{j \in \{l,r,d,u,f,b\}} \left(\mathbf{U} \cdot n|_{i \to j} \right) \; h^2, \tag{3.17}$$

with $\mathbf{U} \cdot n|_{i \to j}$ the outward flux from cell i to cell j.

The integration of Eq. 3.13 over the volume of the cell i finally expresses the sum of the outward

fluxes as the sum of the local source terms:

$$\sum_{j\in\{l,r,d,u,f,b\}} (\mathbf{U}\cdot n|_{i\to j})\ h^2 = -\sum_{s\in S_i} q_s \tag{3.18}$$

(2) *Substitution of Darcy's law into the mass balance equation.* In order to work with equations involving only pressures, we substitute Eq. 3.12 into Eq. 3.18. This yields

$$-\frac{K^{\text{eff}}}{\mu^{\text{eff}}} \sum_{j\in\{l,r,d,u,f,b\}} (\boldsymbol{\nabla} P\cdot n|_{i\to j})\ h^2 = -\sum_{s\in S_i} q_s. \tag{3.19}$$

Let now consider $j = r$ in particular. The value $\boldsymbol{\nabla} P\cdot n|_{i\to r}$ can be rewritten as

$$\boldsymbol{\nabla} P\cdot n|_{i\to r} = \frac{\partial P}{\partial x}|_{i,r}, \tag{3.20}$$

where ${}^{\partial P}/_{\partial x}|_{i,r}$ is the value of the derivate of the pressure in the x-direction, in the cell i, at the interface with the cell r. Using finite difference method to approximate the value of ${}^{\partial P}/_{\partial x}|_{i,r}$, we have

$$\frac{\partial P}{\partial x}|_{i,r} = \frac{P_{i,r} - P_i}{{}^{h}/_{2}} \tag{3.21}$$

with P_i the pressure defined at the center of cell i and $P_{i,r}$ the pressure defined in cell i, at the interface with cell r. Similarly, we have

$$\boldsymbol{\nabla} P\cdot n|_{i\to j} = \frac{P_i - P_{i,j}}{{}^{h}/_{2}} \quad \text{for } j\in\{l,r,d,u,f,b\}\,. \tag{3.22}$$

Substituting Eq. 3.22 into Eq. 3.19, we have

$$-\frac{K^{\text{eff}}}{\mu^{\text{eff}}} \sum_{j\in\{l,r,d,u,f,b\}} \left(\frac{P_i - P_{i,j}}{{}^{h}/_{2}}\right) h^2 = -\sum_{s\in S_i} q_s, \tag{3.23}$$

which can be rewritten

$$-\frac{2K^{\text{eff}}h}{\mu^{\text{eff}}} \sum_{j\in\{l,r,d,u,f,b\}} (P_i - P_{i,j}) = -\sum_{s\in S_i} q_s. \tag{3.24}$$

(3) *Pressure and flux continuity at the interface between two cells.* To finally express $P_{i,j}$ (j in $\{l, r, d, u, f, b\}$) as a function of P_i and P_j, we use the expressions of flux and pressure continuity at the interface between the two cells

$$\mathbf{U} \cdot n|_{i \to j} = -\mathbf{U} \cdot n|_{j \to i} \tag{3.25}$$

and

$$P_{i,j} = P_{j,i}. \tag{3.26}$$

Let consider $j = r$ again. From Eq. 3.12, we know that

$$\mathbf{U} \cdot n|_{i \to r} = -\frac{K^{\text{eff}}}{\mu^{\text{eff}}} \boldsymbol{\nabla} P \cdot n|_{i \to r} = -\frac{K^{\text{eff}}}{\mu^{\text{eff}}} \frac{P_{i,r} - P_i}{h/2}. \tag{3.27}$$

Similarly, we have

$$\mathbf{U} \cdot n|_{r \to i} = -\frac{K^{\text{eff}}}{\mu^{\text{eff}}} \frac{P_{r,i} - P_r}{h/2}. \tag{3.28}$$

Thus the flux continuity (Eq. 3.25) yields

$$-\frac{K^{\text{eff}}}{\mu^{\text{eff}}} \frac{P_{i,r} - P_i}{h/2} = +\frac{K^{\text{eff}}}{\mu^{\text{eff}}} \frac{P_{r,i} - P_r}{h/2} \tag{3.29}$$

i.e.

$$P_{i,r} + P_{r,i} = P_i + P_r. \tag{3.30}$$

From the pressure continuity (Eq. 3.26), $P_{i,r} = P_{r,i}$ and Eq. 3.30 becomes

$$P_{i,r} = \frac{P_i + P_r}{2}. \tag{3.31}$$

Finally, we have

$$P_{i,j} = \frac{P_i + P_j}{2} \quad \text{for } j \in \{l, r, d, u, f, b\}. \tag{3.32}$$

By substituting Eq. 3.32 into Eq. 3.24, we have

$$-\frac{2K^{\text{eff}}h}{\mu^{\text{eff}}} \sum_{j \in \{l,r,d,u,f,b\}} \left(P_i - \frac{P_i + P_j}{2} \right) = -\sum_{s \in S_i} q_s \tag{3.33}$$

and obtain the final expression of the FV discretization of the flow equations in the continuum, for each cell i,

$$\frac{K^{\text{eff}}h}{\mu^{\text{eff}}}\sum_{j\in N_i}(P_i - P_j) = \sum_{s\in S_i} q_s, \tag{3.34}$$

where N_i is the set containing the indices of the inner neighbours to cell i, P_i and P_j are the approximated pressures of cells i and j, S_i is the set of sources in cell i and q_s is the flow rate source term. Finally, the quantified pressure P_i defined at the center of a cell i is considered as a local averaging of the pressure field

$$P_i = \frac{1}{h^3}\int_{V_i} P\, dV. \tag{3.35}$$

In the visualizations of this manuscript, we will consider a *piecewise constant reconstruction of the pressure in the continuum*, although a more precise reconstruction can be obtained by linear interpolation.

If the cell i is on the boundary of the domain, three kinds of boundary condition may be imposed: a pressure P_{bound}, a flow rate q_{bound} or a condition of periodicity. Such conditions may be imposed at up to three surfaces of the cell i (in corners) and the set N_i may respectively contain down to three neighbours (also in corners). For only one face of the cell i coinciding with the domain boundary, the finite volume discretization reads

$$\frac{K^{\text{eff}}h}{\mu^{\text{eff}}}\sum_{j\in N_i}(P_i - P_j) + \frac{K^{\text{eff}}2h}{\mu^{\text{eff}}}(P_i - P_{\text{bound}}) = \sum_{s\in S_i} q_s \tag{3.36}$$

in the case of a pressure condition (note that the boundary pressure is imposed at a distance $h/2$ of the cell center, hence the factor of two),

$$\frac{K^{\text{eff}}h}{\mu^{\text{eff}}}\sum_{j\in N_i}(P_i - P_j) - q_{\text{bound}} = \sum_{s\in S_i} q_s \tag{3.37}$$

in the case of a flow rate condition, and

$$\frac{K^{\text{eff}}h}{\mu^{\text{eff}}}\sum_{j\in N_i}(P_i - P_j) + \frac{K^{\text{eff}}h}{\mu^{\text{eff}}}\left(P_i - P_{\tilde{j}}\right) = \sum_{s\in S_i} q_s, \tag{3.38}$$

where $\tilde{j}$ represents the cell at the opposite side of the domain, in the case of a periodicity condition.

If several surfaces of the cell i coincide with the domain boundary, the relevant expressions among the three above are combined.

3.3.4 Setting of the linear system

Let M_{FV} be the matrix corresponding to the linear system built in Eqs. 3.34-3.38. This matrix is of size (number of FV cells)^2. The expression related to an inner cell i corresponds to the i^{th} row of this matrix, which is filled as follows:

$$M_{\mathrm{FV}}(i,i) = \mathrm{Card}(N_i)\,\frac{K^{\mathrm{eff}}h}{\mu^{\mathrm{eff}}} \tag{3.39}$$

and for each neighbour j of i,

$$M_{\mathrm{FV}}(i,j) = -\frac{K^{\mathrm{eff}}h}{\mu^{\mathrm{eff}}}. \tag{3.40}$$

For each surface of the cell i that coincides with a boundary of the domain where a pressure P_{bound} is imposed (Eq. 3.36), the diagonal component of the matrix is incremented

$$M_{\mathrm{FV}}(i,i) += \frac{K^{\mathrm{eff}}2h}{\mu^{\mathrm{eff}}}, \tag{3.41}$$

so does the i^{th} row of the right-hand side R_{FV}

$$R_{\mathrm{FV}}(i) += \frac{2K^{\mathrm{eff}}h}{\mu^{\mathrm{eff}}}\ P_{\mathrm{bound}}. \tag{3.42}$$

For each surface where a flow rate q_{bound} is imposed (Eq. 3.37), the right-hand side reads

$$R_{\mathrm{FV}}(i) += q_{\mathrm{bound}}. \tag{3.43}$$

For each surface where a periodic condition is imposed, the diagonal component of the matrix is incremented

$$M_{\mathrm{FV}}(i,i) += \frac{K^{\mathrm{eff}}h}{\mu^{\mathrm{eff}}},$$

and

$$M_{\mathrm{FV}}\left(i,\tilde{j}\right) = -\frac{K^{\mathrm{eff}}h}{\mu^{\mathrm{eff}}}, \tag{3.44}$$

where $\tilde{j}$ represents the cell at the opposite side of the domain.

The linear system associated to the FV modelling yields a sparse symmetric matrix, which struc-

ture corresponds to the Fig. 3.5. The structured organization of the Cartesian grid (i.e. no need for adjacency matrix) further yields a multi-diagonal arrangement. The right-hand, which contains the boundary conditions of the FV domain, also has a sparse structure.

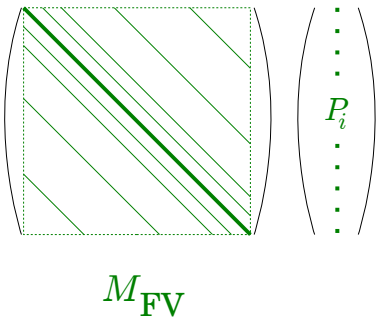

Figure 3.5: **Visualization of the matrix corresponding to the linear system built using the FV approach.** The FV approach yields a sparse, symmetric and multi-diagonal matrix. Green lines represents non-zero components. The structured arrangement of the matrix stems from the intrinsic structured organization of the FV Cartesian grid of discretization.

3.3.5 Bonus: Extension of the FV scheme to non-cubic cells

For simplicity, the finite volume formulation presented in Eq. 3.34 considered cubic cells. Extension of the scheme in a parallelepipedic cell i of size $h_x \times h_y \times h_z$ yields

$$\begin{aligned} &\frac{K^{\text{eff}}}{\mu^{\text{eff}} h_y h_z} \sum_{j \in N_i|_{LR}} (P_i - P_j) \\ +&\frac{K^{\text{eff}}}{\mu^{\text{eff}} h_x h_z} \sum_{j \in N_i|_{DU}} (P_i - P_j) \\ +&\frac{K^{\text{eff}}}{\mu^{\text{eff}} h_x h_y} \sum_{j \in N_i|_{FB}} (P_i - P_j) = \frac{1}{h_x h_y h_z} \sum_{s \in S_i} q_s, \end{aligned} \tag{3.45}$$

where $N_i|_{LR}$, $N_i|_{DU}$ and $N_i|_{FB}$ respectively represent the sets containing the indices of the left and right ($|_{LR}$), down and up ($|_{DU}$) and front and back ($|_{FB}$) neighbouring cells to cell i, P_i and P_j are the approximated pressures of cells i and j, S_i is the set of sources in cell i and q_s is the flow rate source term.

3.4 Computation of the effective properties of the continuum

In the hybrid approach, the capillary bed is replaced by a continuum characterized by two effective properties defined at mesoscopic scale: the effective permeability K^{eff} and the effective viscosity μ^{eff}.

As mentioned in Section 3.3.2 above, both coefficients are usually lumped together into a single effective resistivity $K^{\text{eff}}/\mu^{\text{eff}}$ of the network [Reichold et al., 2009, Smith et al., 2014]. In this work, the effective permeability K^{eff} rather represents the permeability of the network with uniform viscosity, while the effective viscosity μ^{eff} represents the impact of the Fåhræus-Lindqvist effect (Eq. 2.3).

In this section, we detail our method to compute both the effective permeability K^{eff} and viscosity μ^{eff} of the continuum, assuming that the underlying structure of the capillary bed is known. This is the case in this work since we will use generations of synthetic capillary networks, as announced in Section 2. Both the details about the synthetic networks used and the values of the associated effective coefficients will be provided in Section 5.1.3.

To compute K^{eff} and μ^{eff}, the flow is first solved at microscopic-scale in cubic domains of side L containing capillary networks, using the network approach (Eqs. 3.3-3.6). The flow is induced by a pressure drop imposed in one direction of the space, while no flow conditions are imposed on the four other faces. The results are then averaged at mesoscopic scale (more detail in Appendix 8.1) and identified to Darcy's law

$$Q_L = \frac{K_L^{\text{eff}} L}{\mu_L^{\text{eff}}} \Delta_L P, \tag{3.46}$$

where subscript L refers to the network side, $\Delta_L P$ is the imposed pressure drop and Q_L is the resulting global flow rate. The side L of the domain is increased until the effective coefficients become independent of it, meaning that we have reached the mesoscopic scale at which the capillary bed can be considered as a continuum. The side L that corresponds to the convergence of the effective coefficients defines what is commonly called a Representative Elementary Volume (REV) [Bear, 1972, Quintard and Whitaker, 2000], and will be denoted by L_{REV}.

i. Uniform diameter. For a uniform capillary diameter, the effective permeability and viscosity are denoted K^{ref} and μ^{ref}, respectively. This notation aims at differentiating the study with uniform diameters from the study with distributed diameters detailed below. Here, since the diameters are uniform, the viscosity μ^{ref} is also uniform and computed from the *in vivo* viscosity law (Eq. 2.3). The effective permeability K_L^{ref} is then directly computed from Eq. 3.46 for each size L, until convergence. As will be presented in Section 5.1.3, this convergence is immediate for periodic patterns. For random patterns, the effective permeability is computed in a series of network generations, resulting in a statistical study. In this case, the convergence criterion is defined for a standard deviation lower

than 0.1.

ii. Distributed capillary diameters. If the diameter is non-uniform, it typically follows a Gaussian law [Cassot et al., 2006]. In this case, the capillary diameters are statistically generated—so their distribution follows the Gaussian law. Then we study the statistical properties of the resulting permeability and viscosity, following the two steps below:

1. In this study, we define the permeability as depending only on the geometry and topology of the network. To isolate the impact of the network architecture on the permeability, we neglect the viscosity fluctuations and assume the viscosity to be uniform, equal to μ^{ref}. In practice, μ^{ref} is chosen as $\mu\,(d_{cap} = 5.91\,\mu\text{m})$, where $d_{cap} = 5.91\,\mu\text{m}$ represents the typical diameter of a capillary in the human brain microcirculation [Cassot et al., 2006]. We run N computations per side L, with N different diameter distributions. For each domain side L and diameter distribution i in $\{1, ..., N\}$, we compute the corresponding effective permeability $K^{\text{eff}}_{L,i}$ via Eq. 3.46. In this work, the convergence of the permeability, thus the REV side L_{REV}, is established for a standard deviation lower than 0.1. K^{eff} is finally defined as the mean value of the set $\left(K^{\text{eff}}_{L_{REV},i}\right)_{i\in\{1,...,N\}}$.

2. To finally capture the impact of non-uniform viscosities, we run again the same N computations by letting the *in vivo* viscosity law (Eq. 2.3) describe the viscosity fluctuation in each capillary, depending on its diameter. Now that we know the value of $K^{\text{eff}}_{L,i}$ for each realization i in $\{1, ..., N\}$, we can deduce $\mu^{\text{eff}}_{L,i}$ from Eq. 3.46. μ^{eff} is finally defined as the mean value of the set $\left(\mu^{\text{eff}}_{L_{REV},i}\right)_{i\in\{1,...,N\}}$, with L_{REV} the side of the REV defined at the previous step.

3.5 Conclusion

In this section, we have presented the methods to describe blood flow in both the arteriolar and venular trees, and the continuum. We also detailed our way of computing the effective properties of a homogenized capillary bed. In the next section, we will present the development of the multiscale coupling model to apply at the interface between the two frameworks.

4 Multiscale coupling condition to link arteriolar and venular trees to the continuum

So far, we have described two separate frameworks on distinct scales to represent blood flow in brain microcirculation: a network approach for arteriolar and venular trees and a homogenized continuum representation for the capillary network. Each of these descriptions is self-sufficient when boundary conditions and source terms are fixed for each separately. For instance, if q_s and π_s are known in the network approach, we can assemble the set of linear equations Eqs. 3.3-3.6 into a sparse matrix plus a right-hand side and solve this linear system to obtain the pressure at each inner vertex, thus the flow rate in each vessel. However, some of the boundary conditions are in fact not known, but rather correspond to coupling elements with the continuum description. In this case, a coupling condition must be developed to express the relationship between the pressure π_s at the coupled end-tip of the arteriolar or venular vessel and the pressures of the local finite volume cells.

In this section, we present an approach to couple these two frameworks, which is inspired from that of Peaceman [Peaceman, 1978], who developed a "well model" for petroleum engineering (Section 4.1). In such applications, a wellbore model is coupled with a continuum reservoir description, in which details at the scale of the underlying structure are not described. The main idea is to represent the strong gradients that occur in the vicinity of the wellbore, i.e., within a length scale much smaller than the size of a FV cell, by a singular pressure drop term embedded in the coupling condition. To this end, analytical expressions of the pressure field in the vicinity of the coupling points are used to derive relationships between variables of both frameworks. The main advantage of the resulting well model is that it expresses a linear relationship between the pressure at the circumference of the well, which assumed to be uniform, and the pressure of the coupled finite volume cell. Thus it can be independently applied to each coupling sites and a single linear system is solved for both the network and continuum parts.

In this section, we will first provide details about the well models developed by Peaceman for petroleum engineering (Section 4.1). The purpose is both to explain why it is a relevant source of inspiration, and to highlight its limitations with regard to our application to brain microcirculation.

In particular, because of differences in scales between oil reservoirs and the human cortex, important modifications to the original well models will be made to adapt the idea to the context of brain microcirculation. This will be presented in Section 4.2.

4.1 Inspiration: the well model developed for petroleum engineering

To evaluate the productivity of a wellbore, numerical simulations are widely exploited in petroleum engineering, traditionally using finite volume or finite element methods. One major difficulty in modelling oil reservoir is to account for the presence of the wellbores (see Fig. 4.2**(a)**), i.e. to describe the *strong pressure gradients* they induce in their vicinity [Dumkwu et al., 2012]. Before we get into details, a few figures are given to understand the challenge of considering the wellbores in simulations at the scale of the whole reservoir.

An oil reservoir is typically 1-100 m wide, 1-10 km long and 10-1000 m deep. The largest oil field discovered in the world, the Ghawar field in Saudi Arabia, even measures 280×30 km^2 of surface area. The numerical capacity of today computers prevents the size h of the discretization cells of such domain to be more than ∼100 m large and ∼10 m deep [Ding, 2004]. By contrast, the typical diameter of a wellbore r_w is about ∼1 cm in diameter at its deepest endpoint, i.e. about four orders of magnitude smaller than the horizontal dimension of a mesh cell, up to six orders of magnitude in the case of Ghawar field.

Therefore, the difficulty of accounting for wellbores in reservoir simulations stems from the fact that the well represents a singularity at the scale of the reservoir. This scale difference defined by the ratio h/r_w will be referred as *scale separation* in the remainder of the manuscript. In particular, this scale separation prevents the use of grid refinement in the vicinity of the wells because of the computational cost it would represent. On the other hand, if the discretization grid is not refined, the pressure of the well passing through a mesh cell is not a good approximation of the cell pressure itself. To address this issue, the idea came out at the end of the 1960s to represent the well as a source term in the simulator [Schwabe et al., 1967].

4.1.1 The idea of Peaceman's well model

The first well model was proposed by Peaceman in 1978 [Peaceman, 1978] in the case of a vertical fully penetrating well, i.e. a vertical well passing through the entire mesh cell (see Fig. 4.1). Such a configuration corresponded to the well bore structure of early petroleum exploitation fields. Nowa-

days, the rarefaction of oil resources makes it more difficult to extract, thus the architecture of a well bore is much more complex, with horizontal and directional wells (see Fig. 4.2). While lots of researchers developed alternatives [Williamson et al., 1981, Ding and Renard, 1994, Ligaarden, 2008, Jenny and Lunati, 2009], the Peaceman's well model has been extended multiple times [Peaceman, 1983, Peaceman, 1990, Peaceman et al., 1993, Erwing et al., 1999, Durlofsky, 2000, Chen and Zhang, 2009, Ribeiro and Maliska, 2014] and remains the numerical approach implemented in most of the commercial softwares for reservoir simulation.

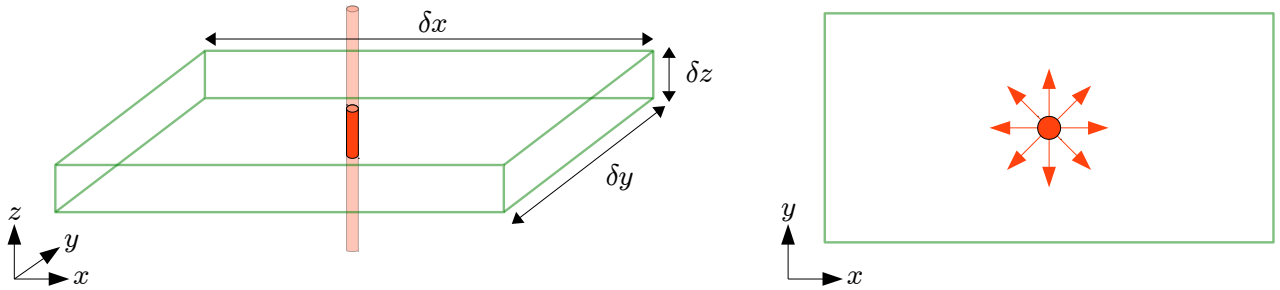

(a) **(b)**

Figure 4.1: **A vertical fully penetrating well (orange cylinder) crossing a parallelepipedic FV discretization cell (green lines). (a)** In a three-dimensional view, the discretization cell is much larger in the horizontal direction than vertically, i.e. $\delta z \ll \delta x, \delta y$. **(b)** An injection (source) or production (sink) well induces a radial flow in the xy-plan.

Here, we briefly present the development of the first Peaceman well model (1978) for vertical fully penetrating wells [Peaceman, 1978], as displayed on Fig. 4.1. This model is proposed for a two-dimensional application, which is commonly considered as sufficient since the well bore induces a radial flow (see Fig. 4.2**(a)**) and the discretization in the depth of the reservoir is typically much smaller than in the two other directions (see Fig. 4.1**(a)**). Furthermore, the domain is assumed to be homogeneous and isotropic, the fluid to be monophasic, and the domain to be discretized over a Cartesian coarse grid of cubic cells. All the hypotheses listed here are similar to those made in this thesis, as announced in Section 3.1.

The well model aims at expressing the injection (source) or production (sink) flow rate q as a linear function of the pressure p_w at the circumference of the well and the pressure p_0 of the crossed discretization cell. The main advantage of such linear relationship is that it can be applied to each wellbore independently. Thus, we focus here on a single wellbore to explain the development of the well model.

This model is based on an analytical expression of the radial Darcy flow (Eqs. 3.12-3.13) in the

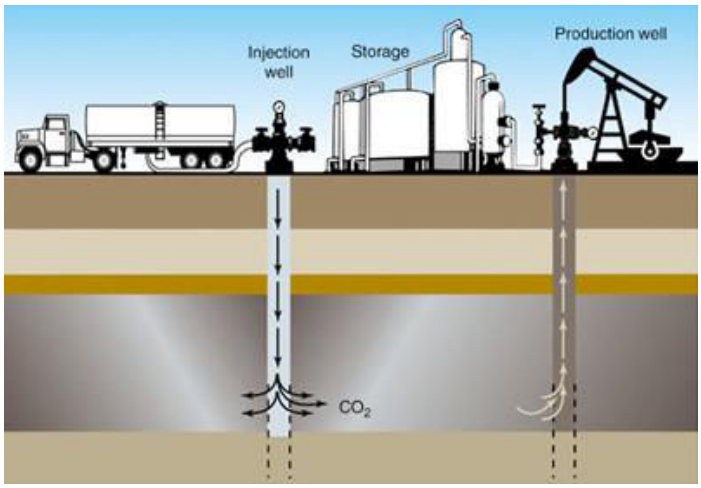

(a) Source: Science & Technology review, Probing the Subsurface with Electromagnetics Fields, Lawrence Livermore (https://str.llnl.gov/str/November01/Kirkendall.html)

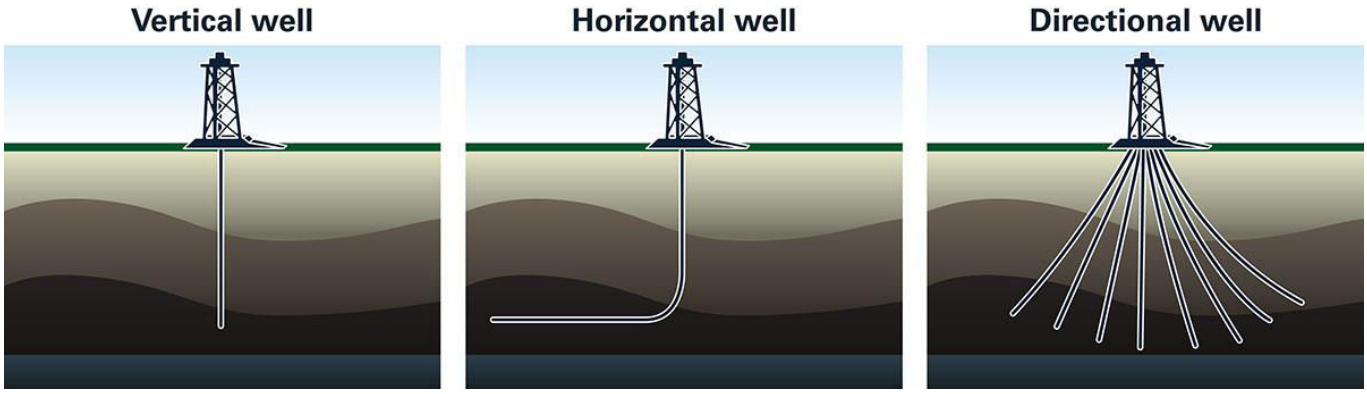

(b) Source: Uncovering North American Energy, The will to drill, Tortoise (http://www.uncoverenergy.com/the-will-to-drill/)

Figure 4.2: **Evolution of the architecture of well bores. (a)** Two types of well exist: *injection* wells inject substances (mainly CO_2 or water) in the oil reservoir to maintain the reservoir pressure, heat the oil or lower its viscosity; *production* wells are located close to injection wells and extract oil. **(b)** For many years, the only way to build them was to drill vertically. Nowadays, more productive horizontal and directional wells exist.

vicinity of the well

$$p(r) = p_w - \frac{q\mu}{2\pi Kh}\, ln\left(\frac{r}{r_w}\right) \quad \text{for } r \geq r_w, \tag{4.1}$$

with μ the fluid viscosity, K the permeability of the reservoir, h the side of a discretization cell, and r_w the radius of the well. Note that such approximation presents a singularity for $r = 0$, which treatment is avoided by defining its validity domain beyond the circumference of the well, for $r \geq r_w$.

Peaceman further introduces a fictitious radius r_0, termed *equivalent radius*, which represents the

distance from the well center, which verifies

$$p_0 = p_w - \frac{q\mu}{2\pi Kh}\, ln\left(\frac{r_0}{r_w}\right). \tag{4.2}$$

The expression of q finally stems from the Eq. 4.2

$$q = \frac{2\pi Kh}{\mu}\frac{p_w - p_0}{ln\left({}^{r_0}/_{r_w}\right)}. \tag{4.3}$$

Note that since the couple (p_0, r_0) verifies Eq. 4.1, it can also be considered as a reference for the analytical expression of the radial flow, such as Eq. 4.1 can be rewritten

$$p\left(r\right) = p_0 - \frac{q\mu}{2\pi Kh}\, ln\left(\frac{r}{r_0}\right). \tag{4.4}$$

To find the expression of r_0 in Eq. 4.3, Peaceman considers the numerical two-dimensional resolution of Darcy's flow in the xy-plane (see Fig. 4.1**(a)**)

$$-\frac{K}{\mu}\nabla^2_{xy} p = -\delta q, \tag{4.5}$$

with $\nabla^2_{xy} = {}^{\partial^2}/_{\partial x^2} + {}^{\partial^2}/_{\partial y}$ the Laplacian defined in the xy-plane. To take into account the third dimension z, Eq. 4.5 is averaged over the thickness $h = \delta z$ of the discretization mesh (see Fig. 4.1**(a)**)

$$-\frac{K}{\mu}\int_{\delta z} \nabla^2_{xy} p\, dz = -\int_{\delta z} \delta q\, dz \tag{4.6}$$

$$\Rightarrow -\frac{Kh}{\mu}\nabla^2_{xy} p = -\int_{\delta z} \delta q\, dz \tag{4.7}$$

$$\Rightarrow -\frac{Kh}{\mu}\left(\frac{\partial^2 p}{\partial x^2} + \frac{\partial^2 p}{\partial y^2}\right) = -\int_{\delta z} \delta q\, dz. \tag{4.8}$$

Then, the integration of Eq. 4.8 in the xy-plane yields

$$-\frac{Kh}{\mu}\int_{\delta x\times\delta y}\left(\frac{\partial^2 p}{\partial x^2} + \frac{\partial^2 p}{\partial y^2}\right) dxdy = -\int_{\delta x\times\delta y\times\delta z} \delta q\, dxdydz \tag{4.9}$$

$$\Rightarrow -\frac{Kh}{\mu}\int_{\delta x\times\delta y}\left(\frac{\partial^2 p}{\partial x^2} + \frac{\partial^2 p}{\partial y^2}\right) dxdy = -q. \tag{4.10}$$

Further, the second derivates involved in the integral of Eq. 4.10 are expressed using the Finite Difference (FD) method over the discretization grid schematized in Fig. 4.3. Applied to cell 0, this

yields

$$-\frac{Kh}{\mu}\int_{\delta x\times\delta y}\left(\frac{p_2-2p_0+p_1}{h^2}+\frac{p_4-2p_0+p_3}{h^2}\right)dxdy=-q \tag{4.11}$$

$$\Rightarrow -\frac{Kh}{\mu}\left(\frac{p_2-2p_0+p_1}{h^2}+\frac{p_4-2p_0+p_3}{h^2}\right)h^2=-q, \tag{4.12}$$

which can finally be rewritten as

$$\Rightarrow -\frac{Kh}{\mu}\left(p_1+p_2+p_3+p_4-4p_0\right)=-q. \tag{4.13}$$

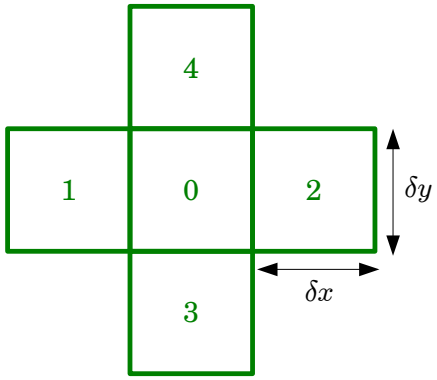

Figure 4.3: **Schematics of the discretization grid used in Eq. 4.11.**

One of the key assumptions of the Peaceman's well model is that all the pressures p_1 to p_4 of the neighbouring cells verify both the radial approximation (Eq. 4.4) and the FD scheme (Eq. 4.13). In particular, the discretization cells must be large enough, so that *the pointwise* radial expression is a good approximation of the *averaged* pressure of a discretization cell of this domain, as displayed in Fig. 4.4. Under this hypothesis, we deduce from the combination of Eqs 4.4 and 4.13 that

$$p_1=p_2=p_3=p_4=p_0-\frac{q\mu}{2\pi Kh}\,ln\left(\frac{h}{r_0}\right). \tag{4.14}$$

Then the substitution of Eq. 4.14 into Eq. 4.13 yields

$$-\frac{Kh}{\mu}\left\{4\left[p_0-\frac{q\mu}{2\pi Kh}\,ln\left(\frac{h}{r_0}\right)\right]-4p_0\right\}=-q, \tag{4.15}$$

which can be simplified as

$$r_0=exp\left(-\frac{\pi}{2}\right)h\simeq 0.2h. \tag{4.16}$$

As detailed in [Peaceman, 1978], this factor of 0.2 was confirmed by two other approaches involving numerical simulations and exact solution of the flow in known configuration.

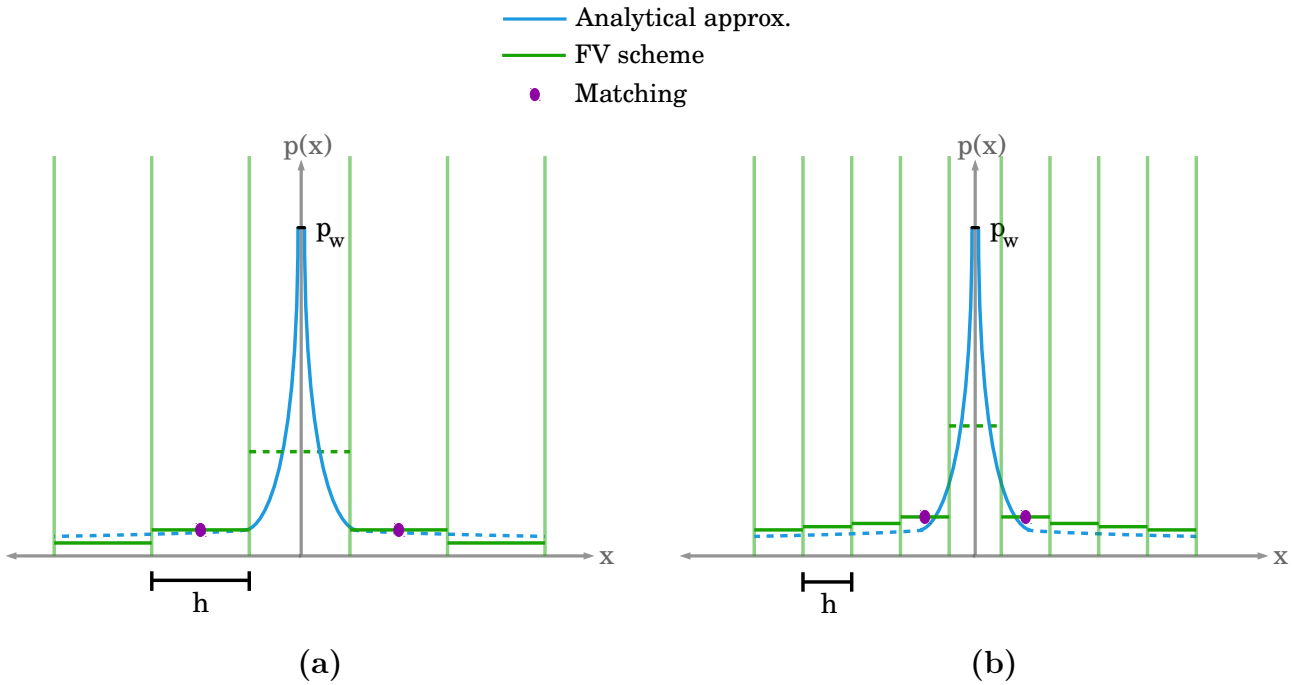

(a) **(b)**

Figure 4.4: **Matching of the analytical approximation of the pressure field in the vicinity of the wellbore with the rest of the continuum.** One-dimensional pressure profiles are plotted in the neighbourhood of a wellbore for two sizes h of the discretization cells. Cell pressures are displayed in green and the analytical solution of Darcy's law (Eq. 4.1) is plotted in blue. The pressure p_w represents the pressure at the circumference of the wellbore. In **(a)**, h is large enough, so that the pointwise expression of the analytical solution is a good approximation of the averaged pressure of a discretization cell. This is not the case in **(b)**.

Extensions of the Peaceman well models to anisotropy [Peaceman, 1983], horizontal wells [Peaceman et al., 1993], non-Darcy effects [Erwing et al., 1999], heterogeneous medium [Wolfsteiner et al., 2003], non-centered wells [Peaceman, 1990, Agaev, 1996], partially penetrating wells [Dogru et al., 2010], or three-dimensional problems [Ribeiro and Maliska, 2014] also exist. They involve more complex analytical solutions of Darcy's law than Eq. 4.1, but all rely on the approximation of an equivalent radius r_0.

4.1.2 Limits of the well model

While we keep the idea of using analytical expressions to describe the strong pressure gradients building up in the vicinity of coupling points, the Peaceman well model cannot be directly applied to the context of brain microcirculation, for two main reasons.

First, contrary to the wall of a well, which is the main exchange surface for injection or production

flows (see Fig. 4.2**(a)**), the wall of an arteriole or venule in the brain is impermeable, meaning that no radial flow is induced along its path. In brain microcirculation, the coupling source terms are located only at the very end points of the arteriolar and venular trees, at their connections with the capillaries. Thus, couplings at endpoints induce spherical-like flows instead of radial. This configuration corresponds to the question of partially penetrating well, which has already been discussed in petroleum engineering, but is generally treated as a secondary correction factor embedded in the initial well model [Lu et al., 2009, Dogru et al., 2010].

Second, important scale differences between oil reservoirs and the human cortex (see Fig. 4.5) imply that the treatment of the coupling source term as a singularity is less straightforward in the human cortex than in oil reservoir. On the one hand, the vessel diameter in the brain is only 10 times smaller than the typical side of a discretization cell, while the well diameter is at least 1 000 times smaller. On the other hand, the pore size in brain microcirculation, i.e. the typical length l_{cap} of a capillary, is only $\sim$5 times smaller than the typical side of a discretization cell, contrary to the pore size in reservoir, which is negligible (10 000 times smaller). In other words, the pore in human cortex has a dominant role compared to the vessel diameter, contrary to the pore in oil reservoir. Thus, the scale separation in brain microcirculation is governed by the ratio h/l_{cap}, instead of h/r_w in the petroleum context, and is much less pronounced. This last point questions the consideration of the capillary bed as a continuum, thus the validity of Darcy's law (similar to Eq. 4.2), in the closest vicinity of the coupling point. In particular, this questions the use of the pressure at the circumference of the vessel as a reference to define an analytical solution of Darcy's law, as in Eq. 4.2.

In Section 4.2 below, we detail the development of a multiscale coupling model adapted to the context of human brain microcirculation, inspired by the Peaceman's well model.

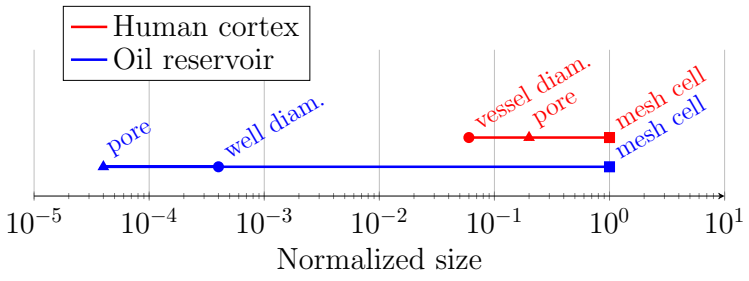

Figure 4.5: **Scale differences between oil reservoirs and the human cortex.** Three characteristic length scales are presented for both petroleum and cerebral applications: the pore size of the porous medium (oil reservoir or capillary bed), the diameter of the coupled component (wellbore or arteriolar/venular vessel) and the size of a discretization cell in the finite volume representation of the continuum. Each length is normalized by the typical size of a mesh cell in the corresponding application.

4.2 Adaptation to the context of brain microcirculation

In this section, we adapt the Peaceman's well model developed for reservoir simulations in petroleum engineering, to the brain microcirculation. For that purpose, we will bring important modifications to the original well model, taking into account the main physical differences between oil reservoirs and the human cortex (detailed in Section 4.1.2 above).

4.2.1 Geometry, vocabulary and conventions

The same conventions as in Sections 3.2.1 and 3.3.1 are adopted, as well as the simplifications and hypotheses presented in Section 3.1. In particular, the capillary bed is assumed to be isotropic and homogeneous, and the hematocrit is assumed to by uniform. In addition, Reynolds number is low ($\ll 1$) in the whole system and inertial effects can be neglected. Finally, the pulsatility is negligible.

To detail each step of the development presented in this section, several domains of interest and notations will be progressively introduced all along this section. For convenience, a nomenclature is provided below, where these domains are sorted according to three classes: **(1)** the network domains contain vessels, **(2)** the finite volume domains contain discretization cells, and **(3)** the continuous domains are subdomains of $\mathbb{R}^3$.

Nomenclature

(1) *Network domains*

- Ω_{AV} is the set of network vessels in the arteriolar and venular trees;
- s is a coupling point, at the interface between Ω_{AV} and Ω_{FV};
- Ω_{cap} is the set of capillary vessels connected to a coupling point.

(2) *Finite volume domains*

- Ω_{FV} is the set of cells used to discretize the continuum;
- $\Omega_{FV}^{\varepsilon}$ is a reduction of Ω_{FV}, which excludes the sets $\Omega_{FV,neigh}^{s}$;
- $\Omega_{FV,neigh}^{s}$ is the set of cells that contains the cell coupled to the coupling point s and its neighbours, including the diagonal neighbours;
- $\overline{\Omega}_{FV,neigh}^{s}$ is a reduction of $\Omega_{FV,neigh}^{s}$, which excludes the coupled cell;
- $\overline{\Omega}_{sph}^{s}$ is the set of cells that share a face with $\Omega_{FV,neigh}^{s}$;
- $\Omega_{sph}^{s,\varepsilon}$ is an extension of $\overline{\Omega}_{sph}^{s}$, which further includes the cells sharing a corner with $\Omega_{FV,neigh}^{s}$.

(3) *Continuous domains*

- $\Omega_{lin,s}$ is a spherical subdomain of $\mathbb{R}^3$ of radius l_Γ, centered in the coupling point s;
- Ω_{sph}^{s} is a subdomain of $\mathbb{R}^3$ that corresponds to $\Omega_{FV,neigh}^{s} \cup \overline{\Omega}_{sph}^{s}$.

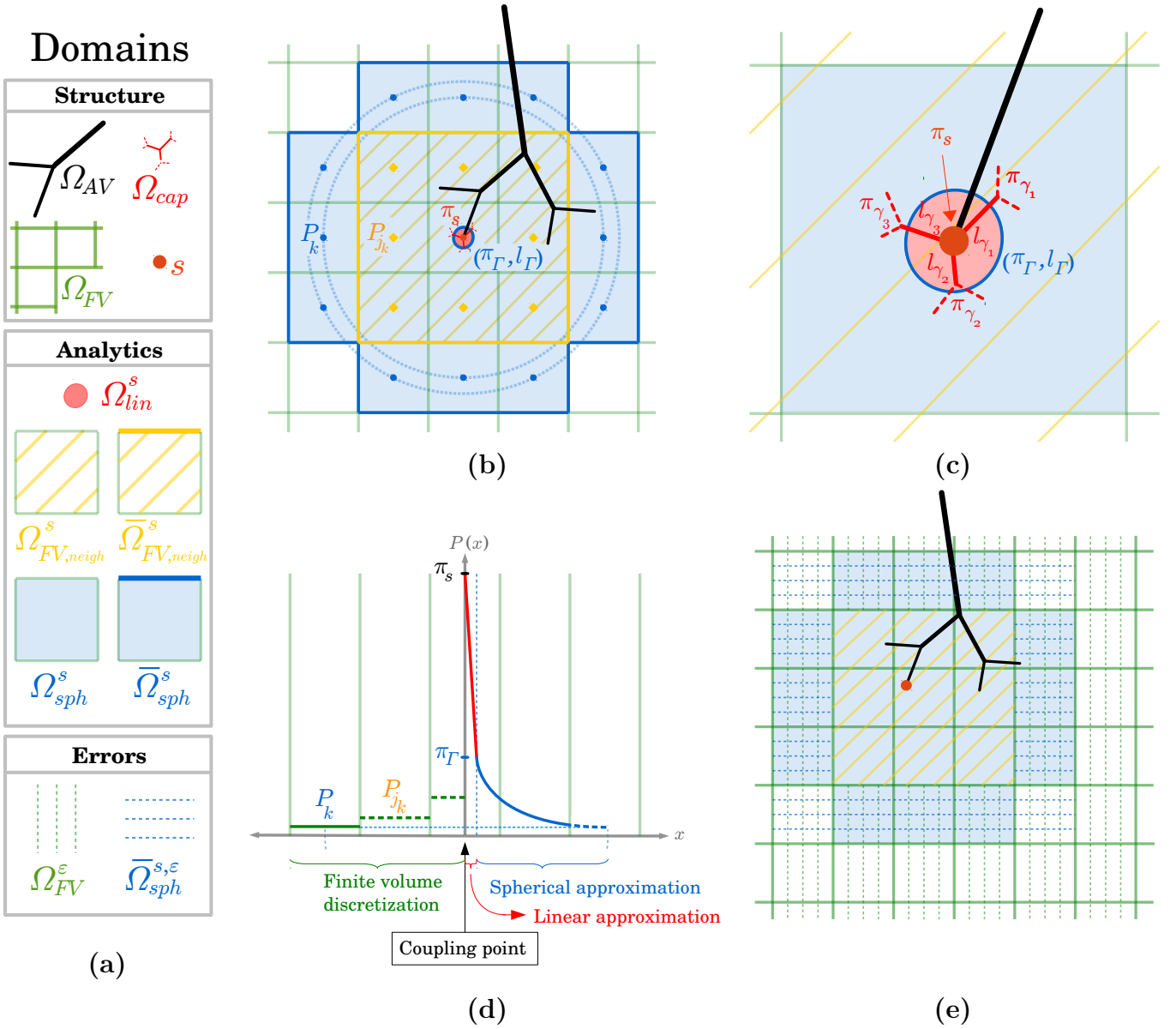

Figure 4.6: **Schematic diagrams of the derivation of the coupling condition between one of the arteriolar or venular end-tips and the continuum representing the capillary bed.** **(a)** The legend displays all the domains used for the development of the coupling model. A detailed nomenclature is provided in Section 4.2.1. **(b)** An arteriolar or venular tree Ω_{AV} (black network) plunges into a FV grid Ω_{FV} (green grid). The capillary vessels in Ω_{cap} that are connected to the coupling point (highlighted by a red dot) are represented in red. The coupling condition describes the relationship between the network pressure π_s at this coupling point and the pressures of the surrounding cells $\Omega^s_{FV,neigh}$, which include the coupled cell. The pressure field is reconstructed in the local neighbourhoods Ω^s_{lin} and Ω^s_{sph} using Eqs. 4.27a and 4.27b. In the most distant cells $\overline{\Omega}^s_{sph}$, the analytical approximation matches with the FV representation further away. To make visualizations easier, a centered coupling is illustrated. **(c)** Detailed view of the coupled cell. The linear and spherical approximations match at a distance l_Γ from the coupling point. π_Γ is the averaged weighted pressure evaluated at this distance. **(d)** 1D pressure profile: FV pressures (green steps) are plotted on the left-hand side while both linear (red) and spherical (blue) approximations are plotted on the right-hand side. **(e)** Domains for the computation of errors. Four regions have been selected to compare hybrid and CN approaches: the arteriolar and venular trees Ω_{AV} (black), the coupling points s (red), the surrounding cells $\Omega^{s,\varepsilon}_{sph}$ (hatched blue) and the rest of the FV domain Ω^ε_{FV} (hatched green) which excludes cells where the pressure field must be analytically reconstructed.

In the same spirit as the Peaceman's well model, the purpose of the coupling model is to express a linear relationship between the pressure π_s at the coupled endpoint of a given arteriolar or venular vessel and the pressures $(P_j)_{j\in\Omega^s_{FV,neigh}}$ of the local finite volume cells $\Omega^s_{FV,neigh}$. The main advantage of such linear relationship is that it can be applied to each coupling point independently. Since each coupling is blind to the others, we focus here on a single coupling point to explain the development of the coupling model.

4.2.2 Analytical approximations of the pressure field in the vicinity of a coupling point

In our approach, because of the scale differences discussed in Section 4.1.2, the pressure field in the neighbourhood of a coupling point is decomposed into two analytical approximations instead of one. In Ω^s_{sph}, up to two FV cells away from the coupling point, a Peaceman-like spherical solution of the continuum equations describes the variation at the scale of h, the side of a FV cell. In addition, in the closest region Ω^s_{lin} to the coupling point, a linear variation captures the network structure at the scale of the capillary vessels connected to this point, according to Eq 3.1.

Let us consider a single coupling point s, at any arteriolar or venular endpoint. The local flow rate q_s corresponds to the coupling term that appears in both Eq. 3.6 for the network approach and Eq. 3.34 for the continuum representation. The coupling condition aims at describing the pressure drop between the pressure π_s at the endpoint of the arteriolar or venular vessel, and the cell pressures $(P_j)_{j\in\overline{\Omega}^s_{FV,neigh}}$ of the FV neighbourhood, where $\overline{\Omega}^s_{FV,neigh}$ represents the set of cells that surround the coupled one (see Fig. 4.6**(b)**).

We first present an analytical solution of Darcy's law (Eqs. 3.12-3.13) close to the coupling point, in the neighbourhood Ω^s_{sph} (Fig. 4.6**(b)**). Assuming a spherical symmetry of the pressure field for a single coupling, we have

$$P(r) = \pi_{ref} - \frac{\mu^{\text{eff}} q_s}{4\pi K^{\text{eff}}}\left(\frac{1}{r} - \frac{1}{l_{ref}}\right), \tag{4.17}$$

with π_{ref} a reference pressure defined at an arbitrary distance l_{ref} to the source, at microscopic scale, and $r \geq l_{ref}$ the distance to the coupling point. This solution yields a $1/r$-decrease of the pressure, as displayed in blue on Fig. 4.6**(d)**.

In order to determine π_{ref} and l_{ref}, we introduce a second analytical approximation of the pressure field for $r \leq l_{ref}$, at microscopic scale. To this end, we extend the network approach (Eqs. 3.3-3.6) to the capillaries Ω_{cap} connected to the point s (see Fig. 4.6**(c)**). Replacing the subscripts β that refer to inner vertices of the arteriolar and venular trees, in Eq. 3.6, by subscripts γ referring to inner

vertices of the capillary bed, this reads

$$\sum_{\gamma \in \mathcal{N}_s} G_{s\gamma} \left(\pi_s - \pi_\gamma\right) = q_s. \tag{4.18}$$

From this equation, we derive a linear pressure drop, as displayed in red on Fig. 4.6**(d)**,

$$\pi_\Gamma = \pi_s - R_\Gamma q_s, \tag{4.19}$$

with π_Γ defined as the weighted average pressure

$$\pi_\Gamma = \frac{1}{\sum_{\gamma \in \mathcal{N}_s} G_{s\gamma}} \sum_{\gamma \in \mathcal{N}_s} G_{s\gamma} \pi_\gamma \tag{4.20}$$

and R_Γ defined as the harmonic average resistance

$$R_\Gamma = \frac{1}{\sum_{\gamma \in \mathcal{N}_s} G_{s\gamma}}. \tag{4.21}$$

Note that Eq. 4.19 can be rewritten as the pointwise formulation

$$P\left(r\right) = \pi_s - \frac{\pi_\Gamma - \pi_s}{l_\Gamma} r \quad \text{for } r < l_\Gamma. \tag{4.22}$$

This expression is valid over a length scale l_Γ that still must be derived.

The idea is now to match both analytical approximations Eqs. 4.17 and 4.22 by imposing $\pi_{ref} = \pi_\Gamma$ in Eq. 4.17. The corresponding reference length l_{ref} is chosen as the length scale l_Γ introduced above, such that $l_{ref} = l_\Gamma$. To this end, we consider that each couple $(\pi_\gamma, l_\gamma)_{\gamma \in \mathcal{N}_s}$, with l_γ the length of the capillary $[s\gamma]$ connected to the coupling point, is fulfills the analytical solution of Darcy's law (Eq. 4.17)

$$P(r) = \pi_\gamma - \frac{\mu^{\text{eff}} q_s}{4\pi K^{\text{eff}}} \left(\frac{1}{r} - \frac{1}{l_\gamma}\right). \tag{4.23}$$

Then multiplying by $G_{s\gamma}$ and summing over $\mathcal{V}_s$, we obtain

$$\sum_{\gamma \in \mathcal{V}_s} G_{s\gamma} P(r) = \sum_{\gamma \in \mathcal{V}_s} G_{s\gamma} \pi_\gamma - \sum_{\gamma \in \mathcal{V}_s} G_{s\gamma} \frac{\mu^{\text{eff}} q_s}{4\pi K^{\text{eff}}} \left(\frac{1}{r} - \frac{1}{l_\gamma}\right), \tag{4.24}$$

which can finally be written as

$$P\left(r\right) = \pi_\Gamma - \frac{\mu^{\text{eff}} q_s}{4\pi K^{\text{eff}}} \left(\frac{1}{r} - \frac{1}{l_\Gamma}\right), \tag{4.25}$$

with l_Γ the weighted average length

$$l_\Gamma = \frac{\sum_{\gamma \in \mathcal{N}_s} G_{s\gamma}}{\sum_{\gamma \in \mathcal{N}_s} \frac{G_{s\gamma}}{l_{s\gamma}}}. \tag{4.26}$$

This length scale l_Γ defines the interface between the domains Ω^s_{lin} and Ω^s_{sph} in Fig. 4.6**(c)**.

At this stage, the pressure field is defined at any point of $\mathbb{R}^3$ in the neighbourhood of the coupling point s. Let r be the distance from a given point of the neighbourhood to the coupling point s. From Eqs. 4.22 and 4.25, we have

$$P(r) = \begin{cases} \pi_s - \dfrac{\pi_\Gamma - \pi_s}{l_\Gamma} r & \text{for } r \leq l_\Gamma \quad (4.27a) \\ \pi_\Gamma - \dfrac{\mu^{\text{eff}} q_s}{4\pi K^{\text{eff}}} \left(\dfrac{1}{r} - \dfrac{1}{l_\Gamma} \right) & \text{for } r > l_\Gamma, \quad (4.27b) \end{cases}$$

as displayed on the right-hand side of Fig. 4.6**(d)**. This system of two analytical approximations replaces the single solution of Darcy's law used in the development of the Peaceman's well model (Eq. 4.1).

4.2.3 Expression of the coupling condition

Following Peaceman's idea, the coupling condition is completed by assuming the existence of a neighbouring domain where both the spherical approximation (Eq. 4.27b and right part of Fig. 4.6**(d)**) and the FV formulation (Eq. 3.34 and left part of Fig. 4.6**(d)**) are valid. In this domain, the *averaged* pressure of a FV cell must match with the *pointwise* spherical expression applied to the distance between the coupling point and the center of the cell (e.g. cell pressure P_k in Fig. 4.6**(d)**). This condition is based on the key assumption that h is sufficiently larger than l_{cap}. We further consider that the matching occurs only in the most distant cells of Ω^s_{sph}, $\overline{\Omega}^s_{sph}$ (see Fig. 4.6**(b)**). Note that the linear approximation is not concerned by this matching since it is enclosed in the coupled cell ($h > l_\Gamma$).

Finally, in any cell k in $\overline{\Omega}^s_{sph}$, the cell pressure is expressed as

$$P_k = \pi_\Gamma - \frac{\mu^{\text{eff}} q_s}{4\pi K^{\text{eff}}} \left(\frac{1}{d_{k,s}} - \frac{1}{l_\Gamma} \right), \quad (4.28)$$

where $d_{k,s}$ is the distance between the coupling point and the center of cell k.

Combining Eqs. 4.19 and 4.28, we can obtain an expression of q_s as a function of π_s and $(P_k)_{k \in \overline{\Omega}^s_{sph}}$. To finally close the expression of the coupling condition and express q_s as a function of π_s and $(P_j)_{j \in \overline{\Omega}^s_{FV,neigh}}$, we use the FV formulation (Eq. 3.34) to express the flow conservation at the interface between the cells of the neighbourhood $\overline{\Omega}^s_{FV,neigh}$ and the rest of the FV domain, i.e. between $\overline{\Omega}^s_{FV,neigh}$

and $\overline{\Omega}^s_{sph}$. The FV discretization reads

$$\frac{K^{\text{eff}}h}{\mu^{\text{eff}}} \sum_{k \in \overline{\Omega}^s_{sph}} (P_{j_k} - P_k) = q_s, \tag{4.29}$$

where P_{j_k} represents the pressure of the unique neighbouring cell j_k of k, which belongs to $\overline{\Omega}^s_{FV,neigh}$ (see Fig. 4.6**(b)**).

By combining Eqs. 4.20, 4.28 and 4.29, we finally obtain the coupling expression

$$q_s = f\left(\pi_s, (P_j)_{j \in \overline{\Omega}^s_{FV,neigh}}\right), \tag{4.30}$$

where f is the following linear function

$$f\left(\pi_s, (P_j)_{j \in \overline{\Omega}^s_{FV,neigh}}\right) = \frac{1}{C_{s,\Gamma}} \left(\frac{1}{\text{Card}\left(\overline{\Omega}^s_{sph}\right)} \sum_{k \in \overline{\Omega}^s_{sph}} P_{j_k} - \pi_s \right), \tag{4.31}$$

with $\text{Card}\,(\cdot)$ the cardinal number of a given set and $C_{s,\Gamma}$ a coupling coefficient defined by

$$C_{s,\Gamma} = R_\Gamma - \frac{\mu^{\text{eff}}}{4\pi K^{\text{eff}}} \left(\frac{1}{\text{Card}\left(\overline{\Omega}^s_{sph}\right)} \sum_{k \in \overline{\Omega}^s_{sph}} \frac{1}{d_{k,s}} - \frac{1}{l_\Gamma} - \frac{4\pi}{h \times \text{Card}\left(\overline{\Omega}^s_{sph}\right)} \right). \tag{4.32}$$

Here, l_Γ represents the weighted average length of the capillaries connected to the coupling point

$$l_\Gamma = \frac{\sum_{\gamma \in \mathcal{N}_s} G_{s\gamma}}{\sum_{\gamma \in \mathcal{N}_s} \frac{G_{s\gamma}}{l_{s\gamma}}}, \tag{4.33}$$

and R_Γ the harmonic average resistance of these capillaries

$$R_\Gamma = \frac{1}{\sum_{\gamma \in \mathcal{N}_s} G_{s\gamma}}. \tag{4.34}$$

Noteworthy, in this formulation, the details of the capillary network in the vicinity of the coupling point are taken into account in the expressions of l_Γ and R_Γ. Moreover, we recall that the FV cells are assumed to be cubic here, although the extension to parallelepipedic cells is straightforward (see details in Section 4.2.6).

Now that the development of the coupling model has been presented, we summarize here the validity domain of each estimation of the pressure field in the FV domain:

- in the closest region Ω^s_{lin} of the coupling point (see Fig. 4.6**(b)**), the pressure field is described by the linear approximation in Eq. 4.27a;
- further away, in $\Omega^s_{FV,neigh} \setminus \Omega^s_{lin}$ (see Fig. 4.6**(b)**), the pressure field is described by the spherical approximation in Eq. 4.27b;
- in the rest of the FV domain Ω^c_{FV} (see Fig. 4.6**(d)**), the pressure field is described by the classical FV scheme in Eqs. 3.34-3.38.

In particular, it is important to note that the FV scheme does not yield a physical estimation of the pressure field in the neighbourhood $\Omega^s_{FV,neigh}$ of the coupling point.

4.2.4 Off-centering: distribution of the coupling source term

The development above is valid for both centered and off-centered couplings, as in Fig. 4.6**(e)**. However, the FV scheme (Eq. 3.34) is not sensitive to the position of the coupling point in a single source cell. Thus, the resulting FV pressure field is independent of the source position in a coupled cell. To properly take into account the off-centering of a coupling point s in the FV part of the hybrid approach, the coupling term q_s is redistributed on each cell i of the neighbourhood $\Omega^s_{FV,neigh}$ with new partial source terms defined by

$$q_{s,i} = \tau_i q_s, \tag{4.35}$$

according to a partition coefficient τ_i

$$\tau_i = \frac{v_i}{h^3}, \tag{4.36}$$

where v_i is the volume of the intersection between the cell i and a fictitious mesh cell centered on the coupling point [Agaev, 1996] (see Fig. 4.7). This definition implies that $\sum_i \tau_i = 1$, yielding $\sum_i q_{s,i} = q_s$, and that, among the 27 cells of $\Omega_{FV,s}$, no more than 8 verify $\tau_i \neq 0$, and $q_{s,i} \neq 0$.

From the point of view of the FV scheme (Eqs. 3.34-3.38), a given cell i of the FV domain is impacted by any coupling located in its neighbours, including those sharing a single corner. Thus,

Eq. 3.34 is finally rewritten as

$$\frac{K^{\text{eff}}h}{\mu^{\text{eff}}} \sum_{j \in N_i} (P_i - P_j) = \sum_{s \in S\left(\overline{N}_i\right)} q_{s,i}, \tag{4.37}$$

where $\overline{N}_i$ is the set of neighbours to cell i, including those sharing a single corner, and $S\left(\overline{N}_i\right)$ is the set of couplings in $\overline{N}_i$.

Combining Eqs. 4.37, 4.35 and 4.30, we finally have

$$\begin{aligned} \frac{K^{\text{eff}}h}{\mu^{\text{eff}}} \sum_{j \in N_i} (P_i - P_j) &= \sum_{s \in S\left(\overline{N}_i\right)} q_{s,i} \\ &= \sum_{s \in S\left(\overline{N}_i\right)} \tau_i q_s \\ &= \sum_{s \in S\left(\overline{N}_i\right)} f\left(\pi_s, \left(P_{j_s}\right)_{j_s \in \overline{\Omega}^s_{FV,neigh}}\right). \end{aligned} \tag{4.38}$$

Note that this distribution of this distribution of the source term q_s is independent of the development of the coupling model represented by the function f.

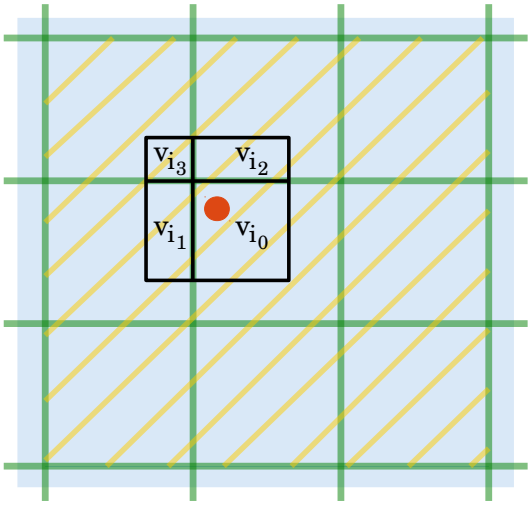

Figure 4.7: **2D schematic diagrams of the distribution of the coupling condition for off-centered coupling point.** To take into account the off-centering of a given coupling point s (red dot), the corresponding flow rate q_s is distributed among each cell i of $\Omega^s_{FV,neigh}$ (yellow hatching) according to the partition coefficient $\tau_i = {}^{v_i}/_{h^3}$, where v_i is the intersection between the cell i and a fictitious mesh cell centered on the coupling point (black square), and h^3 the volume of a cubic discretization cell.

4.2.5 Setting of the linear system and numerical implementation

i. Setting of the linear system. Let M_{hybrid} be the matrix corresponding to the whole linear system associated to the hybrid approach (Fig.). This involves the equations of the network (Eqs. 3.3-3.6), the FV (Eqs. 3.34-3.38) and the coupling (Eqs. 4.30 and 4.38) parts. As schematized in Fig. 4.8, this matrix is composed of M_{FV} (Section 3.3.4), M_{network} (Section 3.2.3) and an extension of size (number of couplings)^2. This latter contains the equations expressing the equality between the coupling condition q_s (Eq. 4.30) and the flow rate of the arteriolar or venular vessel that is connected to the continuum through the coupling point s (Eq. 3.6). For each coupling s, this reads

$$G_{\alpha s}\left(\pi_s - \pi_\alpha\right) = q_s, \tag{4.39}$$

where α is the inner vertex of the network that is connected to the coupling point s. This yields

$$M_{\text{hybrid}}\left(s,s\right) = G_{\alpha s} + \frac{1}{C_{s,\Gamma}}\ \pi_s,$$

where $C_{s,\Gamma}$ is defined in Eq. 4.32,

$$M_{\text{hybrid}}\left(s,\alpha\right) = -G_{\alpha s}$$

and, for each cell k of $\overline{\Omega}^s_{sph}$,

$$M_{\text{hybrid}}\left(s,k'\right) = -\frac{1}{C_{s,\Gamma}\ \text{Card}\left(\overline{\Omega}^s_{sph}\right)},$$

where k' represents the unique neighbouring cell of k which belongs to $\overline{\Omega}^s_{FV,neigh}$. In Fig. 4.8, these modifications corresponds to part C, part c_b and part c_a, respectively.

The coupling also brings some modifications in the network and FV parts of the matrix. In the linear system of the network part, the variable π_s of Eq. 3.5 is no longer a boundary condition but an unknown. This implies (part A of Fig. 4.8)

$$M_{\text{network}}\left(\alpha,\alpha\right) = \sum_{\beta\in\mathcal{N}_{\alpha,\text{in}}} G_{\alpha\beta} + G_{\alpha s}$$

and (part a of Fig. 4.8)

$$M_{\text{hybrid}}\left(\alpha,s\right) = -G_{\alpha s}.$$

Let i be the FV cell containing the coupling point s. The distribution of the coupling condition

among the cells of $\Omega^s_{FV,neigh}$ (Eq. 4.38) yields, for each k of $\overline{\Omega}^s_{sph}$ (part B of Fig. 4.8),

$$M_{\mathrm{FV}}\left(i,k'\right) = M_{\mathrm{FV}}\left(i,k'\right) - \frac{\tau_i}{C_{s,\Gamma}\,\mathrm{Card}\left(\overline{\Omega}^s_{sph}\right)}$$

and (part b of Fig. 4.8)

$$M_{\mathrm{hybrid}}\left(i,k'\right) = \frac{\tau_i}{C_{s,\Gamma}}.$$

Finally, the equations associated to the hybrid approach yield a sparse symmetric matrix M_{hybrid} and a sparse right-hand side only describing the boundary conditions imposed at the inlets and outlets of the arteriolar and venular trees. In summary, the matrix is composed of seven parts displayed on Fig. 4.8:

Part A: the finite volume formulation (Eqs. 3.34-3.38) yields a symmetric sparse block of size (number of cells)^2. Each row i contains 7 components: one diagonal value associated to the cell i and 6 off-diagonal values associated to its neighbours;

Part a: the finite volume formulation applied to the coupled cells (Eq. 4.38) yields a supplementary off-diagonal block of size (number of cells×number of couplings), where the components correspond to the distributed impact of the couplings and the relationship with the associated coupled vertices;

Part B: the network approach (Eqs. 3.3-3.6) yields another sparse block of size (number of inner vertices)^2. Each row α contains $1 + \mathrm{Card}\left(\mathcal{N}_\alpha\right)$ components, where $\mathrm{Card}\left(\mathcal{N}_\alpha\right)$ is the number of neighbouring vertices of the inner vertex α: one diagonal value associated to the inner vertex α and $\mathrm{Card}\left(\mathcal{N}_\alpha\right)$ off-diagonal values associated to its neighbours;

Part b: some inner vertices of the network approach are connected to coupling points instead of boundary nodes, yielding a supplementary off-diagonal block of size (number of inner vertices×number of couplings), where the components correspond to the associated coupled vertices;

Part C: the coupling part (Eqs. 4.30-4.38) yields a simple diagonal block of size (number of couplings)^2. Each row s corresponds to a new unknown, which is associated to the coupled vertex s;

Part $\mathbf{c_a}$: the coupling part is completed by an off-diagonal block of size (number of couplings×number of cells). The components correspond to the connection of each coupled vertex to the FV cells where the coupling condition has been distributed (as in Fig. 4.7);

Part $\mathbf{c_b}$: the coupling part is also completed by an off-diagonal block of size (number of couplings×number of inner vertices). The components correspond to the connection of each coupled vertex to its unique neighbouring vertex in the network part.

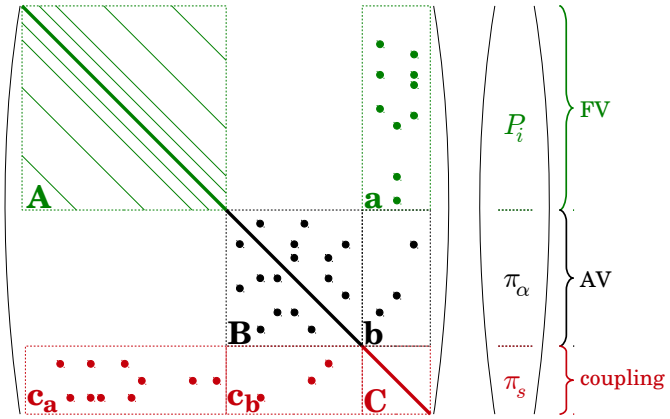

Figure 4.8: **Visualization of the final matrix structure.** Using the hybrid approach, we can compute blood flow by solving a single linear system, assembled from the equations describing the finite volume discretization in the continuum (FV, in green), the network approach in the arteriolar and venular trees (AV, in black) and the coupling model at the interface of the two frameworks (coupling, in red). This yields a sparse matrix that is schematized here. Plain lines and dots represent non-zero values. The components $(P_i)_i$, $(\pi_\alpha)_\alpha$ and $(\pi_s)_s$ are the unknowns of the linear system, corresponding to FV, AV and coupling parts, respectively.

ii. Numerical implementation. Concerning the implementation of this linear system, the sparsity of the final matrix allows us to take advantage of the efficient and scalable numerical tools in the PETSc library [Balay et al., 2016]. We use a block-Jacobi preconditioner, which is very well-suited to parallel computations, and the system is solved via the bi-conjugate gradient iterative method.

As detailed in Section 6 below, the code is composed of three independent parts corresponding to the FV, network and coupling equations, respectively. As a consequence, simulations can be run for both hybrid and Complete Network (CN) configurations, where all the vessels, including the capillaries, are modelled by the network approach. These CN simulations will be used in Section 5 to generate reference fields enabling the evaluation of the accuracy of the hybrid approach.

4.2.6 Bonus: Multiscale coupling condition adapted to non-cubic finite volume cells

In this section, we develop the coupling condition for a discretization of the continuum using non-cubic cells of size $h_x \times h_y \times h_z$. Regardless of the geometry of the mesh cells, the two analytical approximations of the pressure field close to the coupling point remain the linear expression (Eq. 4.19)

$$\pi_\Gamma = \pi_s - R_\Gamma q_s \tag{4.40}$$

and the spherical solution (Eq. 4.28)

$$P_k = \pi_\Gamma - \frac{\mu^{\text{eff}} q_s}{4\pi K^{\text{eff}}} \left(\frac{1}{d_{k,s}} - \frac{1}{l_\Gamma} \right). \tag{4.41}$$

The closing of the coupling condition by expressing the flow conservation at the interface between $\overline{\Omega}^s_{sph}$ and $\overline{\Omega}^s_{FV,neigh}$ (Eq. 4.29), using Eq. 3.45, now reads

$$\begin{aligned} &\frac{K^{\text{eff}}}{\mu^{\text{eff}} h_y h_z} \sum_{k \in \overline{\Omega}^s_{sph}|_{LR}} (P_{j_k} - P_k) \\ +&\frac{K^{\text{eff}}}{\mu^{\text{eff}} h_x h_z} \sum_{k \in \overline{\Omega}^s_{sph}|_{DU}} (P_{j_k} - P_k) \\ +&\frac{K^{\text{eff}}}{\mu^{\text{eff}} h_x h_y} \sum_{k \in \overline{\Omega}^s_{sph}|_{FB}} (P_{j_k} - P_k) = \frac{1}{h_x h_y h_z} q_s, \end{aligned} \tag{4.42}$$

where $\overline{\Omega}^s_{sph}|_{LR}$ contains the left and right cells of $\overline{\Omega}^s_{sph}$, $\overline{\Omega}^s_{sph}|_{DU}$ the down and up cells and $\overline{\Omega}^s_{sph}|_{FB}$ the front and back cells. Combining equations Eqs. 4.40, 4.41 and 4.42, we obtain

$$q_s = f\left(\pi_s, (P_j)_{j \in \overline{\Omega}^s_{FV,neigh}} \right), \tag{4.43}$$

where f is the following linear function

$$\begin{aligned} f\left(\pi_s, (P_j)_{j \in \overline{\Omega}^s_{FV,neigh}} \right) = \frac{1}{C_{s,\Gamma}} \Bigg(&\frac{h_x}{N^{h,s}_{sph}} \sum_{k \in \overline{\Omega}^s_{sph}|_{LR}} P_{j_k} \\ &+ \frac{h_y}{N^{h,s}_{sph}} \sum_{k \in \overline{\Omega}^s_{sph}|_{DU}} P_{j_k} \\ &+ \frac{h_z}{N^{h,s}_{sph}} \sum_{k \in \overline{\Omega}^s_{sph}|_{FB}} P_{j_k} - \pi_s \Bigg) \end{aligned} \tag{4.44}$$

and

$$\begin{aligned} N_{sph}^{h,s} = & \, h_x \, \mathrm{Card}\left(\overline{\Omega}_{sph}^{s}|_{LR}\right) \\ & + h_y \, \mathrm{Card}\left(\overline{\Omega}_{sph}^{s}|_{DU}\right) \\ & + h_z \, \mathrm{Card}\left(\overline{\Omega}_{sph}^{s}|_{FB}\right), \end{aligned} \tag{4.45}$$

with $\mathrm{Card}\,(.)$ representing the cardinal number of a given set. Then,

$$C_{s,\Gamma} = R_\Gamma - \frac{\mu^{\mathrm{eff}}}{4\pi K^{\mathrm{eff}}} \left(\frac{d_{sph}^{h,s}}{N_{sph}^{h,s}} - \frac{1}{l_\Gamma} - \frac{4\pi}{N_{sph}^{h,s}} \right), \tag{4.46}$$

with

$$\begin{aligned} d_{sph}^{h,s} = & \, h_x \sum_{k \in \overline{\Omega}_{sph}^{s}|_{LR}} \frac{1}{d_{k,s}} \\ & + h_y \sum_{k \in \overline{\Omega}_{sph}^{s}|_{DU}} \frac{1}{d_{k,s}} \\ & + h_z \sum_{k \in \overline{\Omega}_{sph}^{s}|_{FB}} \frac{1}{d_{k,s}}. \end{aligned} \tag{4.47}$$

Note that for a regular grid, with $h_x = h_y = h_z$, Eqs. 4.31 and 4.32 are straightforwardly retrieved.

4.2.7 Conclusion

Because of important scale differences between oil reservoirs and the human cortex, the final coupling model presents four main modifications compared to the Peaceman's well model:

- the radial approximation of the pressure field in the vicinity of the coupling site is replaced by a spherical approximation (Eq. 4.27b);
- our model takes into account the detailed structure of the microscopic structure, i.e. the connected capillaries, in the closest vicinity of the coupling point (Eq. 4.27a);
- the domain where both analytical approximations and FV scheme match is defined further away (Eq. 4.28);
- the coupling condition is distributed among the neighbouring FV cells to take into account the off-centering of a coupling point (Eq. 4.38).

5 Validation of the hybrid approach

In this section, we will evaluate the accuracy of the hybrid approach and the multiscale coupling model it includes. In Section 5.1, we will explain how we validate this approach by comparison with a complete network (CN) approach where all the vessels, including the capillaries, are modelled by the network approach presented in Section 3.2. To further highlight the need for a proper multiscale coupling model, we will also compare our results with Simple Hybrid (SH) configurations, where a simple condition of pressure continuity is imposed at the interface between the arteriolar and venular vessels and the continuum. We will also present the network datasets used for validation and the error metrics.

In Section 5.2, we will assess the accuracy of the multiscale coupling model in configurations involving only a few *isolated* arteriolar and/or venular vessels, i.e. not interconnected, coupled to synthetic capillary networks. These synthetic networks will be generated so that their structures comply to the hypotheses used in the derivation of the multiscale coupling model (e.g. isotropy, see Section 3.1). In Section 5.3, the comparison of our results with CN and/or SH simulations will be progressively extended to more realistic, i.e. more anatomically accurate, configurations. First, the synthetic representation of capillary networks will be complexified by adding morphometrical and topological features that typically occur in the brain microcirculation (e.g. trifurcations or distribution of vessels diameters). Second, we will extend the validation of our model to configurations involving anatomic arteriolar and/or venular trees, which display a large number of interconnected coupling points. Finally, an application to a more realistic configuration will be presented in Section 5.4. This application will involve both anatomical arteriolar and venular trees and a physiological-like capillary network.

5.1 How we validate the model

5.1.1 The complete network approach as a reference

The code developed for the hybrid approach can alternately be used to run computations where all the vessels, including the capillaries, are modelled by the network approach presented in Section 3.2. Since such representations are widely adopted in the context of brain microcirculation and have been proven to accurately describe the cerebral hemodynamics [Lorthois et al., 2011a, Lorthois et al.,

2011b, Linninger et al., 2013], we use them to generate reference fields enabling the validation of the hybrid approach. As announced, they are used in the sections below under the name complete network (CN) approaches.

As detailed in Section 2, the network approaches are restricted to relatively small volumes ($\sim$10 mm^3) compared to our objective, which is the whole-brain simulation of hemodynamics and mass transfers. This limitation stems from the fact that they require a description of the vascular network down to the scale of the capillaries. As a consequence, the validation of the hybrid approach is also restricted to such relatively small volumes.

5.1.2 Comparison with a simple hybrid approach

The simple hybrid (SH) approach is similar to our hybrid approach, except that the multiscale coupling model is replaced by a simple condition of pressure continuity at the interface between the arteriolar and venular trees, and the continuum. Thus the coupling equations Eqs. 4.30-4.32 are replaced by

$$P_i = \pi_s, \tag{5.1}$$

where P_i represents the pressure of the coupled cell i, and π_s the pressure of the coupled vertex. Details about the development of the associated linear system are provided in Appendix 8.3.1. Contrary to the multiscale coupling model presented in Section 4, the condition Eq. 5.1 overlooks the fact that the pressure at the endpoint of an arteriolar or venular vessel, which is defined at microscopic scale, has not the same physical meaning that the pressure of a coupled cell, which is defined at mesoscopic scale. Furthermore, it does not take into account the location of the coupling point inside the coupled cell.

In the remainder of the manuscript, the hybrid approach will systematic be qualified as *simple* if referring to SH configurations. If no qualification is specified, the term hybrid approach will refer to simulations involving the multiscale coupling model presented in this work.

5.1.3 Network datasets

i. Arteriolar and venular trees In Section 5.2, the arteriolar and/or venular components will be represented by isolated, i.e. not interconnected, cylinders of length 200 μm and diameter 15 μm. These values typically correspond to those of arteriolar and venular vessels in the human brain microcirculation. In Section 5.3, the anatomic dataset displayed in Fig. 3.1 will be used to validate

the hybrid approach in a more realistic configurations. Such structure involves vessels of lengths in the range 1.85-647.60 μm, and of diameters in the range 7.50-42.64 μm.

ii. Synthetic capillary networks Anatomical data resolved at the scale of capillaries over large volumes are not available yet. With a view to model validation by comparison with CN simulations, calculations will therefore be performed here for synthetic capillary networks.

In Section 5.2, two types of periodic *regular capillary networks* will be used, whose names were chosen according to graph theory [Chen, 1997]: *6-regular* networks, i.e., where each vertex is connected to 6 neighbours; and *3-regular* networks, which respect the physiological connectivity in healthy capillary networks. Such lattices are obtained by periodically repeating elementary patterns, as illustrated in Fig. 5.1. By construction, they are isotropic and homogeneous, which corresponds to the simplifying assumptions made for the development of the hybrid approach.

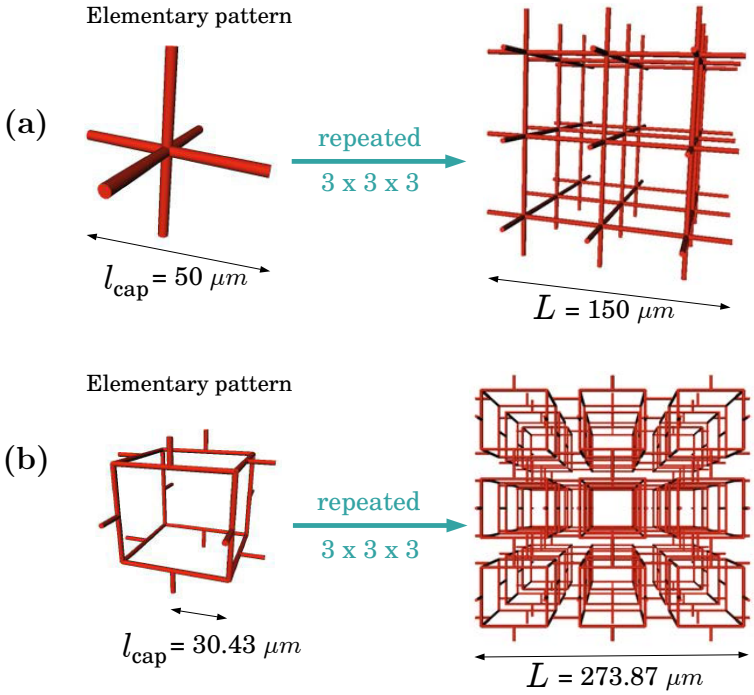

Figure 5.1: **Visualization of the 6- and 3-regular patterns.** **(a)** Elementary pattern of the 6-regular network and example of periodically repeated patterns. **(b)** Elementary pattern of the 3-regular network and example of periodically repeated patterns.

In both cases, the capillaries have uniform lengths, $l_{cap} = 50\,\mu$m in 6-regular networks and $l_{cap} = 30.43\,\mu$m in 3-regular networks, so that the two network types have the same vascular density (see detail in Appendix 8.4). Capillary diameters are either uniform ($d_{cap} = 5.91\,\mu$m) or distributed following a Gaussian distribution with a mean diameter of $5.91\,\mu$m and a standard deviation of $1.30\,\mu$m. These values are characteristic of human capillary networks [Cassot et al., 2006].

To go further and simulate blood flow in statistically realistic capillary networks (Section 5.3 and 5.4), more complex lattices will be used, based on random generations of Voronoi diagrams. They will be termed *Voronoi-like networks* in the remainder of the manuscript. Two-dimensional patterns of Voronoi-like networks (see Fig. 5.2**(a)**) have already been introduced in the literature [Lorthois and Cassot, 2010]. The extension to three-dimensional networks (see Fig. 5.2**(b)**) is still unpublished work in the BrainMicroFlow project [Smith, 2016], and will only be briefly presented in this paragraph.

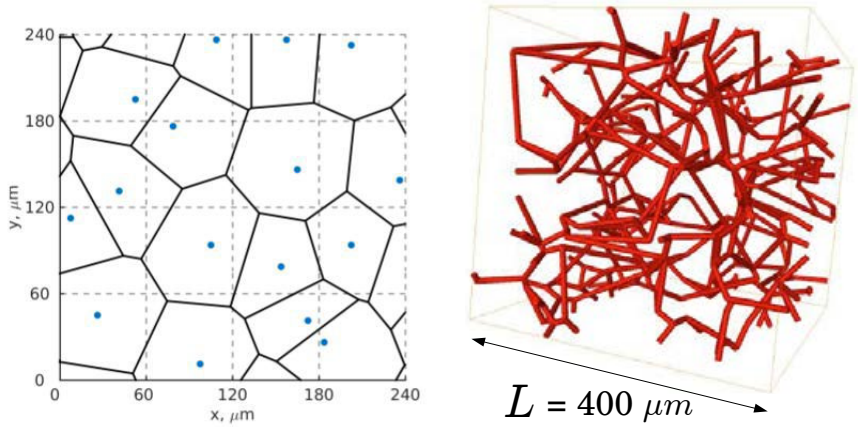

(a) **(b)**

Figure 5.2: **Visualization of a Voronoi-like synthetic pattern.** **(a)** Generation of a two-dimensional Voronoi diagram on a surface of 240×240 μm^2 involving cells of side 60 μm. **(b)** A volume of $(400\,\mu\text{m})^3$ of synthetic network is generated from a three-dimensional Voronoi diagram for the representation of statistically realistic capillary networks.

To build a mesh-like network, the domain is first discretized on a Cartesian grid of cubic cells (dotted lines in Fig. 5.2**(a)**). A seed is randomly placed in each cell, as generator of the Voronoi diagram. The set of edges of the resulting space tessellation corresponds to the capillary vasculature. However, in three-dimensions, such a structure is highly connected (e.g. vertices connected to x neighbours, $x \gg 3$) and poorly related to the topological reality of cerebral capillary networks (e.g. non realistic angles at bifurcations). To improve the structure, a series of cleaning processes are run to remove appropriate edges and reorganize the structure. It has been observed that the final network is statistically equivalent to anatomical capillary networks, e.g. with regard to vascular density, loop structure, and distributions of vascular length, when the initial discretization of the domain involves cells of $70 \times 70 \times 70\,\mu\text{m}^3$ [Smith, 2016] (see Fig. 5.2**(b)**).

The vascular length of the resulting vessels is typically ∼30±20 μm. As for regular networks, the diameters of Voronoi-like networks are imposed either uniform ($d_{cap} = 5.91\,\mu$m) or following a

Gaussian distribution with a mean diameter of 5.91 μm and a standard deviation of 1.30 μm [Cassot et al., 2006].

iii. Computation of equivalent effective parameters The capillary networks presented above are used in CN simulations. In the hybrid approach, the capillary bed is replaced by a continuum where blood flow is characterized by effective parameters (permeability and viscosity) computed at the mesoscopic scale. Our way of computing both the effective permeability K^{eff} and the effective viscosity μ^{eff} has been introduced in Section 3.4. As a reminder, the effective permeability represents the permeability of the network with uniform viscosity, while the effective viscosity represents the impact of the Fåhræus-Lindqvist effect (Eq. 2.3).

In this section, we present the influence of the domain size on the associated effective properties for 6-regular, 3-regular and Voronoi-like capillary networks. First, configurations involving *uniform diameters* will enable us to deduce the permeability K^{ref} and the corresponding uniform viscosity μ^{ref} of each capillary network. As mentioned in Section 3.4, these notations stems from the fact that such values will be considered as references to understand the impact of further introducing *diameter distributions*, which constitutes the second part of this section. The final results are summarized in Table 2.

		K^{ref} (m^2)	μ^{ref} (Pa $\cdot$ s)	REV
d_{cap} const.	6-regular	1.1977×10^{-14}	5.9775×10^{-3}	50 μm
	3-regular	7.1858×10^{-15}	5.9775×10^{-3}	91.29 μm
	Voronoi-like	5.2138×10^{-15}	5.9775×10^{-3}	350 μm
		K^{eff} (m^2)	μ^{eff} (Pa $\cdot$ s)	REV
d_{cap} distr.	6-regular	1.2176×10^{-14}	5.8760×10^{-3}	250 μm
	3-regular	5.6610×10^{-15}	6.1834×10^{-3}	182.58 μm
	Voronoi-like	4.4626×10^{-15}	6.1018×10^{-3}	350 μm

Table 2: **Effective parameters for the continuum representation of the model capillary networks.** This table summarizes the values of effective permeability and viscosity used in this work. Superscripts *ref* refer to effective properties computed in networks with uniform diameter, while superscripts *eff* refer to effective properties computed in networks with distributed diameter.

Uniform capillary diameters. For a uniform capillary diameter $d_{cap} = 5.91\,\mu$m, which corresponds to the typical diameter of a capillary [Cassot et al., 2006], the viscosity is uniform and computed from the *in vivo* viscosity law (Eq. 2.3): $\mu^{\text{ref}} \simeq 5.9775 \times 10^{-3}\,\text{Pa}\cdot\text{s}$. The impact of the domain size L on the permeability value K^{ref} is detailed below for each kind of capillary network and numerical results are displayed in Fig. 5.3**(a)**.

As presented in Fig. 5.3**(a)**, the convergence of the permeability value K^{ref} in 6-regular networks is immediate, with $K^{\text{ref}} \simeq 1.1977 \times 10^{-14}\,\text{m}^2$. This immediate convergence is due to the periodicity of such networks. This implies that the REV side is equal to $l_{cap} = 50\,\mu$m, which is the side of an elementary pattern (see Fig. 5.1**(a)i**). Further, the 6-regular networks present a very specific structure, which allow the theoretical derivation of K^{ref}. Indeed, this network is similar to $N \times N$ parallel vessels of length L, where N represents the number of vessels normal to the direction of interest. Thus we have

$$Q_L = N^2 G_L \Delta_L P, \tag{5.2}$$

with G_L the conductance corresponding to a vessel of length L

$$G_L = \frac{\pi d_{cap}^4}{128 \mu_L^{\text{eff}} L}. \tag{5.3}$$

Noting that $L/N = l_{cap}$ here, we deduce from Eqs. 3.46 and 5.2 a value of K^{ref} that does not depend on L

$$K^{\text{ref}} = \frac{\pi d_{cap}^4}{128 l_{cap}^2}. \tag{5.4}$$

This value is valid for any $L \geq l_{cap}$ and confirms the numerical value of the permeability K^{ref}.

No theoretical formula can be derived to calculate the permeability K^{ref} in the 3-regular network. The REV side and the associated effective parameters are determined by numerical simulations only. As displayed in Fig. 5.3**(a)ii**, the convergence of the value is also immediate, due to the periodicity of the network. This implies that the REV side is equal to $3l_{cap} = 91.29\,\mu$m, i.e. the side of an elementary pattern (see Fig. 5.1**(b)**). The corresponding permeability value is $K^{\text{ref}} \simeq 7.1858 \times 10^{-15}\,\text{m}^2$.

Numerical simulations are also required to determine the effective parameters of the Voronoi-like networks. Furthermore, due to the randomness of the generation of such networks, the values are averaged over 8 different realisations. The means and standard deviations of K^{ref} are plotted in Fig. 5.3**(a)iii**. The REV side is defined at $350\,\mu$m by setting the convergence criteria to a standard

deviation lower than 0.1. The corresponding permeability value is $K^{\text{ref}} \simeq 5.2138 \times 10^{-15}\,\text{m}^2$.

Finally, we also deduce from the numerical results that the thee networks are isotropic because the results overlap in the three directions of the space in all graphs of Fig. 5.3**(a)**.

Distributed capillary diameters. If the diameter is non-uniform, it follows a Gaussian law with a mean diameter of $5.91\,\mu$m and a standard deviation of $1.30\,\mu$m, which is characteristic of human capillary networks [Cassot et al., 2006]. Thus the capillary network is statistically generated, i.e. using 2 000 different diameter distributions, and we study the statistical properties of the resulting permeability and viscosity. The results are presented in Fig. 5.3**(b,d)**. In order to quantify the impact of a diameter distribution on the effective parameters K^{eff} and μ^{eff}, we consider the effective properties K^{ref} and μ^{ref} computed above in the case of uniform capillary diameters (Fig. 5.3**(a)**) as references.

For both 6- and 3-regular, the side of the REV is defined at the convergence of ${}^{K^{\text{eff}}}/_{K^{\text{ref}}}$ for a standard deviation lower than 0.1. This corresponds to a REV side of 250 μm for the 6-regular network, and 182.58 μm for the 3-regular network. The values of K^{eff} and μ^{eff} are then deduced from the ratios ${}^{K^{\text{eff}}}/_{K^{\text{ref}}}$ and ${}^{\mu^{\text{eff}}}/_{\mu^{\text{ref}}}$ reported at these REV sides. $K^{\text{eff}} = 1.2176 \times 10^{-14}\,\text{m}^2$ and $\mu^{\text{eff}} = 5.8760 \times 10^{-3}\,\text{Pa.s}$ for the 6-regular network, and $K^{\text{eff}} = 5.6610 \times 10^{-15}\,\text{m}^2$ and $\mu^{\text{eff}} = 6.1834 \times 10^{-3}\,\text{Pa.s}$ for the 3-regular network. For the Voronoi-like network, the REV side has already been determined at $350\,\mu$m, thus the values of K^{eff} and μ^{eff} are deduced from the ratios ${}^{K^{\text{eff}}}/_{K^{\text{ref}}}$ and ${}^{\mu^{\text{eff}}}/_{\mu^{\text{ref}}}$ reported at this REV side: $K^{\text{eff}} = 4.4626 \times 10^{-14}\,\text{m}^2$ and $\mu^{\text{eff}} = 6.1018 \times 10^{-3}\,\text{Pa.s}$.

By construction, the 6-regular networks are less flow-resistive than the 3-regular and Voronoi-like networks. Indeed, 6-regular lattices correspond to a series of parallel straight cylinders when simulating unidirectional flow. This low-resistivity is translated here by an almost twice larger effective permeability. For the same reason, the viscosity is also slightly lower for 6-regular than for 3-regular and Voronoi-like networks. By contrast, values corresponding to 3-regular and Voronoi-like networks are similar, suggesting that they have similar topological properties. However, the convergence of both effective permeability and viscosity is less pronounced in the case of Voronoi-like networks, with fluctuations occurring beyond the REV side. This suggests that a spatialization of the effective properties might be necessary to accurately characterize blood flow at mesoscopic scale.

Finally, the graphs presented in Fig. 5.3**(b-c)** confirm that the thee networks are isotropic since the results overlap in the three directions of the space.

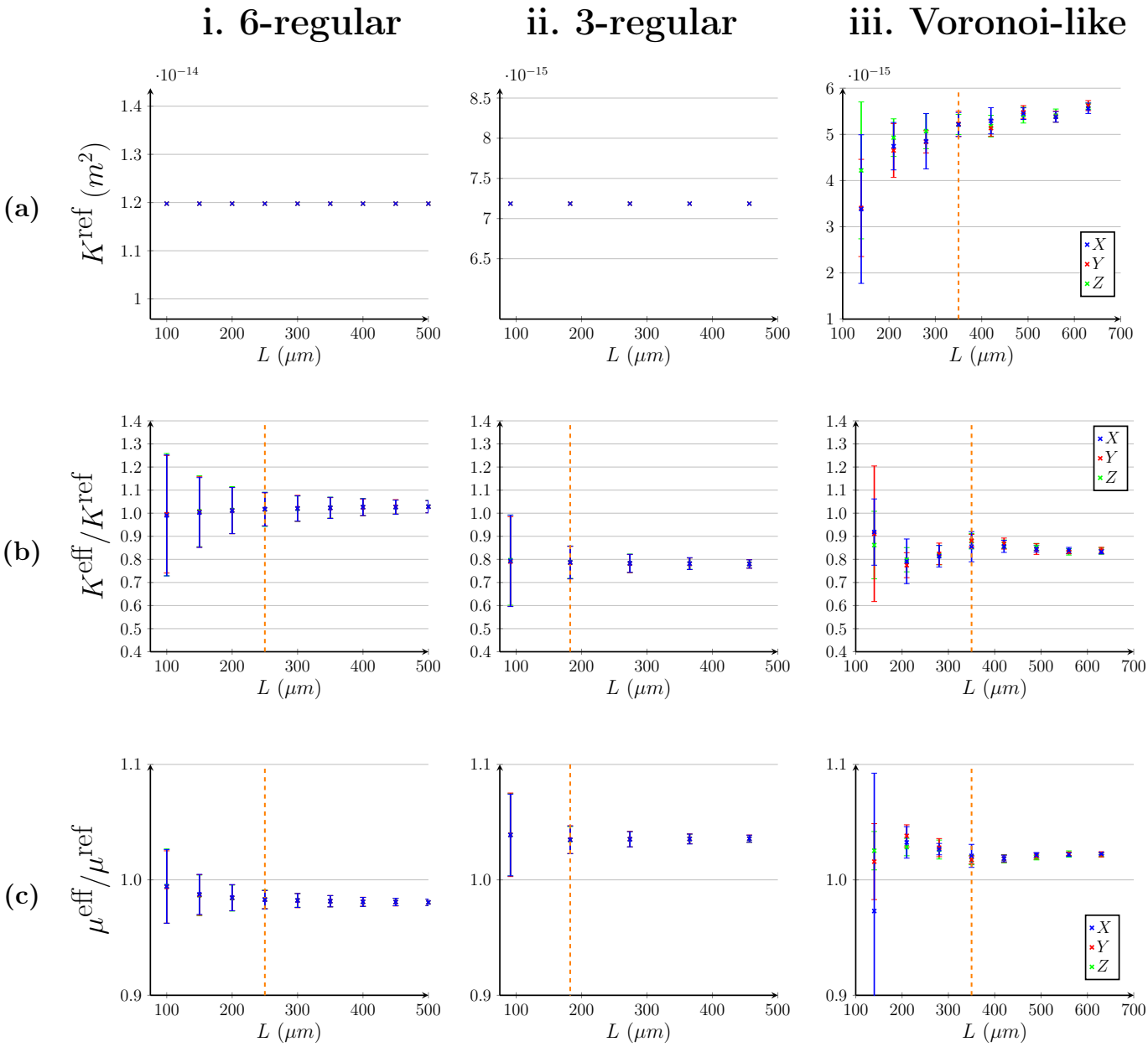

Figure 5.3: **Statistical study for the computation of the effective permeability K^{eff} and viscosity μ^{eff} in 6- and 3-regular, and Voronoi-like capillary networks with uniform length and distributed diameters. The REV side are plotted in orange dashed lines for each networks.** **(a)** First, we derive a reference permeability K^{ref} by assuming a uniform diameter, thus a uniform viscosity μ^{ref}, in the capillaries. The variation of K^{ref} is plotted in function of the side L of the capillary domain. **(b)** Second, we assume the viscosity to be uniform in the capillaries and derive the effective permeability K^{eff} from computations involving 2 000 different distributions of diameters. The mean and standard deviation of the ratio $K^{\text{eff}}/K^{\text{ref}}$ is plotted in function of the side L of the capillary domain. **(c)** Finally, we distribute the viscosity in the capillaries and derive the effective viscosity μ^{eff} at mesoscopic scale from computations involving the same 2 000 different distributions of diameters. The mean and standard deviation of the ratio $\mu^{\text{eff}}/\mu^{\text{ref}}$ is plotted in function of the side L of the capillary domain.

5.1.4 Error metrics for the comparison of the hybrid approach with CN simulations

To evaluate the accuracy of the hybrid model, we compare results of the hybrid approach with CN simulations, where blood flow in all vessels is described by Eqs. 3.3 and 3.5. We consider the four domains of interest illustrated in Fig. 4.6**(e)**: the source points s, the whole arteriolar and venular trees Ω_{AV}, the distant FV neighbourhoods $\Omega_{sph}^{s,\varepsilon}$ of each coupling point s and the rest of the continuum $\Omega_{FV}^{\varepsilon}$, which excludes the neighbourhoods $\left(\Omega_{FV,neigh}^{s}\right)_{s\in S}$ of coupling points. In the arteriolar and venular trees, variables are identical in both approaches, therefore facilitating comparison. To compute errors in subdomains of the continuum, the capillary pressures in the CN approach are averaged over volumes corresponding to the FV cells in the hybrid approach, and capillary flow rates are averaged over surfaces which correspond to the interfaces between two discretization cells. Details about this averaging is provided in Appendix 8.1.

Let Ω be one of the four domains of interest mentioned above. Ω contains two sets of components: the set Ω^p of network vertices or FV cells, where pressures are defined, and the set Ω^q of network vessels or interfaces between two FV cells, where flow rates are defined. For all component ω of Ω^p, the local pressure error ε_ω^p reads

$$\varepsilon_\omega^p = \frac{|p_{\omega,\mathrm{H}} - p_{\omega,\mathrm{CN}}|}{p_{\omega,\mathrm{ref}}}, \tag{5.5}$$

where p represents the pressure value, the subscripts H and CN refer to the hybrid and CN approaches, and the subscript ref refers to the reference value used for normalization. For all component ω of Ω^q, the local flow rate error reads

$$\varepsilon_\omega^q = \frac{|q_{\omega,\mathrm{H}} - q_{\omega,\mathrm{CN}}|}{q_{\omega,\mathrm{ref}}}, \tag{5.6}$$

where q represents the flow rate value. The global errors characterizing Ω are further defined as

$$\varepsilon_\Omega^p = \frac{\sum_{\omega\in\Omega^p} \varepsilon_\omega^p}{\mathrm{Card}\left(\Omega^p\right)} \tag{5.7}$$

and

$$\varepsilon_\Omega^q = \frac{\sum_{\omega\in\Omega^q} \varepsilon_\omega^q}{\mathrm{Card}\left(\Omega^q\right)}. \tag{5.8}$$

For studying the errors distribution, we use the local errors in Eqs. 5.5 and 5.6. To avoid underestimation, these errors are normalized by local reference values, so that $p_{\omega,\mathrm{ref}} = p_{\omega,\mathrm{CN}}$ and $q_{\omega,\mathrm{ref}} = q_{\omega,\mathrm{CN}}$ for all ω. For overall error estimation, we use the global errors of Eqs. 5.7 and 5.8. In this case, errors are normalized by the global pressure drop δP across the sample considered or the global flow

rate q_A at the inlet of the arteriolar vessel, so that $p_{\omega,\text{ref}} = \delta P$ and $q_{\omega,\text{ref}} = q_A$ for all ω in Eqs. 5.5 and 5.6. These global errors are particularly well-suited to compare the variation of errors among several test cases.

5.1.5 Reconstruction of the pressure field in the vicinity of couplings

In the FV domains selected for errors computation (see Fig. 4.6**(e)**), none includes the neighbourhoods $\left(\Omega^s_{FV,neigh}\right)_{s\in S}$ of the coupling points s. Indeed, as precised in Section 4.2.3, the pressure field described by the FV scheme is not representative in $\Omega^s_{FV,neigh}$. Therefore, the comparison with the CN approach is not relevant in this neighbourhood. To go further, the pressure field in $\Omega^s_{FV,neigh}$ should be analytically reconstructed using linear and spherical approximations (Eqs. 4.19 and 4.25). However, such a reconstruction is a complex puzzle when configurations involve more than one coupling, with superposition of independent analytical solutions. In this manuscript, we decided to not compute any error in the neighbourhoods $\left(\Omega^s_{FV,neigh}\right)_{s\in S}$. Thus the FV domain $\cup_{s\in S}\Omega^s_{FV,neigh}$ will be extracted in all the visualizations, as illustrated in Fig. 5.4. In the case of anatomical configurations involving multiple couplings distributed over the whole FV domain, this choice results in no relevant report with regard to this FV domain, as illustrated in Fig. 5.4**(b)**. Thus no visualization of the FV domain will be presented for complex configurations in this section. For the purpose of investigating the accuracy of the hybrid approach in the neighbourhood of couplings, we will rather qualitatively compare plot pressure lines, as will be done in Fig. 5.9**(b)** for instance.

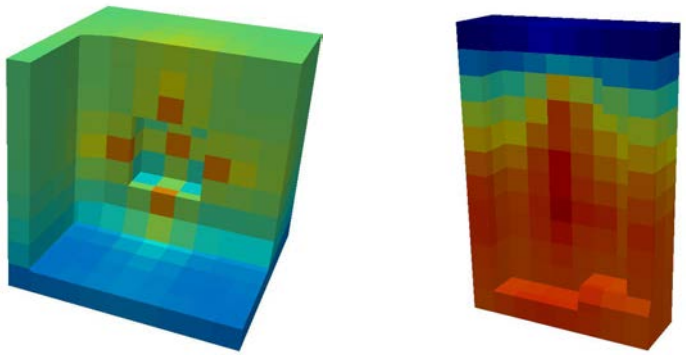

(a) Simple coupling **(b) Multiple couplings**

Figure 5.4: **Examples of visualizations with extraction of the FV neighbourhoods** $\cup_{s\in S}\Omega^s_{FV,neigh}$**. (a)** For simple configurations involving only one coupling, only the 9 cells of $\Omega^s_{FV,neigh}$ are extracted. **(b)** For complex configurations involving multiple couplings, the extraction of $\cup_{s\in S}\Omega^s_{FV,neigh}$ makes the visualization irrelevant, since only the boundary FV cells remain.

Now that the tools for the validation of the hybrid approach have been presented, we detail below all the tests run to assess the accuracy of our approach. In Section 5.2, we first estimate the robustness of the multiscale coupling model, which is at the heart of the hybrid approach, in idealized configurations that might break the assumptions made during its development. Then, in Section 5.3, complexity is added to the morphometry and topology of capillary networks (e.g. diameter distributions). Complexity will also be added to the architecture or the arteriolar and venular vasculature. Finally, the hybrid approach will be validated on a realistic configuration involving anatomical arteriolar and venular trees coupled to a physiologically-accurate capillary network, in Section 5.4.

5.2 Validation of the multiscale coupling model on simple test cases

Here, our goal is to assess the robustness of the coupling model and the relevance of strategies that have been adopted during its development. The tests are run for simple configurations involving only a few couplings. These basic tests aim at isolating the influence of characteristic architectural features (e.g. several couplings in one FV cell). Such features can be considered as *perturbations* in the sense that they might break the assumptions made for the derivation of the coupling model (e.g. isotropy).

To avoid uncertainties related to the computation of effective parameters (see Section 5.1.3), the tests presented in this section only involve 6-regular capillary networks with uniform diameter ($d_{cap} = 5.91\mu m$), which effective permeability and viscosity can be analytically computed (details in Section 5.1.3). In this way, the computed errors can be entirely assigned to the accuracy of the multiscale coupling model. Furthermore, the arteriolar and venular components are represented by isolated vessels, for the purpose of avoiding the treatment of complex vascular trees.

The accuracy of the model is determined by comparing the hybrid approach with CN and/or SH simulations, using the *global error metrics*, Eqs. 5.7 and 5.8, for the four domains of interest illustrated in Fig. 4.6**(e)**. While these errors may not be as representative as local errors, they are adapted to the comparison of several test cases and will enable us to conclude about the importance of the impact of each perturbation.

5.2.1 Configurations and boundary conditions

In the test cases of this section, we will consider two classes of configurations schematized in Figs. 5.5 and 5.6. For convenience, details about these configurations are summarized in Appendix 8.5.

The first class of test cases involve a *single coupling* (Fig. 5.5). In this case, a single arteriole plunges into a cubic 6-regular capillary bed of volume $2.25 \times 2.25 \times 2.25\,\mathrm{mm}^3$ with uniform length $l_{cap} = 50\,\mu\mathrm{m}$ and uniform diameter $d_{cap} = 5.91\,\mu\mathrm{m}$. Because we will want to investigate the impact of the cell size h, we choose to ensure mesh convergence by considering large capillary domains. By placing the coupling at the center of the domain, we also avoid the potential interference of boundaries with the reconstruction of the pressure and flow rate fields. The arteriolar vessel is $l_{art} = 200\,\mu\mathrm{m}$ long and $d_{art} = 15\,\mu\mathrm{m}$ in diameter. As schematized in Fig. 5.5, we impose a constant pressure drop $\delta P = 10\,000\,\mathrm{Pa}$ between the arteriolar inlet and the bottom face of the capillary bed; impermeability (zero flow) on the top of the capillary network; and periodic conditions in the two other directions. For consistency, similar boundary conditions are applied to the faces of the FV domain.

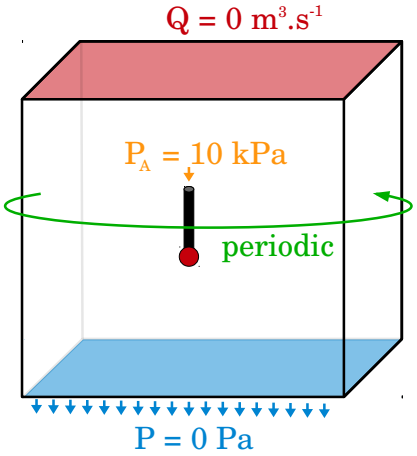

Figure 5.5: **Schematics of the boundary condition in the case of single coupling.** The black box represents either the capillary bed in CN configuration or the continuum in the hybrid approach. For comparison, the boundary conditions imposed at the boundaries of the capillary bed in the CN simulations are similar to those imposed at the faces of the continuum in the hybrid approach. The black cylinder represents the arteriolar vessel. The in- and outflow are illustrated by arrows. The arteriolar end-tips highlighted by a red dot in the coupling site, which is connected to capillaries in CN configuration or connected to the continuum using the coupling model in the hybrid approach. A pressure drop of 10 000 Pa is imposed between the arteriolar inlet and the bottom face of the capillary bed/continuum. A condition of impermeability (i.e. no flow) is imposed at the top face, and periodic conditions are imposed in the two other directions (left-right and front-back).

The second class of test cases involve *several couplings*. The configuration with two couplings occurring in separate FV cells is schematized in Fig. 5.6. In this case, two arteriolar and venular vessels penetrate into a parallelepipedic 6-regular capillary bed of size $4.5 \times 2.25 \times 2.25\,\mathrm{mm}^3$ with uniform length $l_{cap} = 50\,\mu\mathrm{m}$ and uniform diameter $d_{cap} = 5.91\,\mu\mathrm{m}$. The arteriolar and venular vessels are $l_{art} = l_{ven} = 200\,\mu\mathrm{m}$ long and $d_{art} = d_{ven} = 15\,\mu\mathrm{m}$ in diameter. As schematized in Fig. 5.6, we

impose a constant pressure drop $\delta P = 7\,000\,\text{Pa}$ between the arteriolar inlet and the venular outlet; impermeability (zero flow) on the top and bottom of the capillary network; and periodic conditions in the two other directions. For consistency, similar boundary conditions are applied to the faces of the FV domain.

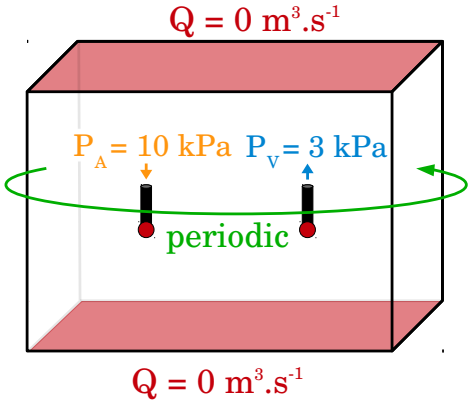

Figure 5.6: **Schematics of the boundary conditions imposed for the validation tests in the case of multi-couplings.** The black box represents either the capillary bed in CN configuration or the continuum in the hybrid approach. For comparison, the boundary conditions imposed at the boundaries of the capillary bed in the CN simulations are similar to those imposed at the faces of the continuum in the hybrid approach. The black cylinders represent the arteriolar and venular vessels. The in- and outflow are illustrated by arrows. The arteriolar and venular end-tips highlighted by red dots in the coupling site, which are connected to capillaries in CN configuration or connected to the continuum using the coupling model in the hybrid approach. A pressure drop of 7 000 Pa is imposed between the arteriolar inlet(s) and the venular outlet(s). A condition of impermeability (i.e. no flow) is imposed at the top and bottom faces, and periodic conditions are imposed in the two other directions (left-right and front-back).

One configuration will involve several couplings occurring *in one FV cell*. In this case, we couple from 2 to 10 arteriolar and venular vessels to a 6-regular capillary bed of side 2.25 mm, in such a way as to locate the couplings in the center cell of the FV domain. For the purpose of generating a realistic spatial arrangement of the couplings (see Fig. 5.7), the arteriolar and venular vessels are randomly generated following an algorithm, which imposes a distance $\geq$100 μm between arterioles and venules. As a result, the proportions of arteriolar and venular vessels vary from one generation to another. However, the number of arterioles is always larger than the number of venules, in agreement with physiological reality. For the purpose of highlighting an average trend when studying the accuracy of the coupling model in case of multi-couplings, 100 different configurations are generated for a given number of couplings. For boundary conditions, as an extension of the configuration schematized in Fig. 5.6, we impose a pressure of 10 000 Pa at each arteriolar inlet and a pressure of 7 000 Pa at each venular outlet; impermeability (zero flow) on the top and bottom of the capillary network; and

periodic conditions in the two other directions. For consistency, similar boundary conditions are applied to the faces of the FV domain.

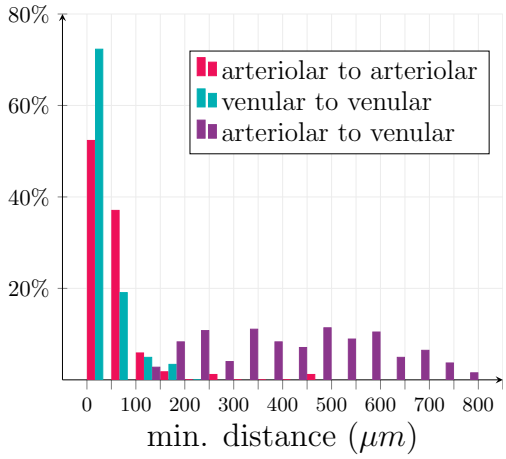

Figure 5.7: **Spatial correlations between coupling sites.** We use anatomically accurate data to illustrate spatial correlations between the coupling sites. Minimum distances have been computed between all coupling points according to their types (arteriolar to arteriolar, venular to venular and arteriolar to venular). The histogram plot presents the percentages of couplings associated to the same range of minimum distance.

All the simulations presented in this section have been run in sequential on one core *Intel(R) Core(TM) i5-4670 CPU @ 3.40GHz*.

5.2.2 Scale separation

An important hypothesis of the coupling model is that the size h of a mesh cell is sufficiently larger than the characteristic length l_{cap} of the capillaries—so that Eq. 4.28 is valid. Thus we focus here on identifying the threshold value of h/l_{cap} for which the FV cells are large enough. This threshold defines what we term the *scale separation* between the capillary bed and the continuum. For that purpose, we consider a test case involving a single coupling. The most sensitive area to the condition of scale separation is *a priori* the distant neighbourhood $\Omega^{s,\varepsilon}_{sph}$ (Fig. 4.6**(e)**), which corresponds to the intermediate zone between the analytical approximations and the FV formulation.

The results are presented in Fig. 5.8**i**. As expected, the errors $\varepsilon^{p}_{\Omega^{s,\varepsilon}_{sph}}$ and $\varepsilon^{q}_{\Omega^{s,\varepsilon}_{sph}}$ fluctuate for small values of h/l_{cap} in the coupling neighbourhood, then decrease with a stabilization for h/l_{cap} close to 4 or $h \sim 200\,\mu$m. The errors $\varepsilon^{p}_{\Omega_{FV}}$ and $\varepsilon^{q}_{\Omega_{FV}}$ also slightly fluctuate but the magnitude of the variations are negligible. The other errors related to the arteriolar component are not impacted by the scale separation. To ensure the validity of the multiscale coupling model and a correct description of the pressure and flow fields in the whole system, we will always use $h/l_{cap} \geq 4$ in the remainder of this manuscript.

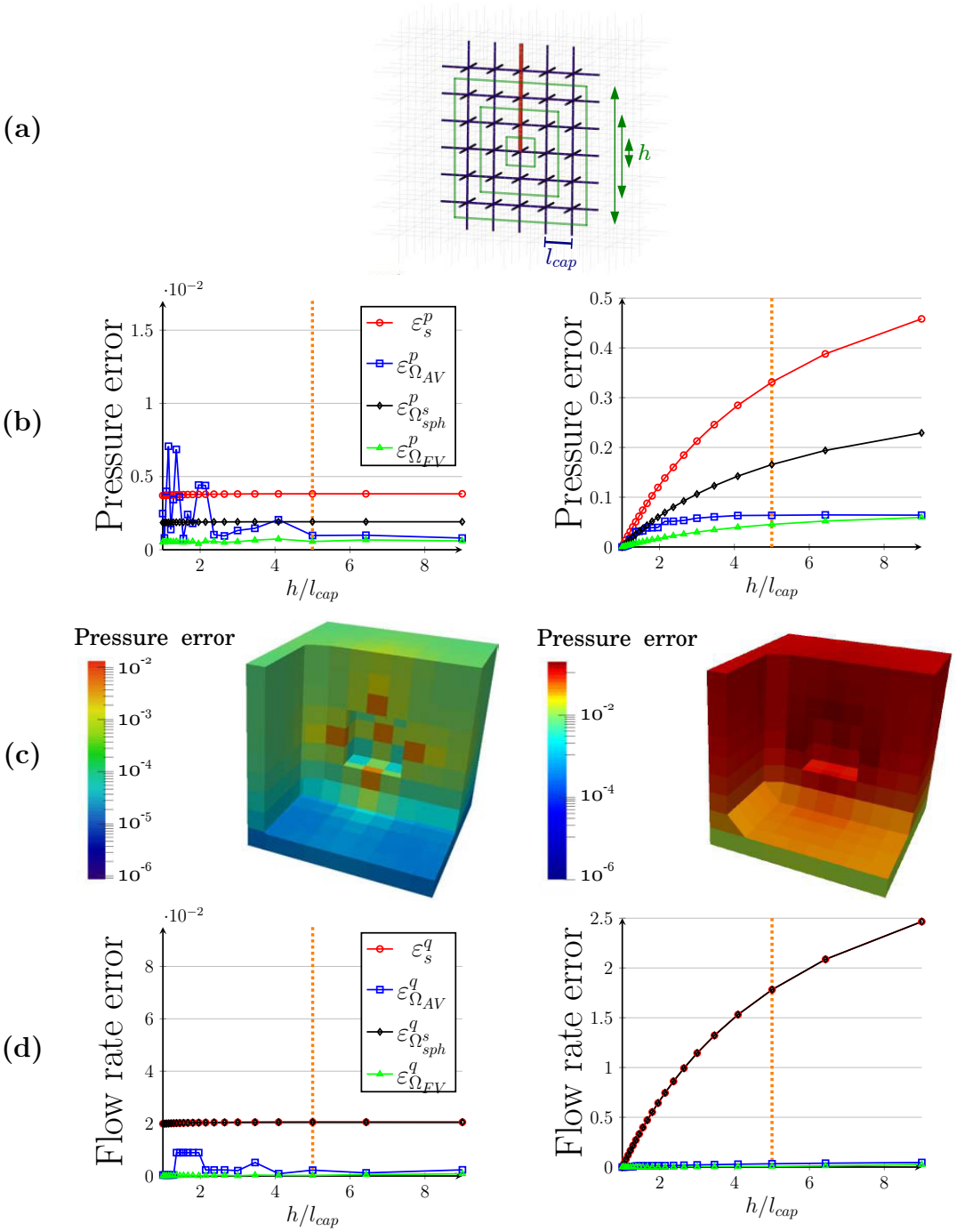

Figure 5.8: **Global pressure and flow rate errors are displayed for the study of *scale separation*. A single arteriole is coupled to a 6-regular capillary network. In the hybrid and SH approaches, the continuum is discretized in coarse FV cells of side h. (a)** *Schematics of the test.* A single coupling is imposed at the center of the coupled cell to study the influence of the ratio h/l_{cap}. **(b)** *Global pressure errors.* Global pressure errors are computed in the four domains of interest defined in Fig. 4.6**(d)**, for both the hybrid **i** and SH **ii** approaches. The errors are normalized by the global pressure drop δP. **(c)** *Distribution of the global pressure errors in the FV domain.* For both the hybrid **i** and SH **ii** approaches, the distributions of the pressure errors are displayed for the ratios h/l_{cap} indicated by orange dotted lines in **(b,d)**. **(d)** *Global flow rate errors.* The flow rate errors are computed in the same four domains of interest, for both the hybrid **i** and SH **ii** approaches. The errors are normalized by the global incoming flow rate q_A.

For comparison, simulations have been run in the same configuration using the SH approach. The results are displayed in Fig. 5.8**ii**. In Fig. 5.8**ii(b)**, the pressure errors are of the same order of magnitude than results presented in Fig. 5.8**i(b)** for the smallest ratio $h/l_{cap} = 1$. Beyond this ratio, all errors related to the SH simulations significantly increase (up to ∼45.8 % for ε_s^p). Further, the distribution of pressure errors in the FV domain (Fig. 5.8**ii(c)**) displays errors in the range [1.22 %; 17.3 %], while they are everywhere lower than 1 % when using the hybrid approach (Fig. 5.8**i(c)**). In Fig 5.8**ii(d)**, the evolution of flow rate errors is critical. While not discernible in this graph, the errors computed in the FV domain slightly increase with the ratio h/l_{cap}, with errors up to 2.5 % and 4.6 % in $\Omega_{FV}^{\varepsilon}$ and $\Omega_{sph}^{s,\varepsilon}$ respectively. By comparison, these error are equal to 0.08 % and 0.23 %, respectively, when using the hybrid approach. Furthermore, the increase in flow rate errors in the arteriolar vessel is dramatic, with errors reaching ∼247 % for large values of h/l_{cap}. Finally, the errors computed from the hybrid simulations remain constant beyond the ratio $h/l_{cap} \geq 4$, while the errors computed from the SH approach highly deteriorate while the side of the FV cells increase. This comparison between the hybrid and SH approaches demonstrates the fact that the multiscale coupling model takes into account the upscaling transition between the arteriolar vessel and the continuum, contrary to the SH approach.

For a ratio $h/l_{cap} = 5$, i.e. $h = 250\,\mu$m, the pressure errors in the capillary medium $\Omega_{\Omega_{FV}}^{\varepsilon}$ are lower than 1% everywhere (Fig. 5.8**i(c)**), showing that the model is highly accurate. Furthermore, the reconstruction of the pressure field using the analytical approximations (Eqs. 4.19 and 4.17) in the vicinity $\Omega_{FV,neigh}^{s}$ of the coupling point is in very good agreement with the reference CN pressure, as displayed in Fig. **5.9(b)**. As expected, the FV representation is accurate beyond two cells away from the coupling but does not describe the strong gradients in $\Omega_{FV,neigh}^{s}$, underestimating the pressure in the coupled cell. The coupling model correctly captures these gradients since the pressures π_{CN} and π_{H} at the coupling point are in very good agreement, with a global error of 0.7 %. By comparison, the difference between these two values is 100 times larger when using the SH approach, with an error of 33 %, as displayed in Fig. 5.9**(b)**. Moreover, because the additional pressure drop building up around the coupling point is not accounted for in SH approach, the pressure in the coupled cell is overestimated (0.39 vs. 1.05 in the hybrid approach, see Fig. 5.9**(b)**). Thus, this local singular pressure drop significantly contributes to the global resistance of the capillary bed, which has been recently shown to dominate the overall intracortical resistance in both human and mice [Lorthois et al., 2011b, Gould et al., 2016]. In other words, this microscopic (or capillary) scale effect, intrinsically linked to the transition between the tree-like arterioles and the mesh-like capillaries, has a huge impact on the pressure field at mesoscopic scale.

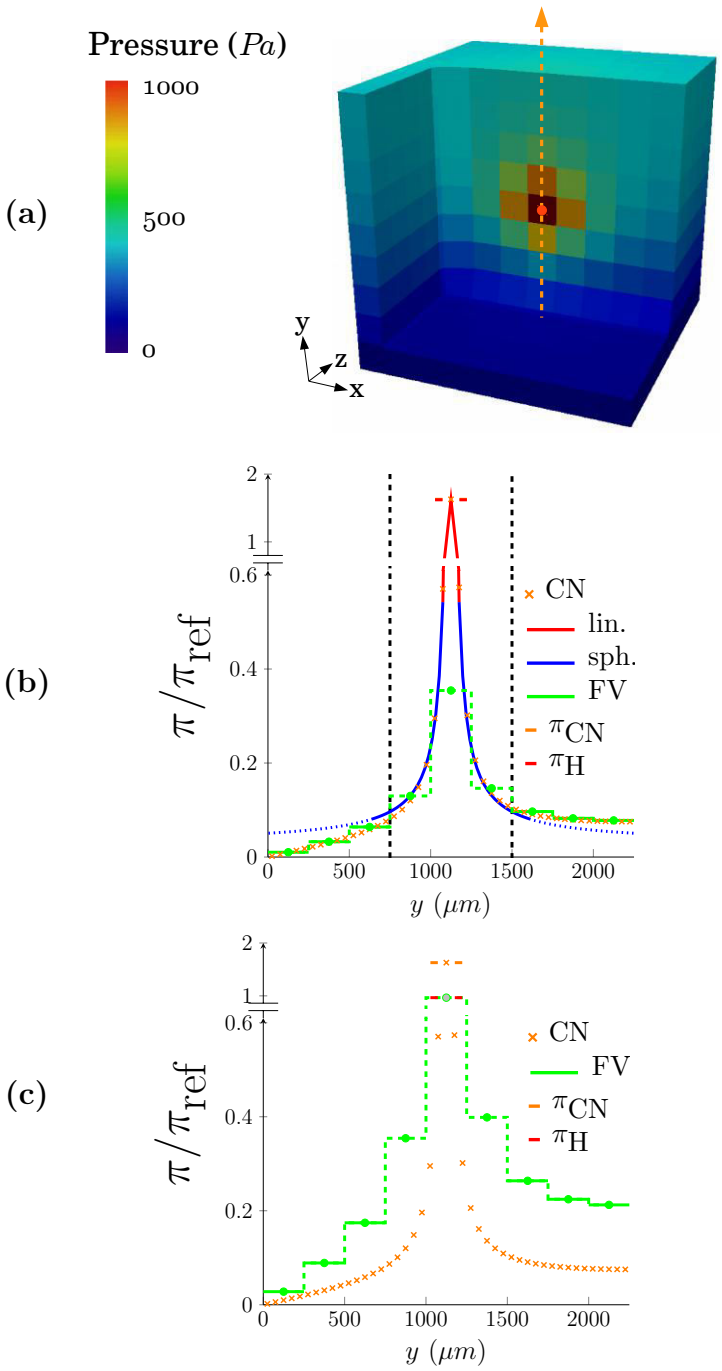

Figure 5.9: **Comparison of pressure fields computed via hybrid and CN approaches.** **(a)** The pressure field is displayed for the configuration involving a single centered coupling between an arteriolar vessel and a 6-regular capillary network. The coupling point is indicated by a large orange dot. **(b)** Pressure profiles resulting from both the CN and hybrid simulations are plotted along a line of interest, which is indicated by orange dashes in **(a)**. The reference pressure field from CN approach is represented by orange crosses. Green steps represent cell pressures of the FV representation, blue and red lines respectively represent linear and spherical approximations. Black dashed lines represent the limit of $\Omega^s_{FV,neigh}$, where pressure field is approximated by analytical solutions. The reconstructed pressure field of the hybrid approach is finally obtained by combining solid lines. The asymmetry of the field far away from the source is caused by the imposed boundary conditions at the limits of the domain. Here $\pi_{\text{ref}} = 5\,000\,\text{Pa}$ is the reference pressure value used for nondimensionalization. **(c)** Pressure profiles resulting from both the CN and SH simulations are plotted along a line of interest, which is indicated by orange dashes in **(a)**. Same color conventions as in **(b)** are adopted.

5.2.3 Off-centering

We now ask whether the off-centering of the arteriolar or venular endpoints in the finite-volume cell affects the accuracy of the result. Off-centering of coupling points can indeed induce asymmetries of the pressure field with regard to the FV grid. To deal with this, we introduce partial sources (Eq 4.37) to distribute the source term among the cells affected by the well model and compare the results with computations where the flow rate is not distributed. In Fig. 5.10, we analyze the impact of the off-centering of a single coupling on the pressure and flow rate errors (Fig. 5.10**(b,d)**) by progressively increasing the distance d_{off} to the FV cell center in the range ${}^{d_{\text{off}}}/_{l_{cap}} \in \left[0.09, {}^{\sqrt{3}}/_{2}\right]$. The ratios ${}^{d_{\text{off}}}/_{l_{cap}} = 0.5$, ${}^{d_{\text{off}}}/_{l_{cap}} = {}^{\sqrt{2}}/_{2}$ and ${}^{d_{\text{off}}}/_{l_{cap}} = {}^{\sqrt{3}}/_{2}$ correspond to extrema of the off-centering with couplings occurring at the intersection between 2, 4 and 8 cells. To make such intersections possible, the continuum is discretized in $10 \times 10 \times 10$ cells, i.e. $h = 225\,\mu$m. In this way, the corners of the FV cells in the hybrid approach coincide with bifurcations of the 6-regular underlying capillary bed in the CN configuration. We see that ignoring the distribution of q_s results in an increase of errors, with errors twice as large in the FV neighbourhood ($\varepsilon^{p}_{\Omega^{s,\varepsilon}_{sph}}$ and $\varepsilon^{q}_{\Omega^{s,\varepsilon}_{sph}}$, plain versus dotted lines in Fig. 5.10).

By reconstructing the analytical approximation of the pressure field in the vicinity of the coupling (Fig. 5.11), we see that the coupling model without distribution of q_s cannot capture the asymmetry of the pressure field. This induces slight over- and underestimations on each side of the coupling point that persist even far away from the source. On the contrary, the reconstructions with q_s distributed are in very good agreement with the reference CN computations.

5.2.4 Boundary effects

Next, we assess the influence of boundary conditions in Fig. 5.12. A single coupling point is initially positioned at the center of the domain (${}^{d_{\text{boundary}}}/_{h} = 4.5$) and progressively brought close to a boundary (${}^{d_{\text{boundary}}}/_{h} = 0.5$) where impermeability conditions have been imposed. Similarly to the first case, $h = 250\,\mu$m here for the purpose of working with centered couplings and avoid potential errors induced by off-centering. Both pressure and flow rate errors (Fig. 5.12**(b,d)**) show that our model is robust provided that at least one cell separates the coupling point from the domain boundary, ensuring that the neighbourhood $\Omega^{s}_{FV,neigh}$ of the coupling point does not intersect it. While the model is less accurate when the coupling occurs in the boundary cell, the increase in errors is small (up to 2.5 % in pressure and 6 % in flow rate).

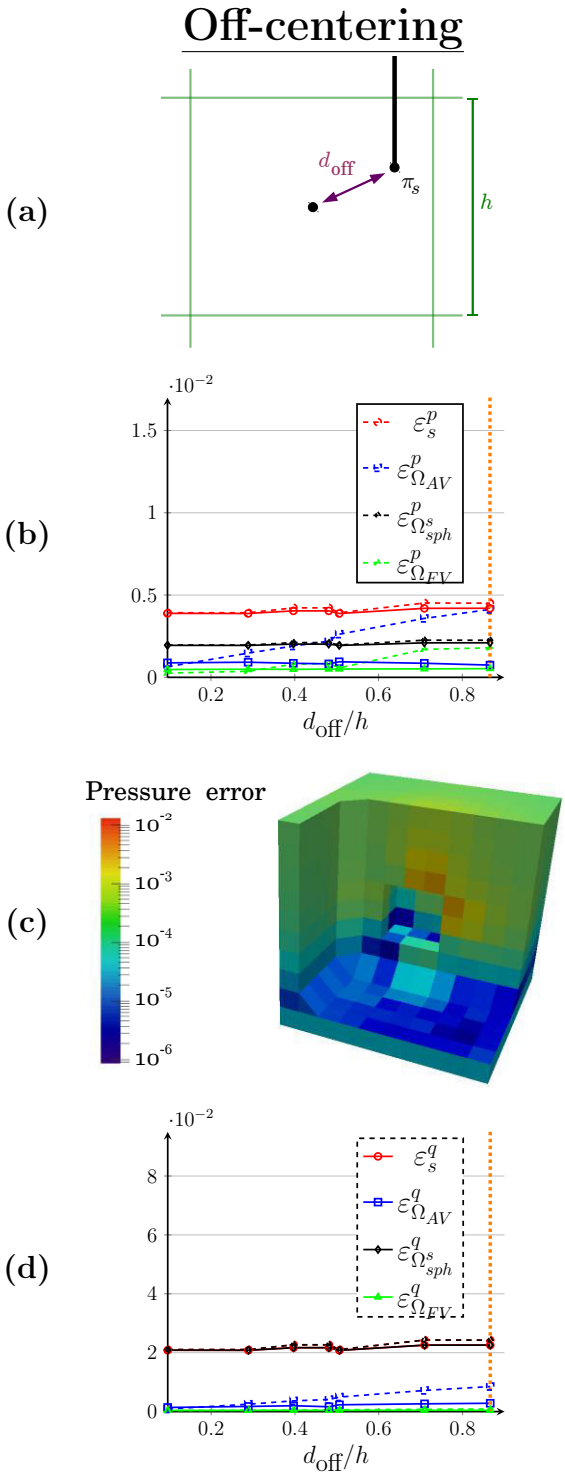

Figure 5.10: **Global pressure and flow rate errors are displayed for the study of *off-centered couplings*. A single arteriole is coupled to a 6-regular capillary network. In the hybrid approach, the continuum is discretized in coarse FV cells of side h.(a)** *Schematics of the test.* A single coupling is imposed in a FV cell, at a distance d_{off} from its center. **(b)** *Global pressure errors.* Global pressure errors are computed in the four domains of interest defined in Fig. 4.6**(d)**. The errors are normalized by the global pressure drop δP. **(c)** *Distribution of the global pressure errors in the FV domain.* The distributions of the pressure errors are displayed for the ratios h/l_{cap} indicated by orange dotted lines in **(b,d)**. **(d)** *Global flow rate errors.* The flow rate errors are computed in the same four domains of interest. The errors are normalized by the global incoming flow rate q_A.

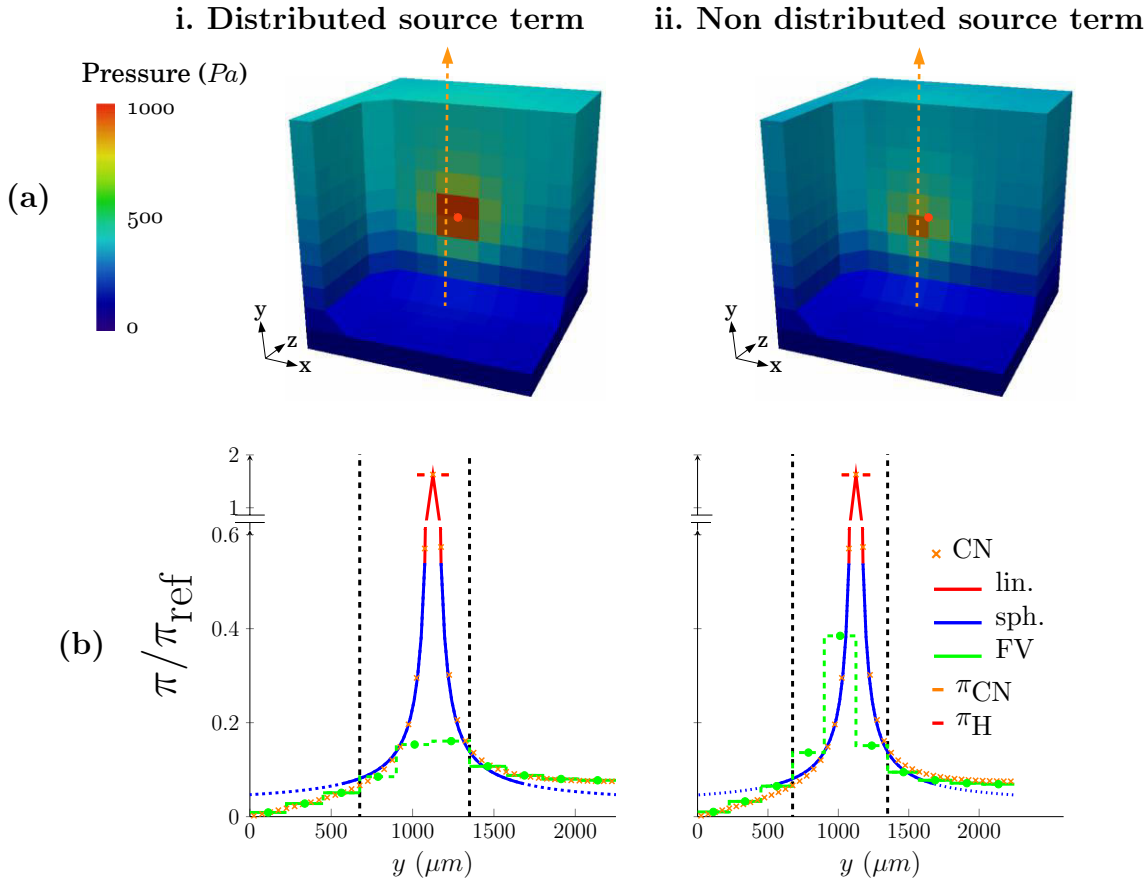

Figure 5.11: **Comparison of pressure fields computed via hybrid and CN approaches. (a)** The pressure fields are displayed for the configuration involving a single off-centered coupling between an arteriolar vessel and a 6-regular capillary network, with (**i**) or without (**ii**) the distribution of the source term among the neighbouring cells impacted by the coupling (Eq. 4.37). The coupling point is indicated by a large orange dot. **(b)** Pressure profiles resulting from both the CN and hybrid simulations are plotted along a line of interest, which is indicated by orange dashes in **(a)**. The reference pressure field from CN approach is represented by orange crosses. Green steps represent cell pressures of the FV representation, blue and red lines respectively represent linear and spherical approximations. Black dashed lines represent the limit of $\Omega^s_{FV,neigh}$, where pressure field is approximated by analytical solutions. The reconstructed pressure field of the hybrid approach is finally obtained by combining solid lines. The asymmetry of the field far away from the source is caused by the imposed boundary conditions at the limits of the domain. Here $\pi_{\text{ref}} = 5\,000\,\text{Pa}$ is the reference pressure value used for nondimensionalization.

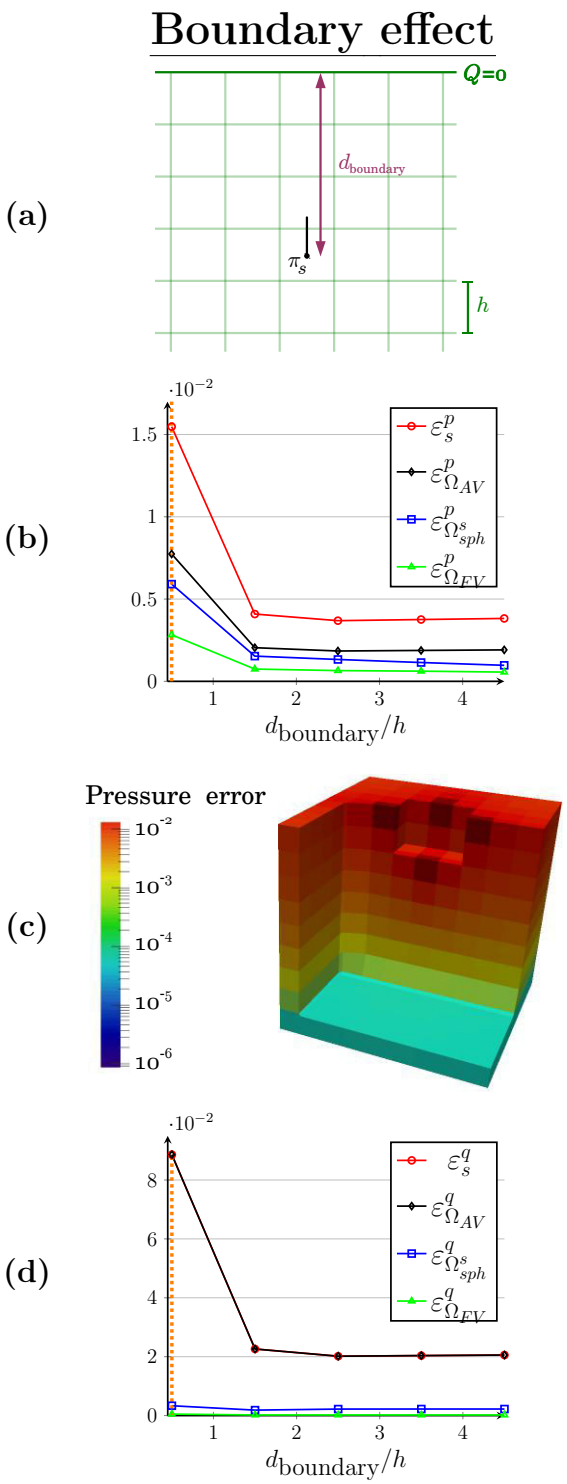

Figure 5.12: **Global pressure and flow rate errors are displayed for the study of *boundary effects*. A single arteriole is coupled to a 6-regular capillary network. In the hybrid approach, the continuum is discretized in coarse FV cells of side h.(a)** *Schematics of the test.* A single coupling is imposed at the center of the coupled cell to study the influence of the ratio h/l_{cap}. **(b)** *Global pressure errors.* Global pressure errors are computed in the four domains of interest defined in Fig. 4.6**(d)**. The errors are normalized by the global pressure drop δP. **(c)** *Distribution of the global pressure errors in the FV domain.* The distributions of the pressure errors are displayed for the ratios h/l_{cap} indicated by orange dotted lines in **(b,d)**. **(d)** *Global flow rate errors.* The flow rate errors are computed in the same four domains of interest. The errors are normalized by the global incoming flow rate q_A.

5.2.5 Interaction between several couplings

The multiscale coupling model presented in this work is linear, meaning that each coupling is blind to the others. In this section, we want to assess the robustness of this strategy when several couplings are located in the same FV neighbourhood, i.e. in neighbouring cells or even in the same cell. This robustness is essential since the density of coupling points can be locally very large in the human cortex (Fig. 3.1).

First, we study in Fig. 5.13**i** the impact of the distance between an arteriolar coupling and a venular coupling on results. Initially separated by 9 cells of side $h = 250\,\mu$m ($d_{AV}/h = 9$), the two couplings are brought closer together until they are in neighbouring cells ($d_{AV}/h = 1$). In Fig. 5.13**i(b,d)**, both pressure and flow rate errors show that the hybrid approach is in very good agreement with the CN reference solution, even for short distances that break the spherical symmetry of the pressure field. For the ratio $d_{AV}/h = 1$, the strong decrease of errors can be explained by the fact that each coupled cell belongs to the neighbourhood $\Omega^s_{FV,neigh}$ of the other one. In this case, a shunt appears at the scale of the FV cells and the pressure field is uniform outside the coupling region.

In Fig. 5.13**ii**, we study the impact of the number of couplings randomly located in one FV cell for a ratio $h/l_{cap} = 5$. The results displayed in Fig. 5.13**ii(b,d)** are errors averaged over the number of couplings (from 2 to 10) and the number of generations for a given number of couplings (100 generations). The pressure errors distribution in Fig. 5.13**ii(c)** has been displayed for 8 couplings, for a randomly selected simulation among the corresponding 100 generations. With regard to pressure errors, the graph in Fig. 5.13**ii(b)** shows that errors increase with the number of couplings, especially in the FV neighbourhood ($\varepsilon^p_{\overline{\Omega}^{s,\varepsilon}_{sph}}$ and $\varepsilon^p_{\Omega_{FV}}$). In this specific configuration with no flow occurring in the FV domain, this increase homogeneously affects the whole continuum since the pressure errors are uniform in this domain, as displayed in Fig. 5.13**ii(c)**. However, errors cumulate in a non critical way since no error larger than 3 % is reported. With regard to flow rate errors, the model is very accurate in describing the flow rate fields in the FV neighbourhood ($\varepsilon^q_{\overline{\Omega}^{s,\varepsilon}_{sph}}$ and $\varepsilon^q_{\Omega_{FV}}$). In the arteriolar and venular vessels (ε^q_s and $\varepsilon^q_{\Omega_{AV}}$), means and standard deviations both decrease with the number of couplings, due to the normalization of errors by the global inlet flow rate. Indeed, contrary to the global pressure drop that remains constant, the global inlet flow rate increases with the number of couplings.

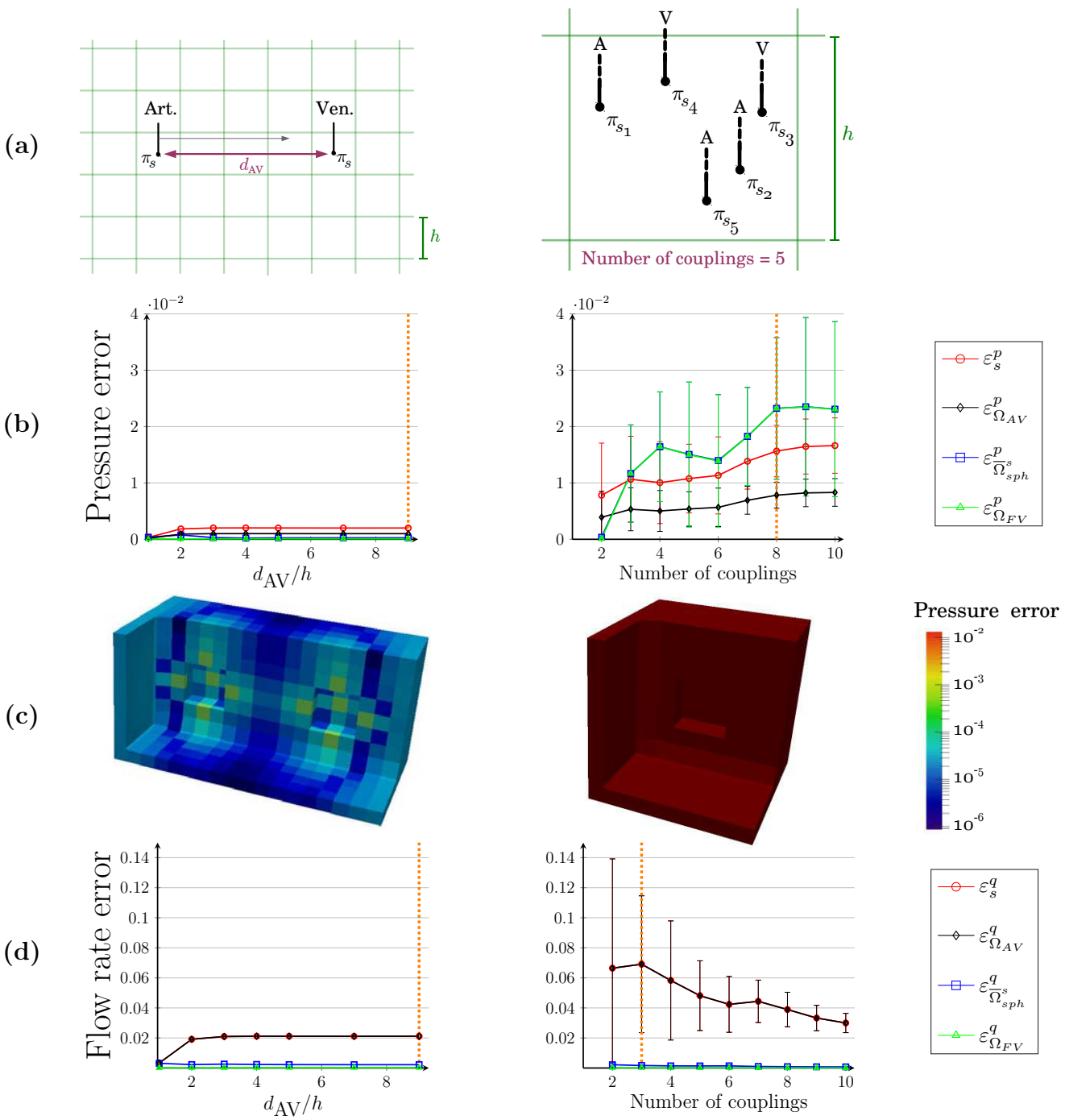

Figure 5.13: **Interaction between several couplings. Global pressure and flow rate errors are displayed for two basic tests involving several arteriolar and venular vessels coupled to a 6-regular capillary network. In the hybrid approach, the continuum is discretized in coarse FV cells of side h.** **(a)** *Schematics of the tests.* In the configuration **i**, an arteriolar and a venular vessels are coupled at the center of two separate cells to study the influence of the distance d_{AV} between the two couplings. In the configuration **ii**, from 2 to 10 couplings are located in a single FV cell. Their locations and types (arteriolar or venular) are pseudo-random. **(b)** *Global pressure errors.* For each configuration, global pressure errors are computed in the four domains of interest defined in Fig. 4.6**(d)**. The errors are normalized by the global pressure drop δP. **(c)** *Distribution of the global pressure errors in the FV domain.* The distributions of the pressure errors are displayed for the ratios h/l_{cap} indicated by orange dotted lines in **(b,d)**. **(d)** *Global flow rate errors.* The flow rate errors are computed in the same four domains of interest. The errors are normalized by the global incoming flow rate q_A.

5.2.6 Summary

For comparison, the results presented in Section 5.2 are summarized in Fig. 5.14. The errors reported correspond to the orange dashed lines displayed on each previous graphs (Figs. 5.8, 5.10, 5.12 and 5.13). Each of these values have been chosen because they are representative of each study.

With regard to pressure errors, the hybrid approach shows very good agreement with the CN approach, with no error larger than 3 %. The largest errors are observed for the "Multi-coupling" study, suggesting that the accuracy of the reconstruction of the pressure field in the continuum is limited by the density of couplings per cell. This limitation does not appear when couplings occur in separate FV cells (see "Two couplings" configuration in Fig. 5.14).

With regard to flow rate errors, the accuracy of the model is mainly limited by boundary effects, with errors up to 9 % in the "Boundary effect" configuration in Fig. 5.14. As mentioned above, the "Multi-coupling" configuration also highlights the dependence of the accuracy of the reconstructed flow rate field upon the density of couplings per FV cell.

What we must remember from Section 5.2:

- by contrast with a simple condition of pressure continuity, the multiscale coupling model captures microscopic scale effects in the vicinity of couplings, yielding an accurate description of the pressure field at mesoscopic scale;
- the coupling model is robust for a ratio $h/l_{cap} \geq 4$;
- the coupling model is robust to off-centering when distributing partial source terms among the neighbouring FV cells (Eq 4.37);
- the coupling model is less accurate when coupling is located in boundary FV cells;
- the close distance between two couplings located in separate FV cells does not affect the accuracy of the hybrid approach;
- the description of the pressure field in the FV domain is sensitive to high density of couplings per cell.

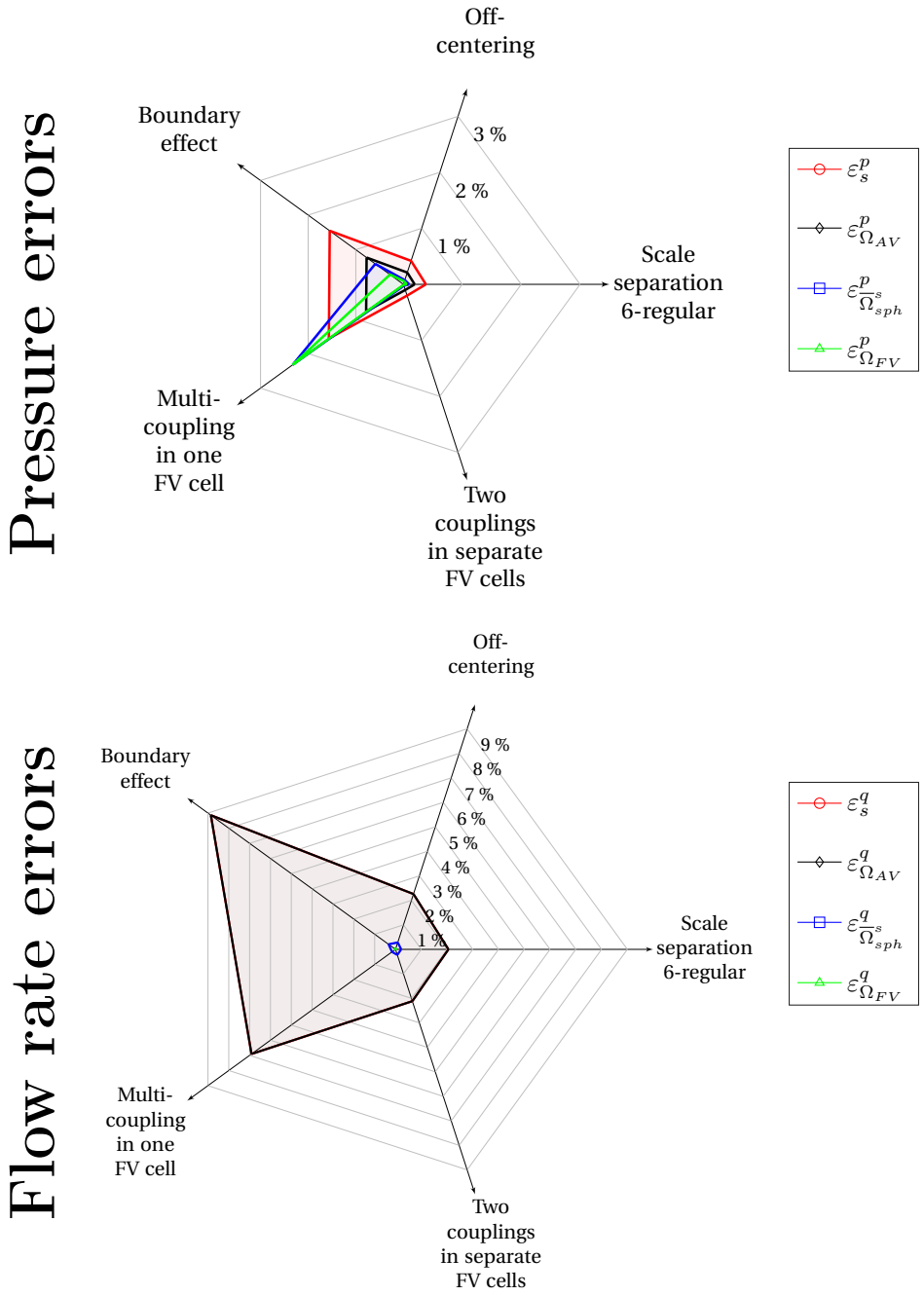

Figure 5.14: **Summary of errors presented in Section** 5.2**.** Pressure and flow rate errors have been computed all along the Section 5.2 for five different configurations reported at the circumference of the diagram (Scale separation, Off-center, etc). Representative or extreme values have been selected and indicated by orange dashed lines in each indivual graph of Figs. 5.8, 5.10, 5.12 and 5.13. They are reported here and combined in a same diagram.

5.3 Extension to more realistic networks

All the tests presented in Section 5.2 involved 6-regular capillary networks with uniform diameter for the purpose of avoiding any uncertainties related to the computation of effective parameters (details in Section 5.1.3). Furthermore, the arteriolar and venular components were represented by isolated cylinders to avoid treating complex tree-like architecture. Here we introduce additional levels of complexity with regard to the representations of both the capillary network and the arteriolar and venular trees.

5.3.1 Morphometrical complexification of the capillary bed

Here, we study simple configurations involving one arteriolar vessel coupled with a 6-regular capillary network of side 2.25 mm, as presented in Section 5.2.1, but adding two complexifications to the capillary bed.

First, according to the paper of Lauwers *et al.* [Lauwers et al., 2008], the diameters of capillaries in human brain microcirculation are distributed, following a Gaussian law with mean 5.91 μm and standard deviation 1.30 μm. In the first configuration of this section, we introduce this diameter distribution in the 6-regular lattice to investigate the impact of such microscopic variations on the accuracy of the coupling model. The corresponding effective permeability and viscosity have been reported in Table 2.

Second, the closest region of the largest arteriolar vessels is known to be non-vascularized [Blinder et al., 2013, Sakadžić et al., 2014], as illustrated in Fig. 5.15. As mentioned in Section 2, these perivascular gaps are termed Virshow-Robin (VR) spaces. In the second configuration of this section, we represent this depleted zone by removing all capillaries in a radial distance $d \leq 50\,\mu$m [Kasischke et al., 2011] around the arteriolar vessel, as displayed in Fig. 5.16**iii(a)**. For this study, the capillary diameters are uniform ($d_{cap} = 5.91\,\mu$m).

In both configurations, the boundary conditions are similar to those defined in Section 5.2.1 for single couplings (see Fig. 5.5).

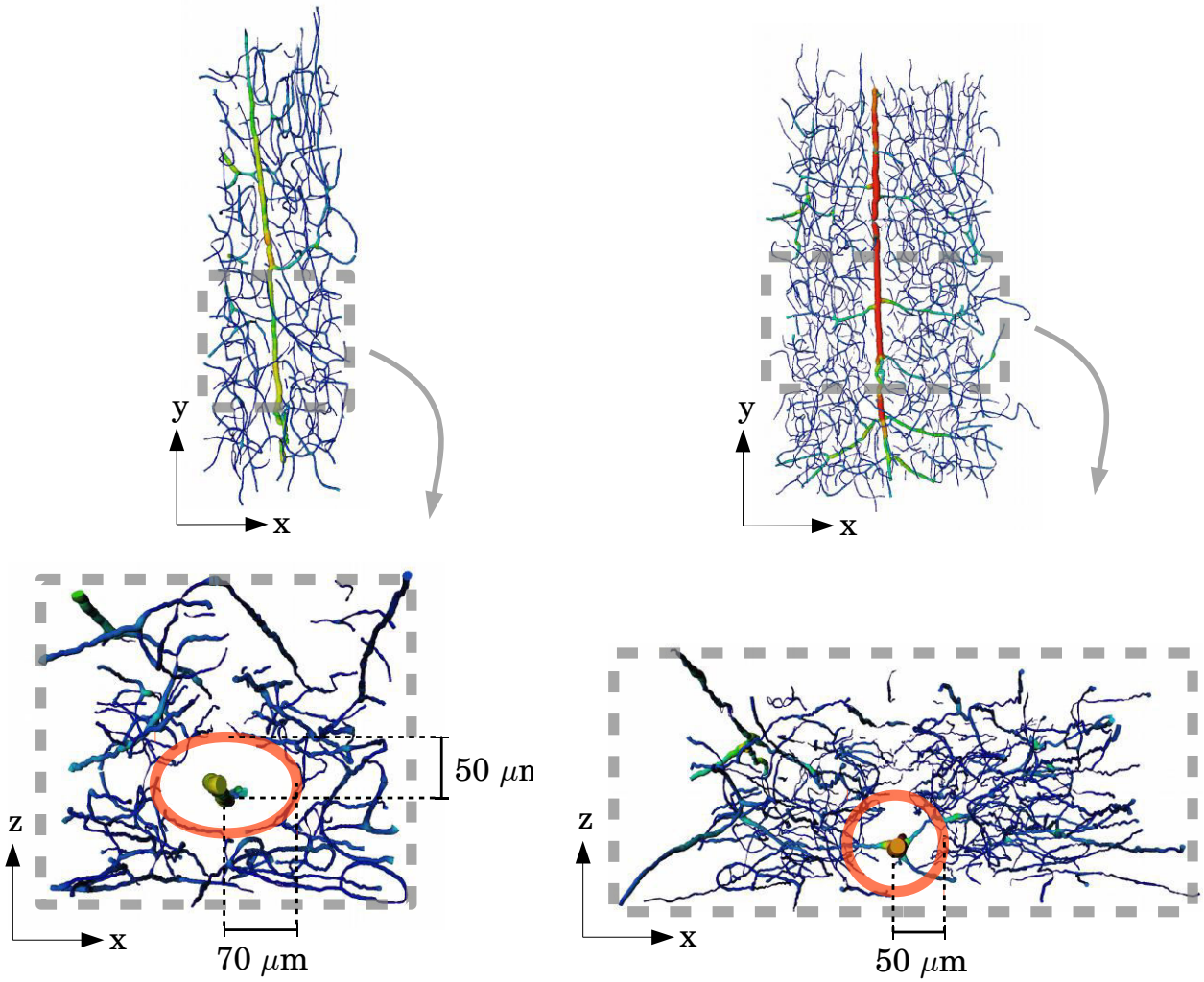

(a) Arteriole **(b) Venule**

Figure 5.15: **Illustration of the Virshow-Robin space around largest arterioles and venules.** Two regions of interest have been extracted from a human anatomical dataset: **(a)** around an arteriole, and **(b)** around a venule. The colormap corresponds to vessel diameters. In both cases, we observe a non-vascularized area up to a radial distance of ~ 50 μm around the arteriole and venule.

In this section, we study whether these complexifications have an impact on the ratio h/l_{cap} over which our model is valid, i.e. on the scale separation. For that purpose, both pressure and flow rate errors are displayed against the ratio h/l_{cap} in Fig. 5.16. As expected, the FV domain $\Omega^{s,\varepsilon}_{sph}$ is the most sensitive, displaying variations until complying the assumption of a sufficiently coarse FV grid, i.e. a ratio h/l_{cap} sufficiently large to ensure the validity of the coupling model. As a reference, the similar study led for 6-regular networks (Section 5.2.2) has been reported in Fig. 5.16**i** for comparison. As a reminder, the validity of our model has been established for $h/l_{cap} \geq 4$ in this study. This threshold will only slightly vary if our model is robust.

In Fig. 5.16**ii(b,d)**, pressure and flow rates errors are averaged over 100 simulations involving 100 different diameter distributions. In Fig. 5.16**ii(c),** the pressure errors distribution has been displayed for a ratio $h/l_{cap} = 5$, for a randomly selected simulation among the 100 realisations. The mean errors show trends similar to the reference (Fig. 5.16**i(b,d)**), with a convergence threshold for a ratio $h/l_{cap} \sim 4$. Thus the introduction of diameters distribution in the capillary bed does not question the validity of the coupling model for $h/l_{cap} \geq 4$. Furthermore, the pressure errors show very good agreement between the hybrid and CN approaches, with no error values larger than 2 %. However, the errors are all about four times larger than the reference ones, highlighting the limitation of the effective parameters in describing microscopic variations of the capillary structure at mesoscopic scale. The flow rate errors even reach 8 % in the arteriolar vessel, with an important standard deviation. However, these value corresponds to the reliability of typical perfusion imaging techniques, which is estimated at ∼10 % [Wintermark et al., 2005]. Furthermore, comparison with SH simulations run for the same configuration (Fig. 5.17) highlights the benefit of our approach. In Fig. 5.17**(a)**, the pressure errors are of the same order of magnitude than results presented in Fig. 5.16**iii(b)** for the smallest ratio $h/l_{cap} = 1.35$. Beyond this ratio, all errors related to the SH simulations significantly increase (up to ∼44 % for ε^p_s). In Fig 5.17**(b)**, the evolution of flow rate errors is critical. While not discernible in this graph, the errors computed in the FV domain slightly increase against the ratio h/l_{cap}, with errors up to 5.6 % and 6.08 % in $\Omega^{\varepsilon}_{FV}$ and $\Omega^{s,\varepsilon}_{sph}$ respectively. Furthermore, the increase in flow rate errors in the arteriolar vessel is dramatic, with errors reaching ∼228 %. Finally, the flow rate error of ∼8 % reported in Fig. 5.16**iii(b)** can be tempered. However, the way such errors cumulate will be investigated in Section 5.4, where a realistic configuration involving multiple couplings will be presented.

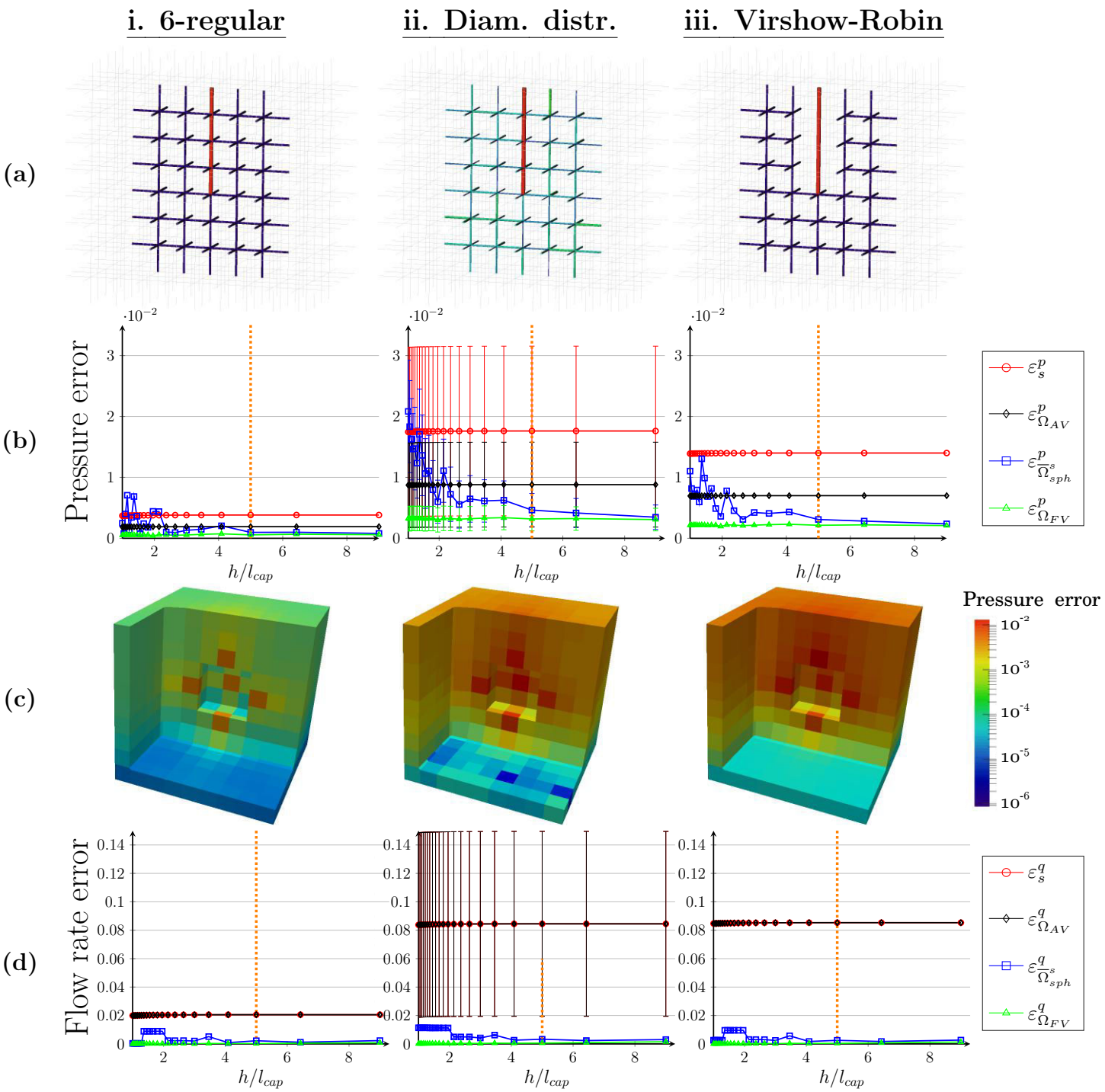

Figure 5.16: **Complexification of the structure of the capillary bed. Global pressure and flow rate errors are displayed for three basic tests involving only one arteriolar vessel coupled to a 6-regular capillary network. In the hybrid approach, the continuum is discretized in coarse FV cells of side h. (a)** *Schematics of the tests.* The configuration **i** is the same as in Fig. 5.8**i**, as a recall for comparison with the two other configurations. In configuration **ii**, the capillary diameters are distributed, following a Gaussian law. In the configuration **iii**, the capillaries close to the arteriolar vessel are removed to represent the Virshow-Robin space. **(b)** *Global pressure errors.* For each configuration, global pressure errors are computed in the four domains of interest defined in Fig. 4.6**(d)**. The errors are normalized by the global pressure drop δP. **(c)** *Distribution of the global pressure errors in the FV domain.* The distributions of the pressure errors are displayed for the ratios h/l_{cap} indicated by orange dotted lines in **(b,d)**. **(d)** *Global flow rate errors.* The flow rate errors are computed in the same four domains of interest. The errors are normalized by the global incoming flow rate q_A.

In Fig. 5.16**iii(b,d)**, pressure and flow rate errors are displayed for the configuration taking into account the VR perivascular space around the arteriole. Similarly to the previous case, the introduction of a non-vascularized region around the arteriolar vessel does not affect the validity of the coupling model for a ratio $h/l_{cap} \geq 4$, and the hybrid approach shows good agreement with the CN simulations, with no pressure error larger than 1.5 %. While flow rate errors reach 8 % in the arteriolar vessel, this result can also be tempered by comparison with SH simulation run for the same configuration (Fig. 5.18). The conclusion is similar to the one presented above. In Fig. 5.18**(a)**, the pressure errors are of the same order of magnitude as the results presented in Fig. 5.16**iii(b)** for the smallest ratio $h/l_{cap} = 1.35$. Beyond this ratio, all errors related to the SH simulations significantly increase (up to ∼48 % for ε_s^p). In Fig 5.18**(b)**, the evolution of flow rate errors are critical. The errors computed in the FV domain slightly increase against the ratio h/l_{cap}, with errors up to 2.97 % and 5.44 % in Ω_{FV}^{ϵ} and $\overline{\Omega}_{sph}^{s}$ respectively. Furthermore, the increase in flow rate errors is dramatic, with errors reaching ∼293 % in the arteriolar vessel. Again, the cumulation of such errors will be investigated in Section 5.4, where a realistic configuration involving multiple couplings will be presented.

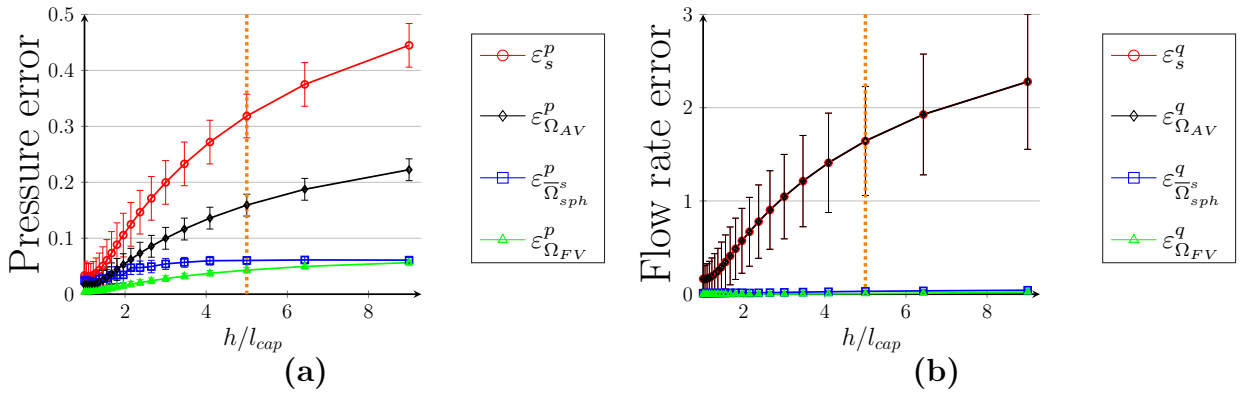

Figure 5.17: **Global pressure and flow rate errors computed by comparing SH and CN approaches in the configuration involving a single arteriolar vessel coupled to a *6-regular network with distributed diameters*. The errors are averaged over 100 realisations involving different diameter distributions. (a)** Global pressure errors are computed in the four domains of interest defined in Fig. 4.6**(d)**, and normalized by the global pressure drop δP. **(b)** Global flow rate errors are computed in the same four domains of interest, and normalized by the global incoming flow rate q_A.

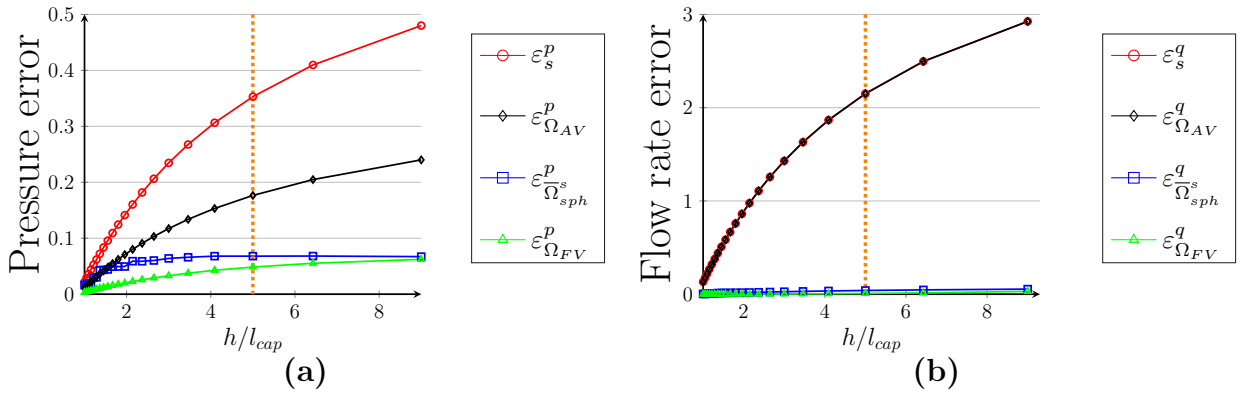

Figure 5.18: **Global pressure and flow rate errors computed by comparing SH and CN approaches in configuration involving a single arteriolar vessel coupled to a *Voronoi-like network*.** **(a)** Global pressure errors are computed in the four domains of interest defined in Fig. 4.6**(d)**. The errors are normalized by the global pressure drop δP. **(b)** Global flow rate errors are computed in the same four domains of interest. The errors are normalized by the global incoming flow rate q_A.

5.3.2 Topological complexification of the capillary bed

For the purpose of investigating the impact of topologically realistic capillary networks on the robustness of the hybrid approach, we continue to study simple configurations involving only one arteriolar vessel, as presented in Section 5.2.1. However, the arteriolar vessel is now coupled here to either 3-regular or Voronoi-like capillary networks. Contrary to 6-regular networks, both 3-regular and Voronoi-like networks respect the physiological 3-connectivity of healthy capillary networks. The Voronoi-like networks further present a realistic non-periodic organization.

In the case of a 3-regular capillary network, the domain is of side 2.25 mm, and the length of a capillary is $l_{cap} = 30.43\,\mu m$ so they present the same vascular density as 6-regular networks (see Appendix 8.4). In Voronoi-like networks, the domain side is 2.24 mm, and $l_{cap} = 36.75 \pm 24.9\,\mu$m. The effective parameters corresponding to these networks have been summarized in Table 2 for both uniform and distributed diameters. For all configurations presented in this section, the boundary conditions are similar to those defined in Section 5.2.1 for single couplings (see Fig. 5.5).

In Fig. 5.19, both pressure and flow rate errors are displayed against the ratio h/l_{cap}. As a recall, the results presented in Section 5.2.2 for scale separation in 6-regular networks with uniform diameter is also displayed in Fig. 5.19**i**. As expected, the FV domain $\Omega^{s,\varepsilon}_{sph}$ is the most sensitive in all configurations, displaying high variations until complying the assumption of a sufficiently coarse FV grid, i.e. a ratio h/l_{cap} sufficiently large to ensure the validity of the coupling model.

In Fig. 5.19**ii**, the error graphs for a 3-regular capillary network show the same trend as the results in 6-regular networks. While the error variations reach higher peaks, they also converge for a ratio of $\sim$4. Such a result shows two things: first, the microscopic details of the capillaries connected to the coupling point are accurately taken into account in the multiscale coupling model; second, the computation of effective properties of the 3-regular network (Section 5.1.3) are very accurate in describing the microscopic capillary vasculature.

In Fig 5.19**iii**, the arteriolar vessel is coupled to a random Voronoi-like capillary network. With regard to the pressure field, we observe an increase in errors in the arteriole (errors ε^p_s and ε^p_{AV} in Fig. 5.19**iii(b)**) compared to the results in 6- or 3-regular networks. However, this increase is reasonable since the pressure error ε^p_s at the coupling point is only 1.5 %. In Fig. 5.19**iii(c)**, the distribution of pressure errors for $h/l_{cap=5}$ shows important variations from one FV cell to another. Such variations also appeared in previous test cases, but according to a spherical pattern around the coupling point. Here, the randomness of the variations in pressure errors suggests that the uniform effective parameters computed in Section 5.1.3 do not describe very accurately the microscopic capillary vasculature.

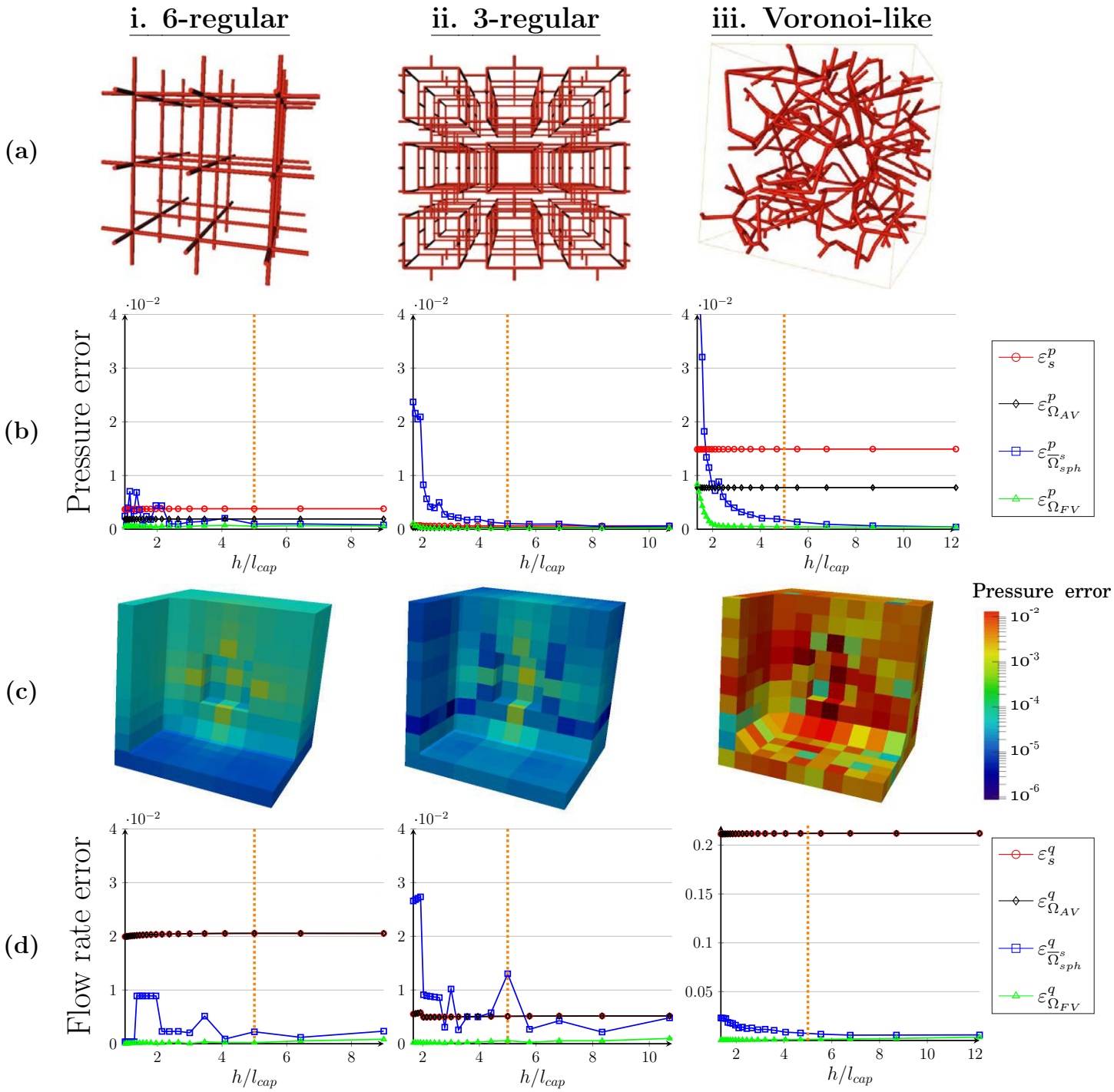

Figure 5.19: **Complexification of the topology of the capillary bed. Global pressure and flow rate errors are displayed for three basic tests involving only one coupling but several capillary architectures. In the hybrid approach, the continuum is discretized in coarse FV cells of side h.** **(a)** *Schematics of the tests.* The configuration **i** is the same as in Fig. 5.8**i**, as a recall for comparison. In configuration **ii**, a single arteriolar vessel is coupled with a 3-regular capillary network. In the configuration **iii**, the arteriolar vessel is coupled to a Voronoi-like capillary network. **(b)** *Global pressure errors.* For each configuration, global pressure errors are computed in the four domains of interest defined in Fig. 4.6**(d)**. The errors are normalized by the global pressure drop δP. **(c)** *Distribution of the global pressure errors in the FV domain.* The distributions of the pressure errors are displayed for the ratios h/l_{cap} indicated by orange dotted lines in **(b,d)**. **(d)** *Global flow rate errors.* The flow rate errors are computed in the same four domains of interest. The errors are normalized by the global incoming flow rate q_A.

In other words, the complex structure of Voronoi-like patterns may induce slight heterogeneities that uniform effective parameters fail at capturing at mesoscopic scale. While the increase in pressure errors is reasonable, the increase in flow rate errors is less satisfying since flow rate errors reach 20 % in the arteriole (ε_s^q and ε_{AV}^q in Fig. 5.19**iii(d)**). Such an error is larger than the estimation of the accuracy of typical perfusion imaging techniques (∼10 %), but remains in the same order of magnitude. For comparison, the same configuration has been used to simulate blood flow using the SH approach, where a simple condition of pressure continuity is imposed at the coupling point. The resulting pressure and flow rate errors are presented in Fig. 5.20. In Fig. 5.20**(a)**, the pressure errors are of the same order of magnitude than results presented in Fig. 5.19**iii(b)** for the smallest ratio $h/l_{cap} = 1.35$. Beyond this ratio, all errors significantly increase (up to 33 % for ε_s^p). In Fig 5.20**(b)**, the evolution of flow rate errors is critical. While not discernible in this graph, the errors computed in the FV domain slightly increase against the ratio h/l_{cap}, with errors up to 4.96 % and 9.10 % in $\Omega_{FV}^{\varepsilon}$ and $\overline{\Omega}_{sph}^{s}$ respectively. Furthermore, the increase in flow rate errors in the arteriolar vessel is dramatic, with errors reaching ∼500 %. Finally, even if the microscopic complexity of Voronoi-like patterns induces difficulties to describe them at mesoscopic scale, the computation of flow using the hybrid approach is much more reliable than SH simulations. To more accurately take into account heterogeneities of the capillary structure in our approach, both the FV scheme and the multiscale coupling model could be adapted (see discussion in Section 7).

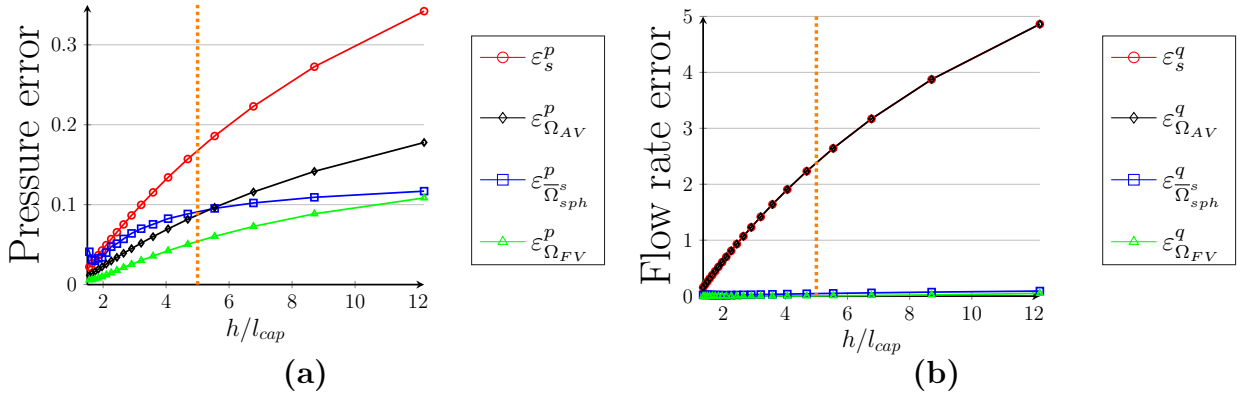

Figure 5.20: **Global pressure and flow rate errors computed by comparing SH and CN approaches in configuration involving a single arteriolar vessel coupled to a Voronoi-like network.** **(a)** Global pressure errors are computed in the four domains of interest defined in Fig. 4.6**(d)**. The errors are normalized by the global pressure drop δP. **(b)** Global flow rate errors are computed in the same four domains of interest. The errors are normalized by the global incoming flow rate q_A.

5.3.3 Complexification of the arterio-venular structures

In all the previous tests, the arteriolar and venular components have been represented by isolated vessels. In this section, we consider the anatomical arteriole displayed on the left-hand side of the Fig. 3.1 (see also Fig. 5.22 below). Such a configuration implies that the flow field between the coupling sites interact not only via the continuum, but also via the network structure. Furthermore, this arteriolar tree displays a high density of coupling points, with a total of 61 endpoints to couple with the continuum. It also involves a large range of vascular diameters from 34 μm at the inlet to 10 μm at the coupling sites.

The transition between the arteriolar/venular component and the capillary bed is usually established for a vessel diameter of $\sim$10 μm [Lorthois and Cassot, 2010], when the tree-like structure of the microvasculature connects to the space-filling mesh-like capillary network. However, the resolution of typical imaging techniques does not always ensure the reconstruction of the arteriolar and venular trees down to the scale of capillaries. In particular, the description of the first capillaries connected to a coupling site, which is required to build the linear approximation in the coupling model (Eq. 4.22), is not ensured.

In this section, we want to investigate two options to deal with this issue (see Fig. 5.21):

- option 1 (Fig. 5.21**(a)**): we define the coupling points at the very end of the arteriolar tree and use statistical values of the capillary bed (e.g. mean length and diameter) to describe the capillary neighbourhood of the coupled endpoints of the arteriolar tree, i.e. to define l_Γ and R_Γ in Eqs. 4.33 and 4.34;
- option 2 (Fig. 5.21**(b)**): we define the coupling points one bifurcation upstream from the very end points of the arteriolar tree and use the description of the terminal arteriolar component to describe the vascular neighbourhood of the coupling site, i.e. to define l_Γ and R_Γ in Eqs. 4.33 and 4.34.

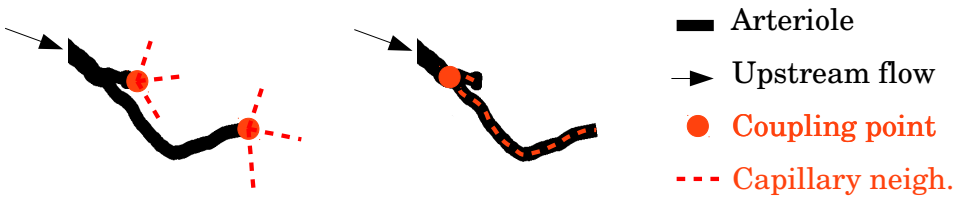

(a) Option 1 **(b) Option 2**

Figure 5.21: **How dealing with the truncation of arteriolar and venular structures? (a)** Option 1: the capillary neighbourhood (dotted red line) is statistically estimated. **(b)** Option 2: the coupling point (red dot) is defined one bifurcation upstream and the end vessels are used as the description of the capillary neighbourhood (dotted red line).

For that purpose, a hierarchical index is assigned to each vessel of the arteriolar tree according to the distance, i.e. the number of bifurcations, from the inlet. To investigate the robustness of each option, the idea is to progressively truncate the arteriolar tree by imposing a maximal hierarchical index. At each truncation, the information about the end arteriolar vessel removed is kept for the description of the vascular neighbours when using option 2.

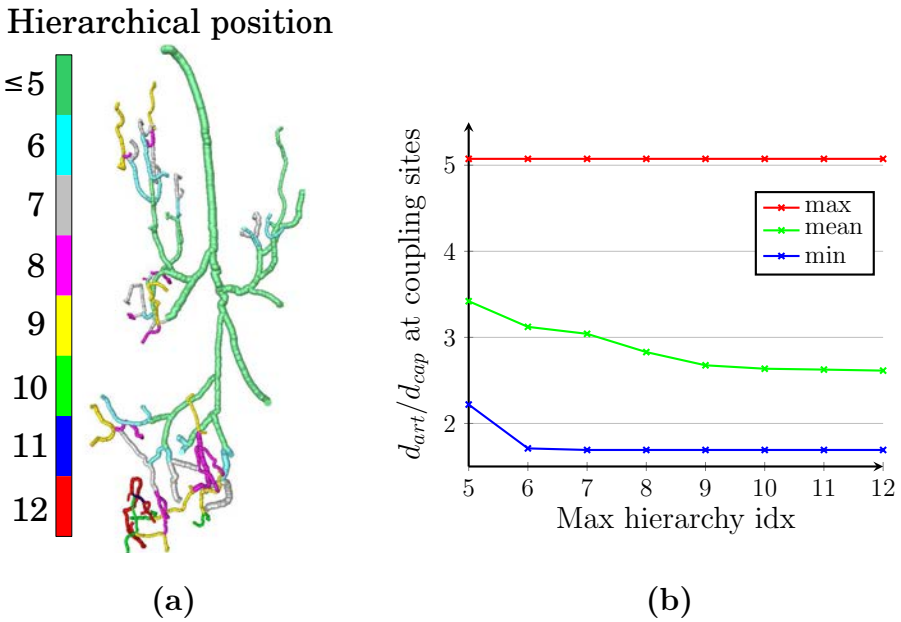

Figure 5.22: **Schematics of hierarchical organization of an anatomical arteriolar tree.** A hierarchical index is assigned to each vessel according to the distance, i.e. the number of bifurcations, from the inlet. **(b)** When truncating the tree by imposing a maximal hierarchical index, the vessel diameters vary at couplings sites. Here are displayed the mean (green), minimal (blue) and maximal (red) vessel diameters at coupling sites according to the maximal hierarchical index imposed.

For comparison with a CN simulation, we consider the configuration where the whole arteriolar tree, i.e. described down to the highest hierarchical index, is coupled to a 6-regular network of $2 \times 3 \times 1.25$ mm^3, containing about 190 000 vessels with uniform diameter ($d_{cap} = 5.91\,\mu$m). Thus the statistical data used in option 1 will be $l_{cap} = 50\,\mu$m and $d_{cap} = 5.91\,\mu$m. The boundary conditions are similar to those defined in Section 5.2.1 for multiple couplings (see Fig. 5.6). The results are presented in Fig. 5.23 for both options presented in Fig. 5.21. Before commenting them, it is worth noting that several perturbations are combined in this configuration, e.g. off-centering and multi-coupling (up to 8 coupling in one cell here). Thus, errors may cumulate, contrary to the other test cases presented earlier in this validation section.

The trends observed in all the graphs of Fig. 5.23 show the importance of working with well-described arteriolar and venular structures. Indeed, a global increase in errors is observed for maximal

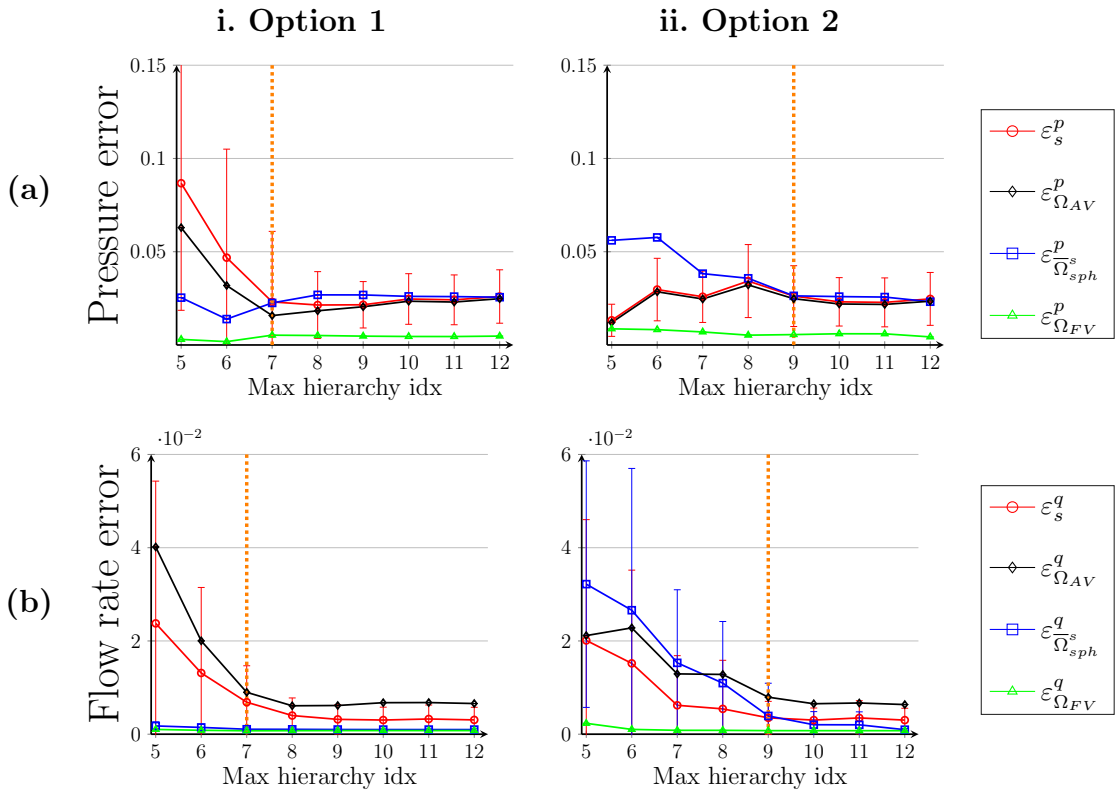

Figure 5.23: **Complexification of the arteriolar and venular structure. Global pressure and flow rate errors are displayed for two tests involving an anatomical arteriole tree coupled with a 6-regular capillary networks. In the hybrid approach, the continuum is discretized in coarse FV cells.** **(a)** *Schematics of the tests.* The configurations **i** and **ii** refer to the options 1 and 2 presented in Fig. 5.21**(a)**, respectively. **(b)** *Global pressure errors.* For each configuration, global pressure errors are computed in the four domains of interest defined in Fig. 4.6**(d)**. The errors are normalized by the global pressure drop δP. **(c)** *Distribution of the global pressure errors in the FV domain.* The distributions of the pressure errors are displayed for the ratios h/l_{cap} indicated by orange dotted lines in **(b,d)**. **(d)** *Global flow rate errors.* The flow rate errors are computed in the same four domains of interest. The errors are normalized by the global incoming flow rate q_A.

hierarchical indexes lower than 7 or 9 when using options 1 or 2, respectively. Moreover, this difference in threshold suggests that the option 1 is more robust to the truncation of the arteriolar component. Furthermore, while the errors $\varepsilon_{FV}^{p,q}$ and $\varepsilon_{\Omega_{sph}^s}^{p,q}$ are not impacted by the truncation when using option 1, they deteriorate for low maximal hierarchical indexes when using option 2, especially in the FV neighbourhood $\Omega_{sph}^{s,\varepsilon}$. In these cases, the description of the capillary neighbourhood using option 2 involves values that are not representative of the microscopic scale. This last result suggests that the multiscale coupling model is less accurate when not embedding information from the scale of capillaries, i.e. when not representing the difference in scales between the arteriolar and venular trees, and the capillary bed/continuum.

5.3.4 Summary

The results presented in Section 5.3.2 are summarized in Fig. 5.24. The errors reported correspond to the orange dashed lines displayed on each previous graphs (Figs. 5.16, 5.19 and 5.23).

With regard to pressure fields, the hybrid approach is in very good agreement with CN simulation in all configurations, with no pressure error larger than 3 %. The largest errors in both FV and arterio-venular domains are induced by the coupling of an anatomical arteriole to a 6-regular network. Since several perturbations are combined in such a configuration (e.g. off-centering and multi-coupling), this result suggests that pressure errors cumulate. However, this cumulation is not critical since errors are lower than 3 %. Increases in pressure errors in the arteriolar vessel (ε_s^p and ε_{AV}^p) are also induced by the morphometrical modifications of the capillary structure (diameter distribution and Virshow-Robin space), showing that the coupling model is sensitive to microscopic variations of the capillary network. The pressure errors in the arterio-venular component (ε_s^p and ε_{AV}^p) are also larger for Voronoi-like network, for which effective parameters can vary spatially.

The values of the flow rate errors confirms that the accuracy of the flow field in the arteriolar vessel is sensitive to the morphometrical variations of the capillary bed (diameter distribution and Virshow-Robin space). The use of Voronoi-like networks is even questionable since it induces slight heterogeneities, which cannot be described by uniform effective properties. These errors are significant, although our model does much better than the SH approach, confirming the need for a multiscale coupling model in the hybrid approach.

What we must remember from Section 5.3:

- the multiscale coupling is valid for a ratio $h/l_{cap} \geq 4$, even for complex capillary networks;
- the coupling model is sensitive to morphometrical variations of the capillary bed (diameter distribution and VR space), especially with regard to the description of flow rate in the arteriolar component;
- if the arteriolar or venular components are not reconstructed down to the scale of capillaries, the hybrid approach is more robust when using a statistical description of the capillary neighbourhood in the coupling points;
- the description of the Voronoi-like networks at mesoscopic scale is not very accurate, due to slight heterogeneities. Further investigation are needed to take them into account in both the FV scheme and the multiscale coupling model (see more details about the future treatment of heterogeneities in Section 7).

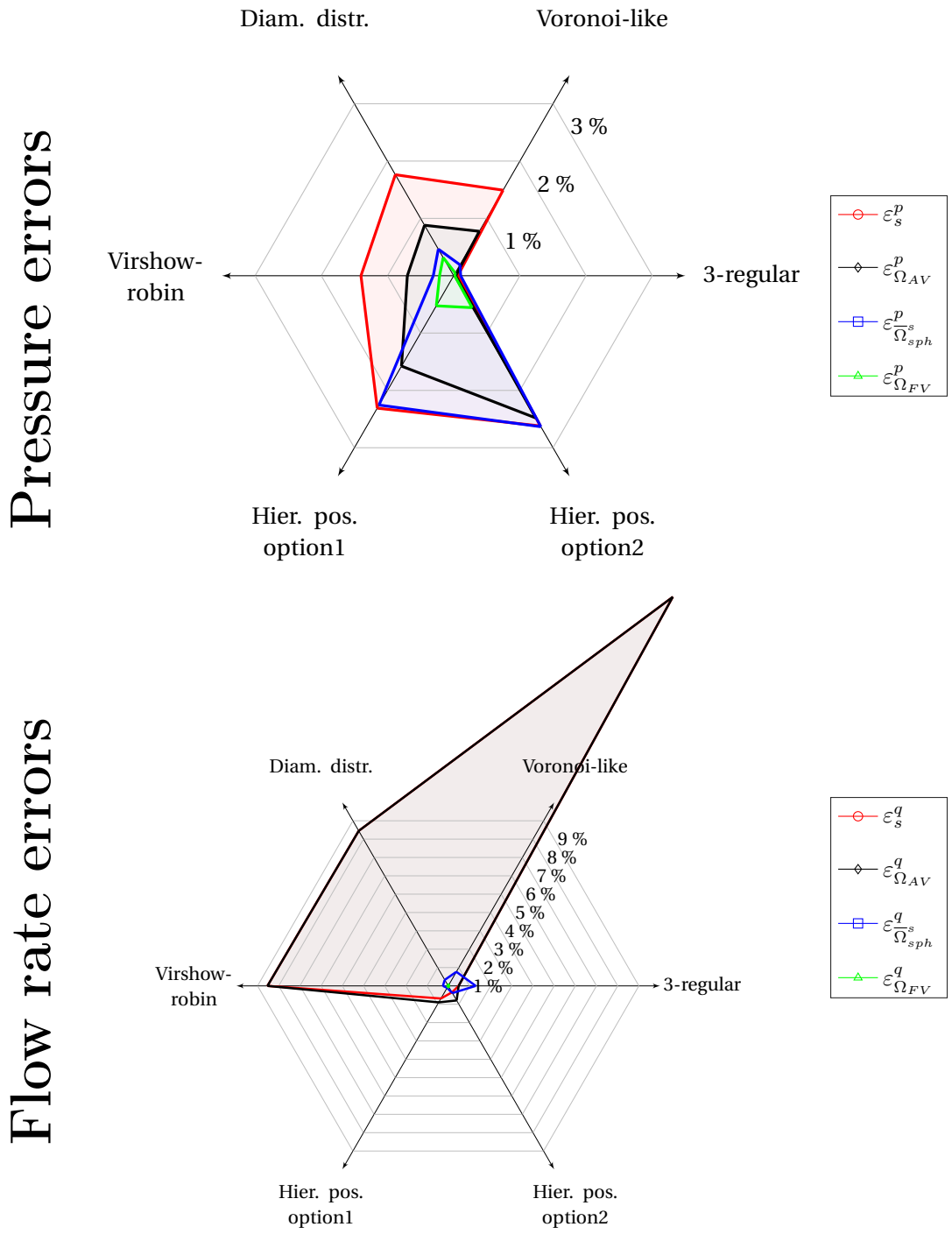

Figure 5.24: **Summary of errors presented in Section** 5.3**.** Pressure and flow rate errors have been computed all along the Section 5.3 for seven different configurations reported at the circumference of the diagram (Scale separation, Off-center, etc). Representative or extrem values have been selected and indicated by orange dashed lines in each indivual graph of Fig. 5.16 and 5.19. They are reported here and combined in a same diagram.

5.4 Validation of the hybrid approach on realistic configuration

In Sections 5.2 and 5.3, we isolated some architectural features that typically occur in the brain microcirculation using idealized configurations. This investigation highlights both the robustness and some potential weaknesses of our approach. In this section, we present a more anatomically accurate configuration, which combines all these morphometrical and topological features and displays a large number of couplings. The aim of this study is to confirm the robustness of the hybrid approach in realistic configuration where errors may cumulate.

5.4.1 More realistic configuration

For that purpose, we consider three arteriolar and venular trees that have been reconstructed from anatomical data [Cassot et al., 2006]. This vasculature is displayed in Fig. 3.1. The vascular trees are connected here to a synthetic 3-regular network of volume $4.11\times2.74\times1.37$ mm^3 with Gaussian diameters distribution and uniform length $l_{cap} = 30.62\,\mu$m. This connection implies 276 coupling points at the interface between the arteriolar and venular vessels, and the capillary bed. Furthermore, the capillaries in the vicinity or arterio-venular vasculature have been removed to represent the Virshow-Robin perivascular space. In the hybrid configuration, the continuum representing the capillary bed is discretized in FV cells of side $h = 152.15\,\mu$m, i.e. $h/l_{cap} = 4.97$, ensuring the validity of the coupling model. In this domain, the flow is characterized by the effective permeability $K^{\text{eff}} = 5.6610 \times 10^{-15}\,\text{m}^2$ and effective viscosity $\mu^{\text{eff}} = 6.1834 \times 10^{-3}$Pa.s. The boundary conditions applied are similar to those presented in Section 5.2.1 for multiple couplings: we impose a pressure $P_A = 10\,000\,\text{Pa}$ at the two arteriolar inlets and a pressure $P_V = 3\,000\,\text{Pa}$ at the venular outlet; impermeability (zero flow) on the top and bottom of the capillary network; and periodic conditions in the two other directions. For consistency, similar boundary conditions are applied to the faces of the FV domain.

As discussed in Section 5.1.5, the comparison of the FV pressure field and pressures computed in CN simulations is not relevant in the neighbourhood $\Omega^s_{FV,neigh}$ of coupling points. Because of the high density of coupling points in the present configuration, the union of all these neighbourhoods represents almost the whole FV domain. The accuracy of the flow field in the FV domain is assessed here by the fact that global flow rate errors computed at coupling points is very low (<0.8 %). In the remainder of this section, we will focus on errors related to the arterio-venular trees only. Furthermore, by contrast to the previous studies, we will compute *local* errors (see Section 5.1.4) for the purpose of investigating pressure and flow rate errors at the scale of individual vessels, thus understanding the spatial distribution of errors.

5.4.2 Presentation of the results

The distributions of local pressure and flow rate errors are displayed in Fig. 5.25. In Fig. 5.25**(a)**, the pressure error field shows that the hybrid approach remains accurate, with no error greater than 10 %. In Fig. 5.25**(b)**, flow rate is much more sensitive, with errors ranging from 0.001 % to 100 %. These large values can be explained by the fact that pressure and flow rate fields are highly correlated (Eq. 3.1) in the sense that slight pressure perturbations at the endpoints of a given vessel can induce very high flow rate error, especially for low pressure drops, i.e. low flow rates. Indeed, the largest errors displayed in Fig. 5.25**(b)** concern the smallest vessels of the trees, close to the coupling points. In these vessels, flow rate values are in the range $10^{-20} - 10^{-24}$ m^3.s. By contrast, flow rate values at the inlets and outlets of the arteriolar and venular trees are about $\sim 10^{-10}$ m^3.s. Furthermore, the use of local flow rate errors, i.e. normalized by the local flow rate, enhances such errors in vessels with low flow rates.

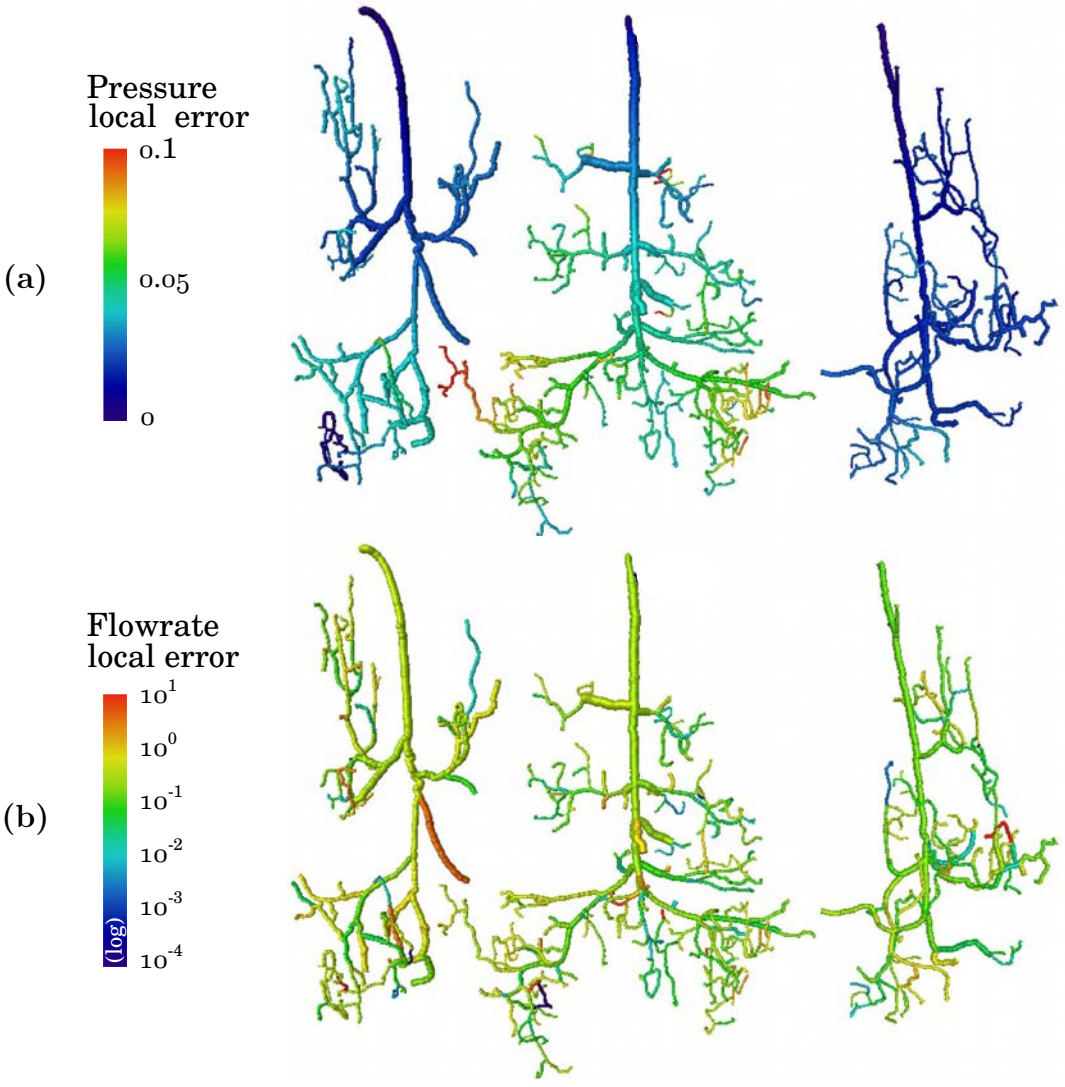

Figure 5.25: **Distribution of pressure and flow rate local errors by comparing the hybrid and CN approaches in three anatomical arteriolar and venular trees.** **(a)** Pressure error maps in arteriolar and venular trees are presented. **(b)** Flow rate error maps in arteriolar and venular trees are presented.

To further assess the fact that large flow rate errors are mainly related to low flow rates and not to the accuracy of the multiscale coupling model, we focus on three perturbations that may affect this accuracy: the off-centering of coupling points in the FV cells, the density of couplings per cell, and the close distance between two couplings. The results are displayed in Fig. 5.26. In the three graphs, no trend clearly appears with regard to the relationship between flow rate errors and off-centering, nor with the number of couplings per cell or the close distance between two couplings. These results show that our hybrid approach, and the coupling model it includes, are robust to realistic configurations involving a large number of couplings. Thus the important flow rate errors reported in Fig. 5.25**(b)** are not induced by limitations of our approach.

To highlight the benefit of the hybrid approach in spite of high flow rate errors, we compare our result with simulations run in the same configuration using the SH method. The results are displayed in Fig. 5.27 for both pressure and flow rate errors. With regard to pressure errors (Fig. 5.27**i(a-b)**), values reach 42 % in the SH approach, while they are lower than 13 % with our hybrid approach. With regard to flow rate errors, results presented in Fig. 5.27**i(a)** shows that the hybrid approach is less sensitive to low flow rates than the SH approach, with a linear fit slope of -0.32 instead of -0.41. Furthermore, Fig. 5.27**i(b)** shows that the flow rate errors induced by hybrid simulations are much less scattered than those induced by SH computations.

Moreover, the large errors highlighted in vessels with low flow rates have a minor impact on the spatial distribution of the source flow rates. This can be verified by comparing the cumulative flow rates deduced from the hybrid approach and CN computations. For that purpose, in each tree, the source flow rates q_s at coupling points are first sorted in decreasing order and the set of cumulated flow rates is defined for n in$\{1, ..., \mathrm{Card}(S)\}$, where S is the set of sources, by

$$Q_s^n = \sum_{s=1}^{n} q_s. \tag{5.9}$$

This means that $Q_s^{\mathrm{Card}(S)}$ must be equal to the inlet or outlet flow rate of the corresponding arteriole or venule. Finally, the results are normalized by this inlet or outlet flow rate. Cumulative flow rates in each tree are displayed in Fig. 5.28. The results show good agreement with CN computations in both hybrid and SH approaches. In particular, the largest values of Q_s^n, i.e. when adding the lowest flow rates, are in very good agreement with the CN reference. This result shows that large errors in vessels with low flow rates do not critically affect the spatial distribution of flow rate in the upstream trees.

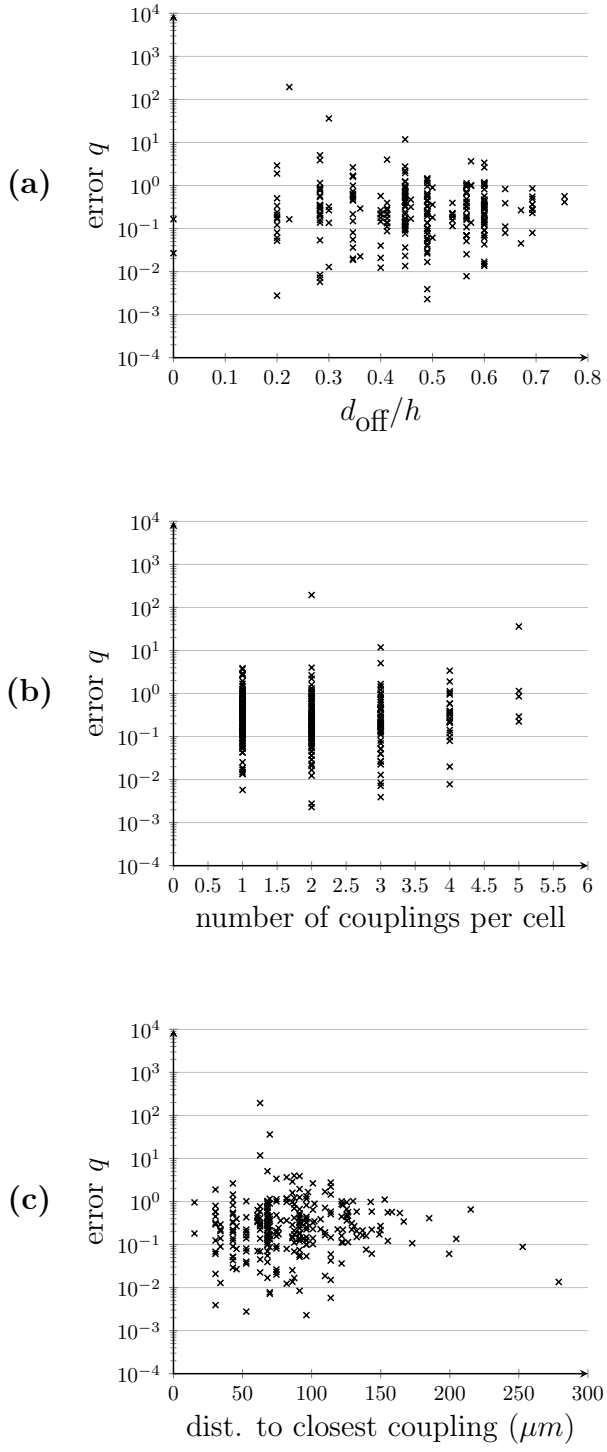

Figure 5.26: **Distribution of flow rate errors computed at the coupling points with regard to potential perturbations.** **(a)** The flow rate errors computed at the coupling points are plotted against the ratio d_{off}/h, where d_{off} represents the distance from the coupling point to the center of the coupled cell, and h represents the side of the FV cell. **(b)** The flow rate errors computed at the coupling points are plotted against the number of couplings per cell. **(c)** The flow rate errors computed at the coupling points are plotted against the distance to the closest coupling point.

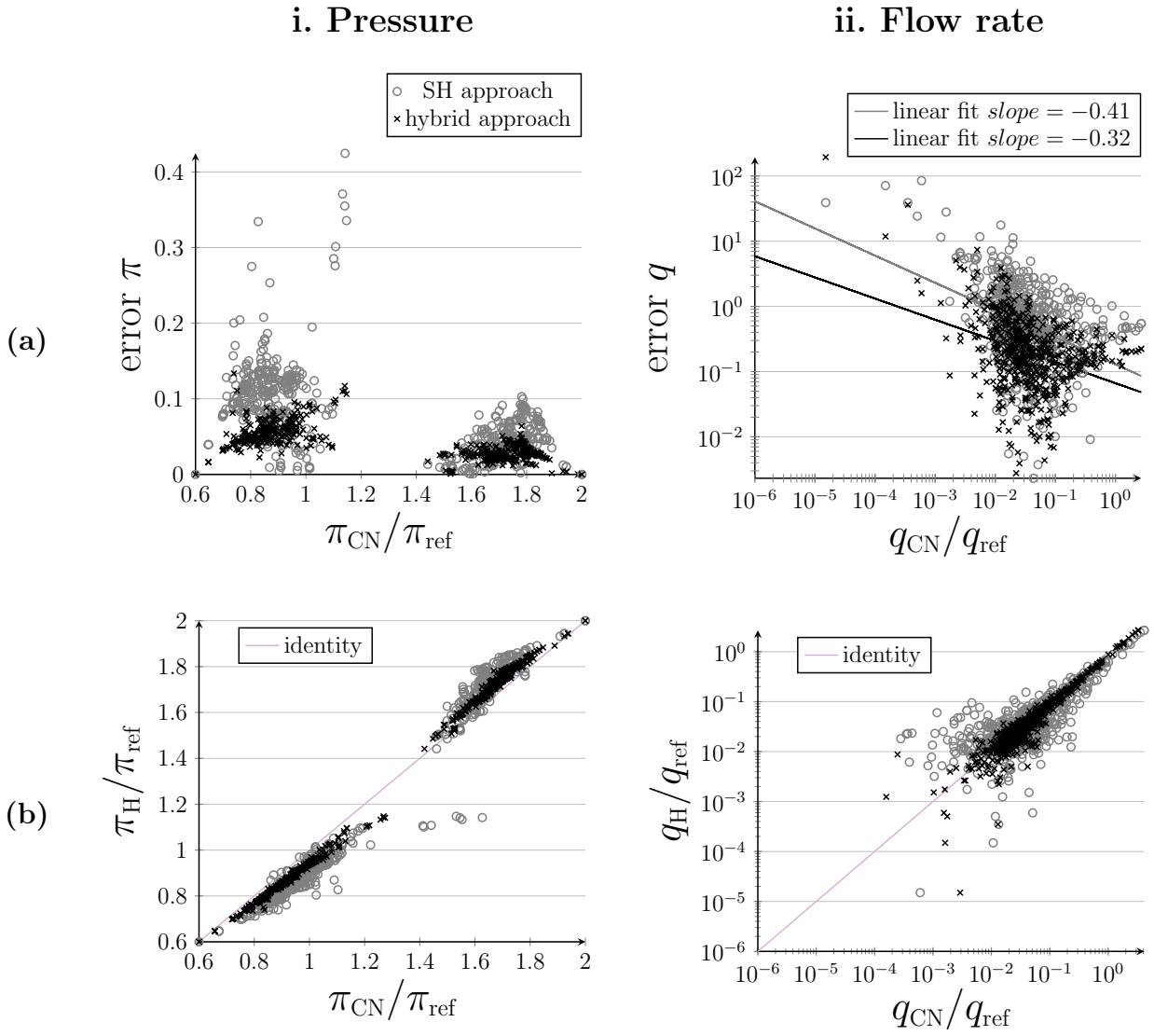

Figure 5.27: **Comparison of hybrid and CN simulations in the three anatomical arteriolar and venular trees.** **(a)** In black crosses, local errors are plotted against local pressure (**i**) or flow rate (**ii**) reference values. Additional errors are represented as gray crosses corresponding to computations without the proposed coupling model (pressure continuity at coupling sites). Here, $\pi_{ref} = 5\,000\,\mathrm{Pa}$ and $q_{ref} = 5 \times 10^{-12}\,\mathrm{m}^3 \cdot \mathrm{s}^{-1}$ are reference pressure and flow rate values used for nondimensionalization. **(b)** The local pressure (**i**) and flow rate (**ii**) values obtained by hybrid (H) and CN simulations are compared. The identity represents the ideal equality between hybrid and CN approaches. Same color conventions as in **(a)** are adopted.

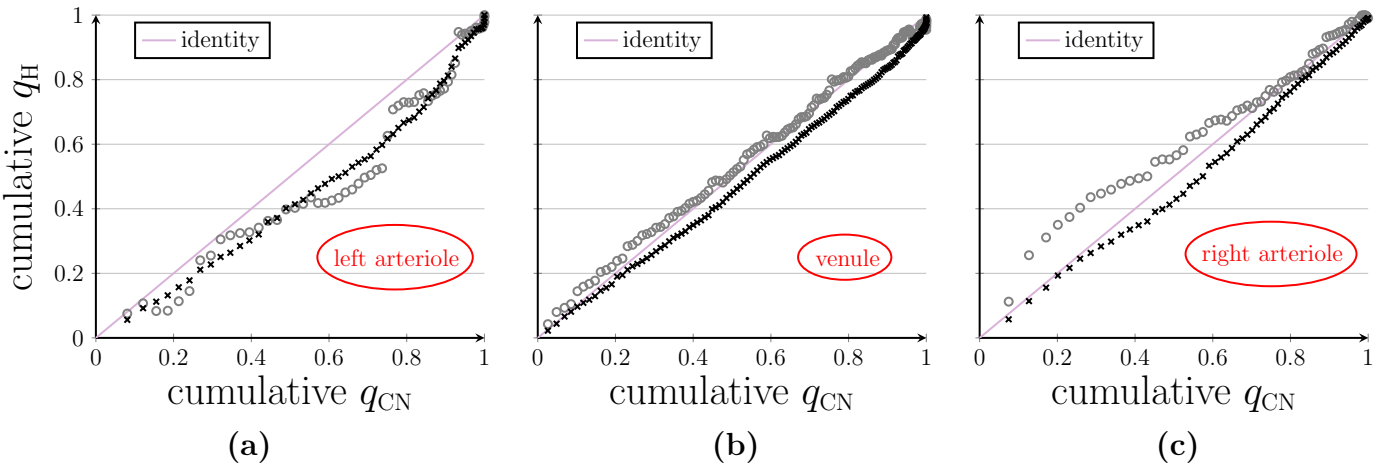

Figure 5.28: **Comparison of cumulative flow rates obtained by hybrid and CN approaches, in each of the three arteriolar and venular trees.** The cumulative flow rates are compared for both hybrid and CN approaches in the left arteriole **(a)**, the venule **(b)** and the right arteriole **(c)**. The same conventions as in Fig. 5.27 are adopted.

Finally, probability density functions of the flow rate in the network vessels have also been computed for both hybrid and CN approaches. The results presented in Fig. 5.29 show very good accuracy as the Gaussian fits overlap, contrary to those obtained with the SH approach. Such results are particularly interesting because they are in line with the philosophy of the standard complete network approach, which has been validated in a statistical sense, rather than a vessel-to-vessel basis, by comparison with *in vivo* data [Pries et al., 1990].

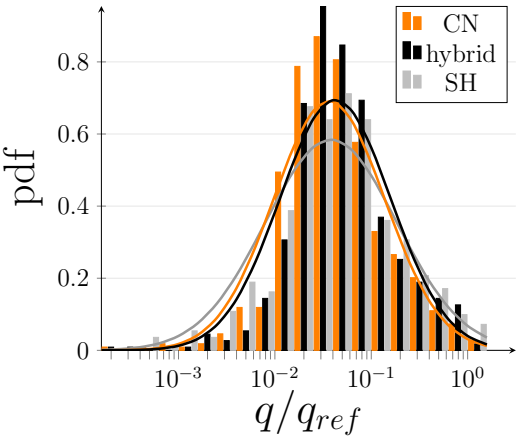

Figure 5.29: **Comparison of probability density functions of flow rate obtained by hybrid and CN approaches, in the three arteriolar and venular trees.** The probability density functions are presented for flow rate using the hybrid approach with (black) or without (gray) the coupling model, and CN approach (orange). Here, $q_{\mathrm{ref}} = 5 \times 10^{-12}\,\mathrm{m}^3 \cdot \mathrm{s}^{-1}$ is reference flow rate values used for nondimensionalization.

In summary, the hybrid approach presented in this work is robust, even in realistic configurations combining several morphometrical and topological perturbations. Assuming that the topology of the synthetic capillary network complies with the hypotheses used during the development of the coupling model (e.g. isotropy and homogeneity), the results are in very good agreement with CN simulations. Furthermore, we pointed out the difficulty of computing relevant flow rate errors, due to the fact that flow rate values involve a large range of orders of magnitude. We proposed alternative ways of investigation to conclude about the accuracy of our approach.

6 Large vascular networks: a computational challenge

The code developed during this thesis, called HybridNetwork-FiniteVolumeCode (HNFV-Code), has been implemented to simulate blood flow dynamics in large vascular networks, using a hybrid approach, and study their topology in smaller representative volumes. It is part of a larger platform called BrainMicroFlow that also contains the program FEM_simulations for direct simulations of mass transfer using the library Feel++ (finite elements method), and a toolbox written in python for the manipulation of input and output files (e.g. format conversion, field extraction), Network-Python-Toolbox. This numerical platform has been deposited with the Agence de Protection des Programmes (APP, France, n°IDDN.FR.001.150009.000.R.P.2017.000.31230) on behalf of the Institut de Mécanique des Fluides de Toulouse (IMFT) and the Centre National de la recherche Scientifique (CNRS). The contribution of the author only concerns the HNFV-Code, thus the two other components of the platform won't be discussed in this section.

6.1 The point of having efficient programming practices

The HNFV-Code has been implemented from scratch and thought as a high-quality computational tool. In a programming point of view, this means that the software should be robust, fast, accurate and easily extensible.

According to the survey of Prabhu *et al.* [Prabhu et al., 2011], special care has to be taken in bridging the gap between researchers and programming tools developers. Most of the time, a code is indeed developed for one specific application and needs to be quickly exploited for the purpose of scientific advances. In this way, researchers usually don't take the time of thinking their coding strategy and choosing appropriate computational resources in a long-term point of view. The paper of Prabhu points out several crucial questions: which language do I use (e.g. MATLAB, FORTRAN, C++, python)? which debugging techniques (e.g. console prints, code investigation, debugger)? how can I enhance the performance of my code (e.g. algorithmic changes, specialized library, compiler flag, loop optimization)? is it worth using parallelism (e.g. message passing, threads, GPU)? The answers to these questions are closely related to the ultimate goal of the software with regard to the scientific application of interest, but also to a variety of parameters such as the time the researcher

can spend coding, the quantity of data to treat or the availability of computational resources.

What about the HNFV-Code? Our program has been thought as a long-term computational tool dedicated to the modelling of blood flow and mass transfer in both microvascular networks and continuums, and to the topological study of large fractal-like trees and capillary networks. This project involves several developers (PhD students and post-doctoral researchers), several algorithmic approaches (e.g. parallelized solvers dedicated to high performance computing or sequential optimized algorithms for graph coverage) and several numerical schemes (discrete network models and finite volume method). The contribution of the author concerns the development of both network and continuum parallel structures, the implementation of parallel linear solvers for blood flow simulation using network, continuum and hybrid approaches, and the writing of complementary tools such as mathematical operations or graph coloring. The collaborators further added a parallel non-linear solver for flow simulation in networks, which takes into account the complex rheology of blood (phase separation), and some sequential geometrical tools for the study of network topology.

For the purpose of collaborating and building an accurate wide-variety computational tool, we took inspiration of existing successful projects (e.g. CHASTE [Mirams et al., 2013]) and discussions about the best practices to adopt in scientific computing [Baxter et al., 2006, Wilson et al., 2014]. On this basis, common strategies have been adopted, following four outlines detailed throughout this section:

- **Collaboration**: the major point is to prevent any new developer to re-invent the wheel. In other words, developers should re-use already implemented components (e.g. numerical schemes, mesh structures, solvers) instead of repeating unnecessary code lines. This implies that the code is readable and sufficiently commented. For that purpose, teamwork is key: syntax conventions, discipline in commenting new functions, coordination platform for discussion and sharing, and pair-programming sessions.
- **Reliability**: scientific softwares are often uncertain and unprovable, sometimes even safety-critical as clinical applications may rely on the resulting simulations. To ensure the reliability of the HNFV-Code, the sources are regularly validated using an external testing unit. Moreover, a collaborative issue tracking tool is available on the coordination platform to report bugs and following their fixing processes.
- **Computational performance:** the HNFV-Code is designed for high performance computing (HPC) with regard to flow and mass transfer modelling. To this end, the compiled language

C++ has been chosen because of its low level (close to machine language) and its flexibility induced by the possibility of defining object-oriented classes. This choice has also been influenced by the fact that most of the external libraries we are interested in (e.g. external software specialized in linear algebra, solvers and preconditioners) are also implemented in C++ in a high performance perspective. Furthermore, the simulations considered may involve a huge quantity of I/O data, requiring an efficient memory management. For that purpose, the code is fully-parallelized using MPI standards, memory leaks are tracked and the binary file format HDF5 is used for big-data simulations.

- **Portability:** in a perspective of collaborations, ultimately with biophysics community, the software should be portable. To this end, all the dependencies are open-access. Moreover, the code is related to an automatic generator of documentation, facilitating sharing. A wiki page is available, which contains the description of key processes, and I/O files can also be manipulated in ASCII format for more readability.

6.2 Coding strategy

6.2.1 Collaboration

The HNFV-Code has been thought as a collaborative and flexible tool for the purpose of easily enriching it with different scientific and numerical approaches.

To lay the groundwork of this project, the *structure* of the code has been conceived up-front so any new class or function should naturally find its place. For four years now, no modification has been brought to the initial layout displayed in Fig. 6.1. The source classes are stored in three main directories:

- Params contains the parametrization of the study: I/O file names and global characteristics of the medium (e.g. effective parameters of the continuum);
- Mesh contains the structural definition and manipulation of the media: the network is treated as a non-structured mesh defined by a connectivity matrix, and the continuum is discretized by a regular grid;
- PDEs contains the construction of the linear systems (filling of the matrix and right-hand side) and their solving. It also contains some post-processing tools (e.g. computation of the global flow rate).

In order to avoid repeating code lines, several "common" directories contain tools that are useful in all the downstream classes (e.g. mathematical tools). As soon as practicable, the concept of inheritance between two C++ classes is also exploited by deriving a class from another. This relationship provides the possibility to reuse functionalities that are already implemented since the derived class has access to the members (variables and functions) of the base class. For instance, two stationary and non-stationary solvers inherit the same base class in the Solver directories of both Network and FiniteVolume parts. Furthermore, any new function and class is rigorously commented to describe its purpose, arguments and returns. In this way, in the case where a developer is not the author or completely forgot part of the code, one can still easily understand and use already implemented statements.

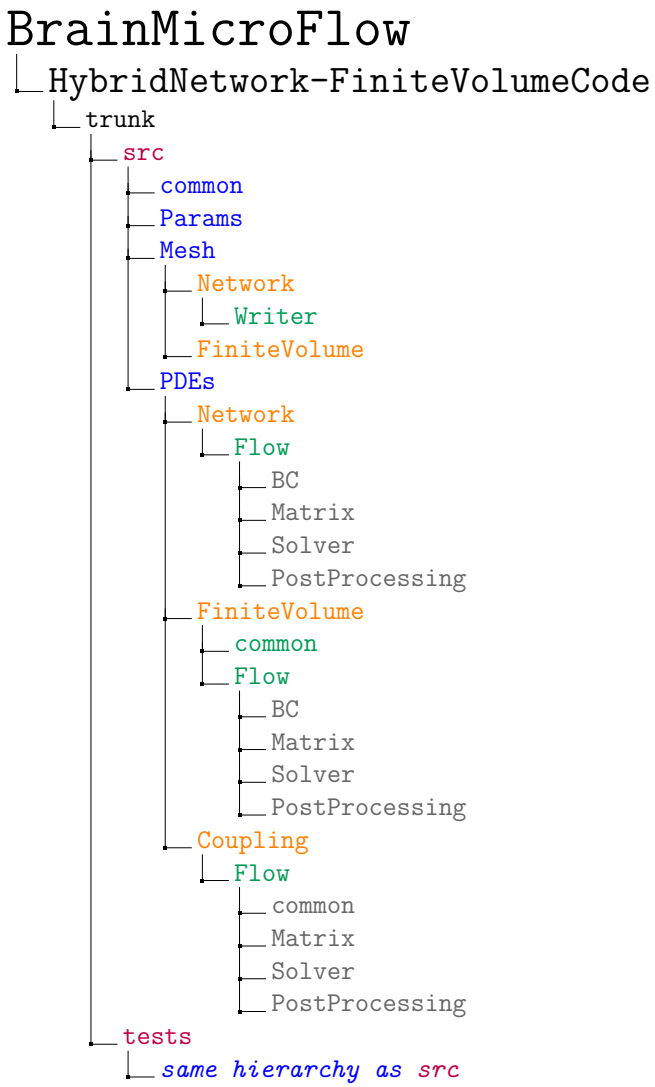

Figure 6.1: **Layout of the HybridNetworkFiniteVolumeCode.** The classes that compose the code are stored in directories, according to this tree structure.

For the purpose of harmonization, some *conventions* have been adopted to make the code consistent with regard to its syntax. Inspired by the rules of the CHASTE software (https://chaste.cs.ox.ac.uk/trac/wiki/CodingStandardsStrategy), a special care is taken in using a common style and formatting. First, all class, function and variable names must be explicit and non-standard abbreviations are prohibited (see Tab. 6). Second, these names obey to a rigorous syntax convention:

- class name (e.g. NetworkFlowSolver): capital first letter, capital letter to separate words, no underscores;
- function name (e.g. computeApparentViscosityOfBlood): use an active verb to describe its purpose, first letter in lower case, then same syntax as class name;
- variable name (e.g. my_vascular_network): lower case letters, underscores to separate words.

Even if these conventions sometimes lead to very long names, they efficiently facilitate the navigation through the code and ultimately make the implementation more rapid.

	✗	✓
class	Class1	NetworkFlowMatrix
function	f	constructRightHandSide
variable	a	nb_vertices

Table 6: **Explicit names.** Examples of accepted and prohibited names for classes, functions and variables. These examples follow the syntax conventions.

Each developer owns a local version of the HNFV-Code. In this way, one can implement new functionalities without disturbing the other developers. This point is particularly crucial when important modifications are brought to a widely used part of the code. Once the local modifications are validated, the developer uploads his new version to a *central repository* managed by GitLab (gitlab.com). Further than protecting the code by archiving its whole history, this free software versioning is in charge of coordinating the modifications of the code and avoid computational conflicts (two developers sometimes modify the same class at the same time). To this end, it reviews the code each time a developer submits a new version and controls its merging with the previous version. GitLab also provides a tool dedicated to issue tracking: each time a developer notices a bug, he can report it and assign the appropriate person to fix it. Moreover, each member of the project can present standard uses of the code by writing documentation in wiki pages. Finally, one is aware of the global advance thanks to the visualization of the activity stream.

Taking advantage of the number of developers, *pair-programming* sessions are regularly scheduled. In these sessions, two persons sit side by side, one implementing, and the other checking and suggesting improvements. The aim of this practice is to improve the quality of the code, to homogenize our way of programming, to facilitate the integration of new developers, and to avoid that a single person takes full responsibility for any crucial part of the code.

6.2.2 Reliability

For the purpose of ensuring the reliability of the code, a series of tests is regularly executed and any failure is immediately reported. The quality of these tests entirely relies on the capacity of planning potential mistakes, from the most obvious to the tiniest one. Far from being universal, the philosophy of testing has to be discussed up-front. Indeed, an infinite variety of tests exists [Bertolino, 2007] and it is crucial to adopt a common strategy to make sense. Concerning the HNFV-Code, the tests can be sorted in two main classes:

- the *one-function-one-test* class is the lowest level of testing. It implies that one test is dedicated to one single functionality of the code. The aim of these tests is to check if a given function performs as expected, in a strict computational point of view, independently of whether the results are physically or mathematically correct. Most of the time, it is actually impossible to isolate a functionality (e.g. any test on a network requires the call of the input files reader first). Thus, this kind of tests is meaningful only if all the functions are tested, from the first computational step, each test validating the testing of the next step. In other words, this strategy implies that the number of tests is equal to the number of functions in the sources. In the implementation of some professional software, the developers even reverse the writing steps and write the test associated to a new functionality before implementing the source code. This strategy is called "test-driven development" [Pitt-Francis et al., 2009] and is the ideal way of testing. Unfortunately, it is extremely time consuming. In our case, we first apply the one-function-one-test approach to crucial parts of the code, then progressively refine our testing during pair-programming sessions. However, it appears to be very difficult to cover 100% of the functions, unless it is the full-time job of one of the developers.
- the *physical tests* verify if the outputs are physically accurate. This is the highest level of testing. The code is considered as a "black box" tool for biophysical applications. Contrary to the one-function-one-test class, the interest of the physical tests is to involve the largest series of functionalities. They actually ignore the intern step-by-step process and verify if any

modifications of the inputs correctly impact the outputs (e.g. constant pressure imposed at each inlet and outlet of a network implies a constant pressure in the whole component). Because the possibility of testing is infinite, due to the number of input files and operations that can be combined, we restrict the tests to our standard use of the code and to critical particular cases (e.g. boundary conditions that may imply a bad conditioning of the matrix).

To offer a quality control process, the testing unit must be independent and cover all the sources. We use the external library *CxxTest* (cxxtest.com), which is a light portable testing framework adapted to C++. This tool automatically checks all the assertions implemented in the tests and displays a detailed report in case of failure. Moreover, this library provides the possibility of building classes, thus the organization of the test files can be the mirror of the sources (see Fig. 6.1), which is very convenient. This choice has also been influenced by its compatibility with GitLab. Indeed, upon each commit on the central repository, all the tests are run to check if no functionality has been inadvertently broken. This process is called "continuous integration". It ensures that the code still performs as intended, in the limit of the accuracy defined by the set of tests. This approach does not guarantee bug-free software but makes them very rare, since the reaction facing a bug must be to implement a test to prevent it.

To measure the coverage of the tests on the entire code, we further combine the test running with the coverage tools *gcov* and *lcov*. The first one flags each executed line and function during the execution, and the second one translates the outputs of the first one into an information file that can be read by the tool *genhtml* to generate a fancy visualization in HTML format. This report highlights the lack of coverage of some parts of the code. For instance, the global coverage in Fig. 6.2 shows that:

- the functions in the post-processing classes are poorly tested. This coincides with the highest level of testing. This lack of testing is not critical in the sense that no further step in the execution process depends on them. Moreover, the outputs resulting from these classes are regularly exploited by the users, thus implicitly validated.
- the class Mesh/Network/Writer is almost not tested. This corresponds to the generation of input files for standards networks (e.g. 6- and 3- regular) or transformed networks (e.g. extraction or duplication). In the same spirit as the outputs, the input files are implicitly validated, mostly by visualization tools. Furthermore, automatic controls are implemented in the code to verify the entries, sending error messages if the input files are not built correctly (e.g. detection of a boundary node with no boundary condition assigned).

- the classes related to the coupling part also present a low rate of testing. This is explained by the fact that several coupling models have been implemented and investigated before finding the version we present in this manuscript. Thus a lot of functions are kept as a history but not exploited in the end.

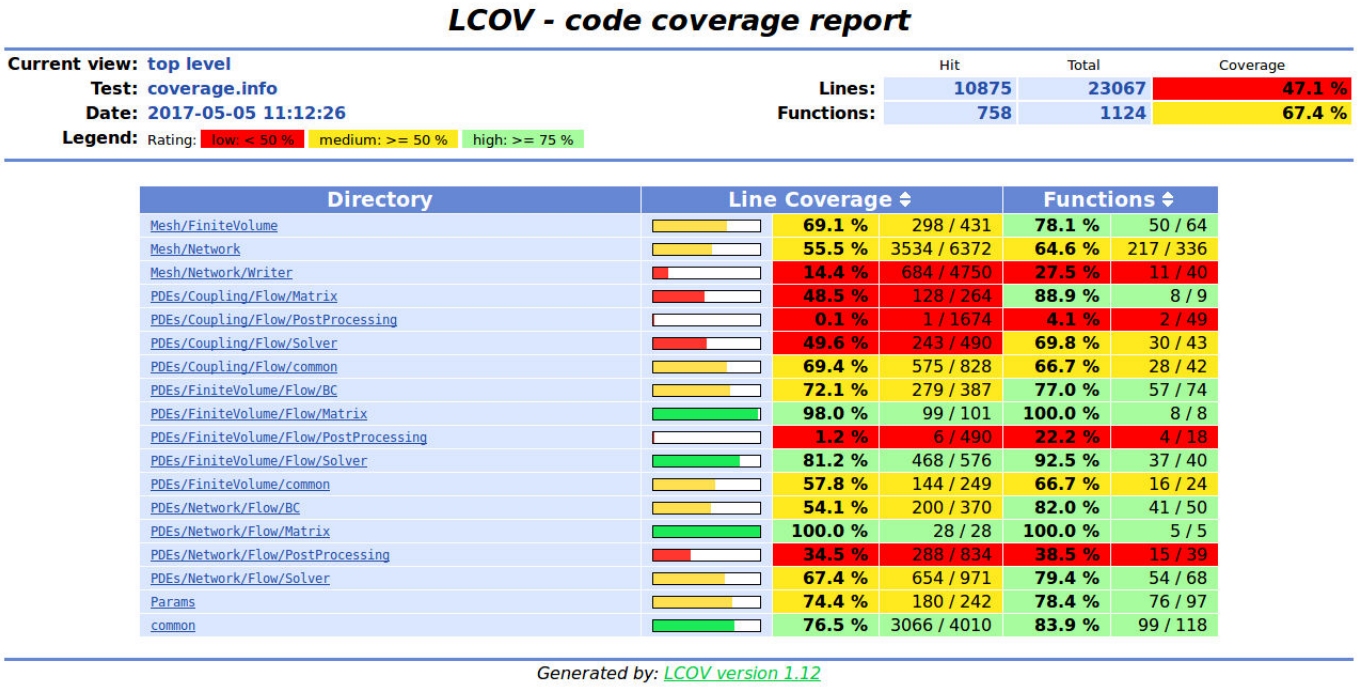

LCOV - code coverage report

			Hit	Total	Coverage
Current view:	top level	**Lines:**	10875	23067	47.1 %
Test:	coverage.info	**Functions:**	758	1124	67.4 %
Date:	2017-05-05 11:12:26				
Legend:	Rating: low: < 50 % medium: >= 50 % high: >= 75 %				

Directory	Line Coverage		Functions	
Mesh/FiniteVolume	69.1 %	298 / 431	78.1 %	50 / 64
Mesh/Network	55.5 %	3534 / 6372	64.6 %	217 / 336
Mesh/Network/Writer	14.4 %	684 / 4750	27.5 %	11 / 40
PDEs/Coupling/Flow/Matrix	48.5 %	128 / 264	88.9 %	8 / 9
PDEs/Coupling/Flow/PostProcessing	0.1 %	1 / 1674	4.1 %	2 / 49
PDEs/Coupling/Flow/Solver	49.6 %	243 / 490	69.8 %	30 / 43
PDEs/Coupling/Flow/common	69.4 %	575 / 828	66.7 %	28 / 42
PDEs/FiniteVolume/Flow/BC	72.1 %	279 / 387	77.0 %	57 / 74
PDEs/FiniteVolume/Flow/Matrix	98.0 %	99 / 101	100.0 %	8 / 8
PDEs/FiniteVolume/Flow/PostProcessing	1.2 %	6 / 490	22.2 %	4 / 18
PDEs/FiniteVolume/Flow/Solver	81.2 %	468 / 576	92.5 %	37 / 40
PDEs/FiniteVolume/common	57.8 %	144 / 249	66.7 %	16 / 24
PDEs/Network/Flow/BC	54.1 %	200 / 370	82.0 %	41 / 50
PDEs/Network/Flow/Matrix	100.0 %	28 / 28	100.0 %	5 / 5
PDEs/Network/Flow/PostProcessing	34.5 %	288 / 834	38.5 %	15 / 39
PDEs/Network/Flow/Solver	67.4 %	654 / 971	79.4 %	54 / 68
Params	74.4 %	180 / 242	78.4 %	76 / 97
common	76.5 %	3066 / 4010	83.9 %	99 / 118

Generated by: LCOV version 1.12

Figure 6.2: **Global test coverage.** The coverage of the tests can be visualized by combining the use of the tools gcov, lcov and genhtml. assigned

More precise observations can also be made by exploring the coverage report on lines in each file (Fig. 6.3):

- a lot of unexecuted lines correspond to the sending of error messages (e.g. solver divergence in Fig. 6.3**(a)**), meaning that we actually check if the code functionalities work well in valid configurations but not if it performs as expected in case of failure;
- some unexecuted lines correspond to unreached cases. These generally correspond to non-physical cases (e.g. a network node with two neighbours in Fig. 6.3**(b)**) that have been anticipated during the implementation but that are rarely reached in standard executions of the code;
- the test coverage is generated on a sequential execution of the tests (on one processor), thus the lines dedicated to a parallel execution are not tested (e.g. updating of ghosted values in Fig. 6.3**(c)**). It would be interesting to adapt the coverage process to an execution on several processors in the future.

(a)

```
  235          :     //-------------------------------------------------------------------------------------------solve system Ax=rhs
  236          :     //PCView(pc,PETSC_VIEWER_STDOUT_SELF);
  237       7528 :     m_ierr = KSPSolve(ksp,rhs,x);CHKERRV(m_ierr);
  238          :     //PetscScalar emin, emax;
  239          :     //m_ierr = KSPComputeExtremeSingularValues(ksp,&emax,&emin);CHKERRV(m_ierr);
  240          :     //if(m_rank==0) { cout<<"    -> matrix conditioning : emax/emin = "<<emax/emin<<endl; }
  241          :
  242       7528 :     m_ierr = KSPGetConvergedReason(ksp,&reason);CHKERRV(m_ierr);
  243       7528 :     if (reason<0)
  244          :     {
  245          0 :         cerr<<STOPMSG<<"divergence of the iterativ linear system solver =("<<endl;
  246          0 :         m_ierr = KSPGetIterationNumber(ksp,&it);CHKERRV(m_ierr);
  247          0 :         if(m_rank==0)
  248          :         {
  249          0 :             cout<<"  > number of iterations ="<<it<<endl;
  250          0 :             cout<<"  > diverged reason = "<<reason<<endl;
  251          0 :             cout<<"    > -3 : KSP_DIVERGED_ITS"<<endl;
  252          0 :             cout<<"    > -4 : KSP_DIVERGED_DTOL"<<endl;
  253          0 :             cout<<"    > -9 : KSP_DIVERGED_NANORINF"<<endl;
  254          0 :             cout<<"    > -10 : KSP_DIVERGED_INDEFINITE_MAT"<<endl;
  255          :         }
  256          0 :         exit(1);
  257          :     }
  258          :     else
  259          :     {
  260       7528 :         m_ierr = KSPGetIterationNumber(ksp,&it);CHKERRV(m_ierr);
  261       7528 :         m_ierr = KSPGetResidualNorm(ksp,&rnorm);CHKERRV(m_ierr);
  262       7528 :         if(m_rank==0 && m_display_info){cout<<" -> Convergence of the linear system : nb it = "<<it<<" & rnorm = "<<rnorm<<endl;}
  263          :     }
  264          :
  265       7528 :     KSPDestroy(&ksp);
```

(b)

```
  305     787122 :                 if(nb_neigh_edges==2)
  306          :                 {
  307          0 :                     m_ierr=VecGetValues(m_network_pressure,1,&num_vertex,&pressure_vertex);CHKERRV(m_ierr);
  308          0 :                     for(i=0;i<nb_neigh_edges;i++)
  309          :                     {
  310          0 :                         local_idx=mp_net_mesh->getNeighVertexFromLoc(num_vertex,i);
  311          0 :                         pressure_neigh=mp_net_solver->getPressureFromVertex(local_idx,m_network_pressure);
  312          0 :                         if(pressure_neigh>=pressure_vertex)
  313          :                         {
  314          0 :                             local_edge_idx=mp_net_mesh->getNeighEdgeFromLoc(num_vertex,i);
  315          0 :                             hematocrit_feeding=getHematocritFromEdge(local_edge_idx);
  316          :                         }
  317          :                     }
  318          0 :                     for(i=0;i<nb_neigh_edges;i++)
  319          :                     {
  320          0 :                         local_idx=mp_net_mesh->getNeighVertexFromLoc(num_vertex,i);
  321          0 :                         pressure_neigh=mp_net_solver->getPressureFromVertex(local_idx,m_network_pressure);
  322          0 :                         if(pressure_neigh<=pressure_vertex)
  323          :                         {
  324          0 :                             local_edge_idx=mp_net_mesh->getNeighEdgeFromLoc(num_vertex,i);
  325          0 :                             new_hematocrit=hematocrit_feeding;
  326          0 :                             setHematocritFromEdge(local_edge_idx,new_hematocrit,m_hematocrit_buffer);
  327          :                         }
  328          :                     }
  329          :                 }
  330          :                 else
  331          :                 {
  332     787122 :                     m_ierr=VecGetValues(m_network_pressure,1,&num_vertex,&pressure_vertex);CHKERRV(m_ierr);
  333    3193470 :                     for(i=0;i<nb_neigh_edges;i++)
  334          :                     {
  335    2406348 :                         local_idx=mp_net_mesh->getNeighVertexFromLoc(num_vertex,i);
  336    2406348 :                         pressure_neigh=mp_net_solver->getPressureFromVertex(local_idx,m_network_pressure);
  337    2406348 :                         if(pressure_neigh>=pressure_vertex)
  338          :                         {
  339    1619226 :                             local_edge_idx=mp_net_mesh->getNeighEdgeFromLoc(num_vertex,i);
  340    1619226 :                             hematocrit_feeding=getHematocritFromEdge(local_edge_idx);
  341    1619226 :                             flowrate_feeding=mp_net_solver->getAbsoluteFlowRateFromEdge(local_edge_idx,m_network_flowrate);
  342    1619226 :                             sum_rbc_flowrate+=hematocrit_feeding*flowrate_feeding;
  343          :                         }
  344          :                     }
  345    3193470 :                     for(i=0;i<nb_neigh_edges;i++)
  346          :                     {
  347    2406348 :                         local_idx=mp_net_mesh->getNeighVertexFromLoc(num_vertex,i);
  348    2406348 :                         pressure_neigh=mp_net_solver->getPressureFromVertex(local_idx,m_network_pressure);
  349    2406348 :                         if(pressure_neigh<=pressure_vertex)
  350          :                         {
```

(c)

```
  367       7534 :     if(nb_proc>1)
  368          :     {
  369          0 :         m_ierr = VecGhostUpdateBegin(network_flow_rate,INSERT_VALUES,SCATTER_FORWARD);CHKERRV(m_ierr);
  370          0 :         m_ierr = VecGhostUpdateEnd(network_flow_rate,INSERT_VALUES,SCATTER_FORWARD);CHKERRV(m_ierr);
  371          :     }
```

Figure 6.3: **Zoom in on standard unexecuted areas.** These three screenshots result from the test coverage using gcov, lcov and genhtml. The numbers in yellow represent the line number in the file. The blue lines correspond to executed lines (the number on the left-hand side of the colon shows how many times) and the red lines correspond to unexecuted lines. **(a)** The error report in case of divergence of the solver is not tested. **(b)** The non physical case where a network node has two neighbours is not tested. **(c)** Operations dedicated to a parallel execution of the code is not tested.

Finally, it is quite challenging to evaluate the exact test coverage of the code and its relevance from this report. We can indeed conclude that the unexecuted functions (about 30%) are not tested, but not that the executed functions (about 70%) are tested. However, some trends can be observed concerning the unexecuted functions and lines, providing a valuable tool to improve or re-orient our testing strategies (e.g. focus on poorly tested parts of the code).

6.2.3 Computational performance

In a perspective of high performance computing and efficient memory management, the HNFV-Code is written in *C++*. This object-oriented language is fast and readable, thus used by a large community of programmers. It allows modular code since one can easily add extensions and create inheritance from existing functionality. In this way, it makes the code easier to abstract, to modify and to document. Moreover, this language is particularly adapted if testing is required since testing platforms have been specifically developed for C++.

The choice of C++ has also been influenced by the fact that it makes the code very well suited for the use of the external library *PETSc* (https://www.mcs.anl.gov/petsc/). PETSc is a suite of data structures and functions for the scalable solution of scientific applications modelled by partial differential equations. It is a powerful tool that provides efficient routines related to linear algebra. It is specialized in the optimization of the manipulation of sparse vectors and matrices and offers a large variety of pre-conditioners and iterative linear or non-linear solvers. Furthermore, all its intern structures (e.g. regular grids, vectors, matrices) are very well suited for parallel programming and a lot of crucial parallelized operations on these structures are already implemented and wrapped in the library. Although the PETSc library is quite invasive and requires that all the code fits well with its use, it also considerably eases the route to rapid parallelization of the entire code.

Since the PETSc library relies on *Message Passing Interface* (MPI) standards [Gropp et al., 1996, Gropp et al., 1999], the HNFV-Code has also been fully parallelized using MPI routines (more details in Section 6.3 below). Furthermore, this choice fits with our purpose of portability since the HPC platforms mostly use distributed memory. In a long term view, this would be interesting to take advantage of the recent computational breakthroughs concerning multi-threading parallelization by integrating shared-memory paradigm such as OpenMP. Inspiration could be taken from already existing hybrid MPI/OpenMP parallelizations [Rabenseifner et al., 2009, Smith and Bull, 2001].

In the case of big-data simulations, high performance computing is closely related to an efficient

management of the memory. The parallelization of the code handles the inner memory management by distributing the job among the available processors during the execution. The outer management, which concerns the manipulation of heavy input and output files, is treated by using the *HDF5* file format (https://support.hdfgroup.org/HDF5/). This binary file format is specifically designed to store large amounts of data that potentially involve an unlimited variety of datatypes. Moreover, the data are clearly organized thanks to the HDF5 hierarchical structure and the possibility of integrating metadata. The HDF5 suite also includes efficient and human-friendly tools to manage, manipulate, view and analyze the generated files.

For now, the optimization of the code relies on manual executions of *gprof* [Graham et al., 1982, Graham et al., 2004] and *valgrind* [Nethercote and Seward, 2003], which are respectively in charge of measuring the speed of each part of the code and tracking memory leaks during the execution. In the future, these tools should be automatically called, in the same spirit as the testing.

6.2.4 Portability

The HNFV-Code is implemented for the purpose of being shared with the other communities (e.g. experimental researchers), even with non-developers researchers or doctors for clinical applications. Because the code is still in an intensive development and testing process, it is not ready yet to be publicly available. However, some strategies have been adopted in this perspective.

First, the GitLab platform enables the owners of the project to control the access of new members. Several *access levels* are available and reading/writing rights can be adapted to each member according to its status: the guests can only read the wiki pages and create new issues; the reporters can further access the code (reading right); the developers can further submit new versions, write wiki pages and take part to the issue tracking; the masters can further modify any part of the project, accept new members, cancel old profiles, even remove the whole project from the platform. Thus GitLab eases the sharing of the software, still ensuring its safety.

Second, the functions in the entire code are rigorously commented in a specific syntax related to the generator of documentation *Doxygen* (www.doxygen.org). Inside the code, the developers describe the purpose, arguments and returns of each function by using a series of tags that will be recognized by Doxygen (Fig. 6.4**(a)**). Then Doxygen automatically generates the corresponding documentation in the HTML format (Fig. 6.4**(b)**). This documentation offers a playful way to navigate through the code since all the classes and functions are linked to each other according to

different criteria (e.g. inclusion or inheritance). Thanks to this readable documentation, users can easily write new scripts based on the HNFV-Code without entering in the depth of the code. For standard use, key processes are also described in wiki pages on the GitLab platform.

While the HDF5 format for I/O files is very well suited for big-data simulations, it is not human readable and requires some practice for manipulation and analyze. The HNFV-Code also recognizes and generates ASCII files, which can easily be opened and read in any file editor. While this format is not adapted for high performance computing, it makes it easy to get started with the HNFV-Code, especially for non-developers.

Finally, all the dependencies have been chosen with the condition of open-access rights: PETSc, MPI, SCons (compiler, scons.org), CxxTest, Doxygen.

(a)

```
/**
  * This function solves the system Ax = rhs at a given time
  *
  * @param A PETSc matrix : system matrix
  * @param rhs PETSc vector corresponding to the right-hand side
  * @param x PETSc vector corresponding to the unknowns vector of the linear system
  */
void solveSystem(Mat A, Vec rhs, Vec x);
```

(b)

void FiniteVolumeFlowSolverBase::solveSystem (Mat A,
Vec rhs,
Vec x
)

This function solves the system Ax = rhs at a given time

Parameters

A PETSc matrix : system matrix

rhs PETSc vector corresponding to the right-hand side

x PETSc vector corresponding to the unknowns vector of the linear system

Figure 6.4: **Documentation of the code using Doxygen. (a)** Each function of the code is commented using specific tags. **(b)** Doxygen extracts the tags to generate a documentation in HTML format.

6.3 Parallelization of the code

Originally, softwares have been written in a perspective of automated sequential execution. In this case, as illustrated in Fig. 6.5, a given problem is divided into basic instructions (e.g. logical, arithmetic or reading/writing operations), which exploit a given dataset and are successively executed on a single processing unit. One sequential execution is usually referred as a *task*. However, computer scientists take interest in problems of larger and larger size and sequential softwares present rapid physical limitations, mainly due to the overheating induced by the high frequency of executions on a single processing-unit.

For three decades now, the performance of supercomputers keeps growing due to the improvement of manufacturing technology. In particular, the reduction of the size of the material components have led to a complete reorganization of the supercomputer architecture, which contains an ever-growing number of elementary processing-units. This cumulation have opened the way to parallel computing, where the tasks and data are distributed among several processing-units. In this way, the execution frequency is theoretically multiplied by the number of processing-units. However, this new paradigm implies the management of communications (e.g. synchronization and data sharing) between the different physical units. The reduction of this new cost represents the main challenge in parallel high-performance computing [Kumar et al., 1994].

In this section, we introduce some vocabulary and detail the different material components that compose a standard supercomputer. Then we present the parallelization paradigm that we apply in the HNFV-Code and the system we have adopted to minimize the inter-units communications. Finally, the performance of the resulting parallelized code will be evaluated in Section 6.3.4.

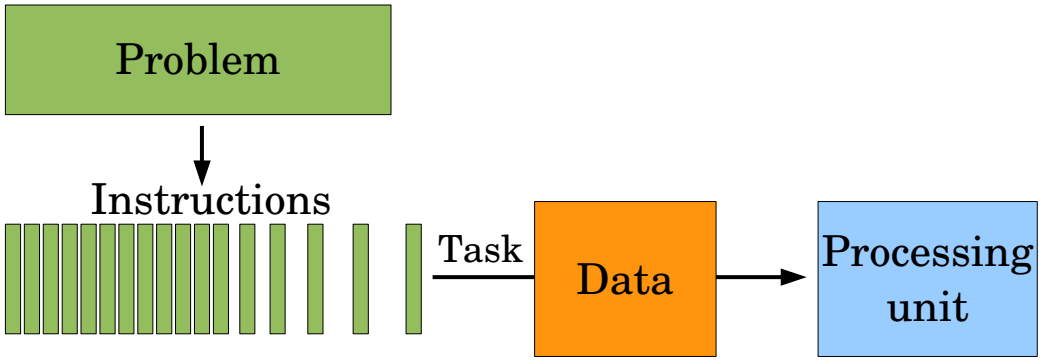

Figure 6.5: **Sequential execution of a given problem.** A problem (green) is divided into a succession of basic instructions. The execution of an instruction (or task) is based on a given dataset (orange) and is carried out by a processing unit (blue).

6.3.1 Generalities: Supercomputer architecture and parallel programming

One elementary processing unit within a computer is called a *central processing unit* (CPU). This defines the smallest electronic circuitry of the computer that is dedicated to the execution of a basic operation. In modern computers, several CPUs can be contained on a single integrated circuit chip. In this case, they are called *cores* and the chip is referred as a multi-core *processor*, as schematized in Fig. 6.6. In the rest of the manuscript, the terms "processing unit" and "CPU" will both refer to an elementary processing unit.

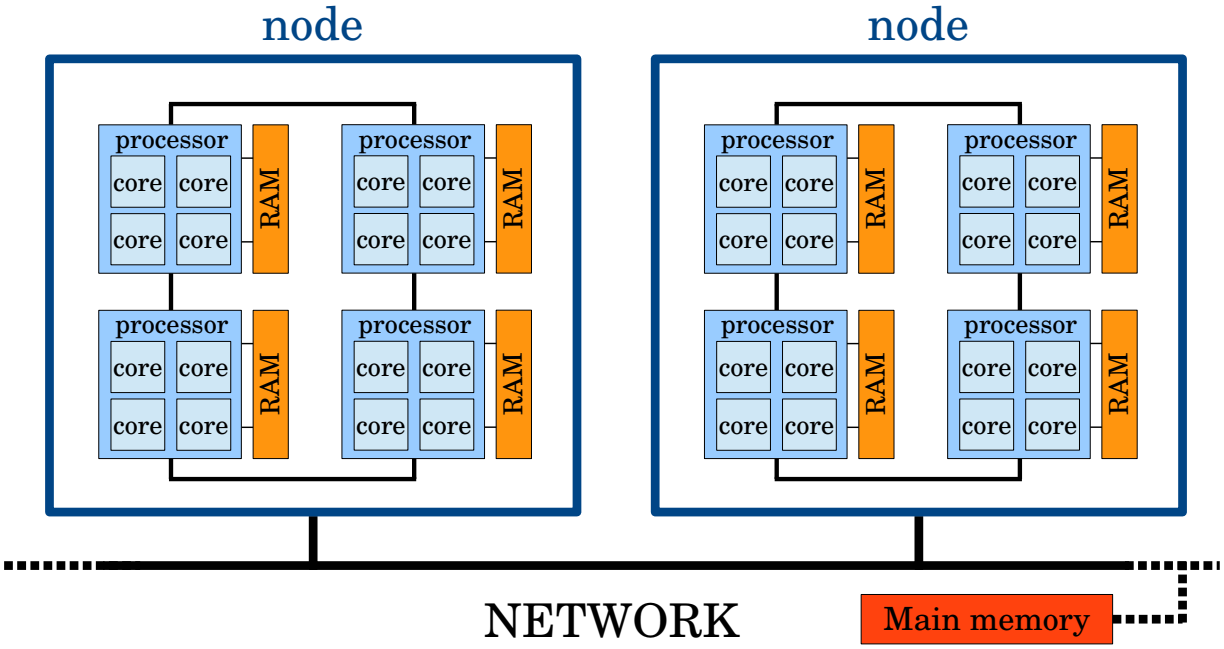

Figure 6.6: **Standard architecture of supercomputers.** A supercomputer network connects several nodes (dark blue), which contain several processors (medium blue), which contain several cores (light blue). The main memory is represented in red-orange. The Random-Access Memory (orange) is a temporary storage device dedicated to one processors. The communication network is represented by the black lines.

Each processor is linked to a device of data storage, called *Random-Access Memory* (RAM, see Fig. 6.6). This device temporary stores information that is used by the processor for the purpose of reducing the time required to read or write data items, irrespective of their physical location in the main memory. This proximity of the memory device with the processing unit significantly increases the clock rate of local operations, with comparison with a off-chip traveling of the information.

In standard personal computers, a server is usually composed of a multi-core processor containing more or less four cores, depending on their performance characteristics. Supercomputers actually represent a network of hundreds of interconnected servers, each one called *node* (see Fig. 6.6). For instance, the EOS supercomputer (CALMIP, France) contains 612 nodes composed of 2 processors,

which contain 10 cores each. This represents a computer power of more than 12 000 CPUs, implying a very complex communication network.

The multiscale architecture of supercomputers, and more particularly the fact that several cores share the same memory unit, opens the way to two kinds of parallelisms: the shared- and distributed-memory approaches.

At the scale of the processor, several cores can simultaneously work on the same amount of data, as depicted in Fig. 6.7**(a)**. This approach is referred as a *shared-memory* parallelism or multi-threading. Its implementation is relatively easy since all the processing units have access to the entire data resources and do not need to be aware of the operations of the other processing units. This parallelism is actually implicitly handled by the hardware but special directives can be implemented by the developers in a perspective of optimization, using standard programming techniques such as *OpenMP* (http://www.openmp.org/). The main difficulty induced by this strategy is the synchronization of the tasks to avoid access conflict when two cores try to work on the same data item. This situation can indeed cause a loss in time performance by creating a queue or even corrupt the data item. One solution to improve the performance of a shared-memory execution is to involve several processors, each of them having access to the whole dataset. But this induces an additional difficulty concerning the coherence of the memory. Indeed, the change of a data item in a given processor needs to be immediately reflected on the other processors and the protocols in charge of memory coherence can quickly become overloaded. Beyond these difficulties, the main constraint of the shared-memory system is that the size of the memory required to solve the problem of interest is limited by the capacity of the RAM, thus this approach is not adapted for very large applications.

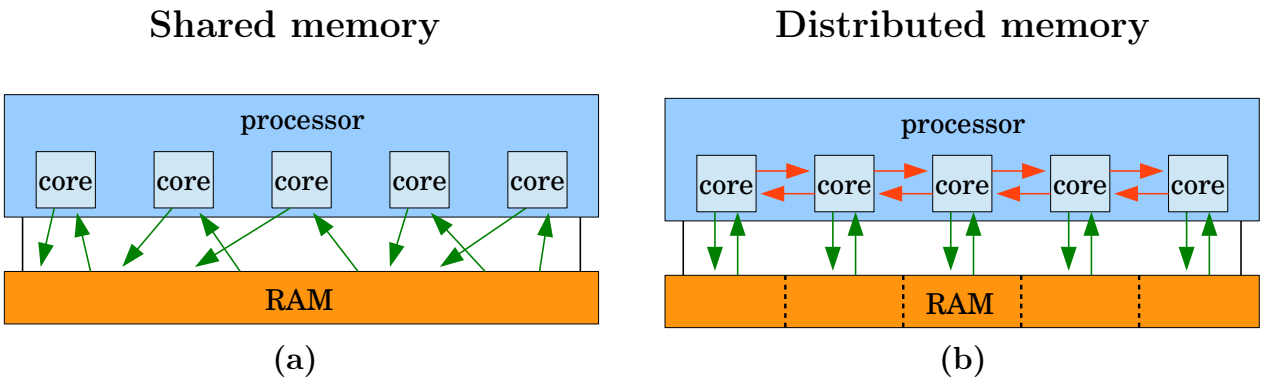

Figure 6.7: **Shared- VS distributed-memory systems.**

By contrast with a shared-memory system, the principle of a *distributed-memory* parallelism is to partition the data among the processing units, as illustrated in Fig. 6.7**(b)**. In this case, the cores can work independently on different datasets. The main advantage of this approach is that the size of the problem can theoretically be divided by the number of available cores, making of it the preferential method for very large applications. However, the inevitable synchronization of the tasks requires communications between the different processing units. These directives have to be explicitly given by the developer, using standard message-passing system, such as *Message Passing Interface* (MPI, http://mpi-forum.org/). The implementation of the distributed-memory parallelism is thus more complex than a shared-memory parallelism. In a perspective of performance, the main difficulty of this approach is to minimize the number of the communications between the processing units. For that purpose, the data have to be carefully distributed among the different processing units in order to limit the interdependency of the tasks. The distributed-memory paradigm has been chosen for the parallelization of the HNFV-Code, thus this point will be discussed in more detail in the next Section 6.3.2.

Beyond the scope of this manuscript, it is worth noting that some hybrid approaches exist to optimize the parallel performance of a code. For instance, MPI/OpenMP approach combine the advantages of both shared- and distributed-memory parallelisms [Smith and Bull, 2001, Rabenseifner et al., 2009]. For the last decade, the architecture of the Graphics Processing Unit (GPU) has also evolved into a high parallel and multithreading environment, motivated by the demand for high-definition three-dimensional graphics on personal computers. This optimized architecture, which may contain thousands of cores, opened the way to a new paradigm with regard to parallel computing [Van Luong et al., 2013]. CPU/GPU computing is now recognized as a powerful performance accelerator [Ryoo et al., 2008].

6.3.2 Parallelization of the HybridNetwork-FiniteVolume code

The HNFV-Code is implemented in a perspective of high-performance computing and applications to very large problems involving billions of unknowns, thus we adopted a distributed-memory approach, using MPI standards. As mentioned in Section 6.3.4, the use of the library PETSc is closely related to this strategy since all the vectorial structures of this library are also based on MPI standards. Moreover, the combination PETSc+MPI has already proven itself with regard to large-scale simulations [Knepley et al., 1998, Katz et al., 2007, Guo et al., 2010].

The main computational cost of a problem based on Partial Differential Equations (PDEs) is to solve the associated linear system. A standard approach to parallelize a solver is to divide the corresponding matrix and right-hand side into subgroups of contiguous rows, each subgroup being dedicated to an available processing unit [Demmel et al., 1993, Benzi and Tuuma, 2002, Mayer, 2009]. In this way, the loop on rows that is involved in the solver algorithm (e.g. conjugate gradient) can be parallelized without any communications between the processing units [Basermann, 1995, Kotlyar et al., 1996].

As highlighted by the construction of the matrix in Sections 3.2.3 and 3.3.4, each line of the matrix is associated to a physical entity of the problem: a discretization cell in the finite volume domain or an inner vertex in the network. Thus the division of the matrix and right-hand side in subgroups of rows actually corresponds to a partitioning of the physical domain of interest, as illustrated in Fig. 6.8. To ensure the efficiency of the parallel execution, two main constraints must be imposed on this partitioning:

- first, each processing unit must treat the same amount of tasks, as far as it can be. In this way, the distribution of the workload is optimized and the lost time that the processing units spend waiting for each other at the end of parallel tasks is minimized;

- second, the MPI communications between the processing units must be minimized to avoid slowing down the execution by synchronizing operations, which implies that the CPUs have to wait for each other. These kind of communications mainly occur when two neighbours are located on two different processing units. Indeed, the computation of a component of the linear system, which is related to a given physical entity, requires some communications with its neighbours. For instance, the expression of a cell pressure requires to identify the location of each of its six neighbours (e.g. Eq. 3.38 must be applied in case of periodicity, i.e. if the neighbour is at the opposite size of the domain). Concerning the network part, the expression of a node pressure requires the computation of the conductance in the neighbouring vessels (Eqs. 3.3-3.5). To prevent critical degradation of the computational performance due to unnecessary MPI communications, the exchange surface between the different partitions of the physical domain must be minimized.

For illustration, some examples of bad partitioning have been represented in Fig. 6.9.

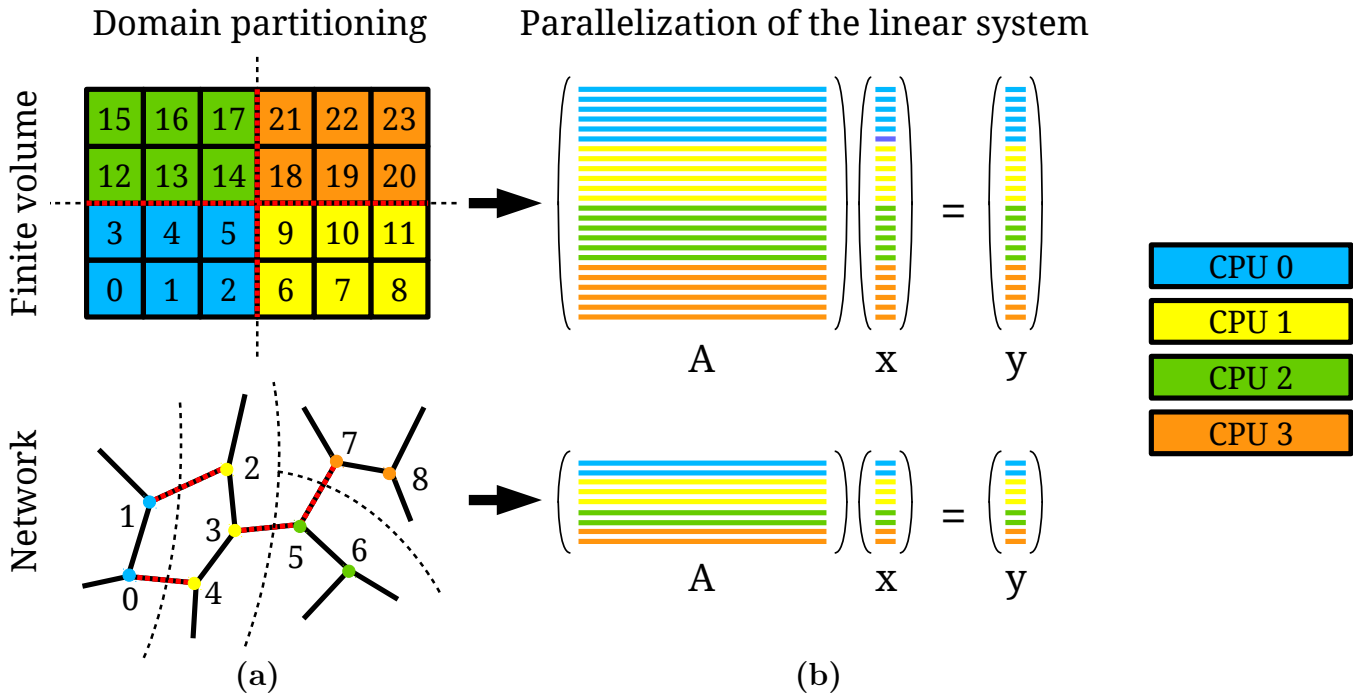

Figure 6.8: **Two-dimensional representation of the correspondence between the domain partitioning and the parallelization of the associated linear system. (a)** Two FV and network domains are divided into partitions. Each color defines the physical entities (cells or inner vertices) assigned to a CPU. The red dotted lines point the locations that will induce MPI communications between two CPUs. **(b)** The parallelized linear systems that correspond to the domain partitionings on the left are presented.

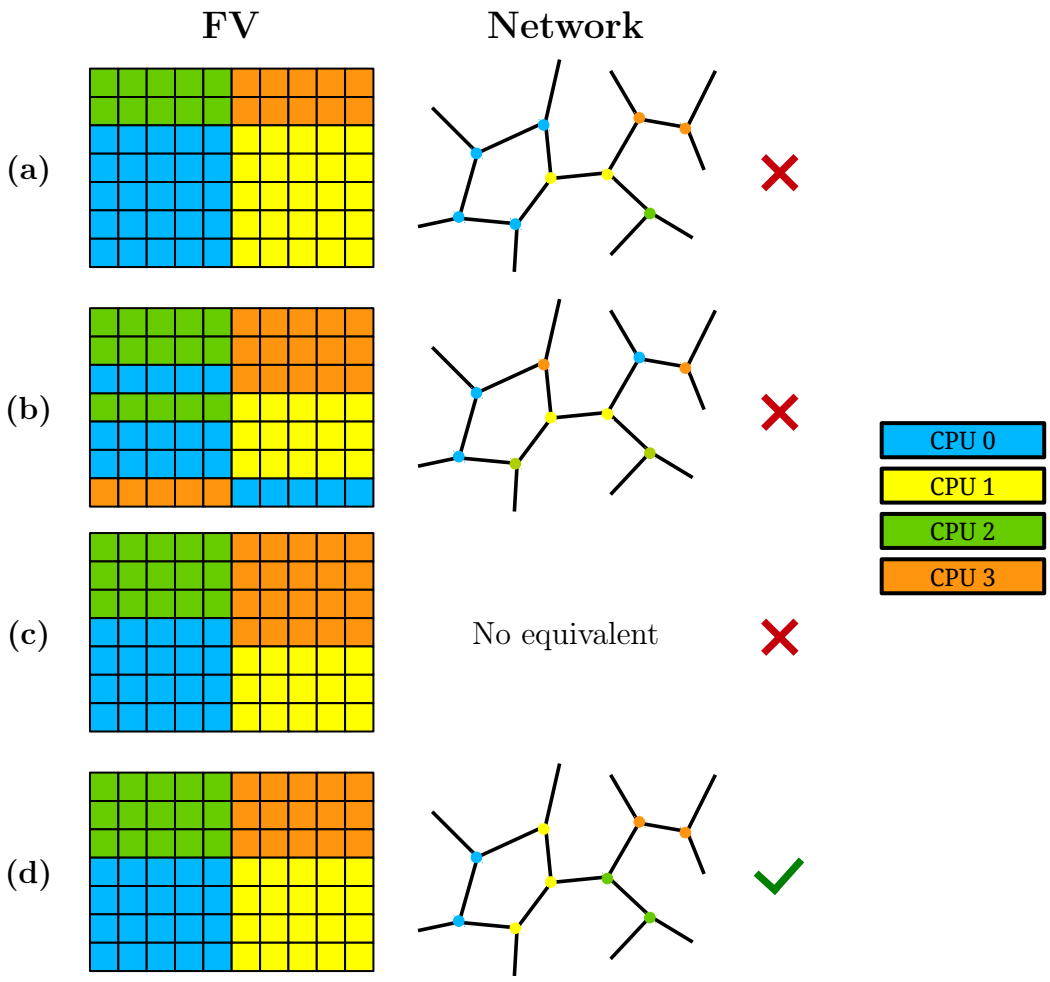

Figure 6.9: **Examples of bad partitioning of a FV or network domain. Partitionings displayed on a same line for the FV or network domain are independent.** **(a)** The workload balance among the processing units can be optimized. **(b)** The physical non-contiguity of the components belonging to the same processing units induces avoidable MPI communications between the processing units. **(c)** Concerning the FV domain, the non-homogeneity of the partitioning in one direction ("stairs" configuration) induces avoidable MPI communications between the processing units. **(d)** For comparison, a correct partitioning is represented for both FV and network domains.

In addition to the minimization of the exchange surface between the processing units, a strategy to reduce the cost of the MPI communications is to create *ghost* components. In a given processing unit, the ghost components are actually a copy of all the neighbours that are located on other processing units. Usually, only the direct neighbours are concerned by the ghosting but the pattern of ghosts can be extended if access to a more distant neighbourhood is needed. With regard to the model implemented in the HNFV-Code (Eqs. 3.3-3.5, 3.34-3.38 and 4.30-4.37), only the direct neighbours are needed. A two-dimensional representation of ghost components is provided in Fig. 6.10 for both FV and network domains. Since the ghosts are contained on the local memory, the access time is largely reduced compared to an off-unit traveling of the information. Then the developer decides when to update the "real" component from its copy, and vice versa. Since most of the operation on ghosts is about getting some information, instead of setting new values, this updating can actually be operated only a few time during the parallel execution, thus considerably reducing the number of MPI communications compared to a configuration without ghosts.

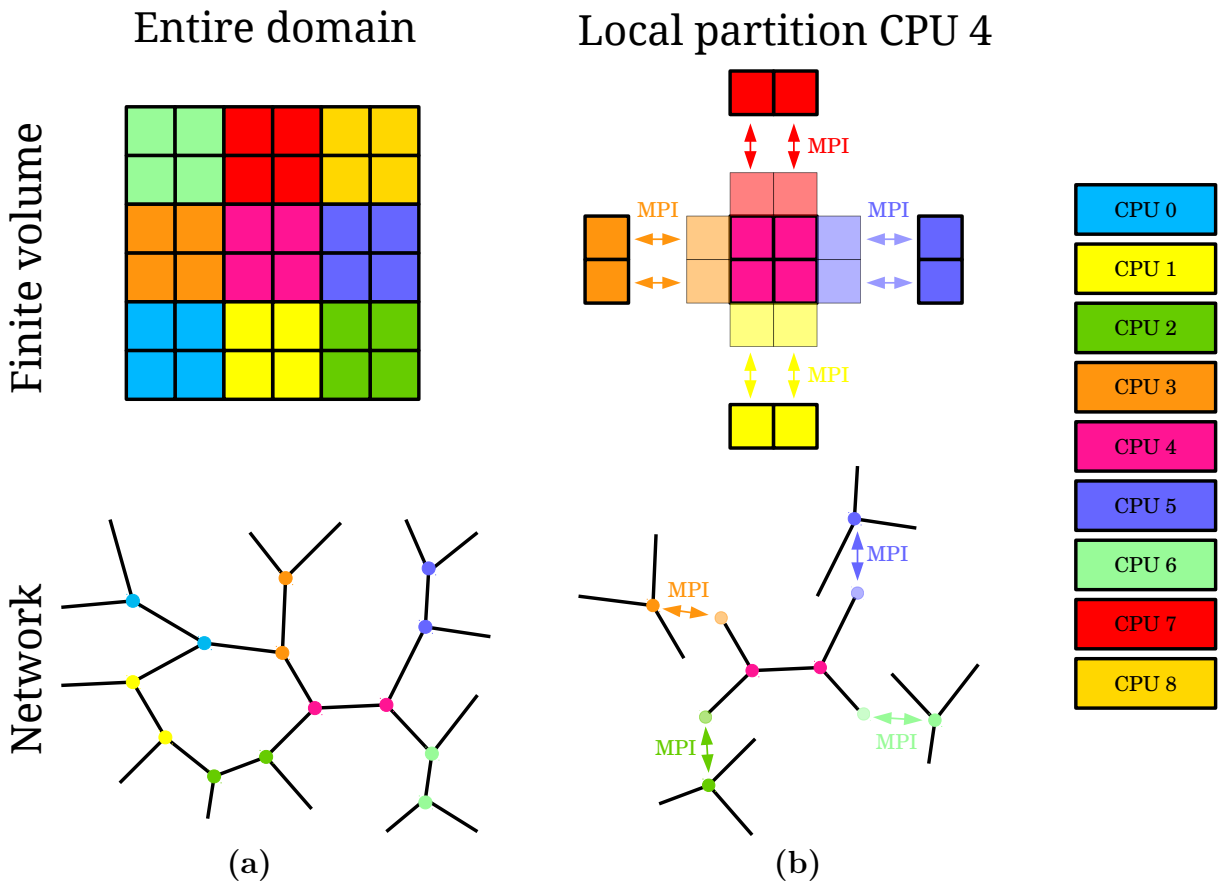

Figure 6.10: **Two-dimensional representation of FV and network ghost components.** **(a)** A FV domain of $6 \times 6 \times 6$ cells is distributed among 9 processing units and a 14-vertices network is partitioned among 7 processing units. Each color represents the territory of a processing unit. **(b)** The partitions are scattered for both FV and network domains to highlight the ghost components in the CPU 4. The ghosts are displayed with transparency and their colors remind that they are a copy of entities contained in other processing unit. In the case of a network, the edges at the interface between two partitions are also ghosts. The arrows represent the MPI communications induced by the updating of ghost values.

As a summary, partitioning is a crucial point to reduce the computational cost of a parallel program, especially with regard to the MPI communications [Kumar et al., 1994]. That is why it has been widely discussed for three decades now [Vanderstraeten and Keunings, 1995, Gilbert et al., 1998, Karypis and Kumar, 1999, Walshaw and Cross, 2000, Ahusborde and Glockner, 2011]. Moreover, a series of MPI-based partitioning libraries exist for applications to structured or unstructured meshes, e.g., PT-Scotch (http://www.labri.fr/perso/pelegrin/scotch/) or Chaco (http://www.cs.sandia.gov/CRF/chac_p2.html). In the next Section 6.3.3, we present the two specialized tools we use in the HNFV-Code.

6.3.3 Partitioning tools for HNFV-Code

The parallelization of the HNFV-Code is schematized in Fig. 6.11. The initial structure and boundary conditions are first read in sequential. Then the partitioning tool is in charge of reorganizing and distributing the initial dataset among the available processing units, according to the constraints mentioned in Section 6.3.2. Once the partitioning is done, all the processing units compute some local additional information, such as the vessels conductances in the network part or the harmonic permeability in the FV part. Then the matrix and right-hand side are assembled, each processing unit taking in charge its subgroups of rows defined by the partitioning. The solver is finally executed in parallel and the resulting pressure and flow rate vectors are gathered for the purpose of being written in the outputfiles.

As highlighted by the Fig. 6.11, the partitioning is a crucial part of the execution since the efficiency of all the following operations depend on it. In this section, we describe the partitioning algorithms that are used in the HNFV-Code, through two different tools: the DMDA object included in the PETSc library for the management of structured grids is perfectly adapted to the division of the FV mesh, and the ParMETIS library specialized in graph partitioning is optimized for the distribution of the unstructured network mesh among the processing units.

i. Partitioning a structured grid with the DMDA tool of the PETSc library.

The PETSc library contains a partitioning tool called DMDA (Distributed Arrays), which is specialized in partitioning structured grids. Let $M = M_x \times M_y \times M_z$ be the number of discretization cells of the FV domain, where M_x, M_y and M_z represent the number of cells in each direction. The goal of the DMDA tool is to divide the FV domain in parallelepipedic subdomains. To minimize

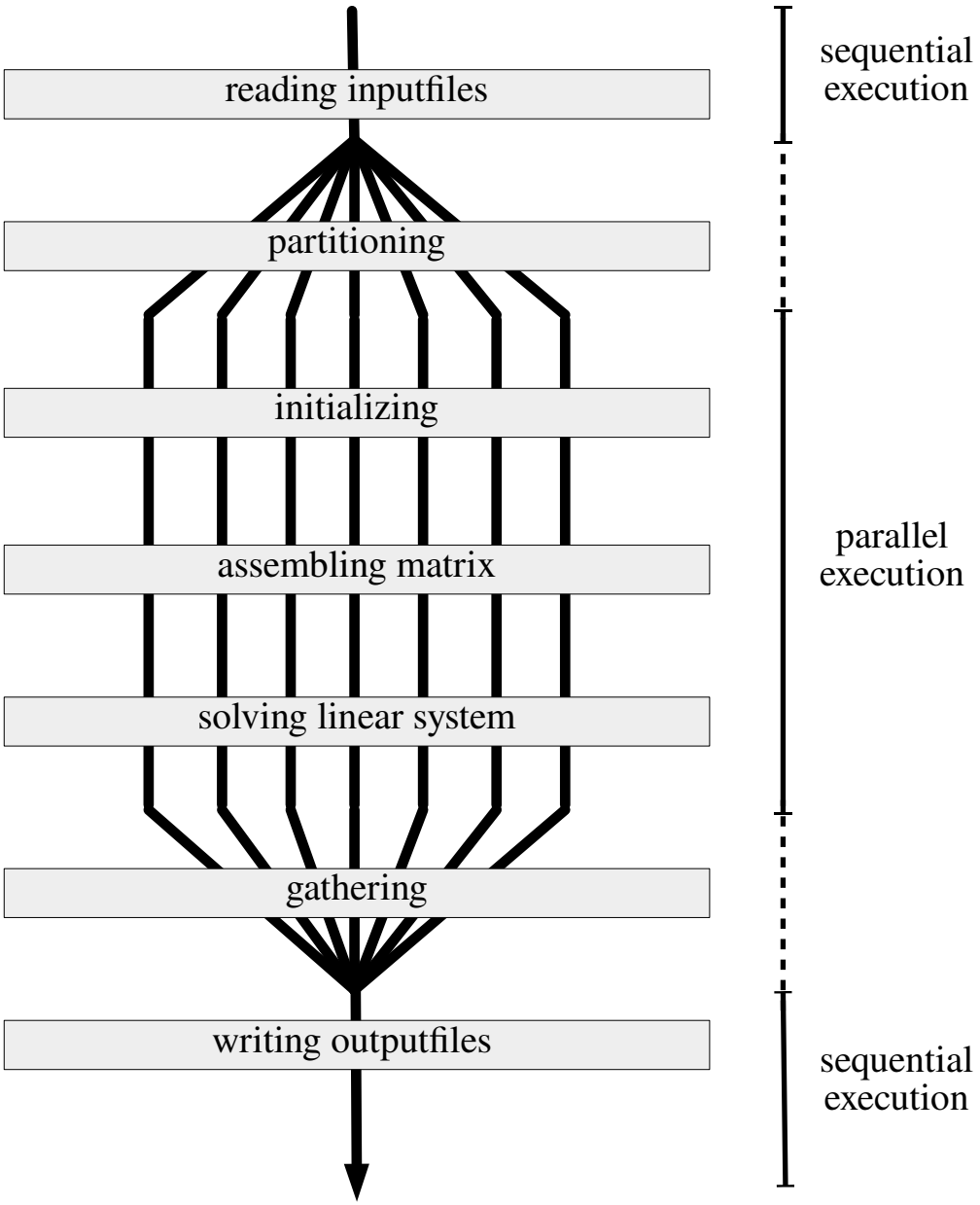

Figure 6.11: **Schematics of the parallelization of the HNFV-Code.**

the cost of exchange surface between the processing units, one strategy is to impose an homogenized partitioning per direction, meaning that "stairs" configurations such as Fig. 6.9**(c)** are prohibited. In particular, this constraint implies that a CPU does not communicate with more than 6 neighbouring CPUs. Assuming that this constraint is complied, let p be the total number of processing units, and p_x, p_y and p_z be the number of processing units assigned per direction, such that $p = p_x \times p_y \times p_z$. As an illustration, the partitioning of a three-dimensional FV domain discretized in $9 \times 7 \times 3$ cells among $p = 6$ CPUs is represented in Fig. 6.12. In this case, $p_x = 2$, $p_y = 3$ and $p_z = 1$.

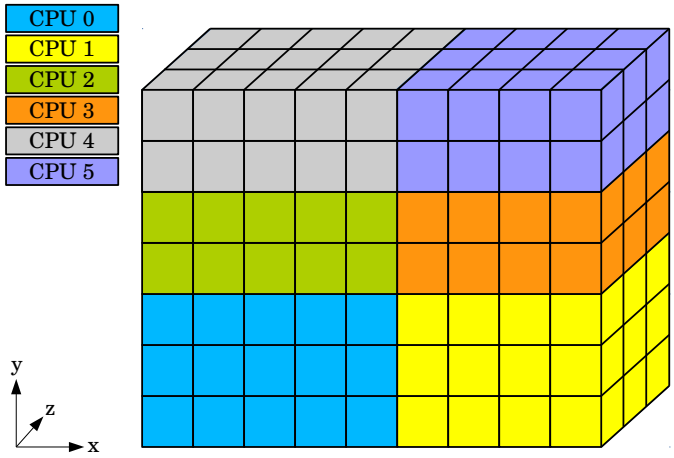

Figure 6.12: **Partitioning of a FV domain discretized in** $9 \times 7 \times 3$ **cells among 6 CPUs.**

In this section, we present the algorithm executed by the DMDA tool to compute p_x, p_y and p_z, provided that M_x, M_y and M_z are known. The corresponding extract of the source code is available in Appendix 8.6, lines 140-171. The entire source code in available online (http://www.mcs.anl.gov/petsc/petsc-3.5/src/dm/impls/da/da3.c).

In this script, the goal of the partitioning algorithm is to get as close as possible to the ideal workload balance formulated by

$$\frac{M_x}{p_x} = \frac{M_y}{p_y} = \frac{M_z}{p_z}, \tag{6.1}$$

with the initial constraint

$$p = p_x \times p_y \times p_z. \tag{6.2}$$

In particular, Eq. 6.1 implies

$$p_x = \frac{p_y M_x}{M_y} \text{ and } p_z = \frac{p_y M_z}{M_y}. \tag{6.3}$$

Combining Eqs. 6.1 and 6.3 yields

$$\begin{aligned} \frac{p_y M_x}{M_y} \times p_y \times \frac{p_y M_z}{M_y} &= p \\ \Rightarrow p_y^3 \times \frac{M_x M_z}{M_y^2} &= p \\ \Rightarrow p_y^3 &= \frac{p M_y}{M_x M_z}. \end{aligned} \tag{6.4}$$

From this equality, the value of p_y is set as

$$p_y = \left\lfloor 0.5 + \sqrt[3]{\frac{p M_y}{M_x M_y}} \right\rfloor, \tag{6.5}$$

where $x \mapsto \lfloor x \rfloor$ is the floor function and $x \mapsto \lfloor 0.5 + x \rfloor$ returns the closest integer to x.

If $p_y = 0$, then $p_y = 1$.

Otherwise, we decrement p_y until p/p_y is an integer, for consistency.

If $p_y = 0$, then $p_y = 1$.

At this stage, the value of p_y is defined. Similarly, we search for the values of p_x and p_z such that

$$\begin{aligned} p_x \times p_y \times p_z &= p \\ \Rightarrow p_x \times p_z &= \frac{p}{p_y} \end{aligned} \tag{6.6}$$

and

$$\begin{aligned} \frac{M_x}{p_x} &= \frac{M_z}{p_z} \\ \Rightarrow p_z &= \frac{p_x M_z}{M_x} \end{aligned} \tag{6.7}$$

Combining Eqs. 6.6 and 6.7 yields

$$\begin{aligned} p_x \times \frac{p_x M_z}{M_x} &= \frac{p}{p_y} \\ \Rightarrow p_x^2 &= \frac{p M_x}{p_y M_z}. \end{aligned} \tag{6.8}$$

From this equality, the value of p_x is set as

$$p_x = \left\lfloor 0.5 + \sqrt{\frac{p M_x}{p_y M_z}} \right\rfloor. \tag{6.9}$$

If $p_x = 0$, then $p_x = 1$.
Otherwise, we decrement p_x until $p/p_x p_y$ is an integer, for consistency.
If $p_x = 0$, then $p_x = 1$.

Now that the values of p_x and p_y are defined, Eq. 6.2 yields

$$p_z = \frac{p}{p_x p_y}. \tag{6.10}$$

Finally, if $p_x < p_z$ while $M_x > M_z$, we switch the values of p_x and p_z for consistency.

It is important to note that this algorithm cannot partition any domain of size $M_x \times M_y \times M_z$ among any number p of processing units. Indeed, some combinations of prime number can cause failure, in particular making the last operation (Eq. 6.10) unfeasible. For instance, a domain discretized in $11 \times 11 \times 11$ cells cannot be partitioned on 26 processing units. In this case, Eq. 6.5 returns $p_y = 1$, Eq. 6.9 returns $p_x = 5$, and Eq. 6.10 returns $p_z = 26/5$, which is not an integer. In case of failure, error messages are printed on screen for explanation.

ii. Partitioning a graph with the ParMETIS library.

Contrary to the FV mesh, the network part presents an unstructured architecture, meaning that a connectivity matrix is required to describe how the vertices are connected with each other. As depicted in Fig. 6.8, this implies a more complex partitioning process compared to the division of a structured grid in parallelepipedic domains. This actually yields a complex NP-complete problem. However, many algorithms based on heuristic approaches have been developed that result in more or less reasonable partitioning. The choice between the existing techniques actually relies on the ratio "partitioning quality" over "time consumption" needed by the developer. For detail, an overview of these methods is presented in the technical report of [Schloegel et al., 2000a], or in the thesis of [Trifunovic, 2006].

For the purpose of partitioning the network in the corresponding part of the HNFV-Code, we chose to work with the ParMETIS library developed by [Karypis et al., 2003]. This choice has mainly been motivated by the fact that the PETSc library provides an interface with it. Furthermore, ParMETIS is widely used, thus well documented and discussed on online forums. Unfortunately, the intermediate use of the PETSc library reduces the access to ParMETIS operations since only a few functionalities are proposed via PETSc commands. Referring to the source code (pmetis.c), PETSc makes the link

with only three ParMETIS routines: *ParMETIS_V3_Mesh2Dual* converts structured or unstructured meshes into graphs for the use of one of the two other routines; *ParMETIS_V3_PartKway* partitions unstructured graphs; and *ParMETIS_V3_AdaptiveRepart* re-partitions meshes in case of adaptative mesh refinement. However, even if the investigation in partitioning optimization is limited using the PETSc interface, we consider that the resulting gain in implementation time prevails, especially because the entire HNFV-Code relies on PETSc structures (matrix and vectors). Moreover, the function *ParMETIS_V3_PartKway* we are interested in is a very efficient partitioning tool, which satisfies our current demands.

The *ParMETIS_V3_PartKway* routine is based on the multilevel k-way partitioning algorithm [Karypis and Kumar, 1997, Schloegel et al., 2000b]. Briefly, this algorithm is composed of three steps, which are schematized in Fig. 6.13:

- *coarsening*: the initial graph is successively coarsen by merging pairs of adjacent vertices. The operation is repeated until the graph is composed of k vertices, hence the name of the multilevel k-way algorithm. The value of k is chosen according to the complexity of the coarsening algorithm (up to the number of available processing units in case of rapid algorithm);
- *initial partitioning*: the coarsest graph is divided into k partitions, each partition containing one vertex;
- *uncoarsening*: the coarsening process is reversed and the partitioning is progressively refined until retrieving the initial graph. At each step, the KL/FM-type refinement algorithm [Kernighan and Lin, 1970, Fiduccia and Mattheyses, 1988] is used to optimize the new finer partitioning. Based on the partitioning of the previous coarser graph, the principle of this algorithm is to move each vertex from a partition to another, one at a time, then to compute the gain this displacement represents with regard to the workload balance and the number of edgecuts. This gain can be positive or negative. The vertex is finally relocated on the partition related to the maximal gain.

By avoiding applying any partitioning algorithm directly on the initial graph but on a coarser related graph, the multilevel k-way partitioning algorithm has been shown to produce partitioning of very high quality, while being very fast.

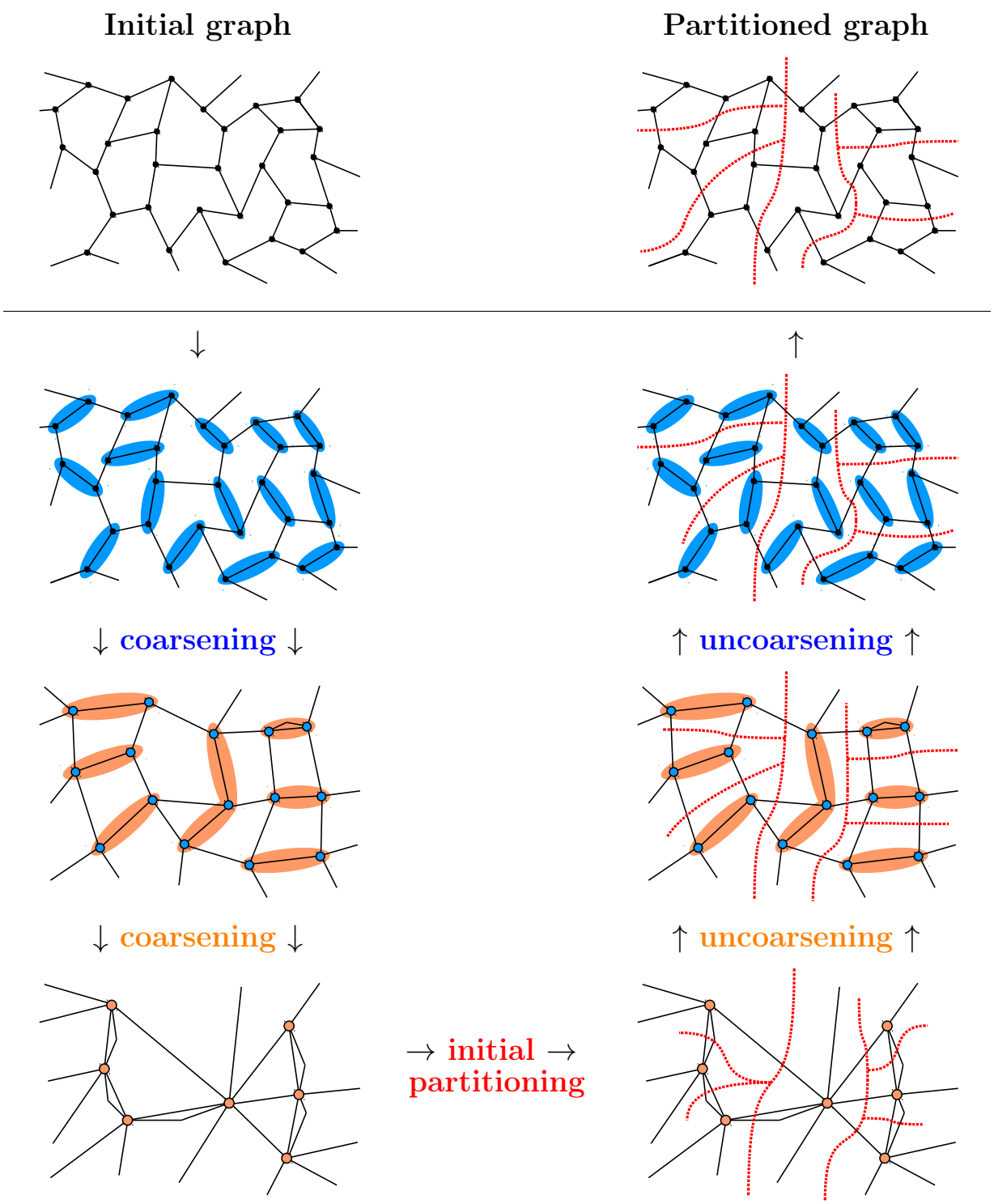

Figure 6.13: **Schematics of the three steps of the multilevel k-way partitioning.** First, the initial graph is coarsen until obtaining a graph with k vertices (left column). Then the coarser graph is cut into k partitions, each of them containing one vertex (last row). Finally, the graph is uncoarsen and the partitioning refined until retrieving the initial structure (right column).

An additional complexity of the graph partitioning compared to the partitioning of a structured grid is the management of the cut edges. Indeed, each cut edge is a component of the structure that is at the interface between two partitions, thus does not clearly belong to one or the other. In the HNFV-Code, we decide to duplicate these edges, as schematized in Fig. 6.14**(b)**. This strategy is very efficient as long as most of the access operations on the cut edges are about getting some values (e.g. length or conductance), since no MPI communication is required. This would not be the case if the edge were assigned to one partition and ghosted on the other. However, if a value carried out by a cut edge is changed, it has to be updated on the other partition. For that purpose, each duplicated edge has a ghost on the other partition (see Fig. 6.14**(c)**). The same strategy is applied to the points that discretize a cut edge. Concerning the model implemented in the HNFV-Code and presented in this manuscript, the access operations mainly are about getting values, since no modification is a priori brought to the graph once it has been partitioned. Thus this approach greatly reduces the cost of MPI communications.

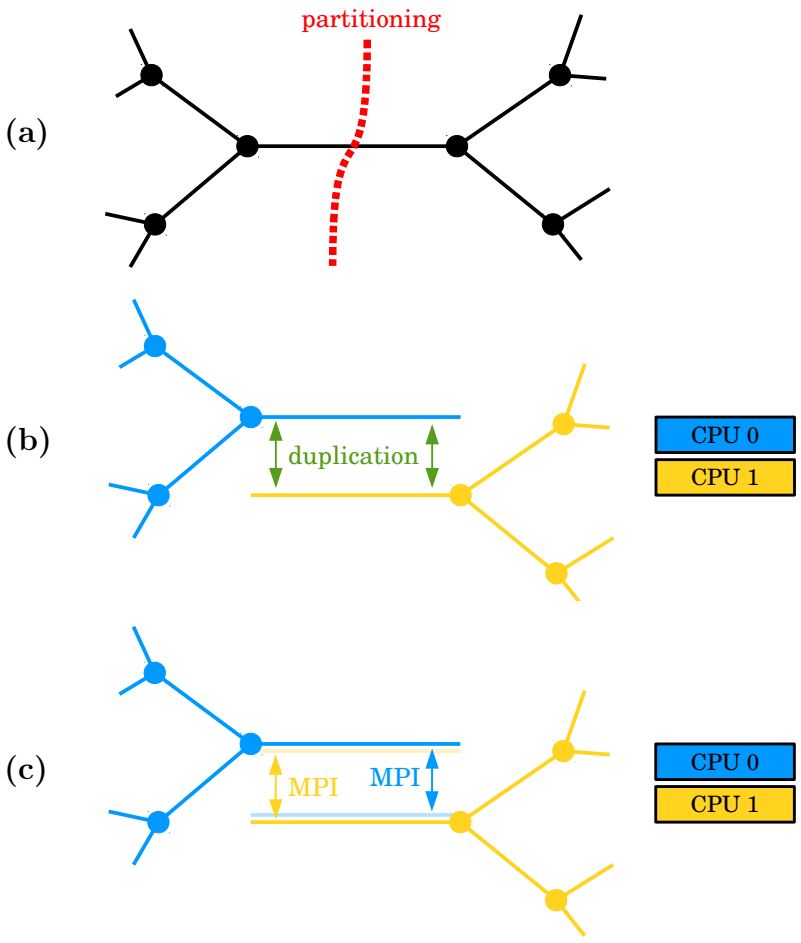

Figure 6.14: **Schematics of the duplication of edges that have been cut by the graph partitioning.** **(a)** A simple network is partitioned among two CPUs. By distributing the vertices, the graph partitioning cut edges. **(b)** In the HNFV-Code, we consider that the cut edge belongs to both partitions, thus we duplicate it. **(c)** If a value carried out by the edge is changed on one partition, it has to updated on the other one. For that purpose, each duplicated edge has a ghost on the other partition, enabling MPI communications.

iii. Management of the reordering induced by the partitioning.

In fact, the partitioning implies a renumbering of the main components (FV cells or inner vertices), as schematized in Fig. 6.15**(a)** for the network part (similar issue appears in the partitioning of the FV domain). This also implies a reordering of the secondary components (edges and points that discretize the edges in the network). Thus the natural-ordering of the user does not correspond to the inner-ordering within the code. For the purpose of returning the outputs in the same format than the inputs, a correspondence table is kept between the indexations before/after partitioning. This table is also needed in case of interaction with the user during the execution.

Furthermore, each partition has its own local renumbering of the components, as schematized in Fig. 6.15**(b)**. For instance, the vertex or cell #32 may be the vertex or cell #3 of the 8th partition. The correspondence table between the global and local indexations must also be kept during the parallel execution.

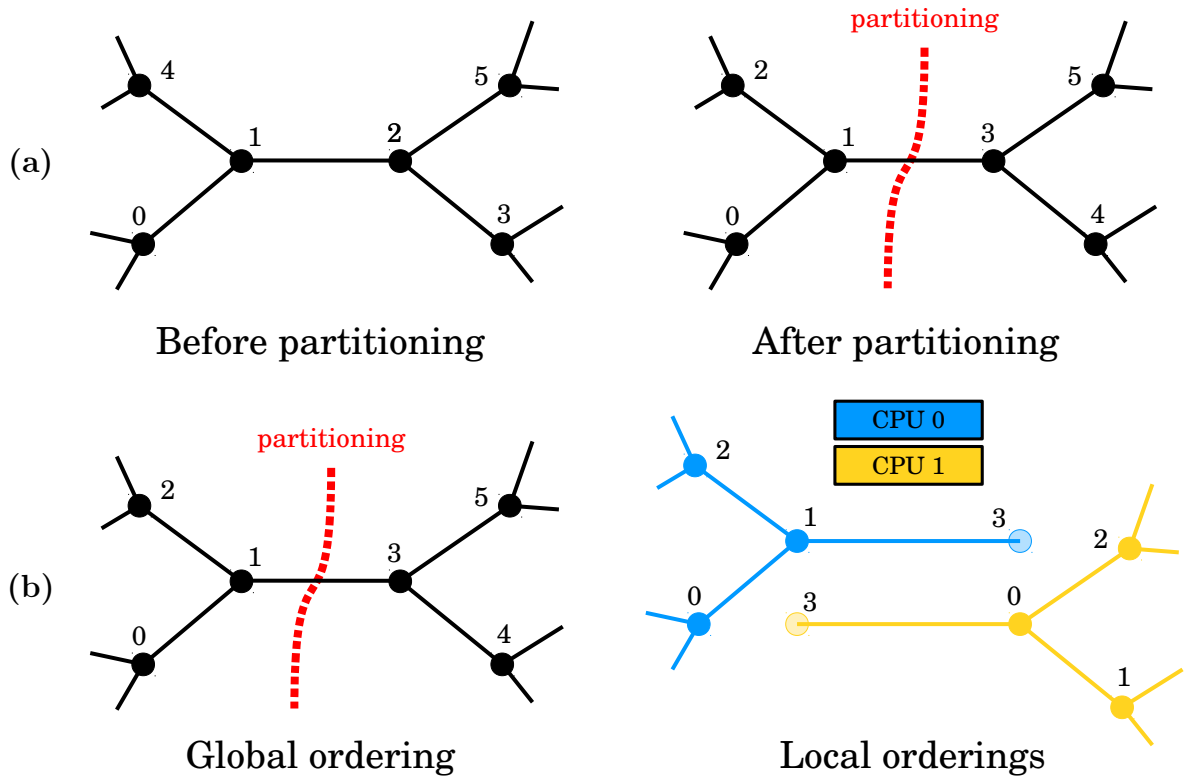

Figure 6.15: **Reordering induced by the graph partitioning.** **(a)** The natural-ordering (before partitioning) of the user does not correspond to the inner-ordering (after partitioning) within the code. **(b)** Each partition has its own local ordering, which starts from 0.

iv. Impact of the partitioning on a hybrid configuration.

A hybrid configuration corresponds to the coupling between a network component and a FV domain, as schematized in Fig. 6.16. At the interface between the two structures, the boundary vertices of the network become coupling points where the coupling model is applied. To build the coupling condition at a given coupling point, we need some information from both the network and the FV cells located in the neighbourhood (see Eqs 4.30-4.37). From a parallel point of view, this corresponds to additional MPI communications if the coupled vertex is not in the same partition than the coupled cell (and its direct neighbours). This situation is pointed out by red arrows in Fig. 6.16.

In the HNFV-Code, the FV and network parts are implemented in two separate frameworks, so do the corresponding partitioning processes. Even in the hybrid context, the FV and network structures are both independently partitioned among all the available processing units, as displayed in Fig. 6.16 for four processing units. They are further initialized separately during the execution. Taking into account the complexity of the two partitioning tools and the fact that the combination of the two partitioning tools must be handled by the developer, we decided to allow the additional MPI communications mentioned above.

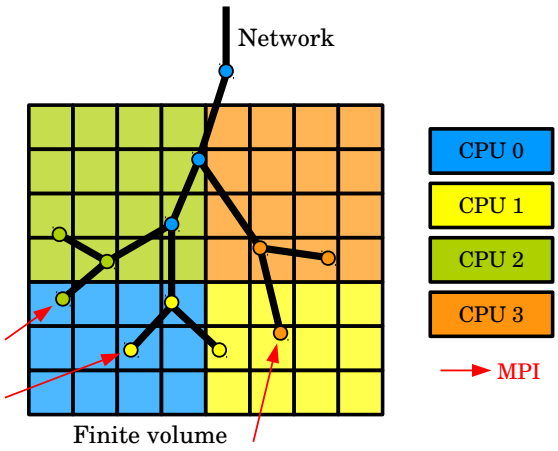

Figure 6.16: **Impact of the partitioning on a hybrid configuration.** Additional MPI communications, highlighted by red arrows, occur if a coupled vertex of the network part is connected to a FV cell that belongs to an other partition.

Now that we have presented the parallelization paradigm that we apply in the HNFV-Code and the system we have adopted to minimize the inter-units communications, we evaluate the performance of the resulting parallelized code in the next section.

6.3.4 Code performance

In this section, we evaluate the performance of the code parallelized according to the strategies presented above. For the purpose of assessing the efficiency of each kind of paradigm used for parallelization (DMDA tool for the FV domain, ParMETIS library for the network part, and DMDA/ParMETIS combination for the coupling part), this evaluation is led for the FV and network parts separately, then for the coupling part. The performance of the code is determined according two common notions of scalability: the *strong* and *weak* scalings.

Strong scaling. The *strong scaling* evaluates the acceleration of the code when adding computational resources to a reference problem. In other words, the problem size is fixed and we observe the impact of increasing the number of processing units on the execution time. In this case, a parallelized program is considered as perfect if the execution time is divided by N when the number of processing units is multiplied by N, based on a reference computation.

Let t_{ref} be the execution time of this reference computation executed on N_{ref} processing units, and t_N the execution time when the problem is solved on N processing units. Ideally, we have

$$t_{ref} N_{ref} = \alpha t N, \quad \text{with } \alpha = 1,$$

i.e.

$$\frac{t_{ref}}{t_N} = \alpha \frac{N}{N_{ref}}, \quad \text{with } \alpha = 1.$$

The ratio t_{ref}/t_N is commonly termed *speedup* and is considered as perfect if scaling linearly. In the graphs below, we estimate the efficiency of the parallelization of the code by plotting this speedup against the ratio N/N_{ref}.

As mentioned above, we expect an ideal linear slope of 1. In fact, two kinds of deviations to the linear trend may occur when executing parallelized programs:

- for low numbers of processing units, bottlenecks may occur with regard to memory management if the number of units does not provide enough storage. In this case, the reference time is underestimated, resulting in an overestimation of the speedup. Such deviation is corrected by defining a reference computation involving more and more processing units, until representing a coherent speedup, as illustrated in Fig. 6.17;

- for high number of processing units, the time-consumption induced by the MPI communications eventually become more important than the benefit of adding computational resources to the total execution time of the program. Thus the speedup progressively reaches a plateau. Such trend is technically inevitable. One goal of evaluating the strong scaling of a parallel program is actually to find a "sweet spot" that corresponds to an execution in a reasonable amount of time, before reaching the saturation point with regard to MPI communications.

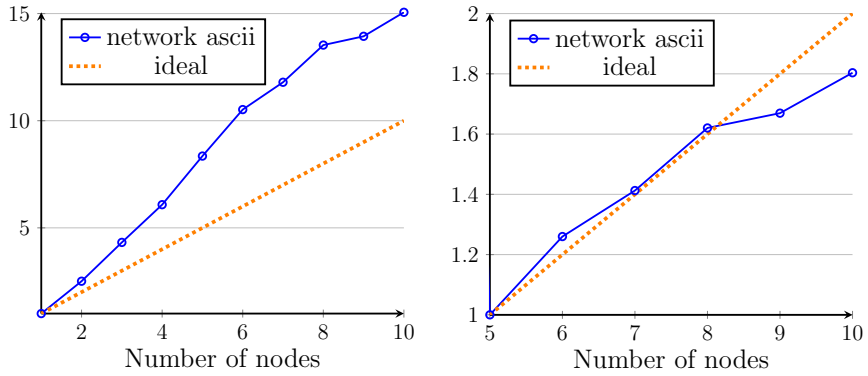

Figure 6.17: **Example of speedup overestimation.** The speedup is plotted for flow computation in a network of ∼1 million vertices. **(a)** When taking the computation on one node as a reference, the speedup is overestimated. (b) When taking the computation on 5 nodes as a reference, the speedup is coherent.

Weak scaling. The weak scaling evaluates the robustness of the parallelization of a code when handling bigger and bigger problems. In this case, the size of the problem increases as the number of processing units, so that the workload of each processing unit remains constant.

Let $t_{ref}^{p_{ref}}$ be the execution time of the computation for a problem of size p_{ref} on N_{ref} processing units, and $t_N^{p_N}$ be the execution time of the computation involving a similar problem of size p_N on N processing units. If $p_N = {}^{N}/_{N_{ref}} p$, thus a perfectly parallelized program yields

$$t_{ref}^{p_{ref}} = t_N^{p_N}.$$

Configuration of the computations. All the graphs below result from computations run on 1 to 10 nodes of the EOS supercomputer (CALMIP, France, Grant 2016-P1541). Each of these nodes contains 20 cores *Intel(R) Xeon(R) CPU E5-2680 v2 @ 2.80GHz*. To avoid memory swap, only 10 cores per node are active here.

The writing of output files has not been parallelized yet, thus no outputs are generated in the computations below to ease the evaluation of the scalability of the code. The reading of input files have also not been parallelized but is an inevitable step. The impact of this sequential part of the execution will be studied in the graphs below.

Scaling: Finite volume part. The flow has been solved here in a finite volume domain discretized in 10 millions of cells. For the purpose of focusing on the steps of the computation that take most of the execution time, the program has first been divided in main steps (e.g. reading, initialization, solving). The execution times of each of these steps are reported in Fig. 6.18. As expected, the solving of the linear system (blue line) takes most of the execution time, while the others steps are negligible, including the sequential reading of the input files. Note that the "solve" step includes both the assembling of the matrix and the solving of the linear system.

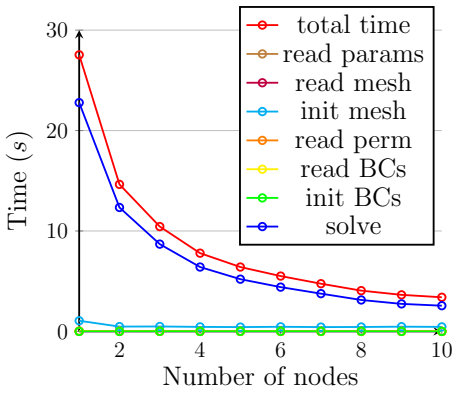

Figure 6.18: **Detailed report of the execution time of a flow computation in the FV domain.**

In Fig. 6.19, the speedup of the FV part of the code is plotted for both the solving step only, and the complete execution. The comparison with the ideal linear trend (orange dotted line) highlights the efficiency of the parallelization tools used for the parallelization of the FV part. The plateau representing the saturation point with regard to MPI communications is not even reached for 10 nodes, meaning that the DMDA tool is very efficient in limiting the number of MPI communications when partitioning the FV domain.

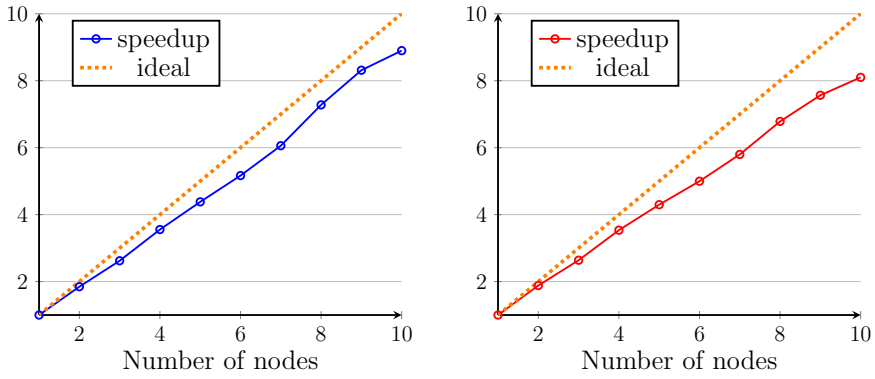

(a) Solver (b) Total

Figure 6.19: **Speedup of the FV part of the code. (a)** The speedup corresponding the solving of the linear system is plotted. **(b)** The speedup corresponding to the complete execution of the computation is plotted.

For the purpose of estimating the robustness of the parallelization with regard to the size of the problem (weak scaling), a similar computation involving a smaller FV domain of 1 million of cells has been run on 1 node. Such computation took 2.03 s, while the execution of the problem with 10 millions of unknowns took 3.4 s on 10 nodes. The small difference between these execution times shows that the parallel complexity of the FV part, i.e. the amount of MPI communications, increases linearly with the size of the problem. This suggests that the FV part can handle computations involving an important amount of unknowns.

Scaling: Network part. The flow has been solved here in a network composed of ∼1 million of vertices. As above, the computation has been divided into main steps and their execution times are reported in Fig. 6.20**(a)**. Contrary to the execution in the FV domain, the reading of input files (purple and yellow lines) is not negligible in the network part. In particular, the sequential reading of the network structure ("read mesh", purple line) takes more time than the solving of the linear system for a number of processing units larger than 3. This is due to the fact that the description of the connectivity of an unstructured network requires much more information than the description of a Cartesian FV grid. As a result, the trend of the total execution time (red line) is eventually governed by the time the code spends reading the input files.

To deal with this issue, one solution is to use the HDF5 binary format instead of an ASCII format, as already discussed in Section 6.1. As displayed in Fig. 6.20**(b)**, this strategy indeed considerably reduces the time spent in reading the network structure ("read mesh", purple line). This reduction is less obvious for the reading of the boundary conditions ("read BCs", yellow line) since this file

contains far fewer information. A a consequence, the trend of the total execution time is improved, since it decreases according to the time spent in solving the linear system.

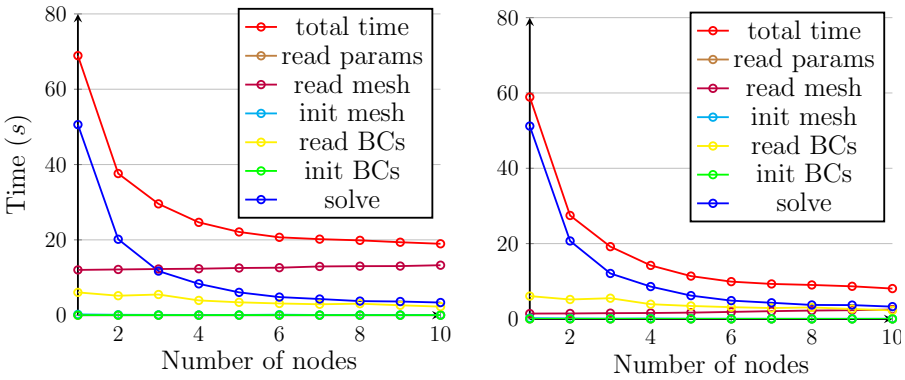

(a) Network - ascii **(b) Network - hdf5**

Figure 6.20: **Detailed report of the execution time of a flow computation in the network.**

In Fig. 6.21, the speedup of the network part is plotted for both the solving step and the complete execution of the computation. As for the FV part, the PETSc solver shows a very good scalability, since the linear slope almost overlaps the ideal one in Fig. 6.21**(a)**. In the solving step, the use of ASCII or HDF5 format makes no difference. However, as displayed in Fig. 6.21**(b)**, the scalability of the entire execution is considerably improved by the use of the HDF5 format. Furthermore, the beginning of the plateau, which highlights the limitation of the parallelization of the network part, starts at a larger number of processing units when using HDF5 format.

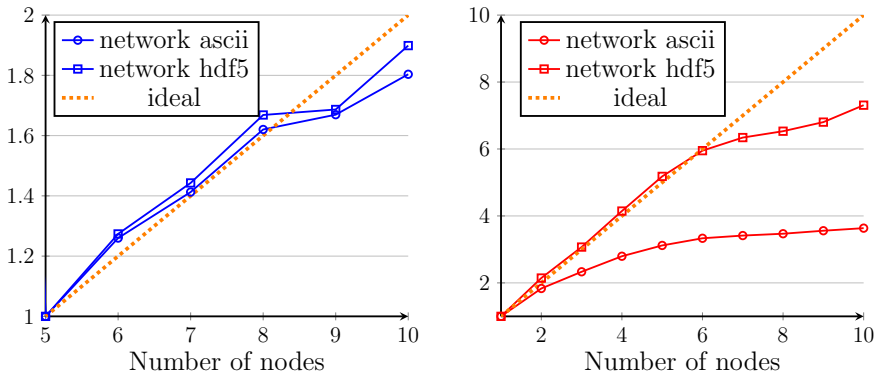

(a) Solver **(b) Total**

Figure 6.21: **Speedup of the network part of the code. (a)** The speedup corresponding the solving of the linear system is plotted. **(b)** The speedup corresponding to the complete execution of the computation is plotted.

With regard to weak scaling, the flow has been solved in a network containing 0.5 million of vertices (described in ASCII format) for comparison. On 1 node, this computation took 3.65 s, while the

computation involving 1 million of vertices and executed on 2 nodes took 37.61 s. This ratio of 10 between the two execution times demonstrates that the parallel complexity of the network part does not evolve linearly with the size of the problem. In other words, the amount of MPI communications does not increase linearly with the size of the network. Again, this is due to the non-structured architecture of the network component. To deal with this issue, libraries including optimized graph coverage should be used (e.g. the Boost Graph Library http://www.boost.org/doc/libs/1_39_0/libs/graph/doc/index.html), in particular when initializing the network and assembling the matrix.

Scaling: coupling part. For the purpose of investigating the scalability of the coupling part, which combines the FV and network parts, a network containing 56 600 vertices has been coupled to a FV domain discretized in ∼3 millions of cells, resulting in 27 400 coupling points. In this study, the input files concerning the network part used ASCII format. However, as displayed in Fig. 6.22, the time spent reading the input files is negligible, due to the small number of vertices compared to the number of FV cells. As reported in Fig. 6.22, the execution time of the complete computation corresponds to the time spent solving the linear system. The other steps are negligible.

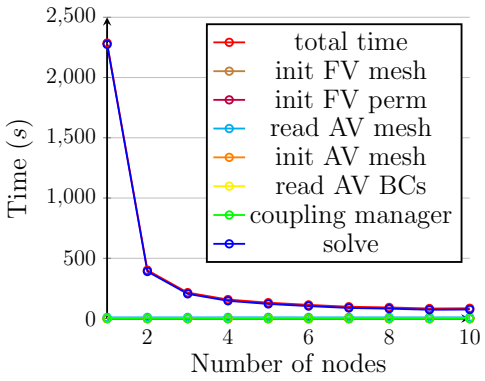

Figure 6.22: **Detailed report of the execution time of a flow computation in a hybrid configuration.**

As a consequence, the speedup of the complete execution is almost identical to the speedup of the solver, as displayed in Fig. 6.23. Both speedup are in very good agreement with the ideal linear slope (orange dotted line), showing that the strategies adopted for the parallelization of the coupling part ensures a good acceleration of the code.

With regard to weak scaling, two computations have been compared: the first one involves a network containing 56 600 vertices coupled to a FV domain discretized in $300 \times 23 \times 70 = 483\,000$ cells; the second involves ten times more unknowns by coupling a network containing 566 000 vertices to a FV domain discretized in $3000 \times 23 \times 70 = 4\,830\,000$ cells. The first was executed on 1 node

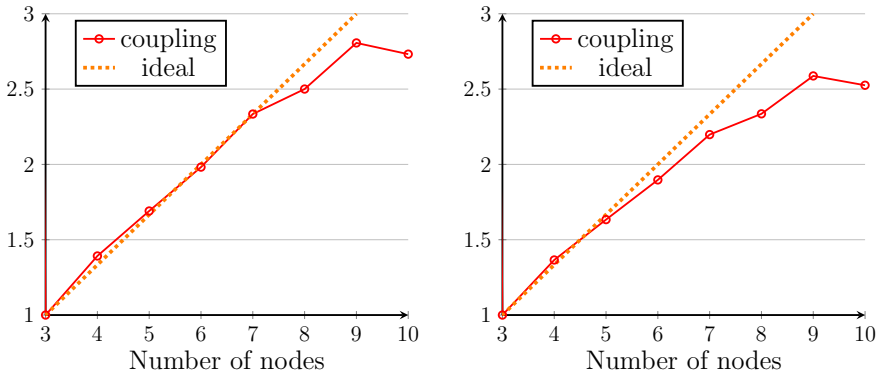

(a) Solver **(b) Total**

Figure 6.23: **Speedup of the coupling part of the code. (a)** The speedup corresponding the solving of the linear system is plotted. **(b)** The speedup corresponding to the complete execution of the computation is plotted.

in 159.29 s, while the second one has been executed on 10 nodes in 657.94 s. The ratio of 4.11 between these two execution times mainly stems from the non-linearity of the parallel complexity of the network part highlighted above. However, since this penalization is reduced since the number of FV cells is more important than the number of vertices in a coupling configuration.

Conclusion about the code scaling. With regard to strong scaling, the HNFV-Code presents a good efficiency in all parts of the code. The FV part is the most efficient and reliable part. The network part is mainly limited by the sequential reading of the input files. However, this impact can be reduced by using HDF5 binary format. The coupling part present an average efficiency between the FV and the network part, meaning that the coupling process implemented in the code does not affect its global scalability.

With regard to weak scaling, the FV part, which treats a structured grid, also presents a good efficiency. On the contrary, the network part, which treats a non-structured component, presents a low efficiency. More time should be spend in optimizing the process of graph coverage embedded in the initialization step and the assembling of the matrix (e.g. by using libraries specialized in graph theory). The coupling part is affected by the low efficiency of the network part. However, the number of vertices is lower than the number of FV cells in realistic coupled configurations, implying that this penalization will have less impact on the hybrid approach than on complete network computations.

7 Conclusions and perspectives

7.1 Conclusions

7.1.1 Challenges

In the present work, we aimed at developing new simulation tools for modelling blood flow dynamics at mesoscopic scale in the whole human brain. For that purpose, we faced two main challenges:

- the multiscale architecture of the brain microcirculation, which makes the development of relevant numerical models difficult;
- the computational cost induced by whole-brain simulations, even using reduced-order models.

This specific aim is part of the BrainMicroFlow project (http://brainmicroflow.inp-toulouse.fr/en/home.html), which aims at combining both the brain imaging techniques and the numerical models at a clinically relevant scale. This combination would represent a valuable tool for understanding better the physiological mechanisms involved in the human brain microcirculation, which is crucial for the study of the neurovascular coupling. In a long term view, this would also enable the development of new diagnosis procedures based on the relationship between brain hemodynamics (e.g. regional blood flow), mass transfers (e.g. diffusion of markers) and pathologies, such as Alzheimer's Disease.

7.1.2 A new hybrid approach

For that purpose, we presented a new hybrid approach for the modelling of blood flow distributions in the human brain microcirculation. In this approach, the capillary bed is replaced by a continuum where blood flow is characterized by effective properties (e.g. permeability) representative at mesoscopic scale. The largest arteriolar and venular vessels are modelled using a standard network approach, with a description of both the architecture and the hemodynamics at the scale of individual vessels.

We first improved the existing hybrid approaches by proposing a new way of computing the effective permeability and viscosity that characterize the flow in the continuum. Both are usually lumped together in a single effective parameter. The particularity of our method is to differentiate the effective permeability, which describes the impact of the microscopic geometry of the medium on

blood flow at mesoscopic scale, from the effective viscosity, which represents the rheological impact of the Fahraeus-Lindqvist effect at mesoscopic scale.

Furthermore, our hybrid approach is new in the sense that it includes a multiscale coupling model at the interface between these two frameworks. A similar, but somehow simpler, coupling issue exists in petroleum engineering when describing flow fields around wellbores in porous rocks. Thus, we took inspiration of the Peaceman well model developed in this context. The adaptation of such a coupling model to the context of brain microcirculation induced important modifications and improvements. The resulting multiscale model relies on analytical approximations of the pressure field in the close vicinity of the coupling points. In our case, we expressed a linear relationship between the pressure at the endpoint of a given coupled arteriolar or venular vessel, and the neighbouring FV cells. The main particularity of this coupling model is that it accounts for the fact that variables at separate scales have distinct physical meanings in the network and continuum parts. We highlighted the need for such a multiscale coupling model by comparing our results with simple hybrid (SH) approach, where a simple condition of pressure continuity is imposed at the interface between the arteriolar and venular trees, and the continuum.

7.1.3 Accuracy and robustness of our hybrid approach

We validated our approach by comparison with a CN network approach, where blood flow is modelled using a classical network approach in the whole microvasculature, including the capillaries. Tests involving idealized configurations led us to conclude about the robustness of the multiscale coupling model to morphometrical and topological constraints that typically occur in the brain microcirculation (e.g. high density of couplings). By progressively complexifying both the capillary and the arterio-venular vasculatures, we further highlighted the accuracy of the hybrid approach in describing blood flow dynamics in anatomically realistic configurations. Further, we pointed out the limitations implied by the main hypotheses made for the development of both the FV scheme and the coupling model (e.g. isotropy). We also gave clues for further extensions of the hybrid model in the future. More details about potential extensions will be provided in the Perspectives section below.

7.1.4 Computational gain of the hybrid approach

The implementation of our hybrid approach yields three main advantages with regard to computational performance:

- the multiscale coupling model presented in this work yields a strong coupling between the network and the continuum parts, i.e. a single linear system to solve for the two frameworks . This represents an important gain in time compared to alternative iterative coupling methods;
- by replacing the capillary network by a homogenized domain discretized on a coarse FV grid, the number of unknowns of the global linear system is considerably reduced;
- considering the capillary bed as a discretized continuum implies the manipulation of a structured component (Cartesian FV grid) instead of an unstructured one (network associated to a connectivity table). This considerably reduces the amount of data to store, thus read and write, for the description of the architecture of the domain. Furthermore, with a view to HPC, this also tremendously reduces the complexity of the partitioning process for simulations that will be run on several processing units.

In the most complex configuration presented in this manuscript, which represents only $\sim 100\,000$ unknowns for the CN approach, and $\sim 1\,000$ unknowns for the hybrid approach, the combination of these advantages already led to an acceleration of $\sim$30 compared to CN simulations. As detailed in Section 7.2 below, the acceleration increases with the size of the problem. Ultimately, this trend will make hybrid simulations of blood flow dynamics possible in the whole human brain, while CN simulations will be untractable.

Implementation of the hybrid approach in a reliable, performant and flexible code. The hybrid approach has been implemented in a code called HNFV-Code, which has been thought as a long-term computational tool. As part of a larger wide-variety numerical platform involving several developers, special care has been taken in adopting efficient coding strategies for the purpose of ensuring collaboration, reliability, performance and portability. For instance, the current use of a central repository, the systematic implementation of tests, the parallelization of the code, and the automatic generation of a detailed documentation, meet each of these four objectives, respectively. While time-consuming, such a strategy has already proven itself in the mid-term during this thesis.

One of the most important design of the HNFV-Code is its HPC architecture. Indeed, it has been fully parallelized using MPI standards and specialized partitioning tools. The scalability of the code, i.e. its efficiency with regard to parallelized executions, has been estimated by strong and weak scalings in each part (FV, network and coupling parts). Such a study has been led on up to 100 cores, i.e. 10 nodes, of the EOS supercomputer (CALMIP, France). The strong scalings

showed very good results in all parts of the code. However, the weak scalings highlighted the fact that the network part could be optimized with regard to the handling of unstructured components on a large number of processing units. In hybrid configurations involving both FV and network parts, the efficiency of the code is affected by the low performance of the network part. Nevertheless, this lost in efficiency is tempered by the very good efficiency of the FV part, since the number of network vertices is typically one order of magnitude lower than the number of FV cells in these cases.

Finally, the accuracy and computational gain of the hybrid approach, combined to the HPC environment of the HNFV-Code, opens the way to whole-brain simulations, as detailed in the Perspectives section below. By contrast, such simulations are clearly untractable using standard network approaches. Furthermore, the independence of each part of the code (FV, network or coupling parts) makes it highly flexible, easing the improvement of models for further extensions of the hybrid approach in the future (e.g. mesh refinement in the FV part or complexification of the coupling equations).

7.2 Perspectives: toward whole-brain simulations and extension of the hybrid approach

7.2.1 Towards whole-brain simulations

The HNFV-Code has been designed for HPC with a view to whole-brain simulations of blood flow dynamics. In this section, we quantify the acceleration provided by the combination of the hybrid approach and the HPC implementation, compared to CN simulations, for volumes up to $\sim$16.2 cm^3, which has not been performed in the context of the human brain microcirculation yet. With a view to additional levels of complexity (e.g. mass transfers), we further provide some ideas of improvement with regard to the computational performance of the code.

Potential of the HPC code In Table 7, the performance of the HNFV-Code is quantified for simulations of blood flow in increasing volumes of the brain. The smallest configuration (AVA) corresponds to the most complex simulation presented in Section 5, i.e. to three anatomical arteriolar and venular trees. Here, these trees are coupled with either 3-regular capillary networks for CN simulations, or equivalent homogenized representations for hybrid simulations. Increased volumes are obtained by repeating this reference pattern in the two directions parallel to the cortical surface.

All simulations have been led on the EOS supercomputer (CALMIP, France). They involved from 1 to 500 cores *Intel(R) Xeon(R) CPU E5-2680 v2 @ 2.80GHz*, depending on the size of the problem. For the purpose of comparison, each execution time has been linearly reported to 1 core in Table 7. For instance, an execution time of 60 s on 10 cores has been reported as 60×10=600 s on one core in the table. Since the time execution depends on the complexity of network representations, it is important to note that only the orders of magnitude of the factors reported in this table are representative. In particular, the use of more or less complex vascular structures for the representation of the capillary bed will importantly affect the time execution of CN simulations.

Compared to CN simulations, the hybrid approach leads to an important gain with regard to the number of unknowns involved in the linear system to solve. This gain seems to remain constant (∼500), regardless of the volume of the cortex. To assess this result, more simulations should be run in larger volumes. However, CN simulations are still untractable for such volumes, due to memory issue implied by the sequential reading of the network input files.

With regard to the time execution, it has been proven in Section 6.3.4 that the format of the input files of the network considerably affects the performance of the code. This is confirmed here since time execution of the AVA 3×3 configuration decreases from 13 400 s to 8 700 s when replacing the ASCII format by the HDF5 binary format in CN simulations. Because the number of vertices in the hybrid approach is about 1 000 times lower than in CN simulations, this gain does not appear in the hybrid results. Indeed, time executions are of the same order for both files format in the hybrid AVA 3×3 configuration. Therefore, comparison in time are only relevant for simulations involving the same format of input files. Considering simulations involving ASCII files, the gain in time increases with the size of the problem, from ∼137 for simulations in 6.48 mm^3 to ∼1 027 for simulations in 58.32 mm^3. Again, simulations should be run in larger volumes to assess this result.

Although memory issues prevented CN simulations to be run in volumes larger than ∼60 mm^3, such a volume is of the same order of magnitude than the biggest volume presented in the literature (∼30 mm^3, [Linninger et al., 2013]). Further, the results displayed in Table. 7 highlight the benefit of using the hybrid approach. Indeed, the hybrid simulations are limited by the sequential reading of the network input files for much larger volumes. One simulation of blood flow have even been performed in a volume of 16.2 cm^3 of the cortex, which has never been presented in the context of the human brain microcirculation.

Config.	Volume	Format	Number of unknowns					Execution time on one EOS core		
			CN	H			gain	CN	H	gain
				Network	FV	Total	CN vs. H			CN vs. H
AVA	6.48 mm^3	ASCII	1 124 196	280	1 920	2 200	510.9	41 s	0.3 s	136.67
AVA 3×3	58.32 mm^3	ASCII	10 057 128	2 520	17 920	20 440	492.03	13 400 s *	13.04 s	1027.61
		HDF5	10 057 128	2 520	17 920	20 440	492.03	8 700 s *	19.87 s	437.86
AVA 5×5	162 mm^3	HDF5	mem. issue	7 000	109 350	110 050	?	?	35.5 s *	?
AVA 20×20	2.6 cm^3	HDF5	mem. issue	112 000	1 310 400	1 422 400	?	?	8 119 s *	?
AVA 50×50	16.2 cm^3	HDF5	mem. issue	700 000	10 935 000	11 635 000	?	?	108 100 s **	?

*run on 50 cores then linearly reported on one core
*run on 500 cores then linearly reported on one core
? unknown because of memory management issue

Table 7: **Computational performance of the HNFV-Code for configurations with increasing volumes.** The reference configuration (AVA) corresponds to the most complex configuration presented in Section 5, i.e. to one venular tree in between two arteriolar trees (therefore the name AVA), coupled with 3-regular capillary networks or equivalent homogenized representations. The configurations with increased volumes are obtained by duplicating this reference configuration. For each configuration, the corresponding volume, the format of the input files, the number of unknowns, and the execution time are provided. Hybrid simulations (H) are compared to CN simulations by computing both the gain in problem size (number of unknowns) and the gain in time (execution time).

Ideas for future improvements. With a view to including additional levels of complexity (e.g. mass transfers), the performance of the code can be improved. For instance, it has been shown in Section 6.3.4 that the HNFV-Code can be optimized to handle the non structured architecture of networks (weak scalings). To deal with this issue, specialized external libraries could be exploited for the management of graphs.

With regard to the partitioning of hybrid configurations, the network and FV parts are independently distributed among the processing units. This distributions could be improved by correlating both the FV and the network partitionings. The idea would be to ensure that both the coupled vertex and the coupled cell involved in one coupling are located on the same processing units. This would reduce the corresponding MPI-communications at the coupling points.

Finally, the sequential execution of both file reading and file writing considerably reduces the execution time. Further, the related memory issue makes CN simulations impossible in volumes larger than $\sim$60 mm^3. These operations should be parallelized in a close future.

The question of anatomical datasets at the scale of a whole human brain. Thanks to its HPC design, the HNFV-Code already makes possible the investigation of physiological mechanisms of the cerebral microcirculation at macroscale. For instance, the impact of capillary occlusions on global blood flow and blood flow regulation could be studied. Since the FV domain is representative at mesoscopic scale, the study of a single occlusion at the scale of a capillary is not possible. However, a local percentage of occlusions can be represented by a lower effective permeability in the corresponding FV cell. Preliminary studies have proven that the hybrid approach remains accurate in such studies, since the size of the REV is robust to up to 40 % of capillary occlusions [Vaninva Versini, 2017]. Furthermore, the impact of vasodilations of the arteriolar and venular vasculature on flow re-organizations can also be investigated, in the same spirit as [Lorthois et al., 2011a]. Local vasodilations would mimic reactions of the microvasculature to the metabolic demand of the functioning of the neuronal network, i.e. to the neurovascular coupling.

At the moment, no anatomical datasets containing the graph representation of arteriolar and venular structure in a whole mouse, not to mention human, brain exists. This means that such studies at brain scale are constrained by the use of synthetic networks. However, recent brain imaging techniques are already able to image all vessels above 7 μm, i.e. all tree-like arterioles and venules, in rat brains of volume $\sim$2 000 mm^3 [Zhang et al., 2015]. With the evergrowing improvement in technologies, we can imagine that this capacity will extend to larger mammals, including humans

(brains of volume$\sim 700\,\mathrm{cm}^3$), in the next decades.

7.2.2 Extension of the hybrid approach

The hybrid approach presented in this manuscript for modelling blood flow distributions has been developed under some assumptions that are not physiologically accurate. In particular, realistic capillary networks induce anisotropies, and the human cortex is not globally homogeneous, since it is divided into several layers of different vascular densities [Duvernoy et al., 1981]. To take into account these properties of the capillary bed, both the FV scheme and the multiscale coupling models must be improved. Furthermore, with a view to mass transfers, representing the hematocrit distribution in the network part is essential [Boas et al., 2008].

Complexification of the capillary networks. Complexifying the structure of the underlying structure of the capillary bed will both impact the FV scheme and the multiscale coupling model (Eqs. 4.30-4.32). Since each of these parts has been implemented separately in the HNFV-Code, the modifications of the associated equations will be easily brought, without endangering the global HPC design of the code.

FV schemes already exist that account for anisotropies [Versteeg and Malalasekera, 2007]. In particular, anisotropies implies that the effective permeability is no more represented by a scalar, but by a tensor with multi-directional components

$$\mathbf{K}^{\mathrm{eff}} = \begin{pmatrix} K_{xx} & K_{xy} & K_{xz} \\ K_{yx} & K_{yy} & K_{yz} \\ K_{zx} & K_{zx} & K_{zz} \end{pmatrix}.$$

Well models accounting for anisotropies also exist in the context of petroleum engineering [Peaceman, 1983]. They are commonly treated by using a change of basis, in order to reduce the complexity of the problem to the one of an isotropic configuration.

With regard to the stratifications of the capillary bed, the possibility of treating an heterogeneous FV domain, i.e. defining a permeability value per cell, is already implemented in the HNFV-Code. However, the multiscale coupling model is not adapted to such a configuration yet. In particular, for coupling points that would be at the interface between two capillary layers, a new definition of

the coefficient permeability K^{eff} will be needed in the expression of the coupling coefficient $C_{s,\Gamma}$ in Eq. 4.32

$$C_{s,\Gamma} = R_\Gamma - \frac{\mu^{\text{eff}}}{4\pi K^{\text{eff}}} \left(\frac{1}{\text{Card}\left(\overline{\Omega}^s_{sph}\right)} \sum_{k \in \overline{\Omega}^s_{sph}} \frac{1}{d_{k,s}} \times -\frac{1}{l_\Gamma} - \frac{4\pi}{h \times \text{Card}\left(\overline{\Omega}^s_{sph}\right)} \right).$$

For instance, we can imagine the computation of a permeability $\overline{K}^{\text{eff}}$ averaged over the cells of the neighbourhood $\Omega^s_{FV,neigh}$.

Complexification of the blood rheology in network model For the purpose of extending the hybrid approach to mass transfers, in particular to the transfers of oxygen, the network approach must be first complexified to take into account the phase separation effect, thus the hematocrit distribution in the vascular network. As discussed in Section 2, such an improvement implies the treatment of non-linearities that are computationally expensive since they are often treated via iterative methods.

A network model accounting for hematocrit distributions has already been implemented in the HNFV-Code, and validated [Berg et al., 2016]. However, extensions are still to be implemented to homogenize the non-linear equations in the capillary bed, nor to adapt the coupling model.

Mass transfer The modelling of molecular exchanges between the microvascular network and the neuronal network is the ultimate goal of our numerical approach. Such a modelling must describe both the mass transport in the capillaries, and the diffusion through the surrounding cerebral tissue. One possible system of equations for mass conservation of a metabolic tracer reads

$$\begin{cases} \frac{\partial C_v}{\partial t} + \boldsymbol{u} \cdot \boldsymbol{\nabla} C_v & = \nabla \cdot (D_v \boldsymbol{\nabla} C_v) \quad \text{in } \Omega_v \\ \frac{\partial C_t}{\partial t} & = \nabla \cdot (D_t \boldsymbol{\nabla} C_t) - k_t C_t \quad \text{in } \Omega_t \\ C_v & = C_t \quad \text{on } \partial\Omega_{vt} \\ \boldsymbol{n}_{vt} \cdot D_v \boldsymbol{\nabla} C_v & = \boldsymbol{n}_{vt} \cdot D_t \boldsymbol{\nabla} C_t \quad \text{on } \partial\Omega_{vt} \end{cases},$$

with subscripts v referring to the vessel, subscripts t referring to the tissue, C the concentration, D the diffusion coefficient et k the metabolic consumption rate. Ω_v represents the vascular domain, Ω_t the tissue domain, and $\partial\Omega_{vt}$ the interface between Ω_v and Ω_t.

The homogenization of these equations has already been done using the volume averaging method

[Billanou, 2010]. This upscaling process has been validated by comparison with Direct Numerical Simulation (DNS), under some simplifying assumptions [Doyeux et al., 2016]. The main difficulty of adapting our hybrid approach for mass transfers primarily concerns the multiscale coupling approach. Indeed, contrary to the blood that does not cross the vascular wall, the molecules diffuse through the endothelial cells of arterioles and venules. As a consequence, the coupling model must be applied all along the arteriolar and venular vasculature, not only at the endpoints of the trees. Such a problem is also encountered when modelling flow and transport in fractured porous medium, and widely investigated in the context of hydrology and petroleum engineering [Sahimi, 2011]. However, the density of fractures in this context is much lower than the density of vessels in the cortex.

7.3 In summary

The human brain microcirculation is a broad field of investigation, in particular because it presents a multiscale architecture. The large spectrum of spatial scales involved represents a real challenge for better understanding physiological and physiopathological mechanisms at the scale of the whole brain. No numerical tool exists yet to perform simulation of blood flow and mass transfers in such a volume.

In this work, we presented a new simulation paradigm, which aims at modelling blood flow distributions in a whole human brain. One of the characteristics of this new tool is that it describes flow fields at mesoscopic scale. This is particularly relevant since this mesoscopic scale matches with the typical resolution of brain imaging methods, such as functional neuroimaging or perfusion imaging techniques. This similarity opens the way to the combination of imaging and numerical investigation tools.

In this manuscript, theoretical and computational foundations have been built. The code developed during this thesis in now operable to lead a variety of physiological study of blood flow distributions, such as flow regulations resulting from capillary rarefaction, multiple capillary occlusions, or vasodilations of the largest vessels. Further extensions are still needed to adapt our approach to realistic capillary networks (provided that anatomical datasets will be available soon), and ultimately to mass transfers. The modelling of blood flow and mass transfers at the scale of a whole human brain would represent a valuable tool to better understanding both the impact of diseased-induced modifications of the vasculature of the brain microcirculation (e.g. vascular occlusions), and the neurovascular coupling.

8 Appendices

8.1 Averaging of microscopic fields to mesoscopic scale

For the purpose of computing effective parameters of the capillary bed, or comparing fields computed in the continuum with corresponding fields in the underlying capillary bed, we have to average the microscopic fields to mesoscopic scale. In this section, we detail our method to average both pressure and flow rate fields from the scale of the capillaries to the scale of a FV cell.

As a recall, the pressure P_i of a given cell i is defined as

$$P_i = \int_{V_i} P \, dV, \tag{8.1}$$

with V_i the volume of the cell i. The flow rate Q_{ij} at the interface between the cell i and the cell j is defined as

$$Q_{ij} = \int_{S_{ij}} Q \, dS, \tag{8.2}$$

with S_{ij} the exchange surface between the cells i and j. In the network part, the pressure π_α defined at a vertex α is a point value, and the flow rate $q_{\alpha\beta}$ of a vessel $[\alpha\beta]$ is lineic.

Averaging of the pressure field. Here, we aim at defining the pressure Π_i of the network averaged at the scale of a cell i. Let consider a vessel v defined by the two vertices α and β. According to the governing equations of blood flow in the network, the pressure linearly evolves from vertex α to β. Thus the pressure at any point x of the segment v is defined as

$$\pi_v(x) = \pi_\alpha + x\frac{\pi_\beta - \pi_\alpha}{l_v}, \tag{8.3}$$

with l_v the length of the vessel v. In this work, we define the averaged pressure Π_i as

$$\Pi_i = \frac{1}{\sum_{v\in\mathcal{V}_i} l_{v,in}} \sum_{v\in\mathcal{V}_i} \int_{v_{in}} \pi_v(x) \, dx, \tag{8.4}$$

with $\mathcal{V}_i$ the set of vessels that are entirely or partially contained in cell i, $l_{v,in}$ the entire or partial length of vessel v contained in cell i, and v_{in} the segment of vessel v contained in cell i.

As an illustration, let consider a single vessel $[\alpha\beta]$, as illustrated in Fig. 8.1. If the vessel is

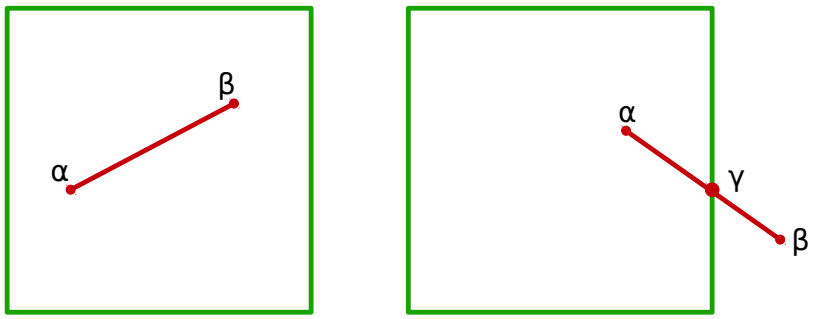

(a) **(b)**

Figure 8.1: **Configurations for illustrating the averaging of network pressure at the scale of a FV cell. (a)** A network vessel (red) defined by the endpoints α and β is entirely contained in a FV cell (green). **(b)** A network vessel (red) defined by the endpoints α and β is partially contained in a FV cell (green). The point γ is located at the intersection between the vessel and the cell.

entirely included in the FV cell i, as displayed in Fig. 8.1**(a)**, we have

$$\Pi_i = \int_{\alpha}^{\beta} \pi(x)\, dx = \frac{\pi(\alpha) + \pi(\beta)}{2}. \tag{8.5}$$

If the vessel is partially excluded from the cell i, as displayed in Fig. 8.1**(b)**, we have

$$\Pi_i = \int_{\alpha}^{\gamma} \pi(x)\, dx = \frac{\pi(\alpha) + \pi(\gamma)}{2}, \tag{8.6}$$

where γ is the intersection point between the vessel and the cell boundary.

Averaging of the flow field. To express the flow rate ϕ_i of the network averaged at the scale of a FV cell i, we consider the set of vessels $\mathcal{V}_{i,cross}$ that cross the cell boundary. By definition, each vessel v of $\mathcal{V}_{i,cross}$ is defined by a vertex $\alpha_{v,in}$ contained in the cell i, and a vertex $\alpha_{v,out}$ outside of the cell i. Here, we define the flow rate q_v of the vessel v as

$$q_v = G_v \left(\pi_{\alpha_{v,in}} - \pi_{\alpha_{v,out}}\right), \tag{8.7}$$

with G_v the conductance of the vessel v, and express the averaged flow rate ϕ_i as

$$\phi_i = \sum_{v \in \mathcal{V}_{i,cross}} q_v. \tag{8.8}$$

The definition of the flow rate q_v in Eq. 8.7 ensures the consistency with the FV scheme (Eq. 3.34) with regard to the signs of inward or outward flows in cell i.

8.2 Two-dimensional analytical solution of Darcy's law

In the Peaceman's well model, the pressure field in the vicinity of the well bore is approximated by an analytical solution of Darcy's flow (Eq. 4.1)

$$p\left(r\right) = p_w - \frac{q\mu}{2\pi K}\, ln\left(\frac{r}{r_w}\right). \tag{8.9}$$

In this section, we detail the development of this solution.

Let u be the velocity field in the vicinity of a well bore. As explained in Section 4.1.1, the penetration of a well bore in the porous rock implies a radial flow at its circumference. The symmetries induced enable us to express the velocity in polar coordinates (r, θ) as

$$u = u\left(r\right) \tag{8.10}$$

with no component in θ-direction.

Mass balance in the porous rock reads

$$\nabla \cdot u = 0 \tag{8.11}$$

and can be rewritten in polar coordinates as

$$\frac{1}{r}\frac{\partial\left(ru\right)}{\partial r} = 0 \Rightarrow \frac{\partial\left(ru\right)}{\partial r} = 0 \tag{8.12}$$

$$\Rightarrow ru = C, \quad C \in \mathbb{R} \tag{8.13}$$

$$\Rightarrow u = \frac{C}{r}. \tag{8.14}$$

From Eq. 8.14, the expression of the flow rate q in the vicinity of the wellbore reads

$$q = \int_S u\, dS \tag{8.15}$$

$$= \int_0^{2\pi} \frac{C}{r}\, r\, d\theta \tag{8.16}$$

$$= 2\pi C. \tag{8.17}$$

Then, Eq. 8.17 is rewritten

$$C = \frac{q}{2\pi}, \tag{8.18}$$

and Eq. 8.14 reads

$$u\,(r) = \frac{q}{2\pi r}. \tag{8.19}$$

Further, Darcy's law is expressed as

$$u = -\frac{K}{\mu}\nabla p \Rightarrow -\nabla p = \frac{\mu}{K}u \tag{8.20}$$

$$\Rightarrow -\frac{\partial p}{\partial r} = \frac{\mu}{K}\frac{q}{2\pi r} \tag{8.21}$$

$$\Rightarrow \int_{r_w}^{R}\frac{\partial p}{\partial r}dr = -\frac{\mu}{K}\int_{r_w}^{R}\frac{q}{2\pi r}dr, \quad \text{with } R > r_w \tag{8.22}$$

$$\Rightarrow p(R) - p(r_w) = -\frac{q\mu}{2\pi K}\left[ln(R) - ln(r_w)\right] \tag{8.23}$$

$$\Rightarrow p(R) = p_w - \frac{q\mu}{2\pi K}ln(\frac{R}{r_w}), \tag{8.24}$$

with r_w the circumference of the wellbore. Finally, Eq. 8.24 is similar to Eq. 8.9.

8.3 Three-dimensional analytical solution of Darcy's law

In the the multiscale coupling model presented in this work, the pressure field in the vicinity of a coupling point is approximated by an analytical solution of Darcy's flow (Eq. 4.17)

$$p\left(r\right) = \pi_{ref} - \frac{\mu^{\text{eff}} q}{4\pi K^{\text{eff}}} \left(\frac{1}{r} - \frac{1}{l_{ref}}\right). \tag{8.25}$$

In this section, we detail the development of this solution.

Let u be the velocity field in the vicinity of the coupling point. As explained in Section 4.2, the pressure field is assumed to be spherical in the vicinity of coupling points. The symmetries induced enable us to express the velocity in spherical coordinates (r, θ, ϕ) as

$$u = u\left(r\right),$$

with no component in θ- and ϕ- directions.

Mass balance in the continuum reads

$$\nabla \cdot u = 0 \tag{8.26}$$

and can be rewritten in spherical coordinates as

$$\frac{1}{r^2}\frac{\partial\left(r^2 u\right)}{\partial r} = 0 \Rightarrow \frac{\partial\left(r^2 u\right)}{\partial r} = 0 \tag{8.27}$$

$$\Rightarrow r^2 u = C, \quad C \in \mathbb{R} \tag{8.28}$$

$$\Rightarrow u = \frac{C}{r^2}. \tag{8.29}$$

From Eq. 8.29, the expression of the flow rate q in the vicinity of the coupling point reads

$$q = \int_S u \, dS \tag{8.30}$$

$$= \int_0^{2\pi} d\phi \int_0^{\pi} \frac{C}{r^2} \, r^2 \, sin\theta \, d\theta \tag{8.31}$$

$$= 4\pi C, \tag{8.32}$$

Then, Eq. 8.32 is rewritten

$$C = \frac{q}{4\pi}, \tag{8.33}$$

and Eq. 8.29 reads

$$u\left(r\right) = \frac{q}{4\pi r^2}. \tag{8.34}$$

Further, Darcy's law is expressed as

$$u = -\frac{K}{\mu}\nabla p \Rightarrow -\nabla p = \frac{\mu}{K}u \tag{8.35}$$

$$\Rightarrow -\frac{\partial p}{\partial r} = \frac{\mu}{K}\frac{q}{4\pi r^2} \tag{8.36}$$

$$\Rightarrow \int_{r_{ref}}^{R} \frac{\partial p}{\partial r}dr = -\frac{\mu}{K}\int_{r_{ref}}^{R} \frac{q}{4\pi r^2}dr, \quad \text{with } R > r_{ref} \tag{8.37}$$

$$\Rightarrow p(R) - p(r_{ref}) = -\frac{q\mu}{4\pi K}\left(\frac{1}{r} - \frac{1}{r_{ref}}\right) \tag{8.38}$$

$$\Rightarrow p(R) = p_{ref} - \frac{q\mu}{4\pi K}(\frac{1}{r} - \frac{1}{r_{ref}}), \tag{8.39}$$

with r_{ref} a reference distance in the vicinity of the coupling point. Finally, Eq. 8.39 is similar to Eq. 8.25.

8.3.1 Implementation of the condition of pressure continuity at the interface between the arteriolar and venular trees, and the continuum

In this section, we detail the construction of the linear system for a hybrid configuration involving a simple condition of pressure continuity at the interface between the arteriolar and venular trees, and the continuum. Such configuration is termed Simple Hybrid (SH) configuration.

The development of both the FV part and the network part of the linear system is similar to the construction presented in Sections 3.2.3 and 3.3.4.

Let π_s be the pressure at the endpoint s of a coupled vessel and P_i the pressure of the corresponding coupled cell i. The condition of pressure continuity reads

$$P_i = \pi_s. \tag{8.40}$$

Note that such condition does not take into account the location of the coupling point inside the FV cell.

As a recall, the FV scheme applied to the cell i reads

$$\frac{K^{\text{eff}}h}{\mu^{\text{eff}}}\sum_{j\in N_i}(P_i - P_j) = \sum_{s\in S_i} q_s, \tag{8.41}$$

with K^{eff} the effective permeability, μ^{eff} the effective viscosity, h the side of the cell, N_i the set of neighbouring cells of i, S_i the set of coupling points in cell i, and q_s the flow rate outgoing (or ingoing) from (or to) an arteriolar or venular coupled vessel. In the network part, the flow equations applied to each coupled vertex s read

$$G_{s's}\left(\pi_s - \pi_{s'}\right) = q_s, \tag{8.42}$$

with s' the single vertex that is connected to s and $G_{s's}$ the conductance of the vessel $[s's]$.

Impact on the FV equations

For the combination of Eqs. 8.41 and 8.42, the equation corresponding to the cell i is rewritten

$$\frac{K^{\text{eff}}h}{\mu^{\text{eff}}}\sum_{j\in N_i}(P_i - P_j) = \sum_{s\in S_i} G_{s's}\left(\pi_s - \pi_{s'}\right) \tag{8.43}$$

and the condition of pressure continuity (Eq. 8.40) yields

$$\frac{K^{\text{eff}}h}{\mu^{\text{eff}}}\sum_{j\in N_i}(P_i - P_j) = \sum_{s\in S_i} G_{s's}\left(P_i - \pi_{s'}\right), \tag{8.44}$$

i.e.

$$\left(\frac{K^{\text{eff}}h\,Card\left(N_i\right)}{\mu^{\text{eff}}} + \sum_{s\in S_i} G_{s's}\right)P_i - \sum_{j\in N_i} P_j - \sum_{s\in S_i} G_{s's}\pi_{s'} = 0. \tag{8.45}$$

Impact on the network equations

For each coupled vertex s, the flow equations applied to its single neighbouring vertex s' reads

$$\sum_{\alpha\in\mathcal{N}_{s',\text{in}}\setminus\{s\}} G_{s'\alpha}\left(\pi_{s'} - \pi_\alpha\right) = G_{s's}\left(\pi_s - \pi_{s'}\right). \tag{8.46}$$

The condition of pressure continuity (Eq. 8.40) yields

$$\sum_{\alpha \in \mathcal{N}_{s',\text{in}} \setminus \{s\}} G_{s'\alpha} \left(\pi_{s'} - \pi_\alpha \right) = G_{s's} \left(P_i - \pi_{s'} \right), \tag{8.47}$$

i.e.

$$\left(\sum_{\alpha \in \mathcal{N}_{s',\text{in}}} G_{s'\alpha} \right) \pi_{s'} - \sum_{\alpha \in \mathcal{N}_{s',\text{in}} \setminus \{s\}} G_{s'\alpha} \pi_\alpha - G_{s's} P_i = 0. \tag{8.48}$$

Impact on the coupling equations

To complete the system of equations, the condition of pressure continuity is applied to each coupled vertex s

$$\pi_s = P_i. \tag{8.49}$$

8.4 6- and 3-regular networks with same vascular density

In this appendix, we detail our way to compute $l_{cap}^{\text{6-regular}}$ and $l_{cap}^{\text{3-regular}}$ in both 6- and 3- regular networks, respectively, so they present the same vascular density, i.e. vascular length per volume.

As illustrated in Fig. 5.1, an elementary pattern of the 6-regular network is contained in a volume $V^{\text{6-regular}} = \left(l_{cap}^{\text{6-regular}}\right)^3$, and the vascular length in such volume is $L^{\text{6-regular}} = 3l_{cap}^{\text{6-regular}}$. This corresponds to a vascular density

$$D^{\text{6-regular}} = \frac{L^{\text{6-regular}}}{V^{\text{6-regular}}} = \frac{3}{\left(l_{cap}^{\text{6-regular}}\right)^2}. \tag{8.50}$$

Considering the 3-regular network, an elementary pattern is contained in a volume $V^{\text{3-regular}} = \left(3l_{cap}^{\text{3-regular}}\right)^3$, and the vascular length in such volume is $L^{\text{3-regular}} = 30l_{cap}^{\text{3-regular}}$. This yields a vascular density

$$D^{\text{3-regular}} = \frac{L^{\text{3-regular}}}{V^{\text{3-regular}}} = \frac{30}{27\left(l_{cap}^{\text{3-regular}}\right)^2}. \tag{8.51}$$

Working with equal density for both networks induces

$$\begin{aligned} D^{\text{6-regular}} &= D^{\text{3-regular}} \\ \Rightarrow \frac{3}{\left(l_{cap}^{\text{6-regular}}\right)^2} &= \frac{30}{27\left(l_{cap}^{\text{3-regular}}\right)^2} \\ \Rightarrow l_{cap}^{\text{3-regular}} &= \sqrt{\frac{10}{27}}\, l_{cap}^{\text{6-regular}}. \end{aligned} \tag{8.52}$$

Assuming $l_{cap}^{\text{6-regular}} = 50\,\mu\text{m}$, this yields $l_{cap}^{\text{3-regular}} = 30.43\,\mu\text{m}$, as presented in Section 5.1.3.

8.5 Details about the configuration of test cases

A series of test cases is used for the purpose of validating the hybrid approach in Section 5. Tables 8 and 9 below summarize the details about the corresponding configurations.

	Test case	*Scale separation*	*Off-centering*	*Boundary effect*	*Two couplings*	*Multi-coupling*
Capillary bed	**Volume**	$(2.25\,\mathrm{mm})^3$	$(2.25\,\mathrm{mm})^3$	$(2.25\,\mathrm{mm})^3$	$4.5{\times}2.25{\times}2.25\ \mathrm{mm}^3$	$(2.25\,\mathrm{mm})^3$
	Type	6-regular	6-regular	6-regular	6-regular	6-regular
	Nb of vessels	279 450	279 450	279 450	556 875	279 450
	Vasc. length	50 μm	50 μm	50 μm	50 μm	50 μm
	Vasc. diameter	5.91 μm	5.91 μm	5.91 μm	5.91 μm	5.91 μm
FV	**Cell side**	50-450 μm	250 μm	250 μm	250 μm	250 μm
Arterioles/venules	**Type**	Isolated	Isolated	Isolated	Isolated	Isolated
	Nb of vessels	2	2	2	2	2
	Nb couplings	1	1	1	2	2-10
	Vasc. length	200 μm	200 μm	200 μm	200 μm	200 μm
	Vasc. diameter	15 μm	15 μm	15 μm	15 μm	15 μm

Table 8: **Details about the configurations used in Section 5.3.1.**

	Test case	*Diam. distr.*	*Virshow-Robin*	*Scale separation*		d_{cap}/d_{AV}	*Hier. idx*	*AVA*
Capillary bed	**Volume**	$(2.25\,\mathrm{mm})^3$	$(2.25\,\mathrm{mm})^3$	$(2.25\,\mathrm{mm})^3$	$(2.25\,\mathrm{mm})^3$	$(2.25\,\mathrm{mm})^3$	$2\times3\times1.25$ mm^3	$4.11\times2.74\times1.37$ mm^3
	Type	6-regular	6-regular	3-regular	Voronoi-like	6-regular	6-regular	3-regular
	Nb of vessels	279 450	279 429	279 450	219 306	279 450	184 900	729 000
	Vasc. length	50 μm	50 μm	30 62μm	50 μm	50 μm	50 μm	30 62μm
	Vasc. diam.	5.91$\pm$1.3 μm	5.91 μm	5.91 μm	5.91 μm	5.91 μm	5.91 μm	5.91$\pm$1.3 μm
FV	**Cell side**	250 μm	250 μm	50-450 μm	50.72-456.45 μm	250 μm	250 μm	152.15 μm
Arterioles/venules	**Type**	Isolated	Isolated	Isolated	Isolated	Isolated	Anatomical	Anatomical
	Nb of vessels	2	2	2	2	2	125	563
	Nb couplings	1	1	1	1	1	10-61	276
	Vasc. length	200 μm	200 μm	200 μm	200 μm	200 μm	12.34-637.52 μm	1.85-647.60μm
	Vasc. diam.	15 μm	15 μm	15 μm	15 μm	15 μm	10-30.52 μm	7.50-42.64 μm

Table 9: **Details about the configurations used in Sections** 5.3.2, 5.3.3 **and** 5.4**.**

8.6 DMDA partitioning algorithm

The DMDA tool of the PETSc library contains an algorithm to partition a three-dimensional structured grid. Here is presented an extract of the corresponding source code. The entire code is available online (da3.c).

In Section 6.3.3, we take interest in computing the number of processing units assigned per direction, provided that the number of discretization cells in each direction are known. This corresponds to the lines 140-171 of the code below. To ease the comprehension of these lines, a tabular is provided to present some variable names of interest (Table 10). This tabular also highlights the correspondence between the PETSc notations and the notations used in the present manuscript (MS), since they have been changed for consistency with the rest of the presentation.

	PETSc notation	MS notation
number of cells in the first direction	M	M_x
number of cells in the second direction	N	M_y
number of cells in the third direction	P	M_z
number of processing units assigned to the first direction	n	p_x
number of processing units assigned to the second direction	m	p_y
number of processing units assigned to the third direction	p	p_z
number of available processing units	$size$	p

Table 10: **Correspondence between the PETSc notations and the notations used in the present manuscript (MS).**

```
1  #undef __FUNCT__
2  #define __FUNCT__ "DMSetUp_DA_3D"
3
4  PetscErrorCode  DMSetUp_DA_3D(DM da)
5  {
6     DM_DA            *dd          = (DM_DA*)da->data;
7     const PetscInt   M            = dd->M;
8     const PetscInt   N            = dd->N;
9     const PetscInt   P            = dd->P;
10    PetscInt         m            = dd->m;
11    PetscInt         n            = dd->n;
12    PetscInt         p            = dd->p;
13    const PetscInt   dof          = dd->w;
14    const PetscInt   s            = dd->s;
15    DMBoundaryType   bx           = dd->bx;
16    DMBoundaryType   by           = dd->by;
17    DMBoundaryType   bz           = dd->bz;
18    DMDAStencilType  stencil_type = dd->stencil_type;
19    PetscInt         *lx          = dd->lx;
20    PetscInt         *ly          = dd->ly;
21    PetscInt         *lz          = dd->lz;
22    MPI_Comm         comm;
23    PetscMPIInt      rank,size;
24    PetscInt         xs=0,xe,ys=0,ye,zs=0,ze,x=0,y=0,z=0;
25    PetscInt         Xs,Xe,Ys,Ye,Zs,Ze,IXs,IXe,IYs,IYe,IZs,IZe,pm;
26    PetscInt         left,right,up,down,bottom,top,i,j,k,*idx,nn;
27    PetscInt         n0,n1,n2,n3,n4,n5,n6,n7,n8,n9,n10,n11,n12,n14;
28    PetscInt         n15,n16,n17,n18,n19,n20,n21,n22,n23,n24,n25,n26;
29    PetscInt         *bases,*ldims,base,x_t,y_t,z_t,s_t,count,s_x,s_y,s_z
         ;
30    PetscInt         sn0=0,sn1=0,sn2=0,sn3=0,sn5=0,sn6=0,sn7=0;
31    PetscInt         sn8=0,sn9=0,sn11=0,sn15=0,sn24=0,sn25=0,sn26=0;
32    PetscInt         sn17=0,sn18=0,sn19=0,sn20=0,sn21=0,sn23=0;
33    Vec              local,global;
34    VecScatter       gtol;
35    IS               to,from;
36    PetscBool        twod;
37    PetscErrorCode   ierr;
38
39    PetscFunctionBegin;
40    if (stencil_type == DMDA_STENCIL_BOX && (bx == DM_BOUNDARY_MIRROR ||
         by == DM_BOUNDARY_MIRROR || bz == DM_BOUNDARY_MIRROR))
41    {
42       SETERRQ(PetscObjectComm((PetscObject)da),PETSC_ERR_SUP,"Mirror
            boundary and box stencil");
43    }
44    ierr = PetscObjectGetComm((PetscObject) da, &comm);CHKERRQ(ierr);
```

```
45
46
47 #if !defined(PETSC_USE_64BIT_INDICES)
48     if (((Petsc64bitInt) M)*((Petsc64bitInt) N)*((Petsc64bitInt) P)*((
       Petsc64bitInt) dof) > (Petsc64bitInt) PETSC_MPI_INT_MAX)
49     {
50       SETERRQ3(comm,PETSC_ERR_INT_OVERFLOW,"Mesh of %D by %D by %D (dof)
           is too large for 32 bit indices",M,N,dof);
51     }
52 #endif
53
54
55     ierr = MPI_Comm_size(comm,&size);CHKERRQ(ierr);
56     ierr = MPI_Comm_rank(comm,&rank);CHKERRQ(ierr);
57
58
59     if (m != PETSC_DECIDE)
60     {
61       if (m < 1) SETERRQ1(PETSC_COMM_SELF,PETSC_ERR_ARG_OUTOFRANGE,"Non-
          positive number of processors in X direction: %D",m);
62       else if (m > size) SETERRQ2(PETSC_COMM_SELF,
          PETSC_ERR_ARG_OUTOFRANGE,"Too many processors in X direction: %
          D %d",m,size);
63     }
64
65     if (n != PETSC_DECIDE)
66     {
67       if (n < 1) SETERRQ1(PETSC_COMM_SELF,PETSC_ERR_ARG_OUTOFRANGE,"Non-
          positive number of processors in Y direction: %D",n);
68       else if (n > size) SETERRQ2(PETSC_COMM_SELF,
          PETSC_ERR_ARG_OUTOFRANGE,"Too many processors in Y direction: %
          D %d",n,size);
69     }
70
71     if (p != PETSC_DECIDE)
72     {
73       if (p < 1) SETERRQ1(PETSC_COMM_SELF,PETSC_ERR_ARG_OUTOFRANGE,"Non-
          positive number of processors in Z direction: %D",p);
74       else if (p > size) SETERRQ2(PETSC_COMM_SELF,
          PETSC_ERR_ARG_OUTOFRANGE,"Too many processors in Z direction: %
          D %d",p,size);
75     }
76
77     if ((m > 0) && (n > 0) && (p > 0) && (m*n*p != size)) SETERRQ4(
         PETSC_COMM_SELF,PETSC_ERR_ARG_OUTOFRANGE,"m %D * n %D * p %D !=
         size %d",m,n,p,size);
78
```

```
79    /* Partition the array among the processors */
80    if (m == PETSC_DECIDE && n != PETSC_DECIDE && p != PETSC_DECIDE)
81    {
82       m = size/(n*p);
83    }
84    else if (m != PETSC_DECIDE && n == PETSC_DECIDE && p != PETSC_DECIDE)
85    {
86       n = size/(m*p);
87    }
88    else if (m != PETSC_DECIDE && n != PETSC_DECIDE && p == PETSC_DECIDE)
89    {
90       p = size/(m*n);
91    }
92    else if (m == PETSC_DECIDE && n == PETSC_DECIDE && p != PETSC_DECIDE)
93    {
94       /* try for squarish distribution */
95       m = (int)(0.5 + PetscSqrtReal(((PetscReal)M)*((PetscReal)size)/((
             PetscReal)N*p)));
96       if (!m) m = 1;
97       while (m > 0)
98       {
99          n = size/(m*p);
100         if (m*n*p == size) break;
101         m--;
102      }
103      if (!m) SETERRQ1(PETSC_COMM_SELF,PETSC_ERR_ARG_OUTOFRANGE,"bad p
             value: p = %D",p);
104      if (M > N && m < n)
105      {
106         PetscInt _m = m;
107         m = n; n = _m;
108      }
109   }
110   else if (m == PETSC_DECIDE && n != PETSC_DECIDE && p == PETSC_DECIDE)
111   {
112      /* try for squarish distribution */
113      m = (int)(0.5 + PetscSqrtReal(((PetscReal)M)*((PetscReal)size)/((
             PetscReal)P*n)));
114      if (!m) m = 1;
115      while (m > 0)
116      {
117         p = size/(m*n);
118         if (m*n*p == size) break;
119         m--;
120      }
121      if (!m) SETERRQ1(PETSC_COMM_SELF,PETSC_ERR_ARG_OUTOFRANGE,"bad n
             value: n = %D",n);
```

```
122
123         if (M > P && m < p)
124         {
125           PetscInt _m = m;
126           m = p;
127           p = _m;
128         }
129       }
130
131       else if (m != PETSC_DECIDE && n == PETSC_DECIDE && p == PETSC_DECIDE)
132       {
133         /* try for squarish distribution */
134         n = (int)(0.5 + PetscSqrtReal(((PetscReal)N)*((PetscReal)size)/((
              PetscReal)P*m)));
135         if (!n) n = 1;
136         while (n > 0)
137         {
138           p = size/(m*n);
139           if (m*n*p == size) break;
140           n--;
141         }
142         if (!n) SETERRQ1(PETSC_COMM_SELF,PETSC_ERR_ARG_OUTOFRANGE,"bad m
              value: m = %D",n);
143         if (N > P && n < p)
144         {
145           PetscInt _n = n;
146           n = p;
147           p = _n;
148         }
149       }
150
151       else if (m == PETSC_DECIDE && n == PETSC_DECIDE && p == PETSC_DECIDE)
152       {
153         /* try for squarish distribution */
154         n = (PetscInt)(0.5 + PetscPowReal(((PetscReal)N*N)*((PetscReal)
              size)/((PetscReal)P*M),(PetscReal)(1./3.)));
155         if (!n) n = 1;
156         while (n > 0)
157         {
158           pm = size/n;
159           if (n*pm == size) break;
160           n--;
161         }
162         if (!n) n = 1;
163         m = (PetscInt)(0.5 + PetscSqrtReal(((PetscReal)M)*((PetscReal)size
              )/((PetscReal)P*n)));
164         if (!m) m = 1;
```

```
165         while (m > 0)
166         {
167            p = size/(m*n);
168            if (m*n*p == size) break;
169            m--;
170         }
171         if (M > P && m < p)
172         {
173            PetscInt _m = m;
174            m = p;
175            p = _m;
176         }
177      }
178
179      else if (m*n*p != size) SETERRQ(PetscObjectComm((PetscObject)da),
            PETSC_ERR_ARG_OUTOFRANGE,"Given Bad partition");
180      if (m*n*p != size) SETERRQ(PetscObjectComm((PetscObject)da),
            PETSC_ERR_PLIB,"Could not find good partition");
181      if (M < m) SETERRQ2(PetscObjectComm((PetscObject)da),
            PETSC_ERR_ARG_OUTOFRANGE,"Partition in x direction is too fine! %D
             %D",M,m);
182      if (N < n) SETERRQ2(PetscObjectComm((PetscObject)da),
            PETSC_ERR_ARG_OUTOFRANGE,"Partition in y direction is too fine! %D
             %D",N,n);
183      if (P < p) SETERRQ2(PetscObjectComm((PetscObject)da),
            PETSC_ERR_ARG_OUTOFRANGE,"Partition in z direction is too fine! %D
             %D",P,p);
184
185      [...]
186   }
```

References

[Agaev, 1996] Agaev, G. (1996). Improved technique for off-center well modelling in multidimensional reservoir simulation. *Society of Petroleum Engineers*, pages 355–360.

[Ahusborde and Glockner, 2011] Ahusborde, E. and Glockner, S. (2011). A 2d block-structured mesh partitioner for accurate flow simulations on non-rectangular geometries. *Computers & Fluids*, 43:2–13.

[Al-Kilani et al., 2008] Al-Kilani, A., Lorthois, S., Nguyen, T.-H., Le Noble, F., Cornelissen, A., Unbekandt, M., Boryskina, O., Leroy, L., and Fleury, V. (2008). During vertebrate development, arteries exert a morphological control over the venous pattern through physical factors. *Physical Review E*, 77:051912.

[Balay et al., 2016] Balay, S., Abhyankar, S., Adams, M. F., Brown, J., Brune, P., Buschelman, K., Dalcin, L., Eijkhout, V., Gropp, W. D., Kaushik, D., Knepley, M. G., McInnes, L. C., Rupp, K., Smith, B. F., Zampini, S., Zhang, H., and Zhang, H. (2016). PETSc Web page.

[Barbee and Cokelet, 1971] Barbee, J. H. and Cokelet, G. R. (1971). The fahraeus effect. *Microvascular research*, (1):6–16.

[Basermann, 1995] Basermann, A. (1995). Parallel sparse matrix computations in iterative solvers on distributed memory machines. In *PPSC*, pages 454–459.

[Baxter et al., 2006] Baxter, S. M., Day, S. W., Fetrow, J. S., and Reisinger, S. J. (2006). Scientific software development is not an oxymoron. *PLoS Comput Biol*, 2:e87.

[Bear, 1972] Bear, J. (1972). *Dynamics of fluids in porous media*. Dover Publications, Inc.

[Benzi and Tuuma, 2002] Benzi, M. and Tuuma, M. (2002). A parallel solver for large-scale markov chains. *Applied Numerical Mathematics*, 41:135–153.

[Berg et al., 2016] Berg, M., Davit, Y., Quintard, M., and Lorthois, S. (2016). Modeling momentum and mass transport in brain microvascular networks. 13èmes Journées d'Étude des Milieux Poreux (JEMP), Anglet, France.

[Bertolino, 2007] Bertolino, A. (2007). Software testing research: Achievements, challenges, dreams. In *Future of Software Engineering*, pages 85–103.

[Billanou, 2010] Billanou, I. (2010). *Modélisation expérimentale et théorique pour la quantification du débit sanguin par Tomographie à Emission de Positrons*. PhD thesis.

[Blanco et al., 2009] Blanco, P. J., Pivello, M., Urquiza, S., and Feijóo, R. (2009). On the potentialities of 3d–1d coupled models in hemodynamics simulations. *Journal of Biomechanics*, 42:919–930.

[Blinder et al., 2013] Blinder, P., Tsai, P. S., Kaufhold, J. P., Knutsen, P. M., Suhl, H., and Kleinfeld, D. (2013). The cortical angiome: an interconnected vascular network with noncolumnar patterns of blood flow. *Nature Neuroscience*, 16:889–897.

[Boas et al., 2008] Boas, D. A., Jones, S. R., Devor, A., Huppert, T. J., and Dale, A. M. (2008). A vascular anatomical network model of the spatio-temporal response to brain activation. *NeuroImage*, 40:1116–1129.

[Bollobás, 2013] Bollobás, B. (2013). *Modern graph theory*, volume 184. Springer Science & Business Media.

[Buxton et al., 2004] Buxton, R. B., Uludağ, K., Dubowitz, D. J., and Liu, T. T. (2004). Modeling the hemodynamic response to brain activation. *NeuroImage*, 23:S220–S233.

[Cassot et al., 2006] Cassot, F., Lauwers, F., Fouard, C., Prohaska, S., and Lauwers-Cances, V. (2006). A novel three-dimensional computer-assisted method for a quantitative study of microvascular networks of the human cerebral cortex. *Microcirculation*, 13:1–18.

[Cassot et al., 2010] Cassot, F., Lauwers, F., Lorthois, S., Puwanarajah, P., Cances-Lauwers, V., and Duvernoy, H. (2010). Branching patterns for arterioles and venules of the human cerebral cortex. *Brain Research*, 1313:62–78.

[Cassot et al., 2009] Cassot, F., Lauwers, F., Lorthois, S., Puwanarajah, P., and Duvernoy, H. (2009). Scaling laws for branching vessels of human cerebral cortex. *Microcirculation*, 16:331–344.

[Cassot et al., 1995] Cassot, F., Vergeur, V., Bossuet, P., Hillen, B., Zagzoule, M., and Marc-Vergnes, J.-P. (1995). Effects of anterior communicating artery diameter on cerebral hemodynamics in internal carotid artery disease. *Circulation*, 92:3122–3131.

[Chen, 1997] Chen, W.-K. (1997). *Graph theory and its engineering applications*, volume 5. World Scientific.

[Chen and Zhang, 2009] Chen, Z. and Zhang, Y. (2009). Well flow models for various numerical methods. *International Journal of Numerical Analysis and Modeling*, 6:375–388.

[Davit et al., 2013a] Davit, Y., Bell, C. G., Byrne, H. M., Chapman, L. A., Kimpton, L. S., Lang, G. E., Leonard, K. H., Oliver, J. M., Pearson, N. C., Shipley, R. J., et al. (2013a). Homogenization via formal multiscale asymptotics and volume averaging: How do the two techniques compare? *Advances in Water Resources*, 62:178–206.

[Davit et al., 2013b] Davit, Y., Osborne, J., Byrne, H., Gavaghan, D., and Pitt-Francis, J. (2013b). Validity of the cauchy-born rule applied to discrete cellular-scale models of biological tissues. *Physical Review E*, 87:042724.

[Demmel et al., 1993] Demmel, J. W., Heath, M. T., and Van Der Vorst, H. A. (1993). Parallel numerical linear algebra. *Acta numerica*, 2:111–197.

[D'Esposito et al., 2003] D'Esposito, M., Deouell, L. Y., and Gazzaley, A. (2003). Alterations in the bold fmri signal with ageing and disease: a challenge for neuroimaging. *Nature reviews. Neuroscience*, 4:863.

[Ding, 2004] Ding, D.-Y. (2004). Modélisation des écoulements en milieu poreux au voisinage des puits.

[Ding and Renard, 1994] Ding, Y. and Renard, G. (1994). A new representation of wells in numerical reservoir simulation. *SPE Reservoir Engineering*, 9:140–144.

[Dogru et al., 2010] Dogru, A. H. et al. (2010). Equivalent wellblock radius for partially perforated vertical wells–part i: Anisotropic reservoirs with uniform grids. *SPE Journal*, 15:1–028.

[Doyeux et al., 2016] Doyeux, V., Davit, Y., Quintard, M., and Lorthois, S. (2016). Upscaling mass transfer in 3d anatomically accurate brain microvascular networks. 13èmes Journées d'Étude des Milieux Poreux (JEMP), Anglet, France.

[Dumkwu et al., 2012] Dumkwu, F. A., Islam, A. W., and Carlson, E. S. (2012). Review of well models and assessment of their impacts on numerical reservoir simulation performance. *Journal of Petroleum Science and Engineering*, 82-83:174–186.

[Durlofsky, 2000] Durlofsky, L. J. (2000). An approximate model for well productivity in heterogeneous porous media. *Mathematical geology*, 32:421–438.

[Duvernoy et al., 1981] Duvernoy, H., Delon, S., and Vannson, J. (1981). Cortical blood vessels of the human brain. *Brain Research Bulletin*, 7:519–579.

[Duvernoy et al., 1983] Duvernoy, H., Delon, S., and Vannson, J. (1983). The vascularization of the human cerebral cortex. *Brain Research Bulletin*, 11:419–480.

[Dzwinel et al., 2003] Dzwinel, W., Boryczko, K., and Yuen, D. A. (2003). A discrete-particle model of blood dynamics in capillary vessels. *Journal of Colloid and Interface Science*, 258:163–173.

[El-Bouri and Payne, 2015] El-Bouri, W. K. and Payne, S. J. (2015). Multi-scale homogenization of blood flow in 3-dimensional human cerebral microvascular networks. *Journal of Theoretical Biology*, 380:40–47.

[Erbertseder et al., 2012] Erbertseder, K., Reichold, J., Flemisch, B., Jenny, P., and Helmig, R. (2012). A coupled discrete/continuum model for describing cancer-therapeutic transport in the lung. *PLoS ONE*, 7:e31966.

[Erwing et al., 1999] Erwing, R., Lazarov, R., Lyons, S., Papavassiliou, D., Pasciak, J., and Qin, G. (1999). Numerical well model for non-darcy flow through isotropic porous media. *Computational Geosciences*, pages 185–204.

[Eymard et al., 2000] Eymard, R., Gallouët, T., and Herbin, R. (2000). Finite volume methods. *Handbook of Numerical Analysis*, 7:713–1018.

[Fan et al., 2003] Fan, J., Flombaum, J. I., McCandliss, B. D., Thomas, K. M., and Posner, M. I. (2003). Cognitive and brain consequences of conflict. *NeuroImage*, 18:42–57.

[Fang et al., 2008] Fang, Q., Sakadžić, S., Ruvinskaya, L., Devor, A., Dale, A. M., and Boas, D. A. (2008). Oxygen advection and diffusion in a three-dimensional vascular anatomical network. *Optics Express*, 16:17530–17541.

[Fiduccia and Mattheyses, 1988] Fiduccia, C. M. and Mattheyses, R. M. (1988). A linear-time heuristic for improving network partitions. In *Papers on Twenty-five years of electronic design automation*, pages 241–247. ACM.

[Figueroa et al., 2006] Figueroa, C. A., Vignon-Clementel, I. E., Jansen, K. E., Hughes, T. J., and Taylor, C. A. (2006). A coupled momentum method for modeling blood flow in three-dimensional deformable arteries. *Computer methods in applied mechanics and engineering*, 195:5685–5706.

[Filipovic et al., 2008] Filipovic, N., Kojic, M., and Tsuda, A. (2008). Modelling thrombosis using dissipative particle dynamics method. *Philosophical Transactions of the Royal Society of London A: Mathematical, Physical and Engineering Sciences*, 366:3265–3279.

[Fish et al., 2007] Fish, J., Nuggehally, M. A., Shephard, M. S., Picu, C. R., Badia, S., Parks, M. L., and Gunzburger, M. (2007). Concurrent atc coupling based on a blend of the continuum stress and the atomistic force. *Computer Methods in Applied Mechanics and Engineering*, 196:4548–4560.

[Formaggia et al., 1999] Formaggia, L., Nobile, F., Quarteroni, A., and Veneziani, A. (1999). Multiscale modelling of the circulatory system: a preliminary analysis. *Computing and visualization in science*, 2:75–83.

[Friston, 2009] Friston, K. (2009). Causal modelling and brain connectivity in functional magnetic resonance imaging. *PLoS Biology*, 7:e1000033.

[Fung and Zweifach, 1971] Fung, Y. and Zweifach, B. (1971). Microcirculation: mechanics of blood flow in capillaries. *Annual Review of Fluid Mechanics*, 3:189–210.

[Gagnon et al., 2015] Gagnon, L., Sakadžić, S., Lesage, F., Musacchia, J. J., Lefebvre, J., Fang, Q., Yücel, M. A., Evans, K. C., Mandeville, E. T., Cohen-Adad, J., et al. (2015). Quantifying the microvascular origin of bold-fmri from first principles with two-photon microscopy and an oxygen-sensitive nanoprobe. *Journal of Neuroscience*, 35:3663–3675.

[Gilbert et al., 1998] Gilbert, J. R., Miller, G. L., and Teng, S.-H. (1998). Geometric mesh partitioning: Implementation and experiments. *SIAM Journal on Scientific Computing*, 19:2091–2110.

[Girouard and Iadecola, 2006] Girouard, H. and Iadecola, C. (2006). Neurovascular coupling in the normal brain and in hypertension, stroke, and alzheimer disease. *Journal of Applied Physiology*, 100:328–335.

[Gould et al., 2016] Gould, I. G., Tsai, P., Kleinfeld, D., and Linninger, A. (2016). The capillary bed offers the largest hemodynamic resistance to the cortical blood supply. *Journal of Cerebral Blood Flow & Metabolism*, 37:52–68.

[Graham et al., 1982] Graham, S. L., Kessler, P. B., and Mckusick, M. K. (1982). Gprof: A call graph execution profiler. In *ACM Sigplan Notices*, volume 17, pages 120–126. ACM.

[Graham et al., 2004] Graham, S. L., Kessler, P. B., and McKusick, M. K. (2004). Gprof: A call graph execution profiler. *ACM Sigplan Notices*, 39:49–57.

[Gropp et al., 1996] Gropp, W., Lusk, E., Doss, N., and Skjellum, A. (1996). A high-performance, portable implementation of the mpi message passing interface standard. *Parallel Computing*, 22:789–828.

[Gropp et al., 1999] Gropp, W., Lusk, E., and Skjellum, A. (1999). *Using MPI: portable parallel programming with the message-passing interface*, volume 1. MIT press.

[Guenther et al., 2006] Guenther, F. H., Ghosh, S. S., and Tourville, J. A. (2006). Neural modeling and imaging of the cortical interactions underlying syllable production. *Brain and Language*, 96:280–301.

[Guibert et al., 2009] Guibert, R., Fonta, C., and Plouraboue, F. (2009). Cerebral micro-vascular networks control the blood pressure distribution when considering in vitro blood rheology models. *Mécanique & Industries*, 10:255–260.

[Guo et al., 2010] Guo, X., Gorman, G., Ashworth, M., Kramer, S., Piggott, M., and Sunderland, A. (2010). High performance computing driven software development for next-generation modelling of the worlds oceans. *Cray User Group*.

[Hamilton et al., 2010] Hamilton, N. B., Attwell, D., and Hall, C. N. (2010). Pericyte-mediated regulation of capillary diameter: a component of neurovascular coupling in health and disease. *Frontiers in Neuroenergetics*, 2.

[Hansson et al., 2002] Hansson, T., Oostenbrink, C., and van Gunsteren, W. (2002). Molecular dynamics simulations. *Current Opinion in Structural Biology*, 12:190–196.

[Harrison et al., 2002] Harrison, R. V., Harel, N., Panesar, J., and Mount, R. J. (2002). Blood capillary distribution correlates with hemodynamic-based functional imaging in cerebral cortex. *Cerebral Cortex*, 12:225–233.

[Heier et al., 1989] Heier, L. A., Bauer, C., Schwartz, L., Zimmerman, R., Morgello, S., and Deck, M. (1989). Large virchow-robin spaces: Mr-clinical correlation. *American Journal of Neuroradiology*, 10:929–936.

[Heinzer et al., 2006] Heinzer, S., Krucker, T., Stampanoni, M., Abela, R., Meyer, E. P., Schuler, A., Schneider, P., and Müller, R. (2006). Hierarchical microimaging for multiscale analysis of large vascular networks. *Neuroimage*, 32:626–636.

[Hirsch et al., 2012] Hirsch, S., Reichold, J., Schneider, M., Székely, G., and Weber, B. (2012). Topology and hemodynamics of the cortical cerebrovascular system. *Journal of Cerebral Blood Flow & Metabolism*, 32:952–967.

[Hsu and Secomb, 1989] Hsu, R. and Secomb, T. W. (1989). A green's function method for analysis of oxygen delivery to tissue by microvascular networks. *Mathematical Biosciences*, 96:61–78.

[Hunter et al., 2012] Hunter, J. M., Kwan, J., Malek-Ahmadi, M., Maarouf, C. L., Kokjohn, T. A., Belden, C., Sabbagh, M. N., Beach, T. G., and Roher, A. E. (2012). Morphological and pathological evolution of the brain microcirculation in aging and alzheimer's disease. *PloS one*, 7:e36893.

[Hyde et al., 2014] Hyde, E. R., Cookson, A. N., Lee, J., Michler, C., Goyal, A., Sochi, T., Chabiniok, R., Sinclair, M., Nordsletten, D. A., Spaan, J., et al. (2014). Multi-scale parameterisation of a myocardial perfusion model using whole-organ arterial networks. *Annals of Biomedical Engineering*, 42:797–811.

[Hyde et al., 2013] Hyde, E. R., Michler, C., Lee, J., Cookson, A. N., Chabiniok, R., Nordsletten, D. A., and Smith, N. P. (2013). Parameterisation of multi-scale continuum perfusion models from discrete vascular networks. *Medical & biological engineering & computing*, 51:557–570.

[Iadecola, 2013] Iadecola, C. (2013). The pathobiology of vascular dementia. *Neuron*, 80:844–866.

[Itti and Koch, 2001] Itti, L. and Koch, C. (2001). Computational modelling of visual attention. *Nature Reviews. Neuroscience*, 2:194.

[Iturria-Medina et al., 2016] Iturria-Medina, Y., Sotero, R., Toussaint, P., Mateos-Pérez, J., Evans, A., Initiative, A. D. N., et al. (2016). Early role of vascular dysregulation on late-onset alzheimer's disease based on multifactorial data-driven analysis. *Nature Communications*, 7.

[Jenny and Lunati, 2009] Jenny, P. and Lunati, I. (2009). Modeling complex wells with the multi-scale finite-volume method. *Journal of Computational Physics*, 228:687–702.

[Karniadakis et al., 2005] Karniadakis, G., Beskok, A., and Aluru, N. (2005). Microflows and nanoflows: fundamentals and simulation. *Cited on*, page 123.

[Karypis and Kumar, 1997] Karypis, G. and Kumar, V. (1997). A coarse-grain parallel formulation of multilevel k-way graph partitioning algorithm. In *PPSC*.

[Karypis and Kumar, 1999] Karypis, G. and Kumar, V. (1999). Parallel multilevel series k-way partitioning scheme for irregular graphs. *Siam Review*, 41:278–300.

[Karypis et al., 2003] Karypis, G., Schloegel, K., and Kumar, V. (2003). Parmetis. *Parallel graph partitioning and sparse matrix ordering library. Version*, 2.

[Kasischke et al., 2011] Kasischke, K. A., Lambert, E. M., Panepento, B., Sun, A., Gelbard, H. A., Burgess, R. W., Foster, T. H., and Nedergaard, M. (2011). Two-photon nadh imaging exposes boundaries of oxygen diffusion in cortical vascular supply regions. *Journal of Cerebral Blood Flow & Metabolism*, 31:68–81.

[Katz et al., 2007] Katz, R., Knepley, M. G., Smith, B., Spiegelman, M., and Coon, E. T. (2007). Numerical simulation of geodynamic processes with the portable extensible toolkit for scientific computation. *Physics of the Earth and Planetary Interiors*, 163:52–68.

[Kernighan and Lin, 1970] Kernighan, B. W. and Lin, S. (1970). An efficient heuristic procedure for partitioning graphs. *The Bell system technical journal*, 49:291–307.

[Kim et al., 2007] Kim, Y., Stolarska, M. A., and Othmer, H. G. (2007). A hybrid model for tumor spheroid growth in vitro i: theoretical development and early results. *Mathematical Models and Methods in Applied Sciences*, 17:1773–1798.

[Knepley et al., 1998] Knepley, M., Sarin, V., and Sameh, A. (1998). Parallel simulation of particulate flows. *Solving Irregularly Structured Problems in Parallel*, pages 226–237.

[Kotlyar et al., 1996] Kotlyar, V., Pingali, K., and Stodghill, P. (1996). Automatic parallelization of the conjugate gradient algorithm. *Languages and Compilers for Parallel Computing*, pages 480–499.

[Kumar et al., 1994] Kumar, V., Grama, A., Gupta, A., and Karypis, G. (1994). *Introduction to parallel computing: design and analysis of algorithms*, volume 400. Benjamin/Cummings Redwood City, CA.

[Lauwers et al., 2008] Lauwers, F., Cassot, F., Lauwers-Cances, V., Puwanarajah, P., and Duvernoy, H. (2008). Morphometry of the human cerebral cortex microcirculation: general characteristics and space-related profiles. *NeuroImage*, 39:936–948.

[Le Noble et al., 2005] Le Noble, F., Fleury, V., Pries, A., Corvol, P., Eichmann, A., and Reneman, R. (2005). Control of arterial branching morphogenesis in embryogenesis: go with the flow. *Cardiovascular Research*, 65:619–628.

[Li et al., 2013] Li, X., Vlahovska, P. M., and Karniadakis, G. E. (2013). Continuum-and particle-based modeling of shapes and dynamics of red blood cells in health and disease. *Soft Matter*, 9:28–37.

[Ligaarden, 2008] Ligaarden, I. S. (2008). Well models for mimetic finite difference methods and improved representation of wells inmultiscale methods.

[Linninger et al., 2013] Linninger, A. A., Gould, I. G., Marinnan, T., Hsu, C.-Y., Chojecki, M., and Alaraj, A. (2013). Cerebral microcirculation and oxygen tension in the human secondary cortex. *Annals of Biomedical Engineering*, 41:2264–2284.

[Lorthois and Cassot, 2010] Lorthois, S. and Cassot, F. (2010). Fractal analysis of vascular networks: Insights from morphogenesis. *Journal of Theoretical Biology*, 262:614–633.

[Lorthois et al., 2011a] Lorthois, S., Cassot, F., and Lauwers, F. (2011a). Simulation study of brain blood flow regulation by intra-cortical arterioles in an anatomically accurate large human vascular network: Part I: Methodology and baseline flow. *NeuroImage*, 54:1031–1042.

[Lorthois et al., 2011b] Lorthois, S., Cassot, F., and Lauwers, F. (2011b). Simulation study of brain blood flow regulation by intra-cortical arterioles in an anatomically accurate large human vascular network. Part II: Flow variations induced by global or localized modifications of arteriolar diameters. *NeuroImage*, 54:2840–2853.

[Lorthois et al., 2014] Lorthois, S., Duru, P., Billanou, I., Quintard, M., and Celsis, P. (2014). Kinetic modeling in the context of cerebral blood flow quantification by $h_2^{15}o$ positron emission tomography:

The meaning of the permeability coefficient in renkin-crone's model revisited at capillary scale. *Journal of Theoretical Biology*, 353:157–169.

[Lu et al., 2009] Lu, J., Zhu, T., Tiab, D., and Owayed, J. (2009). Productivity formulas for a partially penetrating vertical well in a circular cylinder drainage volume. *Mathematical Problems in Engineering*, 2009.

[Lücker et al., 2015] Lücker, A., Weber, B., and Jenny, P. (2015). A dynamic model of oxygen transport from capillaries to tissue with moving red blood cells. *American Journal of Physiology-Heart and Circulatory Physiology*, 308:H206–H216.

[Mayer, 2009] Mayer, J. (2009). Parallel algorithms for solving linear systems with sparse triangular matrices. *Computing*, 86:291–312.

[Mayerich et al., 2011] Mayerich, D., Kwon, J., Sung, C., Abbott, L., Keyser, J., and Choe, Y. (2011). Fast macro-scale transmission imaging of microvascular networks using kesm. *Biomedical optics express*, 2:2888–2896.

[Merrem et al., 2017] Merrem, A., Bartzsch, S., Laissue, J., and Oelfke, U. (2017). Computational modelling of the cerebral cortical microvasculature: effect of x-ray microbeams versus broad beam irradiation. *Physics in Medicine and Biology*, 62:3902.

[Metea and Newman, 2006] Metea, M. R. and Newman, E. A. (2006). Glial cells dilate and constrict blood vessels: a mechanism of neurovascular coupling. *Journal of Neuroscience*, 26:2862–2870.

[Mirams et al., 2013] Mirams, G. R., Arthurs, C. J., Bernabeu, M. O., Bordas, R., Cooper, J., Corrias, A., Davit, Y., Dunn, S.-J., Fletcher, A. G., Harvey, D. G., et al. (2013). Chaste: an open source c++ library for computational physiology and biology. *PLoS Comput Biol*, 9:e1002970.

[Nethercote and Seward, 2003] Nethercote, N. and Seward, J. (2003). Valgrind: A program supervision framework. *Electronic Notes in Theoretical Computer Science*, 89:44–66.

[Nishimura et al., 2006] Nishimura, N., Schaffer, C. B., Friedman, B., Tsai, P. S., Lyden, P. D., and Kleinfeld, D. (2006). Targeted insult to subsurface cortical blood vessels using ultrashort laser pulses: three models of stroke. *Nature Methods*, 3:99–108.

[Passerini et al., 2009] Passerini, T., de Luca, M., Formaggia, L., Quarteroni, A., and Veneziani, A. (2009). A 3d/1d geometrical multiscale model of cerebral vasculature. *Journal of Engineering Mathematics*, 64:319–330.

[Peaceman, 1978] Peaceman, D. (1978). Interpretation of well-block pressures in numerical reservoir simulation. *Society of Petroleum Engineers Journal*, 18:183–194.

[Peaceman, 1983] Peaceman, D. (1983). Interpretation of well-block pressures in numerical reservoir simulation with nonsquare grid blocks and anisotropic permeability. *Exxon Production Research Co.*, 23:531–543.

[Peaceman, 1990] Peaceman, D. (1990). Interpretation of wellblock pressures in numerical reservoir simulation: Part 3 – off-center and multiple wells within a wellblock. *SPE Reservoir Engineering*, 5:227 – 232.

[Peaceman et al., 1993] Peaceman, D. et al. (1993). Representation of a horizontal well in numerical reservoir simulation. *SPE Advanced Technology Series*, 1:7–16.

[Pedley et al., 1971] Pedley, T. J., Schroter, R. C., and Sudlow, M. F. (1971). Flow and pressure drop in systems of repeatedly branching tubes. *Journal of Fluid Mechanics*, 46:365–383.

[Perdikaris et al., 2016] Perdikaris, P., Grinberg, L., and Karniadakis, G. E. (2016). Multiscale modeling and simulation of brain blood flow. *Physics of Fluids*, 28:021304.

[Pitt-Francis et al., 2009] Pitt-Francis, J., Pathmanathan, P., Bernabeu, M. O., Bordas, R., Cooper, J., Fletcher, A. G., Mirams, G. R., Murray, P., Osborne, J. M., Walter, A., et al. (2009). Chaste: a test-driven approach to software development for biological modelling. *Computer Physics Communications*, 180:2452–2471.

[Prabhu et al., 2011] Prabhu, P., Kim, H., Oh, T., Jablin, T. B., Johnson, N. P., Zoufaly, M., Raman, A., Liu, F., Walker, D., Zhang, Y., et al. (2011). A survey of the practice of computational science. In *High Performance Computing, Networking, Storage and Analysis (SC), 2011 International Conference for*, pages 1–12. IEEE.

[Pries, 1996] Pries, A. (1996). Biophysical aspects of blood flow in the microvasculature. *Cardiovascular Research*, 32:654–667.

[Pries et al., 1986] Pries, A., Ley, K., and Gaehtgens, P. (1986). Generalization of the fahraeus principle for microvessel networks. *American Journal of Physiology-Heart and Circulatory Physiology*, 251:H1324–H1332.

[Pries et al., 1992] Pries, A., Neuhaus, D., and Gaehtgens, P. (1992). Blood viscosity in tube flow: dependence on diameter and hematocrit. *American Journal of Physiology-Heart and Circulatory Physiology*, 263:H1770–H1778.

[Pries et al., 1995] Pries, A., Secomb, T. W., and Gaehtgens, P. (1995). Structure and hemodynamics of microvascular networks: heterogeneity and correlations. *American Journal of Physiology-Heart and Circulatory Physiology*, 269:H1713–H1722.

[Pries et al., 1990] Pries, A., Secomb, T. W., Gaehtgens, P., and Gross, J. (1990). Blood flow in microvascular networks. experiments and simulation. *Circulation research*, 67:826–834.

[Quintard and Whitaker, 2000] Quintard, M. and Whitaker, S. (2000). Theoretical analysis of transport in porous media. In *Handbook of Porous Media Second Edition*, pages 1–52. Informa UK Limited.

[Rabenseifner et al., 2009] Rabenseifner, R., Hager, G., and Jost, G. (2009). Hybrid mpi/openmp parallel programming on clusters of multi-core smp nodes. In *Parallel, Distributed and Network-based Processing*, pages 427–436. IEEE.

[Raybaud et al., 1989] Raybaud, C., Strother, C., and Hald, J. (1989). Aneurysms of the vein of galen: embryonic considerations and anatomical features relating to the pathogenesis of the malformation. *Neuroradiology*, 31:109–128.

[Reichold et al., 2009] Reichold, J., Stampanoni, M., Keller, A. L., Buck, A., Jenny, P., and Weber, B. (2009). Vascular graph model to simulate the cerebral blood flow in realistic vascular networks. *Journal of Cerebral Blood Flow & Metabolism*, 29:1429–1443.

[Ribeiro and Maliska, 2014] Ribeiro, G. G. and Maliska, C. R. (2014). Extension of peaceman's and ding's well indexes for application in 3d reservoir simulation with horizontal wells. In *15th Brazilian Congress of Thermal Sciences and Engineering*. ABCM.

[Risser et al., 2007] Risser, L., Plourabouré, F., Steyer, A., Cloetens, P., Le Duc, G., and Fonta, C. (2007). From homogeneous to fractal normal and tumorous microvascular networks in the brain. *Journal of Cerebral Blood Flow & Metabolism*, 27:293–303.

[Roman et al., 2016] Roman, S., Merlo, A., Duru, P., Risso, F., and Lorthois, S. (2016). Going beyond 20 μ m-sized channels for studying red blood cell phase separation in microfluidic bifurcations. *Biomicrofluidics*, 10:034103.

[Rottschy et al., 2012] Rottschy, C., Langner, R., Dogan, I., Reetz, K., Laird, A. R., Schulz, J. B., Fox, P. T., and Eickhoff, S. B. (2012). Modelling neural correlates of working memory: a coordinate-based meta-analysis. *NeuroImage*, 60:830–846.

[Ryoo et al., 2008] Ryoo, S., Rodrigues, C. I., Stone, S. S., Stratton, J. A., Ueng, S.-Z., Baghsorkhi, S. S., and Wen-mei, W. H. (2008). Program optimization carving for gpu computing. *Journal of Parallel and Distributed Computing*, 68:1389–1401.

[Sahimi, 2011] Sahimi, M. (2011). *Flow and transport in porous media and fractured rock: from classical methods to modern approaches*. John Wiley & Sons.

[Sakadžić et al., 2014] Sakadžić, S., Mandeville, E. T., Gagnon, L., Musacchia, J. J., Yaseen, M. A., Yucel, M. A., Lefebvre, J., Lesage, F., Dale, A. M., Eikermann-Haerter, K., et al. (2014). Large arteriolar component of oxygen delivery implies safe margin of oxygen supply to cerebral tissue. *Nature communications*, 5:5734.

[Santisakultarm et al., 2012] Santisakultarm, T. P., Cornelius, N. R., Nishimura, N., Schafer, A. I., Silver, R. T., Doerschuk, P. C., Olbricht, W. L., and Schaffer, C. B. (2012). In vivo two-photon excited fluorescence microscopy reveals cardiac-and respiration-dependent pulsatile blood flow in cortical blood vessels in mice. *American Journal of Physiology-Heart and Circulatory Physiology*, 302:H1367–H1377.

[Schloegel et al., 2000a] Schloegel, K., Karypis, G., and Kumar, V. (2000a). *Graph partitioning for high performance scientific simulations*. Army High Performance Computing Research Center.

[Schloegel et al., 2000b] Schloegel, K., Karypis, G., and Kumar, V. (2000b). Parallel multilevel algorithms for multi-constraint graph partitioning. In *Euro-Par 2000 Parallel Processing*, pages 296–310. Springer.

[Schmid et al., 2017] Schmid, F., Barrett, M. J., Jenny, P., and Weber, B. (2017). Vascular density and distribution in neocortex. *NeuroImage*. Corrected proof.

[Schwabe et al., 1967] Schwabe, K., Brand, J., et al. (1967). Prediction of reservoir behavior using numerical simulators. In *Fall Meeting of the Society of Petroleum Engineers of AIME*. Society of Petroleum Engineers.

[Secomb et al., 2004] Secomb, T. W., Hsu, R., Park, E. Y., and Dewhirst, M. W. (2004). Green's function methods for analysis of oxygen delivery to tissue by microvascular networks. *Annals of biomedical engineering*, 32:1519–1529.

[Shih et al., 2012] Shih, A. Y., Driscoll, J. D., Drew, P. J., Nishimura, N., Schaffer, C. B., and Kleinfeld, D. (2012). Two-photon microscopy as a tool to study blood flow and neurovascular coupling in the rodent brain. *Journal of Cerebral Blood Flow & Metabolism*, 32:1277–1309.

[Shih et al., 2015] Shih, A. Y., Rühlmann, C., Blinder, P., Devor, A., Drew, P. J., Friedman, B., Knutsen, P. M., Lyden, P. D., Mateo, C., Mellander, L., et al. (2015). Robust and fragile aspects of cortical blood flow in relation to the underlying angioarchitecture. *Microcirculation*, 22:204–218.

[Shipley and Chapman, 2010] Shipley, R. J. and Chapman, S. J. (2010). Multiscale modelling of fluid and drug transport in vascular tumours. *Bulletin of Mathematical Biology*, 72:1464–1491.

[Smith, 2016] Smith, A. (2016). Structural and hemodynamic comparison of synthetic and antomical cerebral capillary networks. European Society of Biomechanics, Lyon, France.

[Smith et al., 2014] Smith, A. F., Shipley, R. J., Lee, J., Sands, G. B., LeGrice, I. J., and Smith, N. P. (2014). Transmural variation and anisotropy of microvascular flow conductivity in the rat myocardium. *Annals of Biomedical Engineering*, 42:1966–1977.

[Smith and Bull, 2001] Smith, L. and Bull, M. (2001). Development of mixed mode mpi/openmp applications. *Scientific Programming*, 9:83–98.

[Sourbron, 2014] Sourbron, S. (2014). A tracer-kinetic field theory for medical imaging. *IEEE Transactions on Medical Imaging*, 33:935–946.

[Tang and Karniadakis, 2014] Tang, Y.-H. and Karniadakis, G. E. (2014). Accelerating dissipative particle dynamics simulations on gpus: Algorithms, numerics and applications. *Computer Physics Communications*, 185:2809–2822.

[Trifunovic, 2006] Trifunovic, A. (2006). *Parallel algorithms for hypergraph partitioning*. University of London.

[Tsai et al., 2009] Tsai, P. S., Kaufhold, J. P., Blinder, P., Friedman, B., Drew, P. J., Karten, H. J., Lyden, P. D., and Kleinfeld, D. (2009). Correlations of neuronal and microvascular densities in murine cortex revealed by direct counting and colocalization of nuclei and vessels. *Journal of Neuroscience*, 29:14553–14570.

[Van Luong et al., 2013] Van Luong, T., Melab, N., and Talbi, E.-G. (2013). Gpu computing for parallel local search metaheuristic algorithms. *IEEE transactions on computers*, 62:173–185.

[Vanderstraeten and Keunings, 1995] Vanderstraeten, D. and Keunings, R. (1995). Beyond conventional mesh partitioning algorithms and the minimum edge cut criterion: Impact on realistic applications. Technical report, Society for Industrial and Applied Mathematics, Philadelphia, PA (United States).

[Vaninva Versini, 2017] Vaninva Versini, S. L. (2017). Propriétés macroscopiques de l'écoulement sanguin dans des réseaux capillaires modèle: influence de la complexité géométrique et de la raréfaction. Internship at the Institut de Mécanique des Fluides de Toulouse.

[Versteeg and Malalasekera, 2007] Versteeg, H. K. and Malalasekera, W. (2007). *An introduction to computational fluid dynamics: the finite volume method*. Pearson Education.

[Walshaw and Cross, 2000] Walshaw, C. and Cross, M. (2000). Parallel optimisation algorithms for multilevel mesh partitioning. *Parallel Computing*, 26:1635–1660.

[Waters et al., 2011] Waters, S. L., Alastruey, J., Beard, D. A., Bovendeerd, P. H., Davies, P. F., Jayaraman, G., Jensen, O. E., Lee, J., Parker, K. H., Popel, A. S., et al. (2011). Theoretical models for coronary vascular biomechanics: progress & challenges. *Progress in Biophysics and Molecular Biology*, 104:49–76.

[Weber et al., 2008] Weber, B., Keller, A. L., Reichold, J., and Logothetis, N. K. (2008). The microvascular system of the striate and extrastriate visual cortex of the macaque. *Cerebral Cortex*, 18:2318–2330.

[Werring et al., 2004] Werring, D. J., Frazer, D. W., Coward, L. J., Losseff, N. A., Watt, H., Cipolotti, L., Brown, M. M., and Jäger, H. R. (2004). Cognitive dysfunction in patients with cerebral microbleeds on t2*-weighted gradient-echo mri. *Brain*, 127:2265–2275.

[Whitaker, 1986] Whitaker, S. (1986). Flow in porous media i: A theoretical derivation of darcy's law. *Transport in porous media*, 1:3–25.

[Williamson et al., 1981] Williamson, A. S., Chappelear, J. E., et al. (1981). Representing wells in numerical reservoir simulation: part 1-theory. *Society of Petroleum Engineers Journal*, 21:323–338.

[Wilson et al., 2014] Wilson, G., Aruliah, D., Brown, C. T., Hong, N. P. C., Davis, M., Guy, R. T., Haddock, S. H., Huff, K. D., Mitchell, I. M., Plumbley, M. D., et al. (2014). Best practices for scientific computing. *PLoS Biol*, 12:e1001745.

[Wintermark et al., 2005] Wintermark, M., Sesay, M., Barbier, E., Borbély, K., Dillon, W. P., Eastwood, J. D., Glenn, T. C., Grandin, C. B., Pedraza, S., Soustiel, J.-F., et al. (2005). Comparative overview of brain perfusion imaging techniques. *Stroke*, 36:e83–e99.

[Witthoft et al., 2016] Witthoft, A., Yazdani, A., Peng, Z., Bellini, C., Humphrey, J. D., and Karniadakis, G. E. (2016). A discrete mesoscopic particle model of the mechanics of a multi-constituent arterial wall. *Journal of The Royal Society Interface*, 13:20150964.

[Wolfsteiner et al., 2003] Wolfsteiner, C., Durlofsky, L., and Aziz, K. (2003). Calculation of well index for nonconventional wells on arbitrary grids. *Computational Geosciences*, 7:61–82.

[Zhang et al., 2009] Zhang, J., Johnson, P. C., and Popel, A. S. (2009). Effects of erythrocyte deformability and aggregation on the cell free layer and apparent viscosity of microscopic blood flows. *Microvascular Research*, 77:265–272.

[Zhang et al., 2015] Zhang, M.-Q., Zhou, L., Deng, Q.-F., Xie, Y.-Y., Xiao, T.-Q., Cao, Y.-Z., Zhang, J.-W., Chen, X.-M., Yin, X.-Z., and Xiao, B. (2015). Ultra-high-resolution 3d digitalized imaging of the cerebral angioarchitecture in rats using synchrotron radiation. *Scientific reports*, 5.

[Zilow and Linderkamp, 1989] Zilow, E. P. and Linderkamp, O. (1989). Viscosity reduction of red blood cells from preterm and full-term neonates and adults in narrow tubes (fahraeus-lindqvist effect). *Pediatric research*, (6):595–599.